



# JOURNAL *of the* MEXICAN CHEMICAL SOCIETY

*(J. Mex. Chem. Soc.)  
Former Revista de la Sociedad Química de México (Rev. Soc. Quím. Mex.)*



*Regular Issue*

*J. Mex. Chem. Soc.*

Volume 68

Issue 3

July-September

Year 2024

Quarterly publication

[www.jmcs.org.mx](http://www.jmcs.org.mx)

Mexico City



# JOURNAL *of the* MEXICAN CHEMICAL SOCIETY

*(J. Mex. Chem. Soc.)*

*Former Revista de la Sociedad Química de México (Rev. Soc. Quím. Mex.)*



*Regular Issue*

*J. Mex. Chem. Soc.*

Volume 68

Issue 3

July-September

Year 2024

Quarterly publication

[www.jmcs.org.mx](http://www.jmcs.org.mx)

Mexico City

The *Sociedad Química de México* was founded in 1956 as a non-profit association to promote the development of the professionals and students of chemistry in education, research, services and industry, and for the diffusion of chemical knowledge. The *Sociedad Química de México* organizes annually the *Mexican Congress of Chemistry* and the *National Congress of Chemical Education*, both congresses include activities of current interest for professionals and students of the chemical sciences. It grants annually the “*Andrés Manuel del Río*” *National Award of Chemistry* in the Academic area (field of research and field of education) and in the Technological area (field of technological development). It also grants each year the *Rafael Illescas Frisbie Best Bachelor, Master and Doctoral Thesis in Chemical Sciences Awards* and the biennial *Award of the Sociedad Química de México in honor of the Doctor Mario J. Molina, directed to the professionals in Chemistry Sciences*.

The *Journal of the Mexican Chemical Society (J. Mex. Chem. Soc.)* is the official journal of the *Sociedad Química de México*, it was published as *Revista de la Sociedad Química de México (Rev. Soc. Quím. Mex.)* from 1957 to 2003, changing its name in 2004. The *Journal of the Mexican Chemical Society (J. Mex. Chem. Soc.)* is a scientific, blind, peer reviewed, and open access, free of charge publication that covers all areas of chemistry and its sub-disciplines (i.e. medicinal chemistry, natural products, electrochemistry, material science, computational chemistry, organic chemistry, bioinorganic chemistry, etc). It is devoted to facilitating the worldwide advancement of our understanding of chemistry. It will primarily publish original contributions of research in all branches of the theory and practice of chemistry in its broadest context as well as critical reviews in active areas of chemical research where the author has published significant contributions. The *J. Mex. Chem. Soc.* is a quarterly publication in which language of submission and publication is English. To be suitable for publication in *J. Mex. Chem. Soc.*, manuscripts must describe novel aspects of chemistry, high quality of results and discussion an excellent bibliographic support, and contribute to the development of the field. Routine or incremental works are not suitable for publication in *J. Mex. Chem. Soc.* Authors are encouraged to send contributions in electronic form. Our online submission system guides you stepwise through the process of entering your article details and uploading your files. The *Sociedad Química de México* also publishes since 2007 articles of general interest in the *Boletín de la Sociedad Química de México*.

La *Sociedad Química de México* fue fundada en 1956 como una agrupación sin fines de lucro para promover el desarrollo de los profesionales y estudiantes de la química en las áreas educativa, investigación, servicios e industria, y para difundir el conocimiento de la química. La *Sociedad Química de México* organiza anualmente el *Congreso Mexicano de Química* y el *Congreso Nacional de Educación Química*, en los cuales se desarrollan diversas actividades de interés para los profesionales y estudiantes de las ciencias químicas. Asimismo, otorga anualmente el *Premio Nacional de Química “Andrés Manuel del Río”* en el área Académica (campos de docencia e investigación) y en el área Tecnológica (campo de Desarrollo Tecnológico). También otorga anualmente el *Premio a las Mejores Tesis de Licenciatura, Maestría y Doctorado en Ciencias Químicas, Rafael Illescas Frisbie*. De manera bienal otorga el *Premio de la Sociedad Química de México en Honor al Doctor Mario J. Molina, dirigido a los profesionistas de las Ciencias Químicas*.

El *Journal of the Mexican Chemical Society (J. Mex. Chem. Soc.)*, es la revista oficial de la *Sociedad Química de México*. Desde 1957 y hasta 2003 fue publicada como *Revista de la Sociedad Química de México (Rev. Soc. Quím. Mex.)*, cambiando su nombre en 2004. Es una publicación trimestral que tiene como objetivo coadyuvar al avance del entendimiento de la química; las instrucciones para los autores aparecen en cada fascículo. La *Sociedad Química de México* también publica desde 2007 artículos de interés general en el *Boletín de la Sociedad Química de México*

**Journal of the Mexican Chemical Society**  
(*J. Mex. Chem. Soc.*)

ISSN-e: 2594-0317  
ISSN 1870-249X

former

**Revista de la Sociedad Química de México**  
(*Rev. Soc. Quím. Mex.*)

ISSN 0583-7693

*Journal of the Mexican Chemical Society (J. Mex. Chem. Soc.)*

Quarterly publication.

Editor-in-Chief: Prof. Alberto Vela Amieva

Indexed Journal

Certificate of reserved rights granted by the Instituto Nacional del Derecho de Autor (INDAUTOR): 04-2005-052710530600-102

Certificate of lawful title and content: Under procedure

Postal registration of printed matter deposited by editors or agents granted by SEPOMEX: IM09-0312

Copyright © Sociedad Química de México, A.C.

Total or partial reproduction is prohibited without written permission of the right holder.

The Figures/schemes quality and the general contents of this publication are full responsibility of the authors.

Edited and distributed by Sociedad Química de México, A.C.

Barranca del Muerto 26, Col. Crédito Constructor,

Del. Benito Juárez, C.P. 03940, Mexico City.

Phone: +5255 56626837; +5255 56626823

Contact: [soquimex@sqm.org.mx](mailto:soquimex@sqm.org.mx)

<https://www.sqm.org.mx>

Editorial assistance: [jmcs@sqm.org.mx](mailto:jmcs@sqm.org.mx)

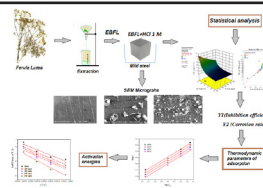
<https://www.jmcs.org.mx>



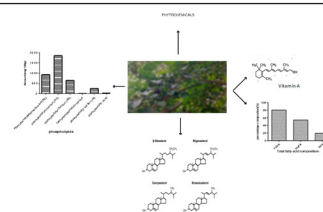
## Table of Contents

### Articles

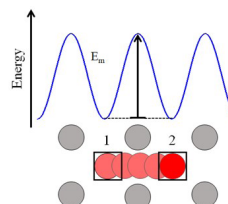
- 344-365 **Experimental and Statistical Investigation of a Novel Green Inhibitor *Ferula Lutea* as Potential Corrosion Inhibiting Carbon Steel in an Acidic Medium**  
*Wafia Boukhedena\**, *Samir Deghboudj*, *Merzoug Benahmed*, *Hocine Laouer*



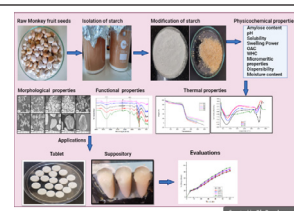
- 366-378 **Bioactive Lipids, Nutritional Benefits and Phytochemicals Present in *Hura Crepitans* Seed Oil**  
*Ayomadewa Mercy Olatunya\**, *Adeolu Jonathan Adesina*



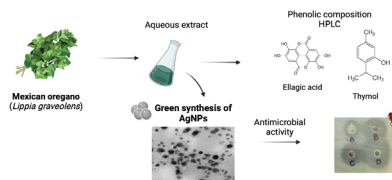
- 379-387 **Ion Migration Study on  $\text{YAlO}_3$ -perovskite through Atomistic Simulations**  
*Rubén O. Miranda-Rosales*, *J. Francisco Gómez-García\**



- 388-401 **Studies on the *Artocarpus lakoocha* Seeds for Drug Delivery**  
*Surabhi Chaurasia\**, *Anima Pandey\**



- 402-411 **Biosynthesis of Silver Nanoparticles Mediated by *Lippia graveolens* Aqueous Extract**  
*Karen M. Soto*, *Montserrat Hernández-Iturriaga*, *Arely Cárdenas*, *Sandra Mendoza\**



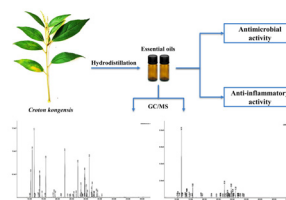
\* The asterisk indicates the name of the author to whom inquiries about the paper should be addressed.



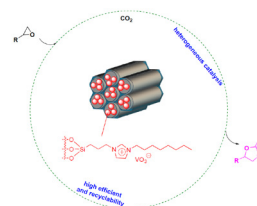
# Table of Contents

## Articles

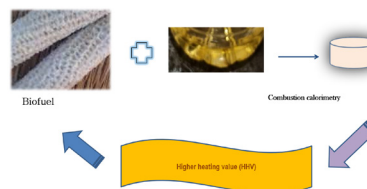
- 412-424** **Chemical Constituents, Antimicrobial Activity and Nitric Oxide Production Inhibitory Activity of Essential Oil from the Leaves of *Croton kongensis* Gagnep. Collected from Two Different Locations in Vietnam**  
*Le D. Chac\**, *Hoang V. Chinh*, *Nguyen T. M. Hong*, *Bui B. Thinh\**



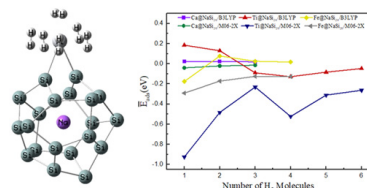
- 425-437** **Novel and Reusable Magnetic Zinc Ferrites Modified SBA-15 Supported Ionic Liquids for Sustainable and Efficient Cycloaddition of CO<sub>2</sub> and Epoxides to Cyclic Carbonates**  
*Yu Lin Hu\**, *Zhi Guo Sun*, *Xiao Bing Liu*



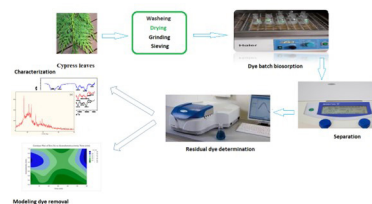
- 438-454** **The Influence of Additives Upon the Energetic Parameters and Physicochemical Properties of Environmentally Friendly Biomass Pellets**  
*Daniela Gheorghe*, *Ana Neacsu\**



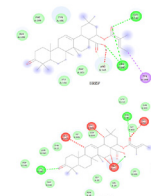
- 455-468** **A DFT Study of the Hydrogen Storage Potentials and Properties of Ca, Fe, and Ti Deposited NaSi<sub>20</sub> Fullerenes**  
*Huixi Yang*, *Bin Liu\**, *Hongjiang Ren\**



- 469-493** **Experimental Studies to Optimize Process Parameters for the Removal of Cationic and Anionic Dyes by Natural Cypress Leaves**  
*Oussama Larabi*, *Afaf Amara-Rekkab\**, *Mohamed Amine Didi*, *Amel Didi*, *Souad Feddane*



- 494-512** **Comparative Vibrational analysis, Electronic Properties, and molecular docking of Lantadene A and B (Potential anticancer agents) - A Computational DFT Study**  
*Anoop Kumar Pandey*, *Shashwat Shukla*, *O.P. Yadav*, *Vijay Singh*, *Apoorva Dwivedi\**



\* The asterisk indicates the name of the author to whom inquiries about the paper should be addressed.

## Table of Contents

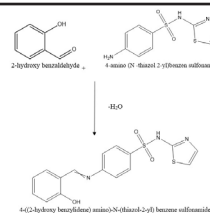
---

### Articles

---

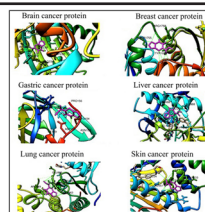
**Quantum Computational Chemistry and  
513-526 Optoelectronic Properties of a New Synthesis Organic  
Compound**

*Dyari Mustafa Mamand, Dara Muhammed Aziz, Hiwa  
Mohammad Qadr\*, Awat Hamad Awla*



**DFT Calculation, ADME/T and Molecular Docking  
527-544 Approach of Methyl 2-oxo-1,2-dihydrofuro[3,4-d]  
pyrimidine-3(4H)carboxylate**

*Gühergöl Uluçam\**



\* The asterisk indicates the name of the author to whom inquiries about the paper should be addressed.

## Experimental and Statistical Investigation of a Novel Green Inhibitor *Ferula Lutea* as Potential Corrosion Inhibiting Carbon Steel in an Acidic Medium

---

Wafia Boukhedena<sup>1,3,\*</sup>, Samir Deghboudj<sup>2,3</sup>, Merzoug Benahmed<sup>4</sup>, Hocine Laouer<sup>5</sup>

<sup>1</sup>Department of Science Materials, Larbi Tebessi University, Constantine Road, 12002 Tebessa, Algeria.

<sup>2</sup>Department of Mechanics, Larbi Tebessi University, Constantine Road, 12002, Tebessa, Algeria.

<sup>3</sup>Mines Laboratory, Larbi Tebessi University, Constantine Road, 12002, Tebessa, Algeria.

<sup>4</sup>Laboratory of Bioactive Molecules and Applications, Constantine Road, 12002, Tebessa, Algeria.

<sup>5</sup>Laboratory for the Valorization of Natural Biological Resources, Ferhat Abbas University, Setif, 19000, Algeria.

\*Corresponding author: Wafia Boukhedena, email: [wafia.boukhedena@univ-tebessa.dz](mailto:wafia.boukhedena@univ-tebessa.dz)

Received October 25<sup>th</sup>, 2022; Accepted June 6<sup>th</sup>, 2023.

DOI: <http://dx.doi.org/10.29356/jmcs.v68i3.1891>

**Abstract.** Carbon steel corrosion inhibition in the presence and absence of *Ferula lutea* butanolic extract (EBFL) as a corrosion inhibitor was investigated. This study focuses on the optimization of three main parameters: inhibitor concentration, immersion time, and temperature, on the corrosion inhibition of X2C30 carbon steel by EBFL based on the weight loss method. A composite-centered design (CCD) of response surface methodology (RSM) was employed to design the experiment utilizing Design Expert software in to assess the experimental factors that influence the process. Both the corrosion rate and the inhibition efficiency were modeled using logarithmic quadratic equations. The achieved correlation between the predicted and experimental values reveals the accuracy of the proposed models. This investigation proved that (RSM) is a useful tool to predict the optimal operating parameters of the examined inhibitor to mitigate carbon steel corrosion. Gravimetric and electrochemical measurements have indicated that extract (EBFL) exhibits corrosion inhibition properties of X2C30 carbon steel in 1 M hydrochloric acid medium.

**Keywords:** Corrosion; carbon steel; *Ferula lutea*; weight loss measurements; surface response methodology.

**Resumen.** Se investigó la inhibición de la corrosión del acero al carbono en presencia y ausencia del extracto butanólico de *Ferula lutea* (EBFL) como inhibidor de la corrosión. Este estudio se centra en la optimización de tres parámetros principales: la concentración del inhibidor, el tiempo de inmersión y la temperatura, sobre la inhibición de la corrosión del acero al carbono X2C30 por el EBFL basándose en el método de la pérdida de peso. Se empleó un diseño centrado en el compuesto (CCD) de la metodología de superficie de respuesta (RSM) para diseñar el experimento utilizando el software Design Expert en para evaluar los factores experimentales que influyen en el proceso. Tanto la velocidad de corrosión como la eficiencia de inhibición se modelaron mediante ecuaciones cuadráticas logarítmicas. La correlación alcanzada entre los valores predichos y los experimentales revela la precisión de los modelos propuestos. Esta investigación demostró que (RSM) es una herramienta útil para predecir los parámetros operativos óptimos del inhibidor examinado para mitigar la corrosión del acero al carbono. Las mediciones gravimétricas y electroquímicas han indicado que el extracto (EBFL) presenta propiedades de inhibición de la corrosión del acero al carbono X2C30 en medio ácido clorhídrico 1 M.

**Palabras clave:** Corrosión; acero al carbono; *Ferula lutea*; medidas de pérdida de peso; metodología de respuesta superficial.

---

## Introduction

Steel and its alloys are widely used in the construction of tanks, pipes and oil refining equipment [1,2]. These installations are highly vulnerable to corrosion and have a low resistance to aggressiveness in the presence of acid solutions, which are often used to remove unwanted scale and rust in many industrial processes. The most widely commercialized and used acid is hydrochloric acid (HCl). To effectively control corrosion of carbon steel there are several methods, however, corrosion inhibitors remain among the most effective and practical methods [3-6].

Inhibitors are being used to control steel dissolution and reduce acid consumption [6,7]. Currently, research on inhibitors includes a variety of activities ranging from protective mechanisms to the monitoring of industrial systems in which inhibitors are utilized, to the discovery and synthesis of new compounds, to the assessment of competitively traded products [8]. Corrosion inhibitors are organic and inorganic substances, which are added to the corrosive environment in an attempt to reduce or eliminate corrosion. These substances are adsorbed to the metal surface and change the structure of the electrical double layer. The adsorption process depends mainly on the molecular structure. However, the use of some organic and inorganic chemical inhibitors is limited because their synthetically produced compounds are very high in cost, their biodegradability is limited and they are toxic, harmful, and dangerous to humans and the environment [9,10]. The most recent research in the domain are focused on the corrosion-inhibiting properties of natural plant extracts [11,12]. These represent extremely rich sources of natural chemical compounds that are eco-friendly and not harmful, cheap, available, and abundant, renewable, and can be extracted by simple processes and techniques.

A substantial number of reports, reviews, and books have been devoted to the use of green plant-based corrosion inhibitors for metals in acidic mediums. It has been stated that plant extracts have excellent inhibiting abilities, with low or no negative impact on the environment. Several types of research are available justifying the suitability of the plant-based inhibitor. Among the various inhibitors of plant origin studied, we mention particularly those dedicated to the protection of metals against corrosion in acidic environments. Valek and Martinez [13] investigated the inhibition of the corrosion of the copper in sulfuric acid 0.5 M by leaf extract of *Azadirachta indica*. The methods used were intensity-potential curves and weight loss. *Azadirachta indica* revealed an efficacy of 86.4 %. The effect of *Punica granatum* extract and its main constituents on the inhibition of mild steel in 2 M HCl and 1 M H<sub>2</sub>SO<sub>4</sub> solutions was examined by M. Behpour et al. [14] using weight loss, potentiodynamic polarization and electrochemical impedance spectroscopy (EIS) for various concentrations of the extract. *Azadirachta indica* exhibited an inhibitory efficiency of 95.8 % in HCl solution and 94.2 % in H<sub>2</sub>SO<sub>4</sub> solution. N. Soltani et al. [15] studied the influence of *Silybum marianum* leaf extract as a corrosion inhibitor of 304 stainless steel in 1.0 M HCl solution. The highest extract concentration, 1.0 g/L, leads to a rise in inhibitory efficiency that reaches 96 %. In recent research, the inhibitory effect of *Laurus nobilis* leaf extract for carbon steel in 1M HCl acid medium was examined [16]. The achieved findings indicated a maximum protection of 92 %, which was obtained after 2.5 h at a concentration of 400 ppm of the extract.

In general, for any material, there is a suitable family of inhibitors to provide satisfactory protection against corrosion. Extracts of certain plants such as *Portulaca grandiflora* [17], *Ficus tikoua leaves* [18], *Neolamarckia cadamba barks* [19], *Ephedra Major* [20], *Thapsia villosa* [21], *Arthrospira platensis* [22], *Sansevieria trifasciata* [23], *Orange peel* [24], have been reported to inhibit corrosion of metals in acid solutions.

Analytical chemistry is increasingly using response surface methodology (RSM) as a tool for optimization. It comprises a group of statistical and mathematical methods based on fitting empirical models to experimental data gathered following the experimental design. To achieve this goal, the studied system is described using linear or square polynomial functions, which are then used to investigate (by modeling) the experimental conditions until its optimization [25-30].

The present work is part of the experimental investigations on the inhibition of corrosion of metal surfaces by the use of green inhibitors. It is in this regard that we examined the corrosion inhibition of a X2C30 carbon steel by the butanolic extract of the plant *Ferula lutea* denominated (EBFL) in a 1 M hydrochloric acid medium. We applied electrochemical and gravimetric techniques to determine the efficiency of the inhibitor, its mode of acting as well as several corrosion parameters. The values of the most significant operational parameters have been optimized using the response surface methodology (RSM) based on composite-centered design (CCP) to enhance the associated responses. The two responses examined were: inhibitory efficiency and corrosion rate. The building



of the experimental design, the statistical analysis, and the graphical representation of the model as well as the optimization study of the factors that influence these responses were carried out using the design-Expert software.

## Materials and methods

### Samples preparation

The material used as the working electrode is a carbon steel of quality X2C30, having the following chemical composition (in % by weight): C (0.35); Si (0.4); Mn (0.8); P (0.035); S (0.035) and Fe remainder. Weight loss measurements were conducted on prepared 1×1×1 cm cubes abraded successively with different grades of emery paper (320, 400, 500, 800, 1000, 1200, and 2000), washed with distilled water, cleaned with acetone, and dried at room temperature before being utilized in the experiments.

### Preparation of HCl solution

The corrosive medium is a 1 M hydrochloric acid solution, obtained by diluting the commercial concentrated acid of HCl 37 % (Merck) with distilled water. The tests were carried out in this solution without and with the addition of different concentrations (200,500 and 800 ppm) of the extract: n-Butanol of the plant *Ferula lutea* (EBFL).

### Solid-liquid extraction

The plant was collected during its flowering period in May in the area of mountain Babor in the province of Setif in eastern Algeria. Solid-liquid extraction employed in this work is a technique, which consists in letting the plant material (cut in small pieces) stay in the water/methanol mixture (aqueous methanol) to extract the active principles (phenolic compounds and flavonoids). The protocol for the n-butanolic extract of *Ferula lutea* was carried out according to the literature reports [20,31,32].

### Weight loss measurements

This method is relatively easy and does not require any important equipment. It consists of exposing surface samples (S) in HCl 1M medium in the absence and presence of different concentrations of the inhibitor (EBFL) maintained at constant temperature for a well-defined time (t) and measuring the mass difference ( $\Delta W$ ) of the samples before ( $W_i$ ) and after ( $W_f$ ) for each test. (1): The loss in weight, corrosion rate, and inhibitor efficiency were established according to the following relationship:

$$CR = \frac{\Delta W}{S.t} \quad (1)$$

The inhibition efficiency ( $IE_w$  %) can be calculated using Equation (2):

$$IE_w \% = \left( \frac{CR_0 - CR_i}{CR_0} \right) \times 100 \quad (2)$$

where,  $CR_0$  and  $CR_i$  are the corrosion rates in the absence and presence of various concentrations of inhibitor respectively. The corrosion rate (CR) and the inhibition efficiency ( $IE_w$ %) are very useful to discuss the adsorption characteristics and thermodynamic parameters that were calculated.

### Response surface methodology

An experimental design is a statistical method to control a multi-parameter (factor) problem by following a pre-conceived program of different experiments to be performed. Its purpose is to minimize the number of experiments in order to achieve accurate results that reflect the real variation of the studied phenomenon concerning its different attributes [28,29,33]. A constrained calculation interval is one of the characteristics of this experimental design. The levels utilized, indicated by the values (-1) and (+1), represent the minimum and maximum level values allocated to the components that are centered around a middle value,

respectively (0). Several parameters influence corrosion inhibition such as inhibitor concentration, immersion time, and temperature. In this work, the responses retained are inhibitory efficiency ( $IE_w$  %) and corrosion rate (CR). Composite Centered Design (CCD) based Response Surface Methodology (RSM) was used to investigate and statistically analyze the effect of (EBFL) on corrosion inhibition of carbon steel in 1M HCl acid medium. These modeling methods allow for mathematical models involving different parameters that affect the inhibition efficiency and the corrosion rate. All the planned experiments as well as the statistical analysis of the results were done with Design-Expert, which is a specialized software for the planning and analysis of experiments. Table 1 depicts the various levels and factors that were further into the design of this experiment.

In this work, a fitting analysis is recommended using a model comprising a logarithmic polynomial interaction effects equation. The most common second-order polynomial equation for generating the relevant model terms and fitting the experimental data is formulated as follows:

$$\ln(Y) = a_0 + \sum_{i=1}^k a_i X_i + \sum_{i=1}^k a_{ij} X_i^2 + \sum_{i=1}^k \sum_{j=1}^k a_{ij} X_i X_j + \varepsilon_i \quad (3)$$

where Y represents the predicted response, i.e., inhibition efficiency ( $IE_w$  %) and corrosion rate (CR),  $a_0$ , the constant parameter,  $X_i$  and  $X_j$  the variables,  $a_i$ , the  $i^{\text{th}}$  linear coefficient of the input factor  $X_i$ ,  $a_{ij}$ , the  $i^{\text{th}}$  quadratic coefficient of the input factors  $X_i$ ,  $a_{ij}$ , the different interaction coefficients between the input factors  $X_i$  and  $X_j$  ( $i=1-3$ ,  $j=1-3$ ), and  $\varepsilon_i$ , the model error [34]. As an alternative to performing a test campaign involving 27 experiments for the inhibition efficiency and another 27 for the corrosion rate test, this number can be minimized to only 17 for each of these two trials, by selecting and applying an experimental design with RSM and CCD Design and using the Design expert software.

**Table 1.** Factor levels of the independent variables of the central composite design

| Factors             | Symbols variables | Min level (-1) | Medium level | Max level (+1) |
|---------------------|-------------------|----------------|--------------|----------------|
| Concentration (ppm) | A                 | 200            | 500          | 800            |
| Temperature (°C)    | B                 | 20             | 35           | 50             |
| Immersion time (h)  | C                 | 1              | 2            | 3              |

### Scanning electron microscopy (SEM)

The samples for surface morphological examinations were immersed in a 1 M HCl solution containing the optimal concentration found of the inhibitor (800 ppm) for 3 hours at 20 °C. Then they were removed, washed quickly with distilled water, and dried. The analyses were performed using a scanning electron microscope; model JEOL JSM-6360 LV.

## Results and discussion

### Weight loss measurements

As depicted in Table, the achieved results of the weight loss tests show that the inhibition efficiency  $IE_w$  (%) increases while the corrosion rate decreases with the increase of the inhibitor concentration (EBFL). The inhibition efficiency reaches a maximum value of 87.44 % corresponding to the critical concentration (800 ppm), the immersion time (3 hours), and the lowest temperature (20 °C). This maximum inhibition efficiency is reached when the inhibitor concentration and immersion time have their maximum values. This behavior can be attributed to strong adsorption of the inhibitor on the surface of the carbon steel (X2C30) [35-38]. On the other hand, the lowest inhibition efficiency of 20.61 % is observed when the inhibitor concentration and immersion time are at the lowest level, and the temperature reaches its highest values, i.e. 200 ppm and 1h, respectively.

**Table 2.** Central composite matrix of factors A, B, and C and the experimental values of responses Y<sub>1</sub> and Y<sub>2</sub>, obtained by weight loss measurements.

| Run | Factor1(A) | Factor 2 (B) | Factor 3 (C) | Response1 (Y <sub>1</sub> ) | Response2 (Y <sub>2</sub> ) |
|-----|------------|--------------|--------------|-----------------------------|-----------------------------|
| N°  | Conc (ppm) | Temp (°C)    | Time (h)     | IE <sub>w</sub> (%)         | CR (mg/cm <sup>2</sup> .h)  |
| 1   | 800        | 20           | 1            | 86.88                       | 0.0316                      |
| 2   | 500        | 35           | 3            | 56.57                       | 0.1412                      |
| 3   | 200        | 20           | 1            | 32.36                       | 0.1785                      |
| 4*  | 500        | 35           | 2            | 47.72                       | 0.1523                      |
| 5   | 200        | 50           | 3            | 29.64                       | 1.3471                      |
| 6   | 500        | 35           | 1            | 42.40                       | 0.1492                      |
| 7*  | 500        | 35           | 2            | 47.72                       | 0.1523                      |
| 8   | 800        | 35           | 2            | 67.77                       | 0.0939                      |
| 9*  | 500        | 35           | 2            | 47.72                       | 0.1523                      |
| 10  | 200        | 35           | 2            | 25.71                       | 0.2163                      |
| 11  | 800        | 50           | 1            | 62.01                       | 0.5353                      |
| 12  | 500        | 20           | 2            | 57.59                       | 0.0636                      |
| 13  | 800        | 20           | 3            | 87.44                       | 0.0223                      |
| 14  | 200        | 20           | 3            | 37.33                       | 0.1113                      |
| 15  | 500        | 50           | 2            | 40.82                       | 0.8913                      |
| 16  | 800        | 50           | 3            | 71.90                       | 0.5380                      |
| 17  | 200        | 50           | 1            | 20.61                       | 1.1186                      |

\*Three points in the center of the model.

### ANOVA and regression models

The analysis of variance (ANOVA) is a statistical test (Fisher-Snedecor test) that enables users to analyze the variances of the values generated by the model and those of the residuals. The software suggested the logarithmic quadratic model used (equations 4 and 5), for both responses (inhibitory efficiency and corrosion rate). The significance of the model, each factor, and the interactions are checked using a Fisher's test (F). The more F is greater, the less probability (Prob>F) is, and the more significant the related model and the main coefficients are. If the value of (Prob>F) is lower than 0.05, then the model is significant at a 95 % confidence level [39]. Values between 0.05 and 0.10 indicate that the model terms are significant at 90 % and values higher than 0.10 denote that the model terms are not significant [40,41].

In this study, we have implemented a central composite design, according to which a test campaign consisting of a set of 17 experiments has been elaborated, with three points corresponding to the center of the model. The trials were numbered from 1 to 17. Table 2 represents the planning matrix giving the different combinations of the basic factors: EBFL inhibitor concentration, temperature, and immersion time. The results

derived from the experimental trials on the samples were used to fit mathematical models that represent the responses of inhibitory efficiency ( $Y_1$ ) and corrosion rate ( $Y_2$ ) as a function of the independent variables A, B, and C: inhibitor concentration, temperature, and immersion respectively. The initial analyses of variance for the two responses are provided in Tables 3 and 4, showing the sum of squares and the mean square for every parameter, where the p-value and F-value are set as the ratio of the mean square effect respectively, and the mean square error. Before excluding insignificant terms, the predictive models are expressed in terms of the variables in the following equations:

$$\begin{aligned} \ln(Y_1) = & 3.85 + 0.48A - 0.16B + 0.095C + 0.019AB - 0.044AC \\ & + 0.045BC - 0.1A^2 + 0.049B^2 + 0.059C^2 \end{aligned} \quad (4)$$

and:

$$\begin{aligned} \ln(Y_2) = & -1.89 - 0.58A + 1.3B - 0.069C + 0.21AB - 7.132 \times 10^{-3} AC \\ & + 0.13BC - 0.047A^2 + 0.47B^2 + 0.029C^2 \end{aligned} \quad (5)$$

**Table 3.** Initial ANOVA results and statistical parameters for response  $Y_1$ .

| Source         | Sum of squares          | df | Mean square                       | F-Value | p-Value Prob>F | Observation        |
|----------------|-------------------------|----|-----------------------------------|---------|----------------|--------------------|
| Model          | 2.70                    | 9  | 0.30                              | 212.39  | < 0.0001       | <b>Significant</b> |
| A-Conc         | 2.30                    | 1  | 2.30                              | 1628.83 | < 0.0001       |                    |
| B-Temp         | 0.24                    | 1  | 0.24                              | 172.07  | < 0.0001       |                    |
| C-Time         | 0.090                   | 1  | 0.090                             | 63.76   | < 0.0001       |                    |
| AB             | $2.772 \times 10^{-3}$  | 1  | $2.772 \times 10^{-3}$            | 1.96    | 0.2040         |                    |
| AC             | 0.015                   | 1  | 0.015                             | 10.95   | 0.0129         |                    |
| BC             | 0.016                   | 1  | 0.016                             | 11.60   | 0.0114         |                    |
| A <sup>2</sup> | 0.027                   | 1  | 0.027                             | 19.42   | 0.0031         |                    |
| B <sup>2</sup> | $6.323 \times 10^{-3}$  | 1  | $6.323 \times 10^{-3}$            | 4.48    | 0.0722         |                    |
| C <sup>2</sup> | $9.210 \times 10^{-3}$  | 1  | $9.210 \times 10^{-3}$            | 6.52    | 0.0379         |                    |
| Residual       | $9.886 \times 10^{-3}$  | 7  | $1.412 \times 10^{-3}$            |         |                |                    |
| Lack of Fit    | $9.886 \times 10^{-3}$  | 5  | $1.977 \times 10^{-3}$            |         |                |                    |
| Pure Error     | 0.000                   | 2  | 0.000                             |         |                |                    |
| Cor Total      | 2.71                    | 16 |                                   |         |                |                    |
| Fit Statistics | Std Dev = 0.038         |    | R <sup>2</sup> = 0.9964           |         |                |                    |
|                | Mean = 3.85             |    | Adjusted R <sup>2</sup> = 0.9917  |         |                |                    |
|                | C.V. % 0.98             |    | Predicted R <sup>2</sup> = 0.9695 |         |                |                    |
|                | Adeq Precision = 50.678 |    |                                   |         |                |                    |



**Table 4.** Initial ANOVA results and statistical parameters for response  $Y_2$ 

| Source         | Sum of squares          | df | Mean square                       | F-Value | p-Value Prob>F | Observation        |
|----------------|-------------------------|----|-----------------------------------|---------|----------------|--------------------|
| Model          | 21.54                   | 9  | 2.39                              | 194.02  | < 0.0001       | <b>Significant</b> |
| A-Conc         | 3.40                    | 1  | 3.40                              | 275.38  | < 0.0001       |                    |
| B-Temp         | 16.85                   | 1  | 16.85                             | 1366.18 | < 0.0001       |                    |
| C-Time         | 0.047                   | 1  | 0.047                             | 3.81    | 0.0921         |                    |
| AB             | 0.35                    | 1  | 0.35                              | 28.74   | 0.0011         |                    |
| AC             | $4.069 \times 10^{-4}$  | 1  | $4.069 \times 10^{-4}$            | 0.033   | 0.8610         |                    |
| BC             | 0.13                    | 1  | 0.13                              | 10.37   | 0.0146         |                    |
| A <sup>2</sup> | $6.016 \times 10^{-3}$  | 1  | $6.016 \times 10^{-3}$            | 0.49    | 0.5075         |                    |
| B <sup>2</sup> | 0.58                    | 1  | 0.58                              | 47.13   | 0.0002         |                    |
| C <sup>2</sup> | $2.269 \times 10^{-3}$  | 1  | $2.269 \times 10^{-3}$            | 0.18    | 0.6809         |                    |
| Residual       | 0.086                   | 7  | 0.012                             |         |                |                    |
| Lack of Fit    | 0.086                   | 5  | 0.017                             |         |                |                    |
| Pure Error     | 0.000                   | 2  | 0.000                             |         |                |                    |
| Cor Total      | 21.63                   | 16 |                                   |         |                |                    |
| Fit Statistics | Std Dev =0.11           |    | R <sup>2</sup> = 0.9960           |         |                |                    |
|                | Mean =-1.66             |    | Adjusted R <sup>2</sup> = 0.9909  |         |                |                    |
|                | C.V. % 6.68             |    | Predicted R <sup>2</sup> = 0.9592 |         |                |                    |
|                | Adeq Precision = 47.301 |    |                                   |         |                |                    |

From the ANOVA (Tables 3 and 4), "F-value" of the model is 212.39 for inhibitory efficiency and 194.02 for corrosion rate respectively, implying that the models are significant. There is only a 0.01 % chance that the model could occur due to noise [30,42]. Probability values less than 0.05 indicate that the model terms are significant [34,43]. In the case of inhibitory efficacy, the factors A, B, C, the interactions AC, BC, and the quadratic effects A<sup>2</sup>, C<sup>2</sup> are significant terms in the model. The P-value obtained for the interaction of type A B is 0.2040 ( $> 0.05$ ). There is therefore no significant effect. Concerning the corrosion rate, the factors A, B, C, the interactions AB, B C, and the quadratic effect B<sup>2</sup> are significant terms in the model.

The regression analysis was examined in depth by evaluating the R<sup>2</sup>, adjusted R<sup>2</sup>, and predicted R<sup>2</sup> determination coefficients. R<sup>2</sup> indicates the proportion of total response variation predicted by the models. Correlation coefficients close to 1 indicate the adequacy of the models and the accuracy of the calculated constants [28]. Adjusted R<sup>2</sup> can be used to prevent probability errors, when a new term is added, and is a useful tool for comparing the explanatory power of models with different numbers of predictors. The predicted R<sup>2</sup> is used in regression analysis to indicate how well the model predicts responses for new observations. The predicted R<sup>2</sup> may be more useful than the adjusted R<sup>2</sup> for comparing models because it is calculated from observations not involved in the model estimation. The coefficients of determination R<sup>2</sup> and adjusted R<sup>2</sup> indicate

the quality of the polynomial fit and should be within about 0.20 of each other, to be in reasonable agreement. Both models have high coefficients of determination ( $R^2=0.9964$  for inhibitory efficiency and  $R^2=0.9960$  for corrosion rate). The adjusted  $R^2$  value often decreases if statistically insignificant factors are added to the model. When  $R^2$  and adjusted  $R^2$  differ significantly, there is a strong chance that insignificant terms are included in the model [44], in our case the  $R^2$  and adjusted  $R^2$  coefficients are close to 1.00 for both models. Based on this study, for the first response (inhibitory efficacy), the predicted  $R^2$  and adjusted  $R^2$  values are 0.9695 and 0.9917, respectively, which suggests that the predicted and experimental inhibitory efficiencies are in perfect agreement. The  $R^2$  equal to 0.9964 is in excellent accordance with the experimental results, which implies that this model can reveal 99.64 % of the variability. Furthermore, for the second response (corrosion rate), the values of  $R^2$ , predicted  $R^2$  and adjusted  $R^2$  are respectively 0.9960, 0.9592, and 0.9909 indicating a high correlation between the observed and predicted values. The coefficient of variation "CV" is the ratio of the standard error of the estimate to the mean value of the observed response and is a measure of the reproducibility of the model, generally a model can be considered reasonable if its CV is not greater than 15 % [45]. Thus, in this study, the obtained coefficient of variation value of 0.98 % (inhibitory efficiency) and 6.68 (corrosion rate) indicates a high precision and reliability of the experiments.

The ANOVA was then replicated after eliminating non-significant terms and the results for inhibitor efficacy and corrosion rate are given in Table 5 and Table 6. The adequacy of the regression models to interpret the experimental data at the 95% confidence level was examined using the ANOVA results. The significance of both main effects and interaction effects in the predictive models was assessed based on their probability values (p values). P-values less than 0.05 necessitated rejection of the null hypothesis suggesting that the particular term significantly affects the measured response of the system [40,41]. Finally, based on the final ANOVA for two responses  $Y_1$  and  $Y_2$ , as well as the interactions with significant effects, a fitted regression model with statistical significance can be reported in the following equations:

$$\text{Lr}(Y_1) = 3.86 + 0.48A - 0.16B + 0.095C + 0.019AB - 0.044AC + 0.045BC - 0.085A^2 + 0.075C^2 \quad (6)$$

and:

$$\text{Lr}(Y_2) = -1.91 - 0.58A + 1.3B - 0.069C + 0.21AB + 0.13BC + 0.47B^2 \quad (7)$$

The normal probability plot of the residuals for the two responses ( $Y_1$ ) and ( $Y_2$ ) is depicted in Fig. 1(a) and 1(b), respectively. The accuracy of the model should be estimated by the difference between the expected values and the actual values (residuals), which are expected to follow a normal distribution. The data in Fig. 1(a) and 1(b) should be evenly distributed and by a forty-five-degree line. The points are reasonably close to a straight line [46,47]. The straight lines obtained for the curves demonstrate that the studied residual follows a normal linear distribution, indicating that the models are appropriate for all examined responses.

**Table 5.** Final ANOVA results and statistical parameters for response  $Y_1$ .

| Source | Sum of squares | df | Mean square | F-Value | p-Value Prob>F | Observation        |
|--------|----------------|----|-------------|---------|----------------|--------------------|
| Model  | 2.69           | 7  | 0.38        | 182.26  | < 0.0001       | <b>Significant</b> |
| A-Conc | 2.30           | 1  | 2.30        | 1090.50 | < 0.0001       |                    |
| B-Temp | 0.24           | 1  | 0.24        | 115.23  | < 0.0001       |                    |
| C-Time | 0.090          | 1  | 0.090       | 42.70   | < 0.0001       |                    |
| AC     | 0.015          | 1  | 0.015       | 7.34    | 0.0241         |                    |
| BC     | 0.016          | 1  | 0.016       | 7.77    | 0.0212         |                    |

| Source         | Sum of squares          | df | Mean square                       | F-Value | p-Value Prob>F | Observation |
|----------------|-------------------------|----|-----------------------------------|---------|----------------|-------------|
| A <sup>2</sup> | 0.022                   | 1  | 0.022                             | 10.30   | 0.0107         |             |
| C <sup>2</sup> | 0.017                   | 1  | 0.017                             | 8.11    | 0.0192         |             |
| Residual       | 0.019                   | 9  | 2.109×10 <sup>-3</sup>            |         |                |             |
| Lack of Fit    | 0.019                   | 7  | 2.712×10 <sup>-3</sup>            |         |                |             |
| Pure Error     | 0.000                   | 2  | 0.000                             |         |                |             |
| Cor Total      | 2.71                    | 16 |                                   |         |                |             |
| Fit Statistics | Std Dev =0.046          |    | R <sup>2</sup> = 0.9930           |         |                |             |
|                | Mean =3.85              |    | Adjusted R <sup>2</sup> = 0.9875  |         |                |             |
|                | C.V. % 1.19             |    | Predicted R <sup>2</sup> = 0.9681 |         |                |             |
|                | Adeq Precision = 46.367 |    |                                   |         |                |             |

**Table 6.** Final ANOVA results and statistical parameters for response Y<sub>2</sub>.

| Source         | Sum of squares          | df | Mean square                       | F-Value | p-Value Prob>F | Observation        |
|----------------|-------------------------|----|-----------------------------------|---------|----------------|--------------------|
| Model          | 21.53                   | 6  | 3.59                              | 362.58  | < 0.0001       | <b>Significant</b> |
| A-Conc         | 3.40                    | 1  | 3.40                              | 343.28  | < 0.0001       |                    |
| B-Temp         | 16.85                   | 1  | 16.85                             | 1703.00 | < 0.0001       |                    |
| C-Time         | 0.047                   | 1  | 0.047                             | 4.74    | 0.0544         |                    |
| AB             | 0.35                    | 1  | 0.35                              | 35.83   | 0.0001         |                    |
| BC             | 0.13                    | 1  | 0.13                              | 12.93   | 0.0049         |                    |
| B <sup>2</sup> | 0.75                    | 1  | 0.75                              | 75.68   | < 0.0001       |                    |
| Residual       | 0.099                   | 10 | 9.896×10 <sup>-3</sup>            |         |                |                    |
| Lack of Fit    | 0.099                   | 8  | 0.012                             |         |                |                    |
| Pure Error     | 0.000                   | 2  | 0.000                             |         |                |                    |
| Cor Total      | 21.63                   | 16 |                                   |         |                |                    |
| Fit Statistics | Std Dev =0.099          |    | R <sup>2</sup> = 0.9954           |         |                |                    |
|                | Mean =-1.66             |    | Adjusted R <sup>2</sup> = 0.9927  |         |                |                    |
|                | C.V. % 5.98             |    | Predicted R <sup>2</sup> = 0.9838 |         |                |                    |
|                | Adeq Precision = 62.898 |    |                                   |         |                |                    |

An appropriate model can be determined based on the distribution of data points around the mean of the response variable as well. A uniformly distributed data point around the mean of the response variable suggests that the model is suitable (Fig. 2). Correlation between the predicted values of the response based on the model equation and the actual values obtained in the experiment were investigated using predicted versus actual plot. It can be seen that the proper correlation to the linear regression fit is obtained in this graph with an  $R^2$  value of 0.9930 and 0.9954 for inhibitory efficacy and corrosion rate, which indicates that the model accurately describes the experimental data. Furthermore, the obtained measured values and their associated predicted values are compared in Table 7. The maximum error for

The plots of the residuals against predicted values for the final ANOVA in the case of the two responses examined are displayed in Fig. 3. From this Figure, it can be observed that there is not a considerable dispersion of the residuals for the two responses. Therefore, it appears that the proposed model was appropriate.

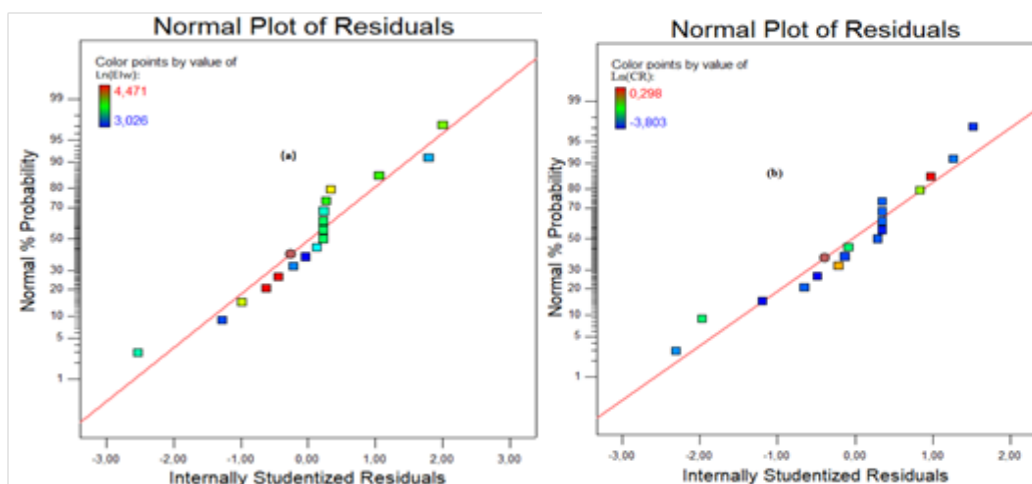


Fig. 1. Normal probability plot of the residuals for: (a) inhibitory efficiency and (b) corrosion rate.

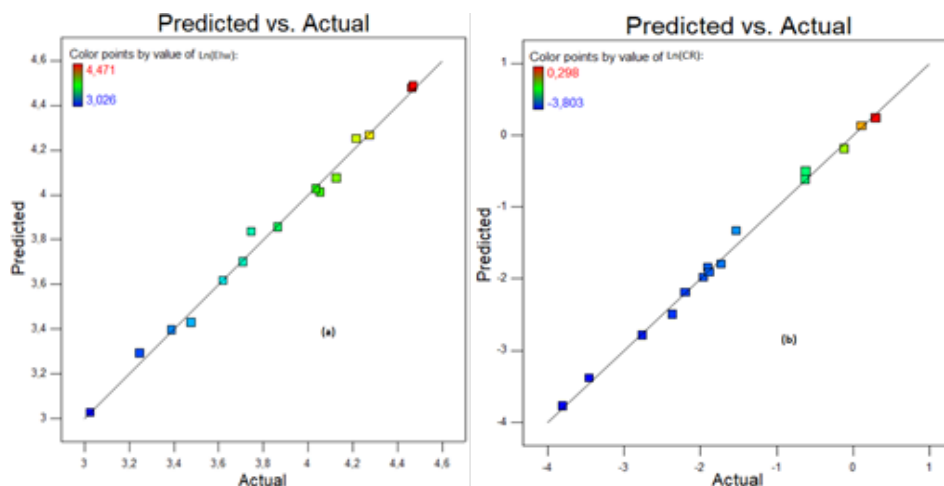
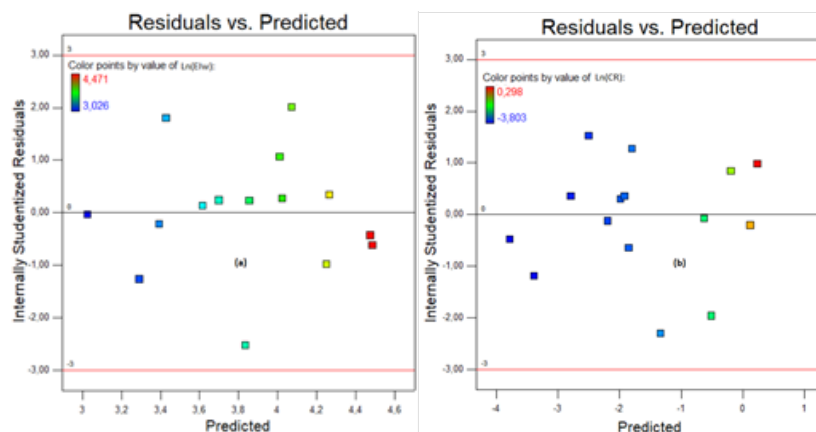


Fig. 2. Plots of predicted versus actual values for (a) inhibitory efficiency and (b) corrosion rate.



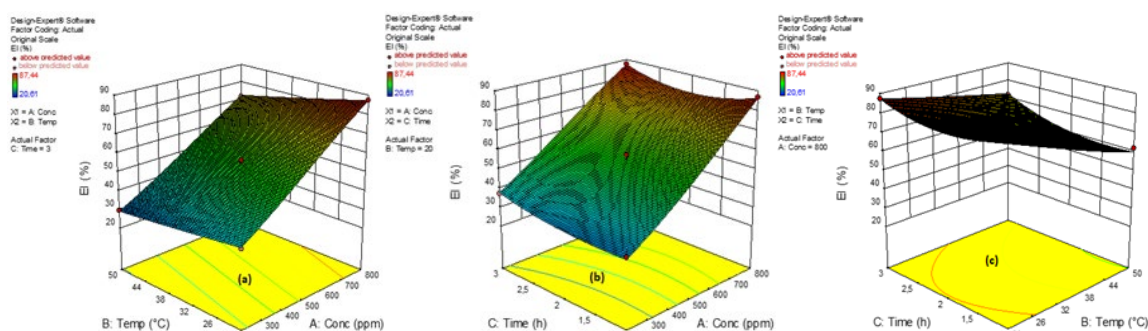
**Table 7.** Comparison between experimental and predicted values and calculation of residuals for the two responses ( $Y_1$ ,  $Y_2$ )

| Run | Response $Y_1$ (%) (%) |                | Response $Y_2$ (mg/cm <sup>2</sup> .h) |               | Residue      |             |
|-----|------------------------|----------------|----------------------------------------|---------------|--------------|-------------|
|     | IEW(measured)          | IEW(predicted) | CR(measured)                           | CR(predicted) | $e_i$ ( IEW) | $e_i$ ( CR) |
| 1   | 86.88                  | 87.38          | 0.0316                                 | 0.0339        | -0.50        | -0.0023     |
| 2   | 56.57                  | 52.59          | 0.1412                                 | 0.1364        | 3.98         | 0.0048      |
| 3   | 32.36                  | 30.72          | 0.1785                                 | 0.1649        | 1.64         | 0.0136      |
| 4   | 47.72                  | 47.67          | 0.1523                                 | 0.1474        | 0.05         | 0.0049      |
| 5   | 29.64                  | 30.41          | 1.3471                                 | 1.2308        | -0.77        | 0.1163      |
| 6   | 42.40                  | 43.20          | 0.1492                                 | 0.1593        | -0.80        | -0.0101     |
| 7   | 47.72                  | 47.67          | 0.1523                                 | 0.1474        | 0.05         | 0.0049      |
| 8   | 67.77                  | 69.65          | 0.0939                                 | 0.0815        | -1.88        | 0.0124      |
| 9   | 47.72                  | 47.67          | 0.1523                                 | 0.1474        | 0.05         | 0.0049      |
| 10  | 25.71                  | 26.51          | 0.2163                                 | 0.2664        | -0.80        | -0.0501     |
| 11  | 62.01                  | 59.44          | 0.5353                                 | 0.5206        | 2.57         | 0.0147      |
| 12  | 57.59                  | 60.35          | 0.0636                                 | 0.0616        | -2.76        | 0.0020      |
| 13  | 87.44                  | 88.98          | 0.0223                                 | 0.0231        | -1.54        | -0.0008     |
| 14  | 37.33                  | 36.67          | 0.1113                                 | 0.1121        | 0.66         | -0.0008     |
| 15  | 40.82                  | 45.33          | 0.8913                                 | 0.8006        | -4.51        | 0.0907      |
| 16  | 71.90                  | 73.79          | 0.538                                  | 0.5607        | -1.89        | -0.0227     |
| 17  | 20.61                  | 20.90          | 1.1186                                 | 1.1429        | -0.29        | -0.0243     |

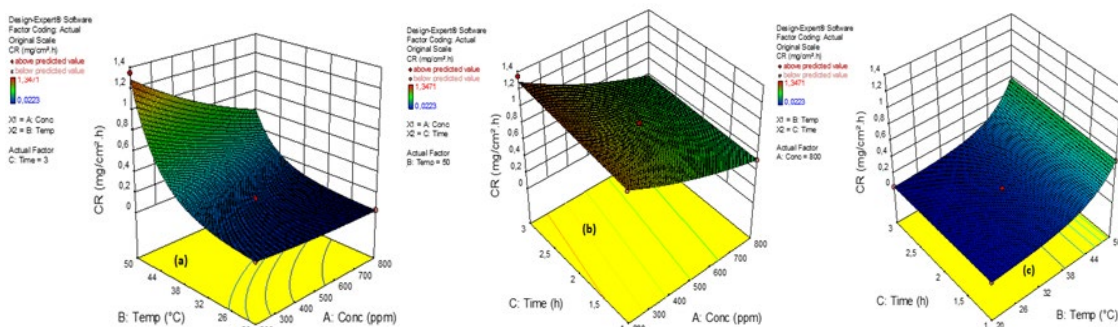
**Fig. 3.** Plot of the residual and predicted values of inhibition efficiency (a) and corrosion rate (b).

### Analysis of 3D response surfaces

3D response surfaces are plotted to enable viewing the simultaneous effects of two parameters on a response. Figures 3 and 4 display the response in terms of inhibition efficiency and corrosion rate respectively. Three combinations of interactions for every condition were statistically determined for each response. From the interactive effects of the extract concentration and temperature variables in Fig. 4(a) by keeping the immersion time at their constant value of 3 hours, we can observe that the inhibition efficiency of carbon steel decreases with an increase in temperature but increases with an increase in the concentration of the EBFL inhibitor. In general, corrosion inhibition depends on the adsorption of the organic inhibitor being used. The rate of desorption of EBFL molecules from the surface of carbon steel becomes more rapid at higher temperatures, which would be expected to be responsible for the decreased inhibition efficiency. Fig. 4(b) showed an interaction between the concentration of an inhibitor and the exposure time on the corrosion inhibition efficiency by maintaining the temperature at a value of 20 °C. The inhibition efficiency increases with both immersion time and increasing EBFL concentration. This Figure shows that the inhibition efficiency of the extract is quite good for an immersion period of 3 h for higher concentrations of EBFL. The interaction between immersion time and temperature shows that inhibition efficiency increases with increasing immersion time. The maximum inhibition efficiency is obtained at the highest immersion time and lowest temperature combination at the constant value of 800 ppm (Fig. 4(c)). This suggests faster adsorption and greater surface coverage on the carbon steel surface by EBFL at higher concentrations. Nevertheless, Fig. 5(a), indicates that the corrosion rate decreases with the increase of the inhibitor concentration and also increases with an increase in the immersion time. Fig. 5(b) illustrates that the corrosion rate decreases with increasing inhibitor concentration and also increases with increasing time, as well as an increase in temperature leads to an increase in the corrosion rate as observed in Fig. 5(c) and decreases with increasing inhibitor concentration. This suggests physical adsorption.



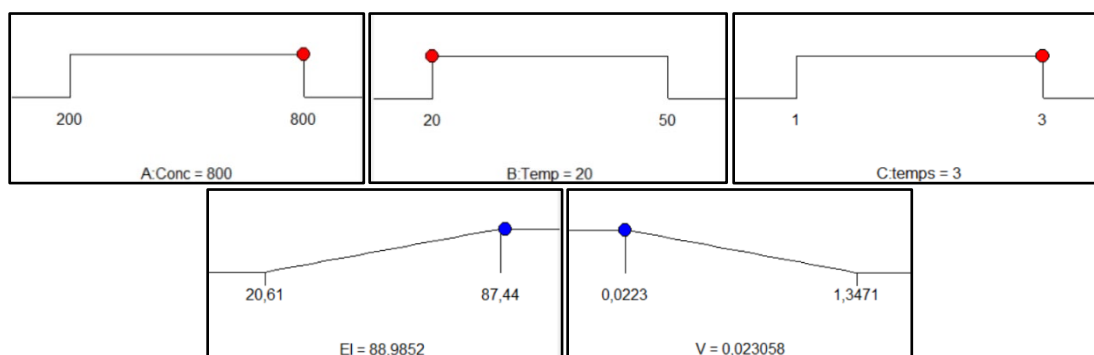
**Fig. 4.** 3D response surface diagrams for Inhibition Efficiency: (a) Temperature versus concentration, (b) Time versus concentration, and (c) Time versus temperature.



**Fig. 5.** 3D response surface diagrams for corrosion rate: (a) Temperature versus concentration, (b) Time versus concentration and (c) Time versus temperature.

### Optimization and confirmation tests of the results

Response surface methodology (RSM) was used to choose the parameters that maximized the inhibition efficiency and corrosion rate of the butanolic extract (EBFL) as a corrosion inhibitor. The concentration of the inhibitor (A), temperature (B), and immersion time (C) were the three factors that were optimized. The predicted values of the responses are the optimal values based on the experimental findings shown in Table 7 and confirmed in Fig. 6, whose values of the optimal solution are close to 1 (or 100 %) for both examinations (Inhibition efficiency and corrosion rate). These values are picked as the parameter values that have the greatest impact on the response factor. According to Table 8, RSM tends to search, among a multitude of solutions, the top 10 best cases out of a large number of possibilities. The highest reported response values for corrosion rate and inhibition efficiency in this context are 0.02306 mg/cm<sup>2</sup>·h and 88.9852 %, respectively.



**Fig. 6.** Optimal conditions selected for parameters influence corrosion inhibition in the absence and presence of EBFL with their responses (inhibition efficiency and corrosion rate)

**Table 8.** Ten best solutions for parameters influencing corrosion inhibition in the absence and presence of EBFL, with their responses (inhibition efficiency and corrosion rate).

| Number | Conc (ppm) | Temp (°C) | Time (h) | IEW (%) | CR (mg/cm <sup>2</sup> .h) | Desirability |
|--------|------------|-----------|----------|---------|----------------------------|--------------|
| 1      | 800.000    | 20.00     | 3.00     | 88.985  | 0.0231                     | 1.00         |
| 2      | 799.795    | 20.026    | 2.984    | 88.744  | 0.0232                     | 1.00         |
| 3      | 799.992    | 20.003    | 2.972    | 88.605  | 0.0232                     | 1.00         |
| 4      | 797.143    | 20.000    | 2.999    | 88.744  | 0.0232                     | 1.00         |
| 5      | 799.987    | 20.002    | 2.950    | 88.301  | 0.0233                     | 1.00         |
| 6      | 799.960    | 20.002    | 2.941    | 88.186  | 0.0233                     | 1.00         |
| 7      | 797.601    | 20.002    | 2.965    | 88.312  | 0.0234                     | 1.00         |
| 8      | 798.887    | 20.002    | 2.930    | 87.360  | 0.0234                     | 1.00         |
| 9      | 799.794    | 20.002    | 2.898    | 87.631  | 0.0235                     | 1.00         |
| 10     | 786.274    | 20.001    | 2.999    | 87.875  | 0.0239                     | 0.999        |

### Calculation of the inhibitory efficiency and the corrosion rate at different temperatures from the models

To better understand the behavior of a metal in an aggressive medium and the nature of the metal/inhibitor interaction in this environment, it is interesting to determine the temperature values provided by the two suggested models in the range of 20 to 50 °C after 3 h of immersion. All the computations of the inhibitor efficiency and the corrosion rate, (Eqs. 6 and 7), were done using MATLAB software. From Table 9, we notice that EBFL has good inhibitory properties against the corrosion of carbon steel in 1M HCl medium. The increase in temperature leads to a decrease of the inhibitory efficiency showing a desorption phenomenon, i.e. the protective layer formed on the steel surface by adsorption of the extract is destroyed. According to [48, 49], this phenomenon was explained by the high sensitivity of the physical interactions of Van Der Waals type between the iron surface and the inhibitor. The inhibitory efficiency ( $IE_w$ ) decreases while the corrosion rate (CR) increases with temperature in the range of 20 °C to 50 °C for all concentrations used. For all these concentrations, the corrosion rate (CR) also increases with temperature but takes lower values than the corrosion rate (CR) in the acid solution only.

**Table 9.** Calculation of the inhibitory efficiency and the corrosion rate from the two models proposed in the absence and presence of different concentrations of EBFL at different temperatures after 3h of immersion.

| T(°C) | C(ppm) | $IE_w$ calculated(%) | CRcalculated(mg/cm <sup>2</sup> •h) |
|-------|--------|----------------------|-------------------------------------|
| 20    | 0      | //                   | 0.1903                              |
|       | 200    | 37.20                | 0.1121                              |
|       | 400    | 53.62                | 0.0661                              |
|       | 600    | 71.69                | 0.0389                              |
|       | 800    | 88.89                | 0.0229                              |
| 30    | 0      | //                   | 0.2665                              |
|       | 200    | 34.55                | 0.1725                              |
|       | 400    | 49.80                | 0.1116                              |
|       | 600    | 66.59                | 0.0722                              |
|       | 800    | 82.57                | 0.0467                              |
| 40    | 0      | //                   | 0.5453                              |
|       | 200    | 32.09                | 0.3874                              |
|       | 400    | 46.27                | 0.2753                              |
|       | 600    | 61.86                | 0.1956                              |
|       | 800    | 76.70                | 0.1390                              |
| 50    | 0      | //                   | 1.6299                              |
|       | 200    | 29.82                | 1.2716                              |
|       | 400    | 42.97                | 0.9921                              |
|       | 600    | 57.96                | 0.7741                              |
|       | 800    | 71.24                | 0.6039                              |



## Adsorption mechanism

### Adsorption parameters

The adsorption processes of inhibitors are governed by the chemical structure of the organic compounds, the nature and surface modification of the metal, the charge distribution in the molecule, and the type of aggressive medium [48]. Therefore, different isotherms including Langmuir, Temkin, Frumkin, and Freundlich, were checked to find the appropriate adsorption isotherm as listed in Table 10. The following relationship defines the value of the coverage rate ( $\theta$ ) of the metal surface by the adsorbed inhibitor:

$$\theta = \frac{IE_w}{100} \quad (8)$$

**Table 10.** The correlation coefficient of different adsorption isotherms at different temperatures.

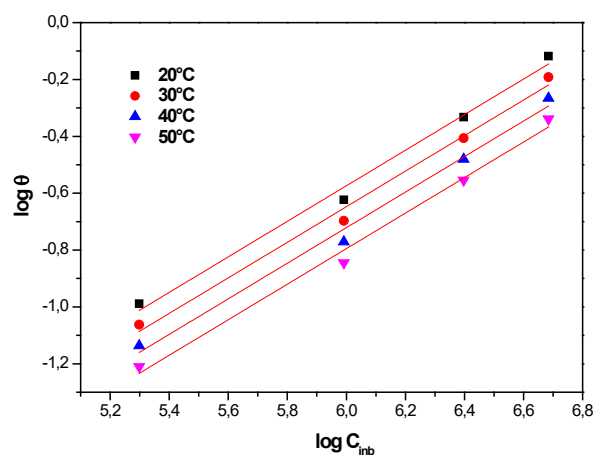
| Isotherms of dsorption | Coefficient of correlation (R <sup>2</sup> ) |        |        |        |
|------------------------|----------------------------------------------|--------|--------|--------|
|                        | 20°C                                         | 30°C   | 40°C   | 50°C   |
| Langmuir               | 0.9243                                       | 0.9242 | 0.9243 | 0.9243 |
| Freundlich             | 0.9922                                       | 0.9922 | 0.9922 | 0.9922 |
| Temkin                 | 0.9556                                       | 0.9555 | 0.9556 | 0.9556 |
| Frumkin                | 0.8119                                       | 0.7908 | 0.7382 | 0.6459 |

After having plotted the different isotherms at different temperatures, the most suitable correlation coefficient for use in our case is the Freundlich isotherm model in which the correlation coefficient of the curves is very close to the unit compared to the others (Fig. 7). From the Freundlich isotherm, we can easily deduce the adsorption constant reported in Table 11.

### Thermodynamic parameters of adsorption

According to the Freundlich isotherm, ( $\theta$ ) is related to the inhibitor concentration  $\ln C_{inh}$  by the following equation :

$$\log \theta = \log K_{ads} + a \log c \quad (9)$$



**Fig. 7.** Freundlich adsorption isotherm of carbon steel in 1M HCl in the presence of EBFL at different temperatures.

**Table 11.** Adsorption constants ( $K_{ads}$ ) at different temperatures.

| Plant | Model Isothermal Freundlich |         |           | $K_{ads}$             |
|-------|-----------------------------|---------|-----------|-----------------------|
|       | Temperature (°C)            | Slope   | Intercept |                       |
| EBFL  | 20                          | 0.62535 | -4.32587  | $1.32 \times 10^{-2}$ |
|       | 30                          | 0.62533 | -4.39951  | $1.23 \times 10^{-2}$ |
|       | 40                          | 0.62535 | -4.47337  | $1.14 \times 10^{-2}$ |
|       | 50                          | 0.62528 | -4.54670  | $1.06 \times 10^{-2}$ |

We note that the values of  $K_{ads}$  decrease with temperature. The equilibrium constant  $K_{ads}$  is related to the standard free energy of adsorption  $\Delta G_{ads}^0$  by the following Eq.10 :

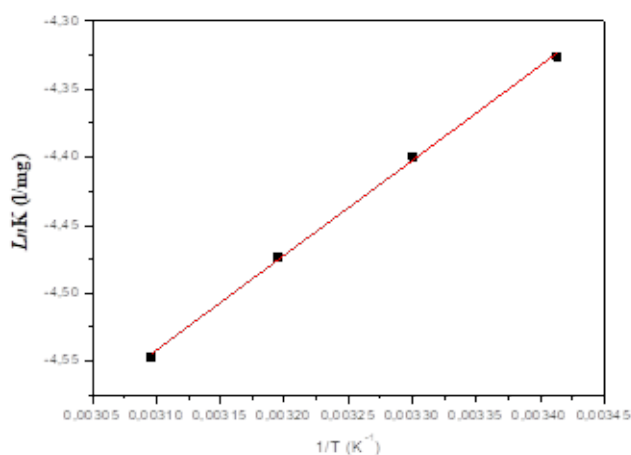
$$\Delta G_{ads}^0 = -RT \ln(C_{H_2O})K_{ads} \quad (10)$$

where:  $C_{H_2O} = 10^6 \text{ mg} / \text{L}$ . R is the gas constant and T represents the absolute temperature. The standard enthalpy of adsorption  $\Delta H_{ads}^0$  can also be deduced from the Vant'Hoff (Eq.11):

$$\ln(K_{ads}) = -\frac{\Delta H_{ads}^0}{RT} + A \quad (11)$$

Fig. 8 exhibits the variation of  $\ln(K_{ads})$  versus  $1/T$ . The slope gives  $\Delta H_{ads}^0$ . Using the Gibbs Helmholtz equation to calculate the standard entropy of adsorption  $\Delta S_{ads}^0$  from the Eq.12:

$$\Delta G_{ads}^0 = \Delta H_{ads}^0 - T\Delta S_{ads}^0 \quad (12)$$

**Fig. 8.** The variation of  $\ln(K_{ads})$  as a function of inverse Temperature.

The thermodynamic data obtained for the EBFL are presented in Table 12.

**Table 12.** Thermodynamic parameters of EDFL in 1 M HCl medium for different temperatures.

| EBFL Thermodynamic parameters |                 |                                 |                                 |                                       |
|-------------------------------|-----------------|---------------------------------|---------------------------------|---------------------------------------|
| T (K)                         | $K_{ads}(mg/l)$ | $\Delta G_{ads}^0(kJ.mol^{-1})$ | $\Delta H_{ads}^0(kJ.mol^{-1})$ | $\Delta S_{ads}^0(J.mol^{-1}.K^{-1})$ |
| 293                           | $1.32.10^{-2}$  | -23.113                         |                                 | 59.130                                |
| 303                           | $1.23.10^{-2}$  | -23.724                         | -5.788                          | 59.195                                |
| 313                           | $1.14.10^{-2}$  | -24.309                         |                                 | 59.173                                |
| 323                           | $1.06.10^{-2}$  | -24.890                         |                                 | 59.139                                |

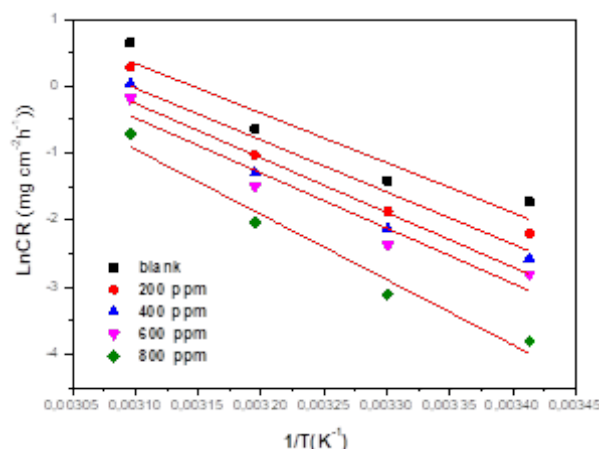
From Table 12, under the same conditions, we see that the  $K_{ads}$  values of the EBFL decrease with increasing temperature. The negative values  $\Delta G_{ads}^0$  indicate the spontaneity of the adsorption process and the stability of the adsorbed double layer on the metal surface. The obtained results of the adsorption  $\Delta G_{ads}$  values close to  $-20$  kJ/mol confirm the physisorption mechanism [20,49]. The enthalpy value calculated from the Vant'Hoff equation is of the order of  $-5.788$  kJ/mol, which shows the exothermic character of the adsorption of the latter on the surface of the carbon steel confirming physisorption. This can also be explained by the decrease of the inhibitory efficiency by increasing the temperature. We note that  $\Delta S_{ads}^0$  in the presence of EBFL is positive. This involves an increase in the disorder that accompanies the adsorption of inhibitory molecules from the solution onto the metal surface [50].

### Determination of activation energies

In this study, the Arrhenius-type dependence observed between the corrosion rate and temperature is represented by the following relationship [51]:

$$\ln CR = \ln A - \frac{E_a}{RT} \quad (13)$$

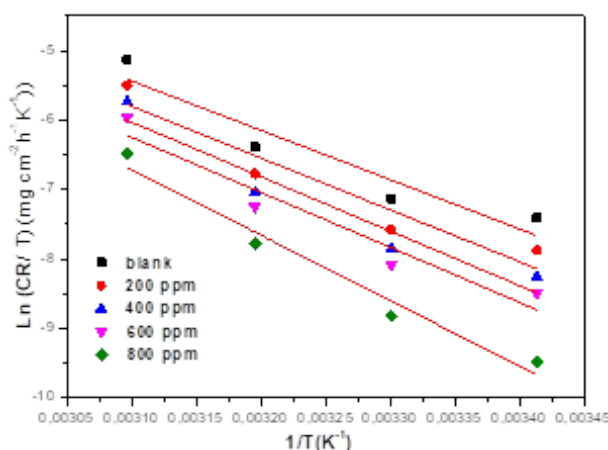
where A is a constant (pre-exponential factor),  $E_a$  is the activation energy, R is the universal gas constant and T is the absolute temperature. A plot of the logarithm of the CR versus  $1/T$  showed a straight line. As exhibited in Fig. 9, the values of apparent activation energy  $E_a$  were obtained from the slope ( $-E_a/R$ ).

**Fig. 9.** Arrhenius diagram of the corrosion rates of carbon steel in 1 M HCl medium in the absence and presence of the different concentrations of EBFL.

The alternative formulation of the Arrhenius relation as expressed in Equation 14 was used to determine the activation enthalpy  $\Delta H_a$  and activation entropy  $\Delta S_a$  values [20,49,52].

$$\ln CR = \left[ \ln \frac{RT}{Nh} + \frac{\Delta S_a}{RT} \right] - \frac{\Delta H_a}{RT} \quad (14)$$

where,  $h$  represents the Planck's constant ( $6.626 \times 10^{-34}$  J.s) and  $N$  is the Avogadro's number ( $6,022 \times 10^{23}$  mol $^{-1}$ ). The plot of  $\ln (CR/T)$  versus  $(1/T)$  showed a straight line (Fig. 10). The values of  $\Delta H_a$  and  $\Delta S_a$  were deduced from the slope ( $-\Delta H_a/R$ ) and intercept  $(\ln(RT/Nh) + \Delta S_a/R)$ .



**Fig. 10.** Alternative Arrhenius diagram of the corrosion rates of carbon steel in 1M HCl medium in the absence and presence of the different concentrations of EBFL.

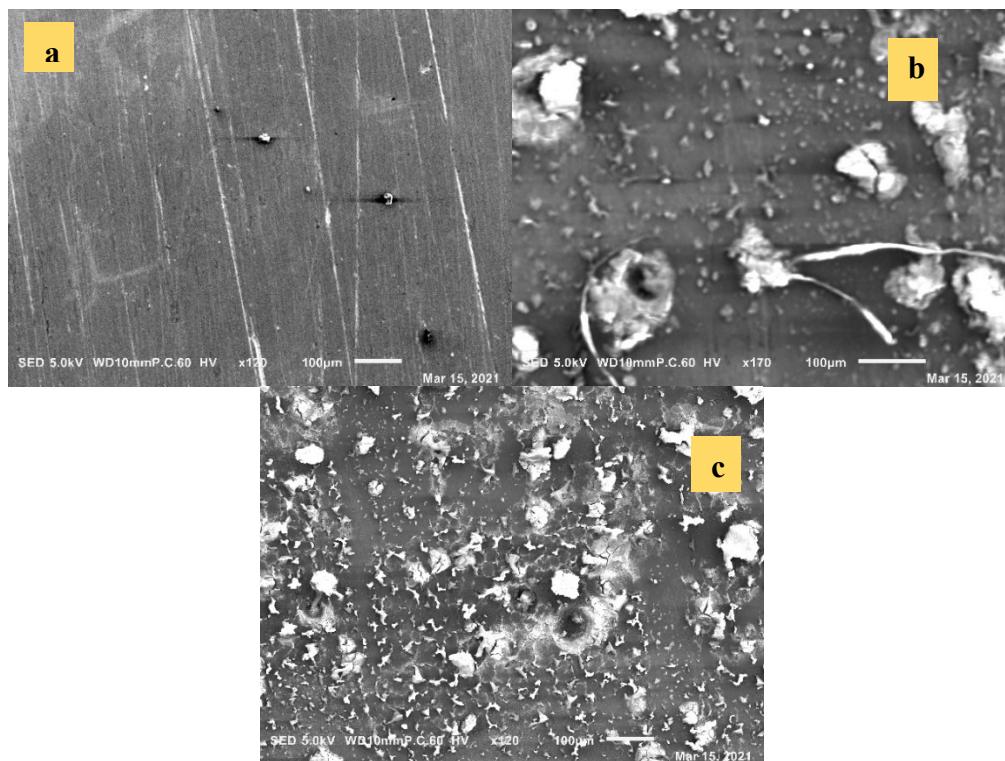
**Table 13.** Activation parameters of X2C30 carbon steel in 1M HCl in the absence and presence of different concentrations of EBFL.

| EBFL (ppm) | $E_a$ (kJ·mol $^{-1}$ ) | $\Delta H_a^0$ (kJ·mol $^{-1}$ ) | $\Delta S_a^0$ (J·mol $^{-1}$ ) |
|------------|-------------------------|----------------------------------|---------------------------------|
| blank      | 55.906                  | 53.350                           | 95.606                          |
| 200        | 63.266                  | 60.710                           | 116.305                         |
| 400        | 70.610                  | 68.054                           | 136.949                         |
| 600        | 78.001                  | 75.445                           | 157.744                         |
| 800        | 85.381                  | 82.825                           | 178.505                         |

The findings achieved in this study reveal that the values of ( $E_a$ ) ranged from 63.266 to 85.381 kJ mol $^{-1}$ . It is obvious that the apparent activation energy ( $E_a$ ) increased with the concentration of EBFL and was more than in the absence of an inhibitor as displayed in Table 13. This increase reflects that the inhibitory molecules of EBFL are physisorbed [52-55]. We note that the change in the values of  $E_a$  may be attributed to the geometric blocking effect of adsorbed inhibitive species on the steel surface. The positive sign of the enthalpy values of activation, thus expressing its difficult course, reveals the endothermic nature of the carbon steel dissolution process.

### Morphological characterization

SEM analysis is a useful tool to characterize the surface morphology of carbon steel samples. Fig. 11(a), 11(b), and 11(c), displayed the surface morphology of carbon steel samples immersed in 1 M HCl solution without and with the addition of 800 ppm of EBFL for 3 h at 293 K. Fig. 11(a) shows the polished lines on the surface of carbon steel before its exposure to the testing environments. Fig. 11(b) show that the surface of the sample is heavily damaged and severely corroded compared However, in the presence of 800ppm of the inhibitor EBFL as shown in Fig. 11(c), the external morphology appears softer, indicating a protected surface. These results support all obtained results cited above.



**Fig. 11.** SEM pictures of carbon steel before corrosion (a) in acid solution (b) and (c) in the presence of 800ppm after 3 h immersion time at 293 K.

### Conclusions

In this work, a Response Surface Methodology (RSM) based on the Composite Centered Design (CCD) was used to study and statistically analyze the effect of the extract (EBFL) on the corrosion inhibition of carbon steel (X2C30), in a 1M HCl acid medium. This statistical method allows the establishment of mathematical models involving different parameters that influence the inhibitory efficiency as well as the corrosion rate, namely: the inhibitor concentration, the immersion time, and the temperature. The weight loss method was employed to evaluate and analyze the inhibitory effect and the influence of specific parameters on the corrosion of the carbon steel electrode.

The different results obtained from this investigation are:

- Quadratic logarithmic models modeled the inhibitory efficiency and corrosion rate as responses. From the statistical analysis ANOVA we confirmed that both obtained models are significant ( $P=0.0001 < 0.05$ ) with a satisfactory correlation between the measured values and those adjusted ( $R^2 = 99.30\%$  and  $R^2_{ajus} = 98.75\%$ ) for the case of inhibitory efficiency and ( $R^2 = 99.54\%$  and  $R^2_{ajus} = 99.27\%$ ) for

the corrosion rate. According to the experimental results obtained with the highest desirability, the highest response values reported for the corrosion rate and inhibition efficiency in this context were 0.02306 mg/cm<sup>2</sup>·h and 88.9852 % respectively.

- The study of the influence of concentration and temperature on the inhibitory efficiency and the corrosion rate was carried out to confirm the adsorption model on the metal surface. Several factors highlighted the physisorption nature of the EBFL adsorption namely: the apparent activation energy of the steel dissolution process, which is higher than the activation energy value, obtained in the case of the acid alone, the negative values of the free energy of adsorption as well as the negative value of the enthalpy of adsorption. The thermodynamic study showed that the adsorption of the extract on the steel surface is spontaneous and follows the Freundlich adsorption isotherm model. SEM micrographs confirmed the adsorption of protective film on carbon steel.

## Acknowledgements

The authors like to thank the Algerian General Direction of Research (*DGRSDT*) for their support.

## References

1. Al-Moubaraki, A.H.; Obot, I.B. *J. Saudi Chem. Soc.* **2021**, 25, 101370. DOI: <https://doi.org/10.1016/j.jscs.2021.101370>.
2. Al-Janabi, Y.T. in: *Corrosion Inhibitors in the Oil and Gas Industry*, Wiley-VCH Verlag GmbH & Co. KgaA, **2020**. DOI: <https://doi.org/10.1002/9783527822140.ch1>.
3. TrabANELLI, G. *Corrosion*. **1991**, 47, 410-419. DOI: <https://doi.org/10.5006/1.3585271>.
4. Liu, J.; Yu, W.; Zhang, J.; Hu, S.; You, L.; Qiao, G. *Appl. Surf. Sci.* **2010**, 256, 4729- 4733. DOI: <https://doi.org/10.1016/j.apsusc.2010.02.082>.
5. Rice, J. *Mechanics of Solids*. Encyclopedia Britannica, 1993.
6. Musa, A.Y.; Khadum, A.A.; Kadhum, A.A.H.; Mohamad, A.B; Takriff, M.S. *J. Taiwan Inst. Chem. Eng.* **2010**, 41, 126-128. DOI: <https://doi.org/10.1016/j.jtice.2009.08.002>.
7. Ameer, M.A. ; Fekry, A.M. *Int. J. Hydrogen Energy*. **2010**, 35, 11387-11396. DOI: <https://doi.org/10.1016/j.ijhydene.2010.07.071>.
8. Khaled, K.F. *Mater. Chem. Phys.* **2011**, 125, 427-433. 542. DOI: <https://doi.org/10.1016/j.matchemphys.2010.10.037>.
9. Balulescu, M.; Herdan, J. *J. Synth. Lubr.* **1997**, 14, 35-45. 544. DOI: <https://doi.org/10.1002/jsl.3000140104>.
10. Zakeri, A. ; Bahmani, E.; Rouh Aghdam, A.S. *Corros. Commun.* **2022**, 5, 25-38. DOI: <https://doi.org/10.1016/j.corcom.2022.03.002>.
11. Yaro, A.S. ; Al-Jendeel, H. ; Khadum, A.A. *Desalination*. **2011**, 270, 193-198. DOI: <https://doi.org/10.1016/j.desal.2010.11.045>.
12. Hussin, M.H. ; Kassim, M.J. *Mater. Chem. Phys.* **2011**, 125, 461-468. DOI: <https://doi.org/10.1016/j.matchemphys.2010.10.032>.
13. Valek, L.; Martinez, S. *Materials Letters*. **2007**, 61, 148-151. DOI: <https://doi.org/10.1016/j.matlet.2006.04.024>.
14. Behpour, M.; Ghoreishi, S.M. ; Khayatkashani, M.; Soltani, N. *Mater. Chem. Phys.* **2012**, 131, 621-633. DOI: <https://doi.org/10.1016/j.matchemphys.2011.10.027>.
15. Soltani, N.; Tavakkoli, N.; Kashani, M.K.; Mosavizadeh, A.; Oguzie, E.E.; Jalali, M.R. *J. Ind. Eng. Chem.* **2014**, 20, 3217-3227. DOI: <https://doi.org/10.1016/j.jiec.2013.12.002>.

16. Dehghani, A.; Bahlakeh, G.; Ramezanzadeh, B.; Ramezanzadeh, M. *J. Ind. Eng. Chem.* **2020**, *84*, 52-71. DOI: <https://doi.org/10.1016/j.jiec.2019.12.019>.
17. Fadhil, A.A.; Khadom, A.A.; Ahmed, S.K.; Liu, H.; Fu, C.; Mahood, H.B. *Surf. Interfaces.* **2020**, *20*, 100595. DOI: <https://doi.org/10.1016/j.surfin.2020.100595>.
18. Wang, Q.; Tan, B.; Bao, H.; Xie, Y.; Mou, Y.; Li, P.; Chen, D.; Shi, Y.; Li, X.; Yang, W. *Bioelectrochemistry.* **2019**, *128*, 49-55. DOI: <https://doi.org/10.1016/j.bioelechem.2019.03.001>.
19. Chaubey, N.; Singh, V.K.; Savita; Quraishi, M.A.; Ebenso, E.E. *Int. J. Electrochem. Sci.* **2015**, *10*, 504-518. DOI: [https://doi.org/10.1016/S1452-3981\(23\)05009-5](https://doi.org/10.1016/S1452-3981(23)05009-5).
20. Boukhedena, W.; Deghboudj, S.; Benahmed, M.; Laouer, H. *J. Mex. Chem. Soc.* **2022**, *66*, 248-271. DOI: <http://dx.doi.org/10.29356/jmcs.v66i2.1630>.
21. Kalla, A.; Benahmed, M.; Djeddi, N.; Akkal, S.; Laouer, H. *Int J Ind Chem.* **2016**, *7*, 419-429. DOI: <https://doi.org/10.1007/s40090-016-0094-8>.
22. Anwar, B.; Khairunnisa, T.; Sunarya, Y. *Int. J. Corros. Scale Inhib.* **2020**, *9*, 244-256.
23. Oguzie, E.E. *Corros. Sci.* **2007**, *49*, 1527-1539. DOI: <https://doi.org/10.1016/j.corsci.2006.08.009>.
24. M'hiri, N.; Veys-Renaux, D.; Rocca, E.; Ioannou, I.; Boudhrioua, N.M.; Ghoul, M. *Corros. Sci.* **2016**, *102*, 55-62. DOI: <https://doi.org/10.1016/j.corsci.2015.09.017>.
25. Kosari, A.; Davoodi, A.; Moayed; M.H.; Gheshlaghi, R. *Corros.* **2015**, *71*, 819-827. DOI: <https://doi.org/10.5006/1578>.
26. Haris, N.I.N.; Sobri, S.; Kassim, N. *Mater. Corros.* **2019**, *70*, 1111-1119. DOI: <https://doi.org/10.1002/maco.201810653>.
27. Okewale, A.; Adesina, O.; Akpeji, B. *Nig. J. Basic Appl. Sci.* **2019**, *27*, 47-56. DOI: <https://doi.org/10.4314/njbas.v27i2.7>.
28. Caglar, A.; Sahan, T.; Selim Cogenli, M.; Yurtcan, A.B.; Aktas, N.; Kivrak, H. *Int. J. Hydrogen Energy.* **2018**, *43*, 11002-11011. DOI: <https://doi.org/10.1016/j.ijhydene.2018.04.208>.
29. Im, J.-K.; Cho, I.-H.; Kim, S.-K.; Zoh, K.-D. *Desal.* **2012**, *285*, 306-314. DOI: <https://doi.org/10.1016/j.desal.2011.10.018>.
30. Liu, Y.; Wang, J.; Zheng, Y.; Wang, A. *Chem. Eng. J.* **2012**, *184*, 248-255. DOI: <https://doi.org/10.1016/j.cej.2012.01.049>.
31. Akkal, S.; Louaar, S.; Benahmed, M.; Laouer, H.; Duddeck, H. *Chem. Nat. Compd.* **2010**, *46*, 719-721. DOI: <https://doi.org/10.1007/s10600-010-9724-0>.
32. Obi-Egbedi, N.O.; Essien, K.E.; Obot, I.B.; Ebenso, E.E. *Int. J. Electrochem. Sci.* **2011**, *6*, 913-930. DOI: [https://doi.org/10.1016/S1452-3981\(23\)15045-0](https://doi.org/10.1016/S1452-3981(23)15045-0).
33. Tinsson, W. in: *Plans d'expérience: constructions et analyses statistiques*. Springer Science & Business Media, **2010**.
34. Montgomery, D. in: *Montgomery: design and analysis of experiments*. John Wiley & Sons, **2017**.
35. Ladurée, D.; Paquer, D.; Rioult, P. *Rec. Trav. Chim. Pays-Bas.* **1977**, *96*, 254-258. DOI: <https://doi.org/10.1002/recl.19770961004>.
36. Obot, I.; Obi-Egbedi, N. *Curr. Appl. Phys.* **2011**, *11*, 382-392. DOI: <https://doi.org/10.1016/j.cap.2010.08.007>.
37. Abdallah, M. *Corros. Sci.* **2002**, *44*, 717-728. DOI: [https://doi.org/10.1016/S0010-938X\(01\)00100-7](https://doi.org/10.1016/S0010-938X(01)00100-7).
38. Ali, S.A.; El-Shareef, A.M.; Al-Ghamdi, R.F.; Saeed, M.T. *Corros. Sci.* **2005**, *47*, 2659-2678. DOI: <https://doi.org/10.1016/j.corsci.2004.11.007>.
39. Lawson, J. in: *Design and Analysis of Experiments with SAS*. Chapman and Hall/CRC, New York, **2010**.
40. Yaghoobi, H.; Fereidoon, A. *Polym. Compos.* **2018**, *39*, E463-E479. DOI: <https://doi.org/10.1002/pc.24596>.
41. Yaghoobi, H.; Fereidoon, A. *J. Nat. Fibers.* **2019**, *16*, 987-1005. DOI: <https://doi.org/10.1080/15440478.2018.1447416>.



42. Cobas, M.; Sanromán, M.A.; Pazos, M. *Bioresour. Technol.* **2014**, 160, 166-174. DOI: <https://doi.org/10.1016/j.biortech.2013.12.125>.
43. Yazici, E.Y.; Deveci, H. *Hydrometallurgy.* **2013**, 139, 30-38. DOI: <https://doi.org/10.1016/j.hydromet.2013.06.018>.
44. Hicks, C.R. in: *Fundamental concepts in the design of experiments*. Holt, Rinehart and Winston, New York, **1964**.
45. Rossi, R.J. in: *Applied biostatistics for the health sciences*. John Wiley & Sons, **2022**.
46. Garba, Z.N.; Bello, I.; Galadima, A.; Lawal, A.Y. *KIJMS.* **2016**, 2, 20-28. DOI: <https://doi.org/10.1016/j.kijoms.2015.12.002>.
47. Anadebe, V.C.; Onukwuli, O.D.; Omotioma, M.; Okafor, N.A. *Mat. Chem. Phys.* **2019**, 233, 120-132. DOI: <https://doi.org/10.1016/j.matchemphys.2019.05.033>.
48. Ahamad, I.; Prasad, R.; Quraishi, M. *Corros. Sci.* **2010**, 52, 933-942. DOI: <https://doi.org/10.1016/j.corsci.2009.11.016>.
49. Boukhedena, W.; Deghboudj, S. *J. Electrochem. Sci. Eng.* **2021**, 11, 227-239. DOI: <https://doi.org/10.5599/jese.1050>.
50. Wang, H.-L.; Fan, H.-B.; Zheng, J.-S. *Mat. Chem. Phys.* **2003**, 77, 655-661. DOI: [https://doi.org/10.1016/S0254-0584\(02\)00123-2](https://doi.org/10.1016/S0254-0584(02)00123-2).
51. Huang, W.; Zhao, J. *Colloids Surf. A.* **2006**, 278, 246-251. DOI: <https://doi.org/10.1016/j.colsurfa.2005.12.028>.
52. Fiala, A.; Boukhedena, W.; Lemallem, S.E.; Brahim Ladouani, H.; Allal, H. *J. Bio-Tribo-Corros.* **2019**, 5, 1-17. DOI: <https://doi.org/10.1007/s40735-019-0237-5>.
53. Kosari, A.; Momeni, M.; Parvizi, R.; Zakeri, M.; Moayed, M.H.; Davoodi, A.; Eshghi, H. *Corros. Sci.* **2011**, 53, 3058-3067. DOI: <https://doi.org/10.1016/j.corsci.2011.05.009>.
54. Umoren, S.A.; Obot, I.B. *Surf. Rev. Lett.* **2008**, 15, 277-286. DOI: <https://doi.org/10.1142/S0218625X08011366>.
55. Ebenso, E.E. *Mat. Chem. Phys.* **2003**, 79, 58-70. DOI: [https://doi.org/10.1016/S0254-0584\(02\)00446-7](https://doi.org/10.1016/S0254-0584(02)00446-7).



## Bioactive Lipids, Nutritional Benefits and Phytochemicals Present in *Hura Crepitans* Seed Oil

---

Ayomadewa Mercy Olatunya\*, Adeolu Jonathan Adesina

Department of Chemistry, Faculty of Science, Ekiti State University, P.M.B 5363, Ado Ekiti Nigeria.

\*Corresponding author: Ayomadewa Mercy Olatunya, email: [ayomadewa.olatunya@eksu.edu.ng](mailto:ayomadewa.olatunya@eksu.edu.ng)

Received January 24<sup>th</sup>, 2023; Accepted September 4<sup>th</sup>, 2023.

DOI: <http://dx.doi.org/10.29356/jmcs.v68i3.1950>

**Abstract.** Bioactive lipids are a group of lipids that can exhibit biological activity, prevent certain deadly diseases, and serve as sources of energy and nutrients for human's daily activities. Thus, the need for their regular availability in the body system. The bioactive lipids (fat-soluble vitamins, phytosterol, and fatty acids), phospholipids, and phytochemicals present in *Hura crepitans* seed oil were investigated using standard analytical procedures. The nutritional, antinutritional, and physicochemical properties were also investigated. The result showed that the seed oil is rich in  $\beta$  sitosterol, campesterol, stigmasterol, and vitamin A. It also has a high percentage of linoleic acid and oleic acid, with a total unsaturated fatty acid of 80.31 %. The total phospholipid content was 3717.91 mg/100 g, with phosphatidylcholine and phosphatidylethanolamine being highly abundant in the seed oil. The sample has 1.63 and 2.714 mg/100 g of saponin and alkaloids, respectively, and 0.530 mg/100 g of oxalate. The oil has a high percentage of oil yield, ionization, and saponification values and a high amount of fat (37.5 %) and protein (27.31 %). Therefore, the oil from this underutilized plant could be of numerous applications in the pharmaceutical, cosmetics, and food industries as sources of important bioactive compounds.

**Keywords:** Bioactive lipids; health benefits; *Hura crepitans*; phytochemicals.

**Resumen.** Los lípidos bioactivos son un grupo de lípidos que pueden exhibir actividad biológica, prevenir ciertas enfermedades mortales y servir como fuentes de energía y nutrientes para las actividades diarias del ser humano. De ahí la necesidad de su disponibilidad regular en el sistema corporal. Los lípidos bioactivos (vitaminas liposolubles, fitosterol y ácidos grasos), fosfolípidos y fitoquímicos presentes en el aceite de semilla de *Hura crepitans* se investigaron utilizando procedimientos analíticos estándar. También se investigaron las propiedades nutricionales, antinutricionales y fisicoquímicas. El resultado mostró que el aceite de semilla es rico en  $\beta$  sitosterol, campesterol, estigmasterol y vitamina A. También tiene un alto porcentaje de ácidos linoleico y oleico, con un total de ácidos grasos insaturados de 80.31 %. El contenido total de fosfolípidos fue de 3717.91 mg/100 g, siendo la fosfatidilcolina y la fosfatidiletanolamina, muy abundantes en el aceite de semilla. La muestra tiene 1.63 y 2.714 mg/100 g de saponina y alcaloides, respectivamente, y 0.530 mg/100 g de oxalato. El aceite tiene un alto porcentaje de rendimiento de aceite, valores de ionización y saponificación y una alta cantidad de grasa (37.5 %) y proteína (27,31 %). Por tanto, el aceite de esta planta subutilizada podría tener numerosas aplicaciones en las industrias farmacéutica, cosmética y alimentaria como fuente de importantes compuestos bioactivos.

**Palabras clave:** beneficios de la salud; fitoquímicos; *Hura crepitans*; lípidos bioactivos.

---

## Introduction

Lipids are large and diverse groups of naturally occurring organic compounds which also perform different functions in the system of living organisms [1]. They have been found to be involved in some biological activities that can help the body to run smoothly. Some of these activities include helping the brain to work well, joint mobilization, energy production, lubrication of the cells which help to protect the delicate organs of the body and also help in internal cellular communication [1]. In addition, they help to transport some vital fat-soluble components (vitamins, sterols) within the body system. Some examples of lipids components include fatty acids, phospholipids, and waxes.

Fatty acids are important constituents of the membrane cell. They are part of lipids which are widely spread in nature and are of important biological, structural and functional roles [2]. Furthermore, fatty acid produces a huge quantity of adenosine triphosphate (ATP) thus, helping to provide energy by storing used calories [3,4]. Apart from this, some lipids also help to improve the health of the human heart which made the American heart Association to recommend a daily triacylglycerol level of 100 mg for a proper functioning of the heart [4].

Bioactive lipids are the group of lipids that can exhibit biological activity and provide health benefits. Some examples of these bioactive lipids are fat soluble vitamins, phytosterols, carotenoids, phenolic lipids, Sphingomyelins [5]. Fat soluble vitamins are vitamins that are soluble in fats and are absorbed and transported in the body like fats. They are also stored in the liver and fat tissue [6].

These fat-soluble vitamins are vitamins A, D, E and K, and they are important for a wide range of biological processes in the body. Vitamins A and E are considered essential vitamins because, the body cannot synthesize them and so, they are obtained from diets while Vitamin K is synthesized in the colon and vitamin D can be synthesized by the body from exposure to sunlight. Although, these vitamins are important, their storage can lead to their excessive accumulation in human body which can also become toxic. This often occur in people that takes single supplements of fat-soluble vitamins rather than from foods rich in vitamins [7].

Phytosterols and phospholipids have been found to have numerous health benefits. This include helping in the development and proper cognition of the brain. They also help to prevent development of certain diseases thus helping the body to be in a condition of total well- being [8–10].

In view of the envisaged vast health benefits and importance of the availability of these lipids to the body system, there is a continuous search for naturally occurring sources of these lipids in some underutilized plants and their plant oils.

*Hura crepitans* plant is commonly known as Sandbox tree. It belongs to the family of Euphorbiaceae and has a height of about 9 meters on the average [11]. It houses the masculine and feminine flowers on the same tree and the back of the tree is covered with spines, the fruits are green when not ripe but turns brown on ripening (as shown in Fig. 1) and the pod explodes violently to liberate their seeds to the surrounding. The seed oil is used as purgative [11] and has also been claimed to be poisonous when ingested in excess amount while it could also cause cornea damage or partial blindness when in contact with the eye [11]. Notwithstanding these shortcomings, some researchers have found that the seeds contain high percentage of poly unsaturated fatty acids, good mineral composition and nutritional composition [11–14], but there is paucity of information to the best of our knowledge on the phospholipids and some bioactive lipids of the seed oil. Therefore, the aim of this research is to investigate the lipids and bioactive lipid profiles, phytochemical composition, nutritional and antinutritional properties and industrial properties` potentials of this underutilized African plant.

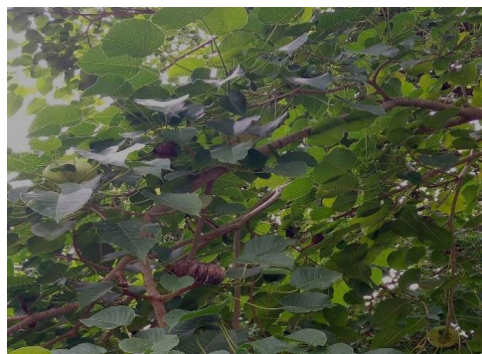


Fig. 1. *Hura crepitans* tree housing both ripe and unripe fruits.

## Materials and methods

### Collection of samples

Matured fruits were collected from *Hura crepitans* trees within Ekiti State University Ado- Ekiti premises and was identified at the Department of Plant Science of the University. The fruits were dehulled manually to obtain the seeds. The seeds were washed with distilled water to remove the contaminants and were air dried at room temperature. The dried seeds were then ground to powder using electric grinder. The powdered seeds were kept in airtight container until further use.

### Extraction of oil

100 g of the powdered sample was loaded into Soxhlet extractor with n hexane as the solvent and the oil was extracted for 8 hours at 60 –70 °C. Extracted oil was then concentrated using a rotary evaporator and was refrigerated until further analysis.

### Determination of phospholipid profile of the sample

The phospholipid profile of the extracted oil was determined using the method of Raheja et al [15], with slight modification. 0.01 g of the extracted oil was added to test tubes, and nitrogen was passed over the oil to completely remove the solvent. Chloroform (0.40 mL) was then added to the tubes, followed by 0.10 mL of a chromo-genic solution. The content of the tube was heated to 100 °C in a water bath for 80 seconds and cooled to room temperature; 5 mL of hexane was then added, and the tube was gently shaken several times. The solvent and the aqueous layer were allowed to separate; the hexane layer was recovered and concentrated to 1.0 mL for GC analysis using a gas chromatography instrument (HP 6890 Powered with HP ChemStation Rev. A 09.01 [1206] software, Agilent Technologies, Inc.) equipped with pulse flame photometric detector. The conditions were as follows: stainless steel column 30 m × 0.25 mm × 0.25 μm (HP-INNOWax, Agilent Technologies, Inc.); column temperature of 250 °C; carrier gas N<sub>2</sub>, 35 mL/minutes and H<sub>2</sub>, 30 mL/minutes. Oven temperature program: initial temperature of 50 °C; first ramping at 10 °C/minutes for 20 minutes and maintained for 4 minutes; second ramping at 15 °C/minutes for 4 minutes and maintained for 5 minutes.

### Determination of the bioactive lipids

#### Phytosterol

The phytosterol profile was determined according to the method of the International Organization for Standardization [16]. After the addition of 1.0 mL of internal standard solution, approximately 250 mg of the oil was saponified with an ethanolic potassium hydroxide solution; the unsaponifiable fraction was isolated by solid-phase extraction on an aluminum oxide column, and the steroid fraction was obtained after thin layer chromatography. Bands were visualized using n-hexane/ethyl acetate (80:20, v/v) as the developing solvent. The sterol profile was analyzed using GC analysis carried out with a HP 6890 Powered with HP ChemStation Rev. A 09.01 (1206) software (Agilent Technologies, Inc.) fitted with a HP-INNOWax column (30 m × 0.25 mm × 0.25 μm, Agilent Technologies, Inc.) equipped with flame ionization detector. Nitrogen carrier gas was used at a flow rate of 35 mL/minute and a pressure of 22 psi, 1 mL/minute. The injector and detector temperatures were 250 °C and 320 °C, respectively, and the oven was programmed to decrease in temperature from 60 to 15 °C at 4 °C/minute. The injection volume was 1 L, with a split ratio of 20:1. The total sterol content was determined by considering all peaks of sterols eluted between cholesterol and Δ<sup>7</sup>-avenasterol. Peaks were identified by comparing the relative retention times of the samples with those obtained from standards.

#### Fatty acids

The fatty acid composition was determined according to Cocks and Rede [17] with slight modification. 0.5 g of the extracted oil was mixed with 3 mL of dimethyl ether and 0.2 mL of sodium methoxide to form a colloidal solution. The solution was allowed to settle and was centrifuged to precipitate. The solid was filtered and the filtrate was kept for GC analysis. 1 μL of the filtrate was injected into the gas chromatography instrument (HP 6890 Powered with HP ChemStation Rev. A 09.01 [1206] software, Agilent Technologies, Inc.) equipped with a flame ionization detector. The conditions were the same as described for determination of

phospholipid composition above. Individual fatty acids were identified by comparing their retention times with a certified fatty acid methyl ester. The relative percentage of each fatty acid was quantified as the percentage of total fatty acids.

## Fat soluble vitamins

### Vitamin A

Quantity of vitamin A present in the sample was determined according to the methods of Sebrell and Harris [18] with slight modification. 1 mL of oil sample was measured into a 250 mL volumetric flask and dissolved in 20 mL of petroleum ether. Acetone (2:1 v/v) mixture was added to the extract. The flask containing the mixture was placed on a shaker to shake at 200 rpm for 20 minutes to ensure uniform mixing at room temperature. The mixture was later centrifuged at 4000 rpm for 10 minutes and the supernatant collected and made up to 50 mL with the solvent mixture. The supernatant was transferred to a 250 mL separatory funnel to separate the organic layer (upper layer). The aqueous layer was discarded, and the organic layer was transferred into the 50 mL volumetric flask and made up with solvent mixture for determination of absorbance. Working standard of  $\beta$ -carotene of range 0 - 50 ppm were prepared from stock solution. The absorbance of samples as well as working standard solutions was read on a Cecil CE2041 UV Spectrophotometer at a wavelength of 450 nm against blank and the amount of vitamin A present in the sample was determined.

### Vitamin E

The vitamin E was determined according to the method of Association of Official Analytical Chemists [19]. 1 mL of the sample was measured, macerated with 10 mL of n hexane in a test tube for 10 minutes and centrifuged for 10 minutes. The solution was filtered; 3 mL of the filtrate was transferred into a dry test tube in duplicates and evaporated to dryness in a boiling water bath. 2 mL of 0.5 N alcoholic potassium hydroxide was added and boiled for 30 minutes in a water bath. Then 3 mL of n-hexane was added and was shaken vigorously. The n-hexane was transferred into another set of test tubes and evaporated to dryness. 2 mL of ethanol was added to the residue and another 1 mL of 0.2 % ferric chloride in ethanol was added. Then 1 mL of 0.5 %, 1, 1-dipyridyl in ethanol was added followed by the addition of 1 mL of ethanol to make it up to 5 mL. The solution was mixed, and absorbance taken at 520 nm against the blank.

### Vitamin K

3 mL of samples and blank was measured separately into test tubes. In each test tube, 2 mL of 0.2 % solution of 2, 4 - dinitrophenyl hydrazine was added and mixed well. It was heated in a water bath to almost dryness and was cooled at room temperature. 15 mL mixture of ammonia and alcohol in ratio 1:1 was added to each test tube and its absorbance was read at 635 nm against blank.

### Vitamin D

2 mL of the oil was measured and 3 mL of hexane was added to it slowly at interval of 60 seconds. The phase was separated by centrifugation at 4000 rpm for 15 minutes. 4 mL of the upper organic phase was transferred to a small beaker and dried under liquid nitrogen gas. The dried extract was solubilized in methanol and the absorbance was taken at 275 nm and the reading was compared with that of standard at different concentrations.

## Determination of phytochemicals and antinutrients

### Saponin content

100 cm<sup>3</sup> of 20 % aqueous ethanol was added to 3 g of the powdered sample in a 250 cm<sup>3</sup> conical flask. The mixture was heated over a hot water bath for 4 hours with continuous stirring at a temperature of 55 °C. The residue of the mixture was re-extracted with another 100 cm<sup>3</sup> of 20 % aqueous ethanol after filtration and heated for 4 hours at a constant temperature of 55 °C with constant stirring. The combined extract was evaporated to 40 cm<sup>3</sup> over water bath at 90 °C. 20 cm<sup>3</sup> of diethyl ether was added to the concentrate in a 250 cm<sup>3</sup> separating funnel and vigorously agitated from which the aqueous layer was recovered while the ether layer was discarded. This purification process was repeated twice. 60 cm<sup>3</sup> of n-butanol was added and extracted twice with 10 cm<sup>3</sup> of 5 % sodium chloride. After discarding the sodium chloride layer, the remaining solution was

heated in a water bath for 30 minutes, after which the solution was transferred into a crucible and was dried in an oven to a constant weight. The saponin content was calculated as:

$$\text{Amount of Saponin} = \frac{\text{Weight of saponin}}{\text{Weight of sample}} \times 100$$

### Tannin content

One gram of the powdered sample in a conical flask was added to 100 cm<sup>3</sup> of distilled water. This was boiled gently for 1 hour and then filtered. Addition of 5 cm<sup>3</sup> Folin-Denis reagent and 10 cm<sup>3</sup> saturated Na<sub>2</sub>CO<sub>3</sub> solution into 50 cm<sup>3</sup> of distilled water and 10 cm<sup>3</sup> of diluted extract (aliquot volume) was carried out after being pipetted into a 100 cm<sup>3</sup> conical flask for color development. The solution was allowed to stand for 30 minutes in a water bath at a temperature of 25 °C after thorough agitation. The optical density was measured at 700 nm using Spectrum Lab 23A spectrophotometer and compared on a standard tannic acid curve using the equation below:

$$\text{Tannic acid (mg/100g)} = \frac{C \times \text{extract volume} \times 100}{\text{Aliquot volume} \times \text{weight of sample}}$$

Where C is the concentration of tannic acid read from the graph.

### Alkaloids content

200 cm<sup>3</sup> of 10 % acetic acid in ethanol was added to 3 g of the powdered sample in a 250 cm<sup>3</sup> beaker and allowed to stand for 4 minutes. The extract was concentrated on a water bath to one-quarter of the original volume followed by addition of 15 drops of concentrated ammonium hydroxide drop wise to the extract until the precipitation was complete immediately after filtration. After 3 hours of mixture sedimentation, the supernatant was discarded and the precipitates were washed with 20 cm<sup>3</sup> of 0.1 M of ammonium hydroxide and then filtered, the residue was dried in an oven and weighed. The percentage of alkaloid is expressed mathematically as:

$$\text{Amount of Alkaloid} = \frac{\text{Weight of alkaloid}}{\text{Weight of sample}} \times 100$$

### Flavonoid

3 g of the powdered sample was mixed with 25 mL of 80 % aqueous methanol. The whole solution was filtered through the whatman filter paper. The filtrate was transferred to a crucible and evaporated into dryness over a water bath and weighed. The amount of flavonoid present in the sample was calculated using the equation below:

$$\text{Flavonoid} \left( \frac{\text{mg}}{100\text{g}} \right) = \frac{\text{Weight of residue}}{\text{Weight of sample}} \times 100$$

### Oxalate content

Exactly 20 cm<sup>3</sup> of 0.3 M HCl in each powdered sample (2.5 g) was extracted thrice by warming at a temperature of 50 °C for 1 hour with constant stirring using a magnetic stirrer. For oxalate estimation, 1 cm<sup>3</sup> of 5 M ammonium hydroxide was added to 5 cm<sup>3</sup> of extract to ensure alkalinity. 2 drops of phenolphthalein indicator, 3 drops of glacial acetic acid, and 1 cm<sup>3</sup> of 5 % calcium chloride was added to make the mixture acidic before standing for 3 hours. This was followed by centrifugation at 3000 rpm for 15 minutes. After discarding the supernatant, the precipitate was washed three times using hot water by mixing thoroughly each time before centrifugation. 2 cm<sup>3</sup> of 3 M tetraoxosulphate (VI) acid was added to each tube and the precipitate dissolved by warming in a water bath at 70 °C. Freshly prepared 0.01 M potassium permanganate (KMnO<sub>4</sub>)

was titrated against the content of each tube at room temperature until the first pink colour appears throughout the solution. The solution was allowed to stand until it returned colorless after which it was heated and re-titrated again until a pink color appears and persists for at least 30 seconds. The amount of oxalate was calculated using the equation below:

$$\text{oxalate composition} = \frac{\text{weight of oxalate}}{\text{weight of sample}} \times \frac{100}{1}$$

### Phytate content

Samples were extracted with 100 mL of 2 % HCl for 3 hours and then filter through a No 1 Whatman filter paper. 25 mL was taken out of the filtrate and place inside a conical flask and 5 mL of 0.3 % of ammonium thiocyanate solution was added as indicator. After which 10 mL of distill, water was added to give it the proper acidity and this was titrated against iron (III) chloride solution until a brownish yellow coloration persist for 5 minutes.

### Determination of the physical, chemical, and nutritional properties of the sample

The physical and Chemical properties (acid, ionization, saponification, peroxide, FFA values) and the nutritional composition of the samples were determined using the method of the Association of Official Analytical Chemists [19].

### Statistical analysis

The analysis was carried out in triplicates and the mean of the three values were calculated using Microsoft Excel package 2016.

## Results and discussion

### Phospholipid composition

The result of the phospholipid composition of the plant is presented in Fig. 2. The result showed that the plant has a high amount of phosphatidyl choline (PC) (1847.27 mg/100 g). This was followed by phosphatidyl ethanolamine (PE) (933.31 mg/100 g) and phosphatidyl serine (PS) (647.79 mg/100 g). Phosphatic acid and lysophosphatidyl choline were detected in averagely low quantities in the plant and the total phospholipid composition of the investigated *Hura crepitans* plant was 3717.91 mg/100 g. Various classes of phospholipid have numerous health benefits because phospholipids are part of the lipid's molecules found in cellular membranes; they are essential lipid molecules that make up the lipid bi-layers of cells.

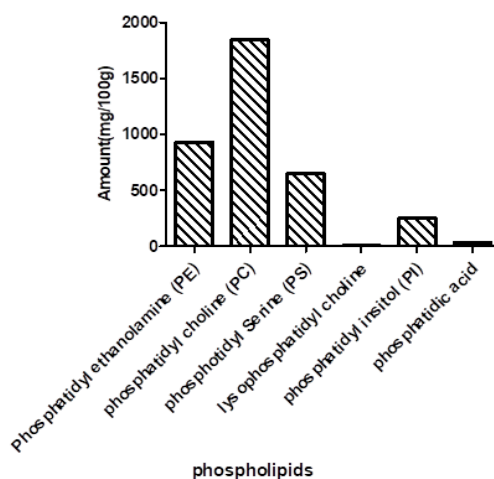


Fig. 2. Phospholipid composition of *Hura crepitans* seed oil.

The high amount of PC and PE in the plant is also of great importance because PC & PE are the most abundant phospholipid in mammalian cell membranes, comprising 30 – 50 % and 15 – 25 % respectively of total phospholipids in the cell [20,21] thus showing that the plant could be a source of these essential phospholipids.

PC has been found to be effective in ameliorating and curing liver disease [22]. It is effective in reducing the development of arthritis and helps to limit inflammatory process of joints [23,24] while PE could be helpful in suppressing cancerous cells, and in producing the energy that powers the whole cells thereby helping to support mitochondrial function [21].

The presence of PC, PE and PS in appreciable quantity coupled with the high amount of total phospholipid detected in the plants showed that the plant could be of great benefit as a potential source of these essential lipids.

### Phytosterol content

The result of the phytosterol content of the investigated plant is presented in Table 1. Based on the results obtained, *Hura crepitans* seed oil had a very high amount of  $\beta$ -Sitosterol which was followed by Campesterol and stigmasterol while the amount of total phytosterol in the plant oil was 881.55 mg/100g. Phytosterols are fatty compounds derived from plants and they represent the greatest portion of unsaponifiable matter in plant lipids. They are bioactive compounds that have been found to have numerous health benefits in the human body system [25].  $\beta$ - sitosterol, Campesterol and stigmasterol are the most common phytosterols in the human diet and these three phytosterols are beneficial to human health.  $\beta$  sitosterol has been found to have the ability to control the formation of inflammation and inflammatory cytokines thus it helps to reduce pains and normalize the function of natural killer cells which play a central role in the pathogenetic mechanisms to prevent diseases [10]. Campesterol and other plant sterols have been found to lower the chance of cardiovascular problems such as heart failure, atherosclerosis, and stroke [26]. Considering the health benefits of these phytosterols, and their high availability in this African plant, *Hura crepitans* seed could be considered as an essential plant for potential industrial sources of these phytosterols and also as nutritional supplements which are essential human nutrients because the human body cannot synthesize these bioactive lipids [25]. A unique contribution of our study is the observation that prior to now, little is known about the phospholipid and phytosterol compositions of *Hura crepitans* seed oil. Thus, making the current study about the first to highlight the rich component of these essential compounds in the plant. Given the potential numerous health benefits of phytosterols and phospholipids, our study has raised the need for further research to explore more about the biochemical composition of *Hura crepitans* seeds.

**Table 1.** Phytosterol composition of *Hura Crepitans* plant.

| Phytosterol composition | Amount (mg/100 g)      |
|-------------------------|------------------------|
| Cholesterol             | $4.653 \times 10^{-5}$ |
| Cholestanol             | $4.699 \times 10^{-4}$ |
| Ergosterol              | $3.71 \times 10^{-6}$  |
| Campesterol             | 104.52                 |
| Stigmasterol            | 79.57                  |
| 5 – avenasterol         | 8.521                  |
| Sitosterol              | 688.94                 |
| <b>Total</b>            | <b>881.55</b>          |

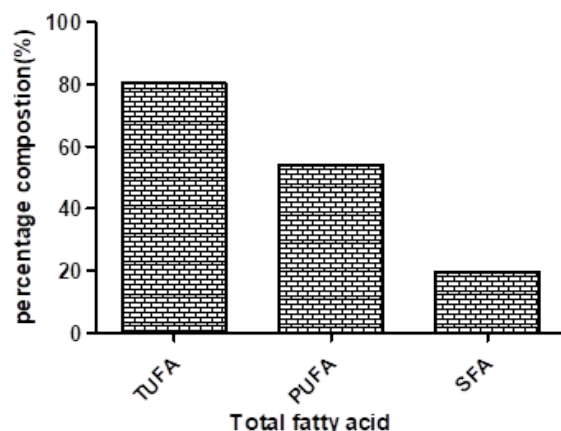
### Fatty acid composition of the investigated plant

The result of the fatty acid composition of *Hura crepitans* plant is presented in Table 2 while the results of the total fatty acids is presented in Fig. 3. As shown in Table 2, the plant has high amount of linoleic and oleic acids (52.25 and 25.50 %) respectively. It also has a total saturated fatty acid composition of 19.69 %, total unsaturated fatty acid composition of 80.31 % and poly unsaturated fatty acid composition of 54.15 % (Fig. 3).

**Table 2.** Fatty acid composition of *Hura crepitans* plant.

| Fatty Acid       | Percentage composition |
|------------------|------------------------|
| Myristic acid    | 0.43                   |
| Palmitic acid    | 12.09                  |
| Palmitoleic acid | 0.60                   |
| Margaric         | 0.069                  |
| Stearic acid     | 5.32                   |
| Oleic acid       | 25.50                  |
| Linoleic         | 52.25                  |
| Linolenic acid   | 1.56                   |
| Arachidic        | 0.88                   |
| Arachidonic      | 0.105                  |
| Behenic acid     | 0.604                  |
| Erucic acid      | 0.230                  |
| Lignoceric acid  | 0.291                  |

The fatty acid profile of the *Hura crepitans* plant presented in this present work is similar to the reports of Ezeh et.al. [27] and Alabi et al. [28] but has higher percentage composition of linoleic fatty acid when compared to the reports of Okolie et al. [29], Abdulkadir et al. [11] and Oyeleke *et al.* [12]. The discrepancies in these results may be due to the differences in geographical location, season of sampling and method of extraction and analysis. Linoleic fatty acids also known as Omega 6 fatty acids are precursor for other omega - 6 fatty acids because the body cannot synthesize long chain fatty acids with odd numbers of carbon atoms [2] but these long chain fatty acids are important for the mammalian cells to perform various biological functions. Linoleic fatty acids are the major components of the adipose tissues like the brain where they take part in the development and maintenance of the central nervous system during both embryonic and adult stages [30]; they also help in sustaining the structural integrity of cellular membranes and serve as signaling molecules [30]. Another important fatty acid present in high amount is oleic acid which was the major monounsaturated fatty acid present in the sample. Oleic acid has antioxidant ability that prevents oxidative stress which can lead to various diseases [31], it is also beneficial in the treatment of type 2 diabetes and insulin sensitivity [32].



**Fig. 3.** Total fatty acid composition of *Hura crepitans* seed oil.



TUFA- total unsaturated fatty acid; PUFA – poly unsaturated fatty acid, SFA- saturated fatty acid

### Fat- soluble vitamins

The result of the fat -soluble vitamin of the plant is presented in Fig. 4. Based on the result obtained, the plant contains majorly vitamin A (116.55  $\mu\text{g}/\text{kg}$ ) and little concentration of vitamins D, E and K. Vitamin A are important in multiple cellular processes like communication, recognition, adhesion and aggregation. These they do by helping in glycoproteins synthesis which are important in the above - mentioned cellular processes [6]. Vitamin A has also been found to be used in treatment of skin cancer, acne, and acne related diseases. It also has antioxidant activity, and it is required for the maintenance of normal mucous membrane and normal vision [6]. Therefore, the plant could be a source of vitamin A for various industrial processes and applications. The vitamin A profile of the *Hura crepitans* plant presented in this work is lower when compared to the reports of Udoh *et al.* [13] and Fowomola & Akindahunsi [14]; the variation in the results may be due to the differences in the processing techniques, season of harvest, method of determination of the parameter and geographical locations which is a reflection of the climatic conditions in which the plant is grown. Despite these differences, all the authors including the present study, have established that *Hura crepitans* contain high quantity of vitamin A thus confirming that the plant could be a good source of the vitamin.



Fig. 4. Fat soluble vitamin composition of *Hura crepitans* plant.

### Phytochemical and antinutritional composition

The results of phytochemical and antinutritional composition of the plant are presented in Table 3. The results showed that the plant contains appreciable amounts of saponin and alkaloid. Other investigated phytochemicals were detected in low quantity in the plant. For the antinutrients, phytate and oxalate were detected in minute quantities in the investigated African plants (Table 3). Saponins can control human cardiovascular disease and reduce blood cholesterol in human [33]. They also possess various pharmaceutical properties like anti-inflammatory [34], immunological adjuvant activities, hemolytic activities, antioxidant properties and anti – cancer effects thus attracting a lot of attention as potential targets for drug discovery and development [35].

Table 3. Phytochemical and Antinutritional composition of *Hura crepitans* plant.

| Phytochemical | Amount (mg/100 g) |
|---------------|-------------------|
| Saponin       | 1.633             |
| Alkaloid      | 2.714             |
| Tannin        | 0.399             |
| Flavonoid     | 0.524             |

| Antinutrients | Amount (mg/100 g) |
|---------------|-------------------|
| Phytate       | 0.210             |
| Oxalate       | 0.530             |

Pure isolated alkaloids and their synthetic derivatives are used as basic medicinal agents because of their analgesic, antispasmodic and antibacterial properties [36]. Therapeutically, alkaloids are particularly well known as anaesthetics, cardioprotective, anti-cancer and anti-inflammatory agents [37,38] and these further highlights the health and industrial benefits of this phytochemical. The fact that these phytochemicals were detected in the investigated plant showed that the plants could be used as a source of the phytochemicals; further affirming its usefulness in the industries to solving sundry human needs problems.

Phytate has been reported to be able to form a complex with protein by the actions of cations (Zn, Ca) which act as a bridge between the negatively charge protein carboxyl and the phytate thereby making the cation unavailable to the body system. Likewise, oxalate binds with another mineral such as calcium to form oxalate salt and complexes which have an inhibitory effect in peptic digestion and can lead to kidney stone disease [13,33,39]. Both antinutrients inhibit the bioavailability of minerals in the body system when ingested in high amount.

It has been suggested that dietary oxalate in the range of 50 – 200 mg is acceptable [40]. However, phytate amounts higher than 50 mg/ day could cause a significant reduction in zinc absorption [41]. The quantity detected in the investigated sample is far lesser than the toxicity level proposed by these researchers [40,41], thus suggesting that it is likely that *Hura crepitans* may be safe and less toxic. Nevertheless, there is need for further research on the antinutritional components of the plant to ascertain its safety.

### Physicochemical properties and the nutritional composition of the plants

The physical and chemical properties of the investigated plant are presented in Table 4 while the nutritional parameters are presented in Table 5. The results of the physical and chemical properties of the investigated plant showed that the sample has percentage oil yield of 58.76 %. It has high iodine and saponification values (159.58 (Wijs) and 193.37 mgKOH/g respectively). It also has high quantity of unsaponifiable matters. The pH is 5.20 and the specific gravity is 0.87 g/mL. Regarding the nutritional composition of the plant, the amount of protein detected in the sample was 27.31 %, carbohydrate of 11.2 % and fat of 37.50 % (Table 5).

**Table 4.** The physical and chemical properties of *Hura Crepitans* seed.

| Parameters                                          | Amount        |
|-----------------------------------------------------|---------------|
| Colour                                              | Golden yellow |
| Percentage oil yield (%)                            | 58.76         |
| pH                                                  | 5.20          |
| Acid value (mgKOH/g)                                | 2.35          |
| Iodine value (Wijs)                                 | 159.58        |
| Peroxide value (Meq/kg)                             | 5.26          |
| Saponification value (mgKOH/g)                      | 193.37        |
| Unsaponifiable matter (g/kg)                        | 14.85         |
| Specific gravity (g/mL)                             | 0.87          |
| Kinetic viscosity (cp)                              | 4.92          |
| Refractive index (n <sub>D</sub> 40) <sup>0</sup> C | 1.45          |
| Free fatty acid (mgKOH/g)                           | 5.21          |

The percentage oil yield of the investigated plant is higher than 25.7 % reported for groundnut by Olatunya et al [42], showing that the plant has higher oil yield than some conventional oil seeds. The low acid value, peroxide value, high iodine, and saponification values of the oil are indication of the oil's potential industrial's benefits. Acid values are indication of edibility of oil. The recommended codex acid value for edible virgin oils is 6.6 mg KOH/g according to Food and Agriculture Organisation [43] the acid value reported for the investigated oil is lower than the recommended value thus indicating that the oil could be safe. Iodine values are used to indicate the level of unsaturation in oil and are also used to classify the oil into drying or non-drying oil.

The high iodine value of the investigated oil is an indication that the plant oil has high level of unsaturation, and this has been further corroborated in the fatty acid composition of the oil. Oils with iodine values greater than 130 mgKOH/g are classified as drying oil; based on this *Hura crepitans* oil could be regarded as a drying oil and therefore, it could be used in the industries to manufacture cosmetics, oil paint and vanishes [44]. In addition, the saponification values are indication of the oil's applicability in the production of soap [45]. The physical and chemical properties of *Hura crepitans* seed oil presented in this work is comparable with the reports of other authors who have previously worked on the plant [46–49]. Owing to the high oil yield of this plant and some of its chemical properties, the seed oil will be of great importance in various industries.

**Table 5.** Nutritional Composition of *Hura crepitans* flour

| Analysis         | Amount (%) |
|------------------|------------|
| Moisture content | 10.5       |
| Ash content      | 7.55       |
| Fat              | 37.5       |
| Crude fibre      | 5.94       |
| Protein          | 27.3       |
| Carbohydrate     | 11.2       |
| Energy (kcal)    | 321        |

The nutritional composition of the plant showed that it is rich in protein, fat, and carbohydrates and has averagely high amount of crude fiber which showed that the seed flour could be used in animal feed. The high ash content of the samples is an indication for presence of minerals. This observation is in agreement with the reports of Oyeleke et al. [12] and Okolie *et al.* [29] on *Hura crepitans* seed flour.

## Conclusions

The samples are rich in phytosterols, phospholipids, vitamin A, polyunsaturated and monounsaturated fatty acids. All these bioactive lipids have been found to have numerous health benefits. They also help the body system to carry out some biological functions; thus, their availability in this plant showed that the plant could be a source of these essential ingredients. The plant also has averagely high quantity of alkaloids and saponin which are some of the major phytochemicals that have been found to be of great importance in pharmaceutical industries thus making this underutilized and readily available plant to be of great usefulness in the pharmaceutical industries as therapeutic agent. The amount of the antinutrients detected in the samples indicated that the plant may be safe and less toxic. The physical, chemical, and nutritional analysis of the plant showed that the plant is rich in protein, carbohydrates, and fat. It also has good chemical properties indicating its potential use in various industries. Therefore, this study showed that (*Hura crepitans*) an underutilized plant, has great industrial potentials and health benefits potentials rather than being considered as a waste. Nevertheless, more research is needed to confirm its safety profile.

## References

1. Olatunya, A. M.; Ajaja, A. K.; Akintayo, E. T. *Sci. Study Res. Chem. Chem. Eng. Biotechnol. Food Ind.* **2021**, 22, 191–199.
2. Nagy, K.; Tiuca, I. D. in: *Importance of Fatty Acids in Physiopathology of Human Body*. In Catala A (ed) Fatty Acids; IntechOpen: London, 2017 ISBN 978-953-51-3302-5.
3. Olatunya, A. M.; Akintayo, E. T. *Res. J. Chem. Environ.* **2019**, 23, 56–61.
4. Stone, N. J.; Robinson, J. G.; Lichtenstein, A. H.; Bairey Merz, C. N.; Blum, C. B.; Eckel, R. H.; Goldberg, A. C.; Gordon, D.; Levy, D.; Lloyd-Jones, D. M. *J. Am. Coll. Cardiol.* **2014**, 63, 2889–2934, <http://dx.doi.org/10.1016/j.jacc.2013.11.002>.
5. Zhang, Y.; Zhang, T.; Liang, Y.; Jiang, L.; Sui, X. *J. Agric. Food Chem.* **2021**, 69, 8929–8943.
6. Ravisankar, P.; Reddy, A. A.; Nagalakshmi, B.; Koushik, O. S.; Kumar, B. V.; Anvith, P. S. *IOSR J. Pharm.* **2015**, 5, 12–28.
7. <https://www.verywellfit.com/fat-soluble-vitamins-2241991>, accessed in September, 2022.
8. Olatunya, A. M.; Omojola, A.; Akinpelu, K.; Akintayo, E. T. *Prev. Nutr. Food Sci.* **2019**, 24, 338–343. DOI: <https://doi.org/10.3746/pnf.2019.24.3.338>.
9. Jayaraman, T.; Kannappan, S.; Ravichandran, M. K.; Anuradha, C. V. *Singapore Med. J.* **2008**, 49, 320.
10. Berger, A.; Jones, P. J.; Abumweis, S. S. *Lipids Health Dis.* **2004**, 3, 1–19. DOI: <https://doi.org/10.1186/1476-511X-3-5>.
11. Abdulkadir, M. N.; Amoo, I. A.; Adesina, A. O. *Int. J. Sci. Res.* **2013**, 2, 440–445.
12. Oyeleke, G. O.; Olayiwola, O. A.; Latona, D. F. *IOSR J. Appl. Chem.* **2012**, 1, 10–13.
13. Udoh, A. P.; Udousoro, I. I.; Sunday, I. U. *Niger. J. Chem. Res.* **2019**, 24, 15–25.
14. Fowomola, M. A.; Akindahunsi, A. A. *J. Med. Food.* **2007**, 10, 159–164.
15. Raheja, R. K.; Kaur, C.; Singh, A.; Bhatia, I. S. *J. Lipid Res.* **1973**, 14, 695–697.
16. International Organisation for Standardization (ISO) *Animal and Vegetable Fats and Oils- Determination of Composition of the Sterol Fraction - Method Using Gas Chromatography*; International Organisation for Standardization: Switzerland, 1991.
17. Cocks, L. V.; Rede, C. V., in: *Laboratory Handbook for Oil and Fat Analysts*; London & New York: Academic Press, **1966**.
18. Sebrell, W.; Harris, R. in: *Descriptive Information on the Chemistry, Physicochemical Properties and Physiology of Vitamin A*. In The Vitamins; Academic Press: New York, **1967**; 1, 140.
19. AOAC *Official Methods of Analysis of AOAC International*; 18th ed.; AOAC International: Maryland USA, **2006**.
20. Zeisel, S. H. *J. Am. Coll. Nutr.* **2004**, 23, 621S-626S. DOI: <https://doi.org/10.1080/07315724.2004.10719433>.
21. Patel, D.; Witt, S. N. *Oxid. Med. Cell. Longev.* **2017**, 2017, 4829180. DOI: <https://doi.org/10.1155/2017/4829180>.
22. Küllenberg, D.; Taylor, L. A.; Schneider, M.; Massing, U. *Lipids Health Dis.* **2012**, 11, 1–16. DOI: <https://doi.org/10.1186/1476-511X-11-3>.
23. Hartmann, P.; Szabó, A.; Eros, G.; Gurabi, D.; Horváth, G.; Németh, I.; Ghyczy, M.; Boros, M. *Eur. J. Pharmacol.* **2009**, 622, 58–64. DOI: <https://doi.org/10.1016/j.ejphar.2009.09.012>.
24. Eros, G.; Ibrahim, S.; Siebert, N.; Boros, M.; Vollmar, B. *Arthritis Res. Ther.* **2009**, 11, 1–10. DOI: <https://doi.org/10.1186/ar2651>.
25. Salehi, B.; Quispe, C.; Sharifi-Rad, J.; Cruz-Martins, N.; Nigam, M.; Mishra, A. P.; Kononov, D. A.; Orobinskaya, V.; Abu-Reidah, I. M.; Zam, W.; et al. *Front. Pharmacol.* **2021**, 11, 599959. DOI: <https://doi.org/10.3389/fphar.2020.599959>.
26. <https://www.healthbenefitstimes.com/nutrition/campesterol>, accessed in December, **2022**.

27. Ezeh, I. E.; Umoren, S. A.; Essien, E. E.; Udoh, A. P. *Ind. Crops Prod.* **2012**, 36, 94–99. DOI: <https://doi.org/10.1016/j.indcrop.2011.08.013>.
28. Alabi, K. A.; Lajide, L.; Owolabi, B. J. *Fountain J. Nat. Appl. Sci.* **2013**, 2, 32–37. DOI: <https://doi.org/10.53704/fujnas.v2i2.28>.
29. Okolie, P. N.; Uaboi-Egbenni, P. O.; Ajekwene, A. E. *World J. Agric. Sci.* **2012**, 8, 359–365. DOI: <https://doi.org/10.5829/idosi.wjas.2012.8.4.1119>.
30. Liu, Q.; Zhang, J. *Neurosci. Bull.* **2014**, 30, 331–345. DOI: <https://doi.org/10.1007/s12264-013-1410-3>.
31. Carrillo, C.; Cavia, M. D. M.; Alonso-Torre, S. R. *Nutr. Hosp.* **2012**, 27, 1860–1865. DOI: <https://doi.org/10.3305/nh.2012.27.6.6010>.
32. Palomer, X.; Pizarro-Delgado, J.; Barroso, E.; Vázquez-Carrera, M. *Trends Endocrinol. Metab.* **2018**, 29, 178–190. DOI: <https://doi.org/10.1016/j.tem.2017.11.009>.
33. Akinyeye, R. O.; Olatunya, A. M. *Med. Aromat. Plant Res. J.* **2014**, 2, 44–49.
34. Hamid, A. A. H.; Saleh, A.; Sidik, N. J.; Rahim, N.; Hadzir, N. M.; Ahmat, N. *Malays. J. Chem.* **2022**, 24, 184–190.
35. Sharma, P.; Tyagi, A.; Bhansali, P.; Pareek, S.; Singh, V.; Ilyas, A.; Mishra, R.; Poddar, N. K. *Food Chem. Toxicol.* **2021**, 150, 112075. DOI: <https://doi.org/10.1016/j.fct.2021.112075>.
36. Eleazu, C. O.; Eleazu, K. C. *Am. J. Food Technol.* **2012**, 7, 214–221.
37. Kurek, J. in: *Alkaloids: Their Importance in Nature and Human Life*; BoD–Books on Demand IntechOpen: UK, London, **2019**.
38. Heinrich, M.; Mah, J.; Amirkia, V. *Molecules.* **2021**, 26, 1836. DOI: <https://doi.org/10.3390/molecules26071836>.
39. Hassan, L. G.; Sokoto, A. M.; Ngaski, M. A.; Anka, S. A.; Chanchang, B. M.; Umar, K. J.; Ogbiko, C. *Bayero J. Pure Appl. Sci.* **2018**, 11, 126–130. DOI: <https://doi.org/10.4314/bajopas.v11i1.22>.
40. Siener, R.; Bade, D. J.; Hesse, A.; Hoppe, B. *J. Transl. Med.* **2013**, 11, 306. DOI: <https://doi.org/10.1186/1479-5876-11-306>.
41. Fredlund, K.; Isaksson, M.; Rossander-Hulthén, L.; Almgren, A.; Sandberg, A. S. *J. Trace Elem. Med. Biol.* **2006**, 20, 49–57.
42. Olatunya, A. M.; Olatunya, O. S.; Akintayo, E. T. *Heliyon.* **2017**, 3, e00414. DOI: <https://doi.org/10.1016/j.heliyon.2017.e00414>.
43. FAO *Codex Standard of Fats and Oils from Vegetable Source*; Food and Agriculture Organisation, **1999**.
44. Dawodu, F. A. *Electron. J. Environ. Agric. Food Chem.* **2009**, 8, 102–110.
45. Aremu, M. O.; Ibrahim, H.; Bamidele, T. O. *Chem. Process Eng. Res.* **2015**, 32, 36–52.
46. Oyekunle, J. A. O.; Omode, A. A. *Int. J. Food Prop.* **2008**, 11, 273–281. DOI: <https://doi.org/10.1080/10942910701302598>.
47. Umoren, S. A.; Ajibesin, K. K.; Bala, D. N. *J. Nat. Appl. Sci.* **2001**, 1, 23–26.
48. Udoh, A. P.; Umoren, I. U.; Michael, E. P. *J. Mater. Environ. Sci.* **2020**, 11, 157–165.
49. Ifijen, I.; Nkwor, A. *Tanzan. J. Sci.* **2020**, 46, 817–827.

## Ion Migration Study on $\text{YAlO}_3$ -perovskite through Atomistic Simulations

---

Rubén O. Miranda-Rosales, J. Francisco Gómez-García\*

Departamento de Física y Química Teórica, Facultad de Química, UNAM. Circuito Exterior S/N, Ciudad Universitaria, C. P. 04510, Ciudad de México, Mexico.

\*Corresponding author: J. Francisco Gómez-García, email: [jfrancisco@comunidad.unam.mx](mailto:jfrancisco@comunidad.unam.mx)

Received April 13<sup>th</sup>, 2023; Accepted September 9<sup>th</sup>, 2023.

DOI: <http://dx.doi.org/10.29356/jmcs.v68i3.2047>

**Abstract.** In this work, we presented an atomistic simulation study on  $\text{YAlO}_3$  perovskite. We simulated the reported crystal structure through the energy minimization process from coulombic and Buckingham potentials with the General Utility Lattice Program (GULP). We determined the formation energy for all point pair defects presented in the system. We found that the anionic Frenkel together with Schottky pair defects are the main defects in the  $\text{YAlO}_3$  perovskite.

Additionally, we performed several energy profile migrations for each ion, and we determined that oxygen migration was the favored migration via the vacancy-vacancy path with 98.70 kJ/mol. In the end, we performed a series of calculations about doping energy, and we calculated that  $\text{Ca}^{2+}$  is the best aliovalent ion for doping  $\text{YAlO}_3$  compound, which involves the minimum doping energy while the aliovalent doping increases the oxygen vacancy defects. We suggested that these atomistic simulations could be used as a tool in the design or optimization of new materials for developing solid electrolytes.

**Keywords:**  $\text{YAlO}_3$  perovskite; atomistic simulations; point defect energy; ion migration.

**Resumen.** En este trabajo presentamos un estudio hecho por medio de simulaciones atomísticas para el compuesto  $\text{YAlO}_3$  con estructura perovskita. La estructura se simuló por medio de la minimización energética de los potenciales de Coulomb y de Buckingham. Se determinó la energía de formación para todos los pares de defectos puntuales que puede presentar el sistema y encontramos que los defectos tipo Frenkel aniónico y los Schottky son los principales en el compuesto de estudio. También determinamos los perfiles energéticos de migración para los iones en el sistema y encontramos que la migración de menor energía corresponde a la de oxígeno vía vacancia-vacancia con una energía de 98.70 kJ/mol. Hacia el final del artículo, presentamos los cálculos referentes a la energía de dopaje y encontramos que el mejor ion para dopar al compuesto  $\text{YAlO}_3$  es el ion  $\text{Ca}^{2+}$ ; esto debido a la menor energía de dopaje involucrada y el hecho de que el dopaje aliovalente incrementa las vacancias de oxígeno en el sistema. Sugerimos que este tipo de estudios pueden ser una herramienta muy versátil en el desarrollo y optimización de nuevos electrolitos sólidos.

**Palabras clave:** Perovskita  $\text{YAlO}_3$ ; simulaciones atomísticas; energía de defectos puntuales; migración de iones.

---

## Introduction

Solid Electrolytes (SE) are materials involved in many technological devices that are directly or indirectly related to renewable energy. Electrolyzers for water splitting [1], [2], electrochemical membranes for gas separation [3], and solid oxide fuel cells (SOFCs) for electricity generation [4] among others, are devices

where the electrolyte plays an important role due to the charge-mass transport. Developing better electrolyte materials will enhance the performance of the electrochemical devices and consequently, will consolidate an energy society with low-carbon fuels, whether hydrogen as an energetic vector is considered [5].

High-Temperature Solid Electrolytes (HTSE) display better performance in ionic transport than room-temperature ones. Additionally, when HTSE are used in electrochemical devices, these show fast catalytic response at electrodes which allows to use of materials based on oxides instead of Pt or Pd electrodes [6]. These characteristics get the attention of the research community for developing new HTSE for electrochemical devices and atomistic simulations could be a useful tool for exploring in silico which materials are candidates to bring out good electrical properties. Thus, in this work, we performed atomistic simulations in  $\text{YAlO}_3$  with perovskite structure since this crystal structure has the main characteristic for exhibiting ionic conductivity as close packed anion arranged together with ions in its high oxidation state which minimizes the electronic conductivity [7]. Besides this, perovskite-type structures could present proton conductivity, which is another form of ionic conductivity [8-10]. Also, we presented a doping study with aliovalent ions; as ionic conductivity depends on the charge carrier concentration, doping systems had the higher concentration [11] due to the extrinsic point defects are much bigger than intrinsic defects.

$\text{YAlO}_3$  exhibits a perovskite-like structure with octahedra tilting. The unit cell is orthorhombic with lattices parameters  $a = 5.33 \text{ \AA}$ ,  $b = 7.375 \text{ \AA}$  and  $c = 5.18 \text{ \AA}$ . This structure presents two crystal positions for oxygen ion, one at  $4c$  (0.475, 1/4, 0.586) and the other at  $8d$  (0.293, 0.044, 0.203) Wyckoff positions, while the cations present only one crystal position;  $4c$  (0.0526, 1/4, 0.4896) for  $\text{Y}^{3+}$  and  $4b$  (0, 0, 0) for  $\text{Al}^{3+}$ . The space group for this crystal structure was reported as  $Pnma$  (No. 62) [12].

Atomistic simulations had been employed to study ion diffusion pathways in several systems showing results very close to experimental values [13–16], thus we used this methodology in this work. Atomistic simulations were carried out using GULP code (version 5.2) [17], [18]. This code uses static modeling techniques based on the classical Born model for ionic solids, allowing the description in mathematical terms of the system energy as a function of particle coordinates. In this model, the integral charge of the ions corresponds to its oxidation state, and the energy interactions ( $V_{ij}$ ) between ions are calculated in terms of long-range coulombic forces and short-range pair potentials with the standard Buckingham potential. This potential simulates the electron cloud overlap (Pauli repulsion) and dispersion interactions (van der Waals) [13]. All these terms are included in equation 1, where  $\kappa$  is the Coulomb constant;  $q_i$  and  $q_j$  are the integral charges of the ions  $i$  and  $j$  respectively;  $r_{ij}$  is the inter-ionic distance and  $A_{ij}$ ,  $\rho_{ij}$ , and  $C_{ij}$  are empirical parameters assigned to each ion-ion interaction, except for the cation-cation interactions which were treated as purely coulombic.

$$V_{ij}(r_{ij}) = \frac{1}{2} \kappa \frac{q_i q_j}{r_{ij}} + A_{ij} \exp\left(\frac{-r_{ij}}{\rho_{ij}}\right) - \frac{C_{ij}}{r_{ij}^6} \quad (1)$$

## Results and discussion

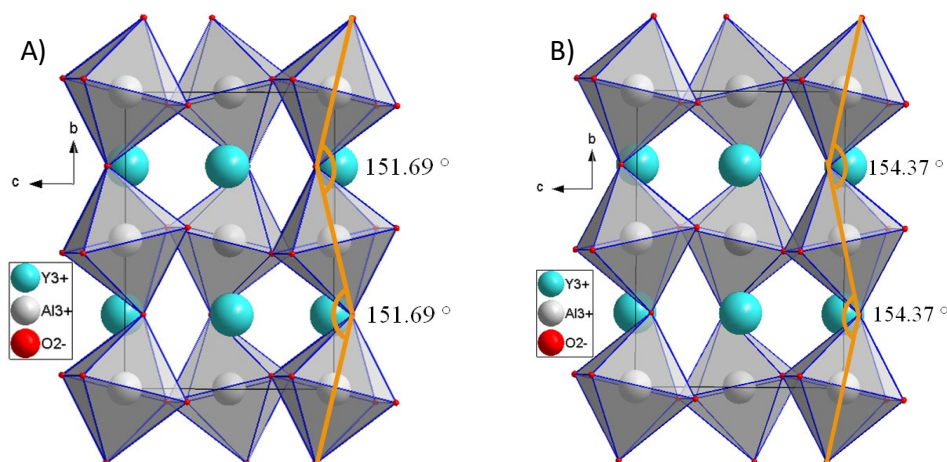
$\text{YAlO}_3$  perovskite crystal structure was calculated using Buckingham pair potentials previously reported for Y-O, O-O [19], and Al-O [20]. These potentials are listed in Table 1 together with core-shell parameters. Crystal structure results are showed in Table 2 where it can be seen that the calculated lattice parameters agreed with those previously reported by Diehl [12]. Calculated atomic coordinates (data not showed) also agreed with experimental ones as can be observed in Fig. 1, where not only coordination polyhedra were the same but the tilting angle was satisfactorily calculated after fitting the  $\rho$  Buckingham parameter for cation-anion interactions.

**Table 1.** Parameters used for  $\text{YAlO}_3$  crystal modeling with GULP, the potentials for Y-O, O-O pairs were taken from [19], and for Al-O pair from [20].

| Ionic pair | $A$ [kJ/mol] | $\rho$ [Å] | $C$ [kJ/mol Å <sup>6</sup> ] | Ion              | $Y^+$ [e] | $k$ [kJ/mol Å <sup>2</sup> ] |
|------------|--------------|------------|------------------------------|------------------|-----------|------------------------------|
| Y-O        | 126395.79    | 0.350865   | 0.00                         | $\text{Y}^{3+}$  | 0.0000    | 9648437.16                   |
| Al-O       | 232481.90    | 0.275805   | 0.00                         | $\text{Al}^{3+}$ | 0.0430    | 38978.15                     |
| O-O        | 2196421.15   | 0.1490     | 4148.87                      | $\text{O}^{2-}$  | 0.2389    | 4052.38                      |

**Table 2.** Structural parameters comparison between reported and simulated structures.

| Parameter                     | Reported | Simulated |
|-------------------------------|----------|-----------|
| $a$ [Å]                       | 5.330    | 5.274     |
| $b$ [Å]                       | 7.375    | 7.406     |
| $c$ [Å]                       | 5.180    | 5.223     |
| $V$ [Å <sup>3</sup> ]         | 203.619  | 204.031   |
| $E_{\text{lattice}}$ [kJ/mol] | --       | -14373.3  |



**Fig. 1.** (A) Reported and (B) calculated crystal structure for  $\text{YAlO}_3$  perovskite.

Since the calculated lattice was close to the experimental one, we performed point defect calculations to obtain the formation energy for associated point defects (Schottky and Frenkel defects). Point defects were calculated using the Mott-Littleton approximation [21] which splits the crystal into three spherical regions to optimize the calculations; the inner region, called Region 1, has the defect at the center, and the ions are strongly affected by the point defect. The ion positions in Region 1 must be calculated for each ion. In the next region, called Region 2a, the ions are slightly affected by the point defect and their positions can be calculated through a potential. In the outer region, called Region 2b, the ions are not affected by the point defect and do not contribute to the defect energy calculation. In this work we use a 14 Å radius for Region 1 and a 30 Å radius for Region 2a, this configuration allowed us to calculate the point defect energy considering the effect of 2300 ions around the point defect; usually, the Mott-Littleton approximation considers at least 300 ions for this kind



of calculations [22]. The calculated energy relative to points defects is listed in Table 3; the interstitial positions used in these calculations were (0.5,0.5,0) for  $Y^{3+}$ , (0.5395, 0.25, 0.25) for  $Al^{3+}$ , and (0.8616, 0.75, 0.875) for  $O^{2-}$ . In this table is possible to see that oxygen vacancy energy for the two crystallographic oxygen ions is very close between them because of the similar crystallo-chemical environment.

**Table 3.** Calculated point defects energy in  $YAlO_3$  perovskite.

| Species        | Energy [kJ/mol] |              |
|----------------|-----------------|--------------|
|                | Vacancies       | Interstitial |
| Y              | 4436.02         | -2192.35     |
| Al             | 5928.85         | -4088.59     |
| O <sub>1</sub> | 2151.65         | -1213.50     |
| O <sub>2</sub> | 2147.71         |              |

We use standard Kröger-Vink defect notation to describe associated defects such as Schottky or Frenkel defects. Symbols as  $V_O^-$  or  $Y_{Al}^x$  are used to describe a single point defect; the main symbol indicates the specie at point defect (usually  $V$  is used for indicating a vacancy), subscript indicates the position in the lattice represented by the atom or ion occupying that site (interstitial positions are represented by  $i$ ), and superscript indicates the charge of the point defect, dots (·) for positive charge, dashes (‘) for negative, and (x) for neutral defects [23].

From point defect and lattice energy, it was possible to determine the formation energy for the intrinsic defects on the  $YAlO_3$  structure according to its corresponding formation reactions listed below in Kröger-Vink notation.



In these equations *null* indicates a perfect crystal without point defects so the formation energy for each intrinsic defect was calculated taking into account the *null* state as a reference value (0 kJ/mol) and, in the case of Schottky defect, lattice energy was considered in the equation due to mass conservation. A couple of examples of those calculations are presented below.

$$E_{Schottky} = \frac{1}{5} \left( E_{V_{Al}^m} + E_{V_Y^m} + E_{V_{O_1}^{2-}} + 2E_{V_{O_2}^{2-}} + E_{YAlO_3} \right) \quad \text{Schottky formation (6)}$$

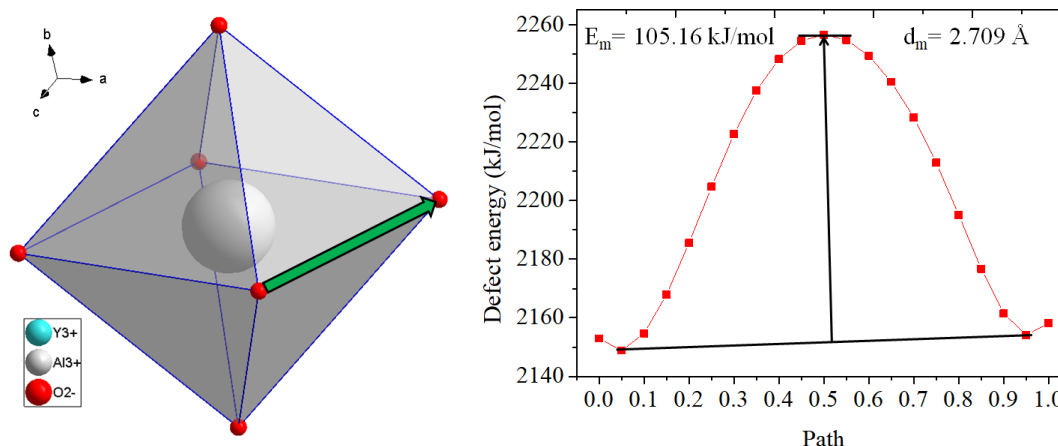
$$E_{Frenkel,Al} = \frac{1}{2} \left( E_{V_{Al}^m} + E_{Al_i^{3+}} \right) \quad \text{Aluminum Frenkel formation (7)}$$

The energy defect formation is normalized to the total number of point defects formed in each reaction. The calculated values are listed in Table 4, where it can be seen that Schottky and anionic Frenkel defects are the most favoured and in consequence, the cationic and oxygen vacancies together with oxygen interstitial are the main defects present in the system.

**Table 4.** Associative defects energy in  $\text{YAlO}_3$  perovskite.

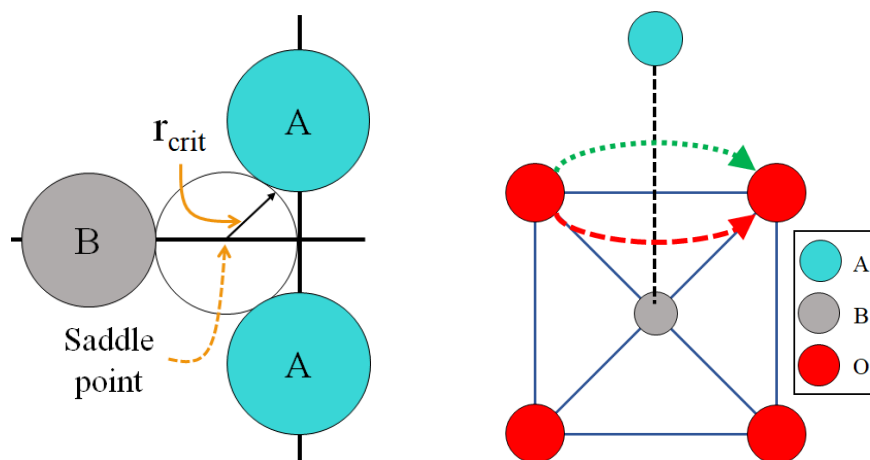
| Associative defect   | Energy/defect [kJ/mol] |
|----------------------|------------------------|
| Schottky             | 487.72                 |
| Frenkel Y            | 1121.83                |
| Frenkel Al           | 920.13                 |
| Frenkel $\text{O}_1$ | 469.08                 |
| Frenkel $\text{O}_2$ | 467.11                 |

Ionic migration calculations were performed firstly, in a linear path formed by two nearest vacancies, determining the energy for an interstitial defect placed along the linear path as can be seen in Fig. 2. Those defects generate a profile where the maximum energy is related to the migration energy in the diffusion process, and then, to the activation energy in the electrical conductivity process [24]. Ionic migration (from vacancy to vacancy) calculations were carried out by  $\text{Al}^{3+}$ ,  $\text{Y}^{3+}$ , and  $\text{O}^{2-}$  species and minimum energy migration results were 413.15 kJ/mol, 926.45 kJ/mol, and 105.16 kJ/mol, respectively. As the oxygen ion migration had a minimal value, the rest of the calculations were focused only on this ion.



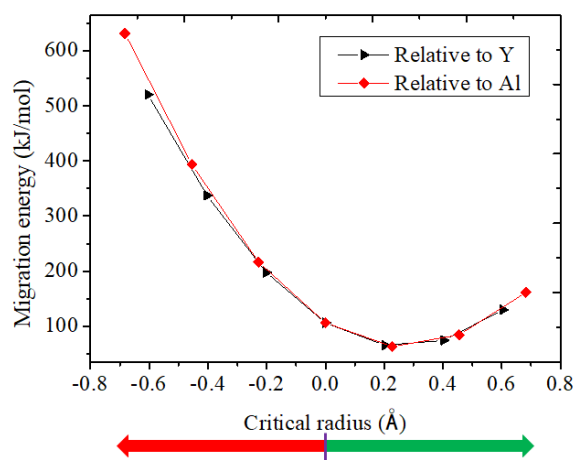
**Fig. 2.** Path and energetic profile migration due to oxygen ion migration in  $\text{YAlO}_3$  compound.

The linear path does not always result in the best path due to the steric effect between ions. In perovskite structure has been reported the presence of a “saddle point” [25] which consists of a space where the steric effects due to  $\text{Al}^{3+}$  and  $\text{Y}^{3+}$  on oxygen ion are minimal, the size of the saddle point is defined by the critical radius ( $r_{\text{crit}}$ ) showed in Fig. 3. In the ideal case, the linear path must contain the saddle point, but due to the Al—O bond length decreases as the path becomes close to the saddle point, it is necessary to evaluate alternative paths in which steric effects are minimal. In this scenario, we calculated the interstitial energy at the saddle point near and far from the  $\text{Al}^{3+}$  (the octahedra center) this is outlined in Fig. 3.



**Fig. 3.** Variation of the migration path for oxygen ions due to the saddle point in perovskite structures.

In the ideal perovskite structure, the saddle point, A sites, and B site positions are in the same plane, but, since  $\text{YAIO}_3$  is a distorted perovskite, saddle point, A, and B sites are not in the same plane and in consequence there are two ways to evaluate an alternative oxygen migration around  $\text{Al}^{3+}$ , one with the saddle point aligned with  $\text{Al}^{3+}$  site (red points in Fig. 4) and a second one aligning the saddle point with  $\text{Y}^{3+}$  positions (black points in Fig. 4). As can be observed in Fig. 4, no matter which of the paths are used, both had a minimum at the same point which is outer from the  $\text{AlO}_6$  octahedra. Additionally, as those calculations were made in the middle of the path, it can be assumed that each point corresponds to the maximum energy for a nonlinear path. A plot of migration energy as a function of the distance of the saddle point was made (Fig. 4), where the minimum migration energy of 98.70 kJ/mol was obtained for migration outside of the octahedra.



**Fig. 4.** Oxygen migration around  $\text{Al}^{3+}$  taking into account the saddle point effect.

Considering the Frenkel disorder, oxygen migration could take place through vacancy and interstitial defect, moreover, the atomistic simulations showed this migration is not favoured by its high migration energy (about 765.03 kJ/mol), but it was calculated that interstitial-interstitial migration had a 98.70 kJ/mol migration energy which is similar to the vacancy-vacancy oxygen migration showed in Fig. 4. According to simulations, oxygen is the main charge carrier in the system because it presents the minimal migration energy; the path

migration could be via vacancy-vacancy in a nonlinear path through the saddle point or via interstitial-interstitial in a linear path; moreover, the presence of oxygen interstitial it would unlikely due to the lack of chemically favoured sites for oxygen ions because the perovskite structure can be seen as a close packed arrangement of oxygen and yttrium ions and the aluminum cations took the octahedra holes [26]. Thus, oxygen migration via vacancy vacancy would be the main way for ionic transport.

High ionic conductivity in SE usually is related to the high concentration of charge carriers, but this is very low when charge carriers come from intrinsic point defects. Doped compounds are usually the solution to enhance the amount of charge carriers, because they keep the same crystal structure, and then, the same migration energy, but the number of point defects can be adjusted according to chemical reaction. Often, doping occurs via aliovalent doping (when a substitution occurs with an ion with a different charge but similar size) and doping the A-site in the perovskite structure yields oxygen vacancies according to the reaction (8) where an oxide with general formula MO is considered.



According to Shannon radii, aliovalent cations for  $Y^{3+}$  (1.019 Å) are  $Ca^{2+}$ ,  $Mg^{2+}$ , and  $Zn^{2+}$  whose ionic radii are 1.12 Å, 0.89 Å, and 0.9 Å respectively [27], thus these cations could be used for doping  $YAlO_3$  perovskite. Atomistic simulations made possible the determination of doping energy according to equation (9) which had been obtained from the reaction (8).

$$E_{doping} = E_{M'_Y} + \frac{1}{2} E_{V_O^{**}} - E_{lattice}^{MO} \quad (9)$$

The crystal structure parameters for CaO, MgO, and ZnO were previously reported [28] and lattice energy was calculated from GULP to determine the energy doping for each aliovalent ion, the results are listed in Table 5 where it can be seen that doping  $YAlO_3$  with  $Ca^{2+}$  implicates the lower energy thus the  $Y_{1-x}Ca_xAlO_{3-x/2}$  system would be the thermodynamically favored system among those formed with the aliovalent ions studied in this work. It would be important to mention that the  $Ca^{2+}$  crystal radius is closer to that for  $Y^{3+}$ , which can be related to the lower doping energy for the  $Y_{1-x}Ca_xAlO_{3-x/2}$  system.

**Table 5.** Doping energy for different aliovalent ions.

| Doping ion | Ionic radius (Å) | Doping energy (kJ/mol) |
|------------|------------------|------------------------|
| $Ca^{2+}$  | 1.12             | 4507.12                |
| $Mg^{2+}$  | 0.89             | 4570.60                |
| $Zn^{2+}$  | 0.90             | 4570.51                |

The method employed in this work could be used as a tool for designing new materials where ionic transport is an important feature. Atomistic simulations require nonexpensive computing infrastructure and results can easily correlated with crystal structure and chemical properties and these calculations can optimize the selection criteria process in the research of new materials for ionic transport.

## Conclusions

We successfully simulated the  $YAlO_3$  crystal structure from electrostatic long-range interactions together with short-range Buckingham potentials. The lattice energy calculated was -14373.3 kJ/mol.

Additionally, formation energy for Schottky and Frenkel pair defects was calculated, and we determined that Schottky defects together with anionic Frenkel defects are the main point defects present in the  $\text{YAlO}_3$  structure due to its low formation energy: 487.72 kJ/mol for Schottky disorder and 467.11 kJ/mol for Frenkel disorder. Considering the point defects present in the compound, we performed migration calculation and we found that the lower migrations energy corresponded to oxygen ion migration via vacancy-vacancy and interstitial-interstitial site with 98.70 kJ/mol in both cases. In the end, we performed atomistic simulations to calculate the doping energy involved in the  $\text{Y}_{1-x}\text{M}_x\text{AlO}_{3-x/2}$  system with  $\text{M} = \text{Ca}^{2+}$ ,  $\text{Mg}^{2+}$ , and  $\text{Zn}^{2+}$ ; we found  $\text{Y}_{1-x}\text{Ca}_x\text{AlO}_{3-x/2}$  system had the minimum doping energy which implied that was the thermodynamically favored system. All these calculations allowed to us select one system in which structural and chemical properties could bring out interesting electrical properties.

## Acknowledgements

The author thanks to the DGAPA-UNAM project number IA208421 for financial support.

## References

1. Xiang, C.; Papadantonakis, K. M.; Lewis, N. S. *Mater. Horizons*. **2016**, 3, 169-173. DOI: <https://doi.org/10.1039/C6MH00016A>.
2. Tang, J.; Xu, X.; Tang, T.; Zhong, Y.; Shao, Z. *Small Methods*. **2022**, 6, 2201099. DOI: <https://doi.org/10.1002/smt.202201099>.
3. Vermaak, L.; Neomagus, H. W. J. P.; Bessarabov, D. G. *Membranes (Basel)*. **2021**, 11, 127. DOI: <https://doi.org/10.3390/membranes11020127>.
4. Dokiya, M. *Solid State Ionics*. **2002**, 152-153, 383-392. DOI: [https://doi.org/10.1016/S01672738\(02\)00345](https://doi.org/10.1016/S01672738(02)00345).
5. Oliveira, A. M.; Beswick, R. R.; Yan, Y. *Curr. Opin. Chem. Eng.* **2021**, 33, 100701. DOI: <https://doi.org/10.1016/j.coche.2021.100701>.
6. Shi, H.; Su, C.; Ran, R.; Cao, J.; Shao, Z. *Prog. Nat. Sci. Mater. Int.* **2020**, 30 (6), 764-774. DOI: <https://doi.org/10.1016/j.pnsc.2020.09.003>.
7. Haile, S. M. *Acta Mater.* **2003**, 51, 5981-6000. DOI: <https://doi.org/10.1016/j.actamat.2003.08.004>.
8. Bonanos, N. *Solid State Ionics*. **2001**, 145, 265-274. DOI: [https://doi.org/10.1016/S01672738\(01\)00951-1](https://doi.org/10.1016/S01672738(01)00951-1).
9. Fop, S. *J. Mater. Chem. A*. **2021**, 9, 18836-18856. DOI: <https://doi.org/10.1039/D1TA03499E>.
10. Meng, Y.; Gao, J.; Zhao, Z.; Amoroso, J.; Tong, J.; Brinkman, K. S. *J. Mater. Sci.* **2019**, 54, 9291-9312. DOI: <https://doi.org/10.1007/s10853-019-03559-9>.
11. Kilner, J. *Solid State Ionics*. **2000**, 129, 13-23. DOI: [https://doi.org/10.1016/S0167-2738\(99\)00313-6](https://doi.org/10.1016/S0167-2738(99)00313-6).
12. Diehl, R.; Brandt, G. *Mater. Res. Bull.* **1975**, 10, 85-90. [https://doi.org/10.1016/0025-5408\(75\)90125-7](https://doi.org/10.1016/0025-5408(75)90125-7).
13. Walker, A. M.; Wright, K.; Slater, B. *Phys. Chem. Miner.* **2003**, 30, 536-545. DOI: <https://doi.org/10.1007/s00269-003-0358-7>.
14. De Souza, R. A.; Maier, J. *Phys. Chem. Chem. Phys.* **2003**, 5, 740-748. DOI: <https://doi.org/10.1039/b209062g>.
15. Chroneos, A.; Yildiz, B.; Tarancón, A.; Parfitt, D.; Kilner, J. A. *Energy Environ. Sci.* **2011**, 4, 2774. DOI: <https://doi.org/10.1039/c0ee00717j>.
16. Wang, X.; Santos Carballal, D.; de Leeuw, N. H. *Phys. Chem. Chem. Phys.* **2023**, 25, 6797-6807. DOI: <https://doi.org/10.1039/D2CP04126J>.
17. Gale, J. D. *Philos. Mag. Part B*. **1996**, 73, 3-19. DOI: <https://doi.org/10.1080/13642819608239107>.

18. Gale, J. D.; Rohl, A. L. *Mol. Simul.* **2003**, 29, 291-341. DOI: <https://doi.org/10.1080/0892702031000104887>.
19. Ruiz Trejo, E. *Solid State Ionics*. **1999**, 123, 121-129. DOI: [https://doi.org/10.1016/S0167-2738\(99\)00092-2](https://doi.org/10.1016/S0167-2738(99)00092-2).
20. Bush, T. S.; Gale, J. D.; Catlow, C. R. A.; Battle, P. D. *J. Mater. Chem.* **1994**, 831. DOI: <https://doi.org/10.1039/jm9940400831>.
21. Mott, N. F.; Littleton, M. J. *Trans. Faraday Soc.* **1938**, 34, 485. DOI: <https://doi.org/10.1039/tf9383400485>.
22. Saiful Islam, M. *J. Mater. Chem.* **2000**, 10, 1027-1038. DOI: <https://doi.org/10.1039/a908425h>.
23. Yet Ming, C. in: *Physical Ceramics: Principles for Ceramics Science and Engineering*; John Wiley & Sons, Inc., **1997**.
24. Gómez Garcia, J. F. in: *Estudio Del Transporte Eléctrico En El Bronce de Niobio: CeNb3O9*, Universidad Nacional Autónoma de México, **2010**.
25. Kilner, J.; Brook, R. *Solid State Ionics* 1982, 6 (3), 237-252. DOI: <https://doi.org/10.1016/0167252>.
26. Woodward, P. M. *Acta Crystallogr. Sect. B Struct. Sci.* **1997**, 53 (1), 32-43. DOI: <https://doi.org/10.1107/S0108768196010713>.
27. Shannon, R. D. *Acta Crystallogr. Sect. A.* **1976**, 32, 751-767. DOI: <https://doi.org/10.1107/S0567739476001551>.
28. Wyckoff, R. in: *Crystal Structures*; Interscience Publishers: New York, New York, **1963**.

## Studies on the *Artocarpus lakoocha* Seeds for Drug Delivery

---

Surabhi Chaurasia\*, Anima Pandey\*

Department of Pharmaceutical Sciences and Technology, Birla Institute of Technology, Mesra 835215, India.

\*Corresponding author: Surabhi Chaurasia, email: [imsurabhichaurasia@gmail.com](mailto:imsurabhichaurasia@gmail.com); Anima Pandey, email: [apandey@bitmesra.ac.in](mailto:apandey@bitmesra.ac.in)

Received July 25<sup>th</sup>, 2023; Accepted September 21<sup>st</sup>, 2023.

DOI: <http://dx.doi.org/10.29356/jmcs.v68i3.2111>

**Abstract.** This study aimed to evaluate the effect of modification on non-conventional native starch derived from the seed of *Artocarpus lakoocha* or monkey fruit (Native Starch). The current study determined the excipient characteristics of native and modified starches by examining their physicochemical properties, flow properties, and release characteristics. It showed better improvement in the physicochemical and functional properties and was helpful in the formulation of immediate-release formulations when tested with paracetamol as a model drug. The results from the Field Emission Scanning Electron Microscopy (FESEM) Micrograph revealed a disruption of the granular structure. FTIR analysis confirmed the carbohydrate nature of the starch. The X-ray diffraction pattern demonstrated the decrease in crystallinity following thermal modification. Here, we utilized waste seeds of *Artocarpus lakoocha* to isolate starch, its modifications, and their usage in effective drug delivery formulations, such as tablets and suppositories, compared to the marketed formulations. In summary, this study aims to assess the effects of starch modification and demonstrates the potential advantages of using starch derived from *Artocarpus lakoocha* seeds. It addresses the need for improved excipients in pharmaceutical formulations, promotes sustainability through waste utilization, and highlights the versatility of these starches in various applications, including drug delivery and functional foods.

**Keywords:** *Artocarpus lakoocha* starch; immediate drug delivery; physical modification; physicochemical properties; suppository; tablet.

**Resumen.** Este estudio tuvo como objetivo evaluar el efecto de la modificación sobre el almidón nativo no convencional derivado de la semilla de *Artocarpus lakoocha* o fruto de mono (Native Starch). El presente estudio determinó las características de los excipientes de los almidones nativos y modificados examinando sus propiedades fisicoquímicas y de flujo así como sus características de liberación. Mostró una mejor mejora en las propiedades fisicoquímicas y funcionales y fue útil en la formulación para su liberación inmediata cuando se probó con paracetamol como fármaco modelo. Los resultados de la micrografía de microscopía electrónica de barrido por emisión de campo (FESEM) revelaron una alteración de la estructura granular. El análisis FTIR confirmó la naturaleza glucosídica del almidón. El patrón de difracción de rayos X demostró la disminución de la cristalinidad después de la modificación térmica. También utilizamos semillas de desecho de *Artocarpus lakoocha* para aislar el almidón, sus modificaciones y su uso en formulaciones efectivas de administración de medicamentos, como tabletas y supositorios, en comparación con las formulaciones comercializadas. En resumen, este estudio tuvo como objetivo evaluar los efectos de la modificación del almidón y demuestra las ventajas potenciales del uso de almidón derivado de semillas de *Artocarpus lakoocha*. Aborda la necesidad de mejorar los excipientes en las formulaciones farmacéuticas, promueve la sostenibilidad mediante la utilización de residuos y destaca la versatilidad de estos almidones en diversas aplicaciones, incluida la administración de medicamentos y los alimentos funcionales.

**Palabras clave:** almidón de *Artocarpus lakoocha*; entrega inmediata de medicamentos; modificación física; propiedades fisicoquímicas; supositorio; tableta.

---

## Introduction

*Artocarpus lakoocha* Roxb. is a deciduous tree belonging to the family Moraceae. It is also known as Monkey fruit in English and Lakuch in Ayurveda. In India it is known as “lakuchi,” “dahu,” and “barhal,” in Thailand as “lokhat,” and in Malaysia is called as “tampang” [1-2]. Starches are natural polysaccharides, Because of their unique characteristics, and serve as a food type for humans and are one of the most essential raw materials for numerous industries. Their resource is cheap, readily available, renewable and biodegradable. However, native starch still has several restricted properties and fails to meet demands in several fields adequately. Almeida et al., evaluated and compared the effect of the utilization of five different non-conventional starches extracted from chickpea, common bean, Peruvian carrot, sweet potato and white bean and four different commercial starches obtained from cassava, corn, potato and rice in pound cake [3].

So far, scientists have discovered a way to modify the native starch's structure and properties to increase its economic efficiency and ease to use. Studies have been conducted on various starch modification processes, specifically physical modification [4]. *Artocarpus heterophyllus* Lam. seed starch has already been reported as a natural starch candidate as a potential pharmaceutical excipient in various pharmaceutical dosage forms, such as binding agents and disintegrants in pharmaceutical tablets [5]. Lakoocha trees have crimson male and orange-yellow female blooms. There are approx. 20 to 30 seeds in a fruit. Generally, *Artocarpus* species are recognized for their therapeutic and nutritional benefits and also have been used medicinally and nutritionally for years [50]. *Artocarpus lakoocha* has been studied for its bioactive properties, extracts, and bioactive compounds from various parts of the plant, including the bark, leaves, seeds, and pericarp, have been found to possess exceptional phytochemicals. [2] However, specific statical data on the availability and constraints for procuring *Artocarpus lakoocha* seeds are not readily available. Many pharmaceutical and food companies utilize starch as a binder and dissolver. Potato, rice, and maize are commercial starches. Unexplored starch sources like *Artocarpus lakoocha* starch offer several advantages over other starches, making it a valuable asset [6]. Significantly less work has been done on *Artocarpus lakoocha* Roxb. seed starches (ASS), includes its modification, formulation, and evaluation. The main aim of this study was to investigate the effect of native and modified starch with its change in functional and physicochemical parameters of starch isolated from *Artocarpus lakoocha* seed. So that in the future, ASS can be used in the pharmaceutical and food industries.

## Materials and methods

### Collection of seeds and isolation of starch from *Artocarpus lakoocha* seed

The seeds were collected from the botanical garden of Birla Institute of Technology, Mesra, Ranchi. Using the method described by Zhang et al. and Banyal *et al.* [6,9,16] with exhibiting minor modification, separated starch was from the seed. The seed was soaked with distilled water to make a paste, and the paste was filtered three times. After drying at 50 °C, the starch was powdered and sieved using a 100 particle sieve size and packed in a closed container and for further analysis. The ground paste was then, immersed in 0.05 % (w/v) sodium hydroxide and left overnight at room temperature. Finally, the resulting suspension was thoroughly washed with water to obtain a clear supernatant. The isolated wet starch was collected and dried overnight in a hot air oven at 50 °C. Fig S1[16].



## **Modification of starch**

### **Ultrasonication of starch (UMS)**

By using an ultrasonicator, ultrasonic modification of starch was done. 30 % (w/v) of the starch solution was prepared. The sample was ultrasonicated for 20 min at 25 °C, the frequency was 20.5 kHz, and the power was 170 watts. The ultrasonicated modified starch was centrifuged at 3000 rpm for 30 min. Then starch was sieved and dried in a hot air oven at 50 °C for 24 hrs [10,11].

### **Pregelatinized modification of starch (PMS)**

For pregelatinized modification of native starch, 10 gm of the starch sample was dissolved in 100 mL of distilled water and incubated at 90 °C for 20, 25, and 35 minutes with constant agitation at 500 rpm. After that, pregelatinized starch was dried for 24 hours at 50 °C. The dried and flaky starch was then powdered using an analytical mill and passed through a sieve with a mesh size of 100  $\mu\text{m}$ , and pregelatinized starch with intervals of 20, 25, and 30 minutes were designated as PM-1, PM-2, and PM-3 respectively [12,13].

### **Starch hydrolysis**

For starch hydrolysate (SH-2) or (SH-4), starch was mixed with solutions of Citric acid, glacial acetic acid, and water and then, heated to 95 °C for 2 and 4 hours respectively. The sediments were washed using ethanol several times after the solvent was removed by an evaporation method. When hydrolysates were dissolved in water, they produced pH values of 3.74 and 3.54 respectively, whereas with phosphate buffer solutions they achieved pH values of 7.11 and 7.07 respectively [14].

### **Physicochemical analysis of starch**

Various techniques were used for the physicochemical analysis of non-conventional starch, which includes percentage yield, moisture, ash, amylose, pH, elemental analysis, water holding capacity, oil absorption capacity, dispersibility, micrometric properties, swelling and solubility (for methods, please refer to *supporting information file*) [9,22].

### **Field emission scanning electron microscope (FESEM)**

Using FESEM (Carl Zeiss, Germany, Sigma 300 model), the morphological properties of starch were determined in which it was done with double-sided carbon adhesive tape for mounting 4-5 mg of starch samples on a sphere of aluminum, and then a thin coating of gold was added on top. Images were recorded at magnifications ranging from 100 to 5.00K at 5 kV accelerating voltage [12, 23].

### **Thermogravimetric analysis**

For the determination of thermostability (Netzsch, Germany LFA-467) model was used. The Alumina crucible containing starch powder (5 mg) was heated from 30 to 600 °C at a rate of 20 °C/min and filled with nitrogen maintaining a flow rate of 20 mL/min [17].

### **Differential scanning calorimetry (DSC)**

DSC (TA Instruments, USA, Q 10) model was used to determine starch thermal properties. 5 mg of starch samples were taken into aluminum pans and sealed for that analysis. At a heating rate of 10 °C/min, samples were scanned from 60 to 300 °C. All samples were equilibrated for 15 minutes. Thermal analysis was performed in a nitrogen atmosphere. The temperatures at the start ( $T_o$ ), peak ( $T_p$ ), end ( $T_c$ ), and  $\Delta H$  have been calculated automatically. ( $T_c - T_o$ ) was used to calculate the gelatinization temperature range (R). The ratio  $H/(T_p - T_o)$  was used to calculate the PHI ( $\phi$ ) [24].

### **Fourier transform infrared spectroscopy (FTIR)**

The Frontier (Perkin Elmer, USA) was used to determine FTIR spectroscopy. The dried KBr and starch samples were combined and pressed to form a pellet and were scanned between 400 and 4000  $\text{cm}^{-1}$  frequency [12].

### **X-ray diffraction (XRD)**

The XRD (model: Bruker Kappa Apex II) was used to determine the crystal properties of dried starch specimens. The instrument was calibrated to 35 mA and 40 kV to a diffraction pattern ( $2\theta$ ) varying from 10 to 80 °C at 15 °C/ minute [16].

### **Application of starches in the drug delivery**

#### **Preparation of tablets**

We used the wet granulation method for the preparation of tablet formulation. All the ingredients were taken in mortar and paste along with paracetamol drug, and then the distilled water was added for the preparation of dough illustrated in Table S1[16,20].

Granules were prepared by passing the resulting wet mass through ASTM # 10 mesh. Then the granules were dried at 45 °C in a hot air oven for 30 minutes. After that, lubricants were added. Finally, the tablets were punched on a 16-station tablet punching machine (Cadmach, Ahmadabad, India).

#### **Evaluation of tablets**

20 tablets from each formulation were taken and weighed to determine the average weight. Erweka Hardness Tester was used for the determination of tablet hardness. Tablet friability was measured using Roche Friabilator. USP disintegration device Erweka ZT3 (Heusenstamm, Germany) was used for the disintegration test [27].

#### **Assay of paracetamol tablet**

Assay of paracetamol was determined by using earlier method described by Venkataswamy 2018 [28].

#### ***In vitro* release study**

For the determination of *in vitro* release, USP type-II dissolving test apparatus (LAB INDIA DS 8000, India) was used while taking, an intestinal medium with a pH of 6.8 buffers and 50 rpm at  $37\pm 0.5$  °C was used for the *in-vitro* release profile. 1 mL sample was taken from an intestinal medium of pH 6.8 buffers using a syringe with a membrane filter (0.45 $\mu$ m) and was replaced with 1 mL of fresh buffer at a predefined interval. The proportion of drug release was estimated using UV-VIS spectroscopy (Shimadzu UV-2450) and absorbance at 243nm [12,20,28].

#### **Formulation of suppository**

Rectal suppositories were made using the fusion method at 36°C on a lipophilic base - cocoa butter. Each one contained 125 mg of paracetamol drug. The molten bases were combined with SH2 and SH4 and then poured into a polyethylene mold. After solidification, the suppositories were stored at 4 °C until use, as illustrated in Table S2 [14].

#### **Evaluation of suppositories**

Twenty suppositories were taken for the weight variation test. Softening time of lipophilic suppositories was determined. Suppositories were disintegrated using the Erweka ZT3 disintegration device (Heusenstamm, Germany) [29].

#### **Assay of acetaminophen-based suppository**

The Assay of the paracetamol suppository was done by the previously described method Khatri *et al.* 2017 [29].

#### **Dissolution test for suppositories (*In vitro* release of suppositories)**

Dissolution apparatus used to evaluate paracetamol suppositories (NS, UMS, PM-1, PM-2, and PM-3). In a stirred beaker, the Suppository was placed on the bottom. While the stirrer spun at 100rpm, maintained the system at  $37 \pm 1$  °C. 1 mL sample was taken and replaced with 1 mL of fresh medium at 0, 5, 10, 15, 20, 25, 30, 35, 40, 45, 50, 55 and 60 minutes. Samples were filtered using a membrane filter (0.45 $\mu$ m) connected

to a syringe and diluted. UV-VIS spectroscopy (Shimadzu UV 2450) was used to measure the absorbance at 243 nm and calculate the % drug release of suppositories [14,29].

## Results and discussion

### Physicochemical analysis of starch

The physicochemical properties of starch are illustrated in Table 1, Micromeritic properties and elemental analysis illustrated in Table S3, swelling and solubility shown in Table 2 and 3.

**Table 1.** Physicochemical properties of NS and modified starch (UMS, PM-1, PM-2, and PM-3)

| Starch | WHC (%)      | Amylose content (%) | Moisture content (%) | Ash content  | pH         | Dispersibility | OAC          |
|--------|--------------|---------------------|----------------------|--------------|------------|----------------|--------------|
| NS     | 179.5 ± 0.01 | 10.954 ± 0.01       | 11.36 ± 0.11         | 0.009 ± 0.01 | 7.1 ± 0.03 | 73.00 ± 0.02   | 15.00 ± 0.25 |
| UMS    | 185.6 ± 0.03 | 24.418 ± 0.03       | 10.1 ± 0.01          | 0.010 ± 0.03 | 7.2 ± 0.01 | 72.00 ± 0.01   | 12.07 ± 0.15 |
| PM-1   | 294.5 ± 0.01 | 25.704 ± 0.02       | 9.54 ± 0.04          | 0.014 ± 0.02 | 7.4 ± 0.04 | 71.00 ± 0.02   | 12.01 ± 0.17 |
| PM-2   | 302.1 ± 0.02 | 33.048 ± 0.04       | 9.23 ± 0.02          | 0.015 ± 0.03 | 7.5 ± 0.01 | 70.00 ± 0.03   | 11.03 ± 0.23 |
| PM-3   | 323.1 ± 0.04 | 42.846 ± 0.03       | 9.11 ± 0.01          | 0.015 ± 0.05 | 7.5 ± 0.03 | 69.00 ± 0.02   | 10.05 ± 0.11 |

**Table 3.** Swelling properties of Native (NS) and modified starch (UMS, PM-1, PM-2, and PM-3).

| Starch | Swelling power (%) |              |              |              |              |
|--------|--------------------|--------------|--------------|--------------|--------------|
|        | 30 °C              | 45 °C        | 60 °C        | 75 °C        | 90 °C        |
| NS     | 2.13 ± 0.34        | 3.78 ± 0.21  | 5.11 ± 0.35  | 7.01 ± 0.21  | 9.58 ± 0.36  |
| UMS    | 4.11 ± 0.11        | 6.65 ± 0.11  | 10.51 ± 0.24 | 12.34 ± 0.34 | 14.37 ± 0.11 |
| PM-1   | 6.31 ± 0.13        | 10.11 ± 0.41 | 11.41 ± 0.11 | 15.11 ± 0.23 | 17.41 ± 0.23 |
| PM-2   | 8.55 ± 0.01        | 11.31 ± 0.35 | 12.42 ± 0.01 | 16.01 ± 0.39 | 19.21 ± 0.16 |
| PM-3   | 9.13 ± 0.12        | 12.52 ± 0.12 | 14.31 ± 0.43 | 18.03 ± 0.32 | 22.64 ± 0.22 |

**Table 4.** Solubility powers of Native (NS) and modified starch (UMS, PM-1, PM-2, and PM-3).

| Starch | Solubility power (%) |              |              |              |              |
|--------|----------------------|--------------|--------------|--------------|--------------|
|        | 30 °C                | 45 °C        | 60 °C        | 75 °C        | 90 °C        |
| NS     | 8.60 ± 0.22          | 8.23 ± 0.09  | 10.06 ± 0.35 | 12.11 ± 0.41 | 14.32 ± 0.24 |
| UMS    | 13.12 ± 0.11         | 14.65 ± 0.12 | 16.21 ± 0.16 | 18.23 ± 0.45 | 19.57 ± 0.13 |
| PM-1   | 14.31 ± 0.14         | 16.12 ± 0.31 | 19.47 ± 0.81 | 22.14 ± 0.23 | 22.36 ± 0.04 |
| PM-2   | 15.55 ± 0.12         | 18.51 ± 0.26 | 22.34 ± 0.56 | 24.21 ± 0.43 | 15.11 ± 0.08 |
| PM-3   | 17.11 ± 0.15         | 19.80 ± 0.14 | 24.56 ± 0.43 | 30.23 ± 0.12 | 33.14 ± 0.23 |

### **Starch yield and moisture content**

The starch yield was found to be 50 % (db) [31]. Moisture content serves as a gauge for the starch's stability when kept in storage. The moisture content of NS, UMS, PM-1, PM-2, and PM-3 was from 9.11 to 11.36 % [32].

### **Amylose, ash, and pH content**

The range of amylose contents of NS, UMS, PM-1, PM-2, and PM-3 were 10.954 %, 24.418 %, 25.704 %, 33.048 %, and 42.846 %, respectively. The amylose content in starch was significantly affected by the pregelatinized treatment. Starch hydrolysis depolymerized and amylose resulting in smaller chain sizes [33]. Ash concentration was reported to range from 0.012 to 0.15 %. The pH of starch was between 7.1-7.5. The pH typically affects the stability of pharmaceutical formulations.

### **Water holding capacity (WHC)**

The WHC of NS samples was found to be  $179 \pm 0.01$  %, whereas UMS, PM-1, PM-2, and PM-3 were reported to be  $185 \pm 0.03$  %,  $294.5 \pm 0.01$  %,  $302.1 \pm 0.02$  and  $323.1 \pm 0.04$  respectively [12]. The findings revealed that the modification of starch increased its water absorption capacity [33,34]. The WHC increases as the pre-gelatinization time increases because starch undergoes hydrothermal treatment, which causes the granules to rupture and release their soluble components.

### **Oil absorption capacity (OAC)**

The oil absorption capacity of the NS sample was found to be  $15 \pm 0.25$  %, whereas for the UMS, PM-1, PM-2, and PM-3 decreased with modification, with values of  $13 \pm 0.15$  %,  $12 \pm 0.17$  %,  $11 \pm 0.23$  %, and  $10 \pm 0.13$  % respectively. Earlier reported OAC was slightly higher values ( $17.00 \pm 1.37$  %) [34].

### **Dispersibility**

NS dispersibility decreased with modification. When particles collide, their kinetic energy increases, and they do not sink to the bottom which further results in dispersion stability depicted in Table 1[9].

### **Micromeritic properties**

#### **Bulk density**

The bulk densities (BD) were between 0.41–0.82 g/cc. NS contains the lowest BD (0.41 g/cc). However, after modification, bulk densities of starch were increased, and PM-3 was the highest ( $0.82 \pm 0.21$  g/cc) [36].

#### **Tapped density**

Tapped densities were  $0.52 \pm 0.01$ ,  $0.62 \pm 0.04$ ,  $0.89 \pm 0.13$ ,  $0.91 \pm 0.71$ , and  $0.93 \pm 0.04$  g/cc of NS, UMS, PM-1, PM-2 and PM-3.

#### **Carr's index and hausner's ratio**

The PM-3 shows a lower Carr's index ( $11.82 \pm 0.34$ ) and Hausner's ratio ( $1.13 \pm 0.06$ ) indicating good flow.

#### **Angle of repose**

The Angle of repose of NS and UMS was  $33.35 \pm 1.06$ , and  $32.16 \pm 0.60$  indicates good flow properties and the value of PM-1, PM-2, and PM-3 ranged between  $28.11 \pm 0.71$ ,  $27.75 \pm 0.22$ , and  $26.35 \pm 1.06$ , with excellent flow properties after modification [37] illustrated in Table 2. Micromeritic found PM-3 valuable for pharmaceutical industries. The Carr's index of pregelatinized starches exhibited a reduction as the pregelatinization time increased, signifying improved compressibility compared to NS. Additionally, a decrease in the angle of repose for all modified starches indicated enhanced powder flow properties. This improvement is likely attributed to the transformation of spherical starch granules into irregular shapes and the filling of void spaces with irregular particles in the pregelatinized and ultrasonicated starch [16].

**Table 2.** Powder characteristics of NS and modified starch (UMS, PM-1, PM-2, and PM-3).

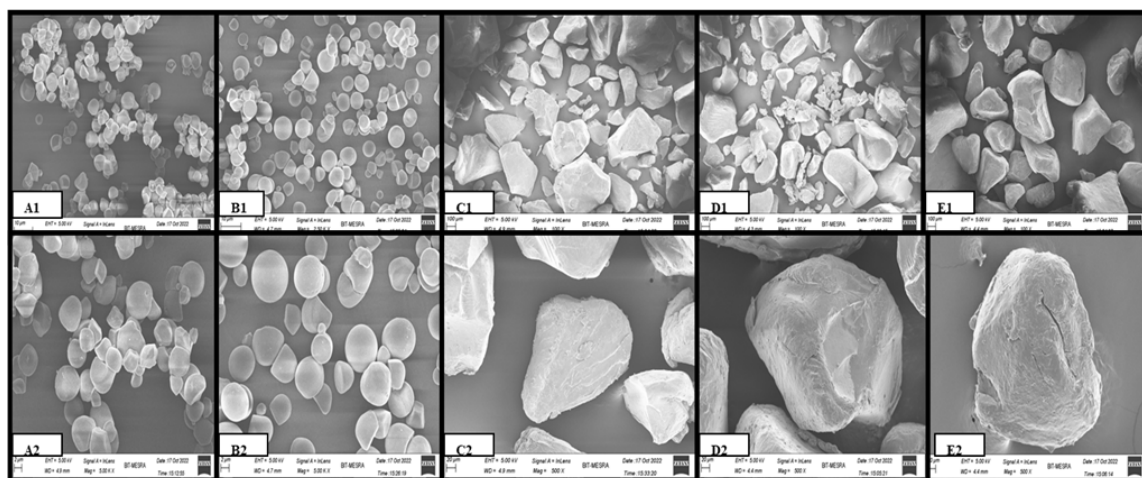
| Sample | Bulk density (g/cc) | Tapped density (g/cc) | Carr's index (%) | Hausner's ratio | Angle of repose (°) |
|--------|---------------------|-----------------------|------------------|-----------------|---------------------|
| NS     | 0.41 ± 0.03         | 0.52 ± 0.01           | 21.15 ± 0.21     | 1.26 ± 0.03     | 33.35 ± 1.06        |
| UMS    | 0.53 ± 0.01         | 0.62 ± 0.04           | 14.5 ± 0.61      | 1.16 ± 0.02     | 32.16 ± 0.60        |
| PM-1   | 0.77 ± 0.49         | 0.89 ± 0.13           | 13.48 ± 0.02     | 1.15 ± 0.03     | 28.11 ± 0.71        |
| PM-2   | 0.79 ± 0.71         | 0.91 ± 0.71           | 13.18 ± 0.51     | 1.15 ± 0.07     | 27.75 ± 0.22        |
| PM-3   | 0.82 ± 0.21         | 0.93 ± 0.04           | 11.82 ± 0.34     | 1.13 ± 0.06     | 26.35 ± 1.06        |

### Swelling and solubility power

The ability of starch to form hydrogen bonds with water molecules influences swelling volume. Because of intermolecular hydrogen bonding in amorphous regions, starch granules swell rapidly at temperatures below 70 °C [38,39]. The reported values for swelling power for the NS, UMS, PM-1, PM-2, and PM-3 were  $9.58 \pm 0.36$ ,  $14.37 \pm 0.11$ ,  $17.41 \pm 0.23$ ,  $19.21 \pm 0.16$  and  $22.64 \pm 0.22$  % respectively illustrated in Table 3 [40]. For NS, UMS, PM-1, PM-2, and PM-3, the solubility percent values were recorded as  $14.32 \pm 0.24$  %,  $19.57 \pm 0.13$  %,  $22.36 \pm 0.04$ , and  $33.14 \pm 0.24$  % respectively illustrated in Table 4. [40]. The study showed that modified starches had a higher solubility index than native starches [41]. Thermal modification altered the granular structure of native starch, enhancing water absorption and improving drug release characteristics. Typically, the swelling power of starch is influenced by the level of amylose content and its water-holding capacity [16].

### Field emission scanning electron microscope (FESEM)

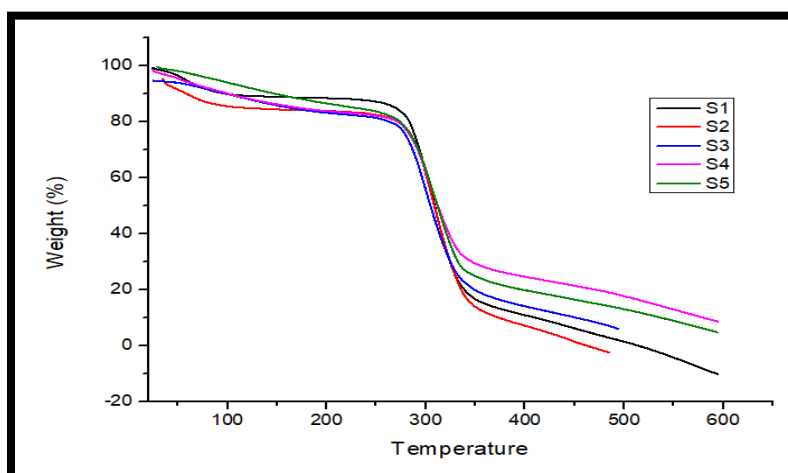
The NS, UMS, PM-1, PM-2, and PM-3 micrographs are shown in Fig. 1. The NS and UMS starch were round to oblong in shape with a smooth surface and texture [42]. Pregelatinized starches were discovered to have an irregular shape, a rough surface and deep groves. The hydrothermal treatment restructured the modified starch granules causing an irregular shape and uneven texture. The groves and crevices on the surface of starch aid in trapping of the drug and facilitating immediate release drug delivery [43].



**Fig. 1.** FE-SEM (5.00kx),( 1.00kx) of NS (A1 and A2), UMS ( B1 and B2), PM-1 ( C1 and C2), PM-2 (D1 and D2), PM-3 (E1 and E2 )

### Thermogravimetric analysis (TGA)

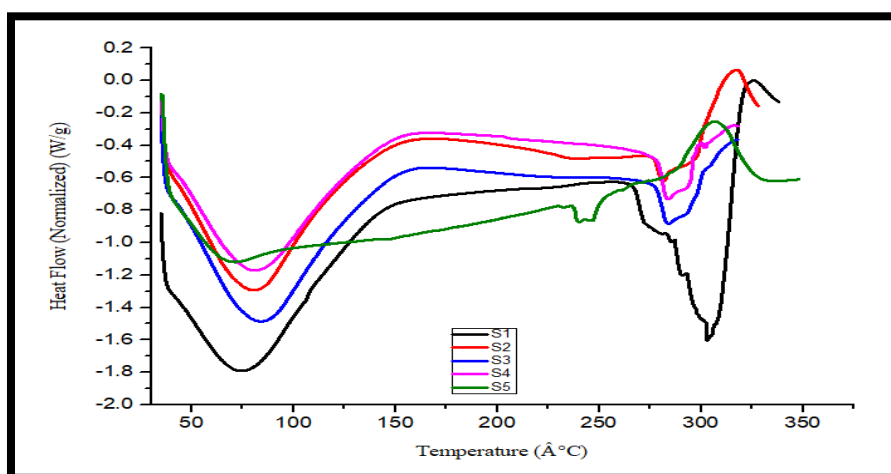
Fig. 2, Fig. S2 illustrates the TGA curve of NS, UMS, PM-1, PM-2, and PM-3 revealing three distinct degradation patterns. The first mass loss occurred at 20 to 240 °C possibly related to bound water evaporation. The de-polymerization of the starch structure causes the second and most significant mass loss in the temperature range of 240-456 °C. The oxidation of organic matter is responsible for the third mass loss between 456 and 600 °C [44]. The thermogram showed starches were chemically stable at 20 to 270 °C.



**Fig. 2.** Thermogravimetric Analysis of native and modified starch S1 (NS), S2 (UMS), S3 (PM-1), S4 (PM-2), S5 (PM-3).

### Differential scanning calorimeter (DSC)

Fig. 3 illustrates the DSC curve. NS, UMS, PM-1, PM-2, and PM-3 starches exhibit wide variations in their PHI ( $\phi$ ),  $\Delta H$ , transition temperatures (onset, peak and conclusion), transition temperature range ( $T_c$  -  $T_o$ ). Three different peaks have resulted in NS, UMS, PM-1, PM-2, and PM-3 starches. NS has a low degree of crystallinity; it's enthalpy of gelatinization was significantly higher than PM-3. H gel indicates the loss of molecular order within the granules. *Artocarpus lakoocha* Roxb. seed starches (ASS) transition temperatures were higher than those previously reported starch [45].



**Fig. 3.** DSC prepared from S1 (NS), S2 (UMS), S3 (PM-1), S4 (PM-2), S5 (PM-3).

### Fourier transform infrared spectroscopy (FTIR)

Fig. 4 shows the FTIR spectra of native and modified starches. The peaks in the  $1000\text{ cm}^{-1}$  region indicated the glucopyranoside ring's presence. Pregelatinized starches resulted in a peak at  $1055\text{ cm}^{-1}$ , which was caused by the starch recrystallizing during the modification process and the presence of OH stretching was characterized by broadband ranging from  $3100$  and  $3300\text{ cm}^{-1}$ . The  $\alpha$ - and  $\beta$ -type glycoside linkages were caused by absorption bands near  $840$  and  $890\text{ cm}^{-1}$  [46]. A distinctive peak showed C-H stretching at  $2931\text{ cm}^{-1}$  [47]. Asymmetric stretching of the C-O molecule has caused a small but sharp peak at  $1650\text{ cm}^{-1}$  [48]. A peak caused C-O-C asymmetry stretching at  $1092\text{ cm}^{-1}$  [49].

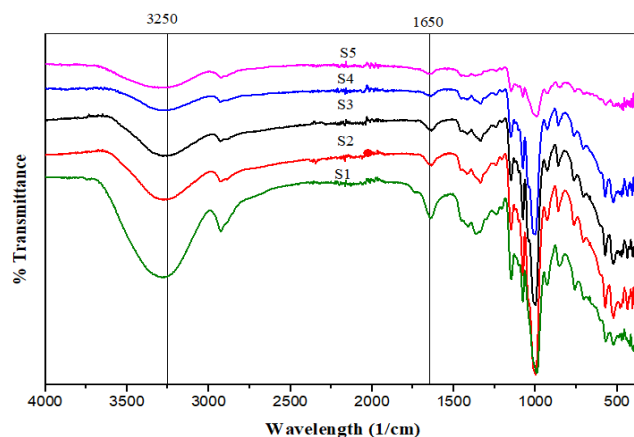


Fig. 4. FT-IR of NS and modified starch S1 (NS), S2 (UMS), S3 (PM-1), S4 (PM-2), S5 (PM-3).

### X-ray diffraction (XRD)

The XRD patterns of NS, UMS, PM-1, PM-2, and PM-3 were shown in Fig. 5 and Fig. S3. The native starches NS and UMS were crystalline when compared to PM-1, PM-2, and PM-3 starches. The crystalline nature of the NS starches was demonstrated by their strong scattering peaks at  $15.126^\circ$ ,  $17.135^\circ$ ,  $17.948^\circ$ ,  $20.058^\circ$ ,  $23.023^\circ$ ,  $26.606^\circ$ ,  $30.538^\circ$  and  $38.379^\circ$  respectively and UMS at  $15.151^\circ$ ,  $17.161^\circ$ ,  $17.916^\circ$ ,  $20.058^\circ$ ,  $23.073^\circ$ ,  $26.538^\circ$ ,  $28.981^\circ$ ,  $30.453^\circ$  and  $38.173^\circ$ . The diffraction pattern of pregelatinized starches revealed the lack of large peaks with very few sharp peaks at  $17.177^\circ$ ,  $22.289^\circ$  and  $34.106^\circ$ , showing a reduction in crystallinity due to heat treatment [16-17]. Pregelatinized starches decreased crystalline peak intensity which further suggests that a broken double helix and fewer crystalline amylopectin regions are present.

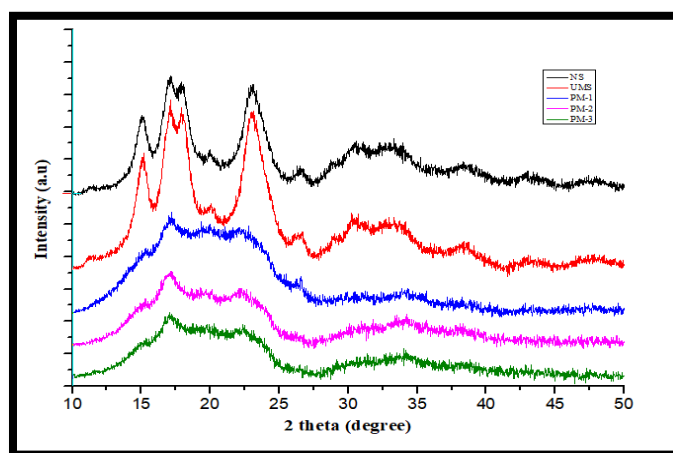


Fig. 5. X-ray diffraction of native and modified starch NS, UMS, PM-1, PM-2, PM-3.

### Evaluation of tablets

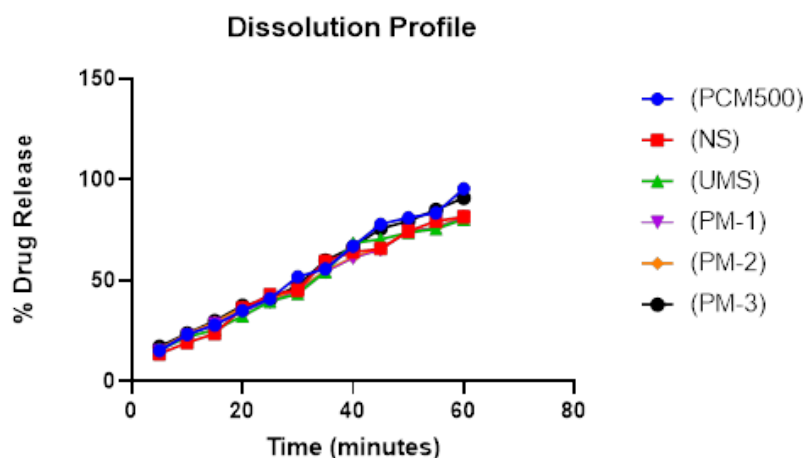
The physical parameters of the paracetamol tablets were shown in Table 5. All of the tablets, hardness, and friability were found to be within the acceptable range United States Pharmacopeia (USP). The Assay ranges from 99.82 to 104.29 %, and the average weight of all the tablets was found to be between 649.00 and 651.66 mg within the USP range. The disintegration time of tablets made with modified starch was shorter than those made with native starch. The amount of paracetamol was calculated from the line of the regression equation,  $y = 0.056x + 0.018$ ,  $R^2=0.995$  (Fig. S4) [12,15,20,24].

**Table 5.** Results of paracetamol tablets evaluation.

| Sample | Thickness (mm) | Diameter (mm) | Hardness (Kg/cm <sup>2</sup> ) | Friability (%) | Weight variation (mg) | DT (min) |
|--------|----------------|---------------|--------------------------------|----------------|-----------------------|----------|
| NS     | 4.22 ± 0.04    | 12.90 ± 0.04  | 6.50 ± 0.51                    | 0.26           | 650.11 ± 0.42         | 3.15     |
| UMS    | 4.32 ± 0.12    | 12.86 ± 0.02  | 6.60 ± 0.42                    | 0.28           | 649.85 ± 0.45         | 2.45     |
| PM-1   | 4.72 ± 0.07    | 12.91 ± 0.07  | 6.87 ± 0.01                    | 0.27           | 650.56 ± 0.34         | 2.19     |
| PM-2   | 4.27 ± 0.02    | 12.98 ± 0.01  | 7.66 ± 0.64                    | 0.30           | 649.11 ± 0.75         | 2.15     |
| PM-3   | 4.36 ± 0.03    | 12.88 ± 0.03  | 7.87 ± 0.22                    | 0.31           | 651±23 ± 0.11         | 2.09     |

### In vitro dissolution study

Fig. 6 illustrates an in-vitro dissolution study of tablets prepared with non-conventional native starch and modified starches along with commercial paracetamol tablets. All of the tablets demonstrated faster drug-release properties. However, when compared to the commercial and other modified starches, PM-3 demonstrated faster drug release. This could be because starch formed a loose granular structure, resulting in less binding capacity. The drug release was found to increase with increasing pre-gelatinization time. Finally, PM-3 can be a promising excipient for immediate-release formulations [12,16,20].



**Fig. 6.** In vitro release profile of paracetamol tablets using NS and modified starch (UMS, PM-1, PM-2, and PM-3).

### Evaluation of suppositories

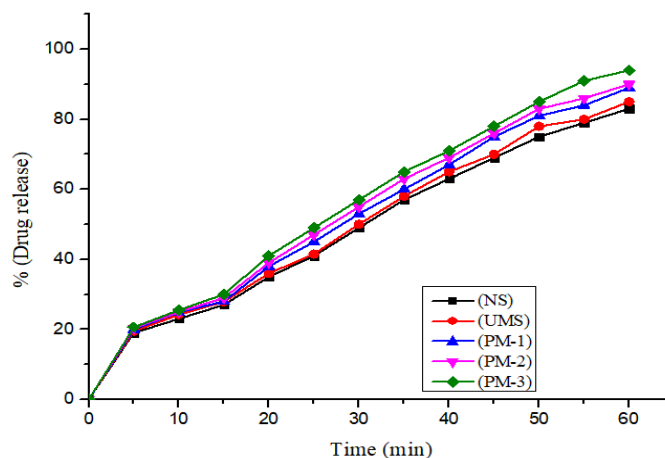
The absorption of suppositories at 243 nm standard value was 0.987. The amount of Acetaminophen was calculated from the line of regression equation  $y = 0.051x + 0.030$ ,  $R^2 = 0.987$  from Fig. S5.



Table 6 summarizes the average results of the physicochemical test, and Fig. 7 shows the results of dissolution. The uniformity of mass of single-dose preparation test of all series of suppositories was found to be within 5 %, meeting USP requirements. The softening time of all suppositories was found to be within the USP range. All suppositories were dissolved within 60 minutes. The percentage of drug release of paracetamol suppositories was determined at a body temperature of 37°C. The percentage was 99.05 %. The use of modified starch as a physicochemical active suppository excipient appears to be promising [14].

**Table 6.** Results of paracetamol suppositories evaluation.

| Sample | Average weight (g) | Softening time(min) | Disintegration time(min) | Drug content (%) |
|--------|--------------------|---------------------|--------------------------|------------------|
| NS     | 1.319 ± 0.01       | 24.31 ± 0.03        | 14.32 ± 0.02             | 83 ± 0.06        |
| UMS    | 1.326 ± 0.06       | 28.2 ± 0.01         | 17.43 ± 0.04             | 85 ± 0.02        |
| PM-1   | 1.349 ± 0.02       | 20.32 ± 0.05        | 20.87 ± 0.03             | 89 ± 0.01        |
| PM-2   | 1.352 ± 0.01       | 18.78 ± 0.02        | 15.21 ± 0.01             | 90 ± 0.03        |
| PM-3   | 1.354 ± 0.03       | 15.31 ± 0.01        | 10.26 ± 0.02             | 95 ± 0.02        |



**Fig. 7.** *In vitro* release profile of Acetaminophen suppositories using NS and modified starch (NS, UMS, PM-1, PM-2, and PM-3).

## Conclusions

In this study, we thoroughly examined the physicochemical and functional properties of non-conventional native and modified starches derived from *Artocarpus lakoocha* seeds. We found that these seeds yielded a starch content of 50 % (w/w). Through our investigations, we observed significant improvements in the physical characteristics of the starch after modifying the amylose content. Specifically, properties such as swelling power, solubility, WHC, and OAC exhibited enhancement. Our analysis using techniques like FTIR confirmed the presence of carbohydrates in native and pregelatinized starches. Furthermore, the hydrothermal treatment led to a notable reduction in crystallinity, which was substantiated by XRD and FESEM micrographs of both native and modified starches. Thermal stability, as revealed by TGA, demonstrated the suitability of these starches for various applications. Tablets formulated with both native and modified starches exhibited

favorable in-vitro drug release profiles, underscoring their potential as excipient for immediate-release dosage forms. Additionally, the improved flow properties of the modified starches proved advantageous during tablet formulation processes, including mixing and compression. Our study also delved into the impact of starch hydrolysates on various physicochemical properties of suppositories. Notably, we found that starch hydrolysates could serve as cost-effective pharmaceutical aids, enhancing the physicochemical characteristics of suppositories. In summary, our investigation highlights *Artocarpus lakoocha*-derived non-conventional native and modified starches as promising excipients for immediate-release dosage forms. These findings offer potential avenues for the development of efficient pharmaceutical formulations.

## Acknowledgements

The first author is thankful to the Head of, Department of Pharmaceutical Sci. & Tech., BIT, Mesra and Central Instrumental facility, BIT, Mesra, India.

## References

1. Pai, V.; Akhilraj, T. M. *Eco. Env. Cons.* **2022**, *28*, 179-182. DOI: <http://doi.org/10.53550/EEC.2022.v28i03s.026>.
2. Gupta, A.K.; Rather, M.A.; Kumar Jha, A.; Shashank, A.; Singhal, S.; Sharma, M.; Pathak, U.; Sharma, D.; Mastinu, A. *Plants*. **2020**, *9*, 1329. DOI: <https://doi.org/10.3390/plants9101329>.
3. Almeida, E. L.; Marangoni, A. L.; Steel, C. J. *Food Technol.* **2013**, *43*, 2101-2108. DOI: <https://doi.org/10.1590/S0103-84782013001100028>.
4. Le, T. H. T.; Nguyen, H. T.; Nguyen, V. K.; Nguyen, T. L.; Nguyen, T. T. *Mater. Sci. Forum.* **2020**, *991*, 150-156.
5. Nayak, A. K.; Alkahtani, S.; Hasnain, M. S. *Polym. Nat. Compos.* **2022**, 213-240.
6. Zhang, Y.; Li, B.; Xu, F.; He, S.; Zhang, Y.; Sun, L.; Zhu, K.; Li, S.; Wu, G.; Tan, L. *Trends Food Sci Technol.* **2021**, *107*, 268-283. DOI: <https://doi.org/10.1016/j.tifs.2020.10.041>.
7. Weng, L.; Zhang, Y.; Yang, Y.; Wang, L. *Int. J. Mol. Sci.* **2014**, *15*, 6328-6342. DOI: <https://doi.org/10.3390/ijms15046328>.
8. Eswaramoorthy, R.; Hailekiros, H.; Kadir, F.; Endale, M. *Adv. Appl. Bioinforma. Chem.* **2021**, *14*, 13. DOI: <https://doi.org/10.2147/AABC.S290912>.
9. Banyal, S.; Shukla, A.K.; Kumari, A.; Kumar, A.; Khatak, A.; Luthra, A.; Kumar, M. *Waste Biomass. Valori.* **2022**, 1-14. DOI: <https://doi.org/10.1007/s12649-022-01945-0>.
10. Martins, A.; Beninca, C.; Bet, C.D.; Bisinella, R.Z.B.; de Oliveira, C.S.; Hornung, P.S.; Schnitzler, E. *J. Therm. Anal. Calorim.* **2020**, *142*, 819-828. DOI: <https://doi.org/10.1007/s10973-020-09298-3>.
11. Nawaz, H.; Waheed, R.; Nawaz, M.; Shahwar, D. *Chem. Prop. Starch.* **2020**, *9*, 13-35. DOI: <https://doi.org/10.5772/intechopen.88870>.
12. Singh, A.; Kumar, K. *J. Int. J. Biol. Macromol.* **2020**, *165*, 1431-1437. DOI: <https://doi.org/10.1016/j.ijbiomac.2020.10.027>.
13. Charoenthai, N.; Sanga-ngam, T.; Kasemwong, K.; Sungthongjeen, S.; Puttipipatkachorn, S. *Starch-Stärke.* **2022**, *74*, 2100263. DOI: <https://doi.org/10.1002/star.202100263>.
14. Belniak, P.; Świąder, K.; Szumiło, M.; Hyla, A.; Poleszak, E. *Saudi Pharm. J.* **2017**, *25*, 365-369. DOI: <https://doi.org/10.1016/j.jsps.2016.09.004>.
15. Das, D.; Kumar, K. *J. Int. J. Biol. Macromol.* **2019**, *124*, 1033-1039. DOI: <https://doi.org/10.1016/j.ijbiomac.2018.11.182>.
16. Mondal, A.; Kumar, K. *J. Int. J. Biol. Macromol.* **2019**, *140*, 1091-109. DOI: <https://doi.org/10.1016/j.ijbiomac.2019.08.094>.

17. Varma, C. A. K.; Kumar, K. J. *Int. J. Biol. Macromol.* **2018**, *118*, 2156-2162. DOI: <https://doi.org/10.1016/j.ijbiomac.2018.07.057>.
18. Deshkar, D.; Gupta, R. N.; Kumar, K. J. *Int. J. Biol. Macromol.* **2019**, *122*, 417-424. DOI: <https://doi.org/10.1016/j.ijbiomac.2018.10.079>.
19. Rengadu, D.; Gerrano, A. S.; Mellem, J. J. *Int. J. Biol. Macromol.* **2020**, *147*, 268-275. DOI: <https://doi.org/10.1016/j.ijbiomac.2020.01.043>.
20. Kulkarni, S. D.; Sinha, B. N.; Kumar, K. J. *Int. J. Biol. Macromol.* **2013**, *61*, 396-403. DOI: <https://doi.org/10.1016/j.ijbiomac.2013.07.027>.
21. Sobowale, S. S.; Olatidoye, O. P.; Atinuke, I.; Emeka, O. C. *Trans. R. Soc. S. Afr.* **2022**, *77*, 89-99. DOI: <https://doi.org/10.1080/0035919X.2022.2036265>.
22. Mehfooz, T.; Ali, T. M.; Hasnain, A. J. *Food Meas. Charact.* **2019**, *13*, 1058-1069. DOI: <https://doi.org/10.1007/s11694-018-00021-3>.
23. Molavi, H.; Razavi, S. M. A.; Farhoosh, R. *Food Chem.* **2018**, *245*, 385-393. DOI: <https://doi.org/10.1016/j.foodchem.2017.10.117>.
24. Deepika, V.; Kumar, K. J.; Anima, P. *Int. J. Biol. Macromol.* **2013**, *55*, 193-200. DOI: <https://doi.org/10.1016/j.ijbiomac.2012.11.027>.
25. Guo, Z.; Zeng, S.; Zhang, Y.; Lu, X.; Tian, Y.; Zheng, B. *Food Hydrocoll.* **2015**, *44*, 285-291. DOI: <https://doi.org/10.1016/j.foodhyd.2014.09.014>.
26. Zhu, F.; Cui, R. *Int. J. Biol. Macromol.* **2015**, *148*, 601-607. DOI: <https://doi.org/10.1016/j.ijbiomac.2020.01.028>.
27. Wisudyaningsih, B.; Wijiani, N.; Anggraeni, V. *Pharm. Educ.* **2023**, *23*, 207-211. DOI: <https://doi.org/10.46542/pe.2023.232.207211>.
28. Venkataswamy, M. **2018**. DOI: <https://doi.org/10.13140/RG.2.2.24488.42248>.
29. Khatri, T. C. *World J. Pharm. Res.* **2017**, *6*, 163-175.
30. Chaurasia, S.; Pandey, A.; June. *Medical Sciences Forum.* **2022**, *12*, 5. DOI: <https://doi.org/10.3390/eca2022-12712>.
31. Chua, S. D.; Kho, E. P.; Lim, S. F.; Hussain, M. H. *Adv. Mater.* **2021**, 1-23. DOI: <https://doi.org/10.1080/2374068X.2021.1878702>.
32. Zhang, Y.; Zuo, H.; Xu, F.; Zhu, K.; Tan, L.; Dong, W.; Wu, G. *Food Hydrocoll.* **2022**, *110*, 106154. DOI: <https://doi.org/10.1016/j.foodhyd.2020.106154>.
33. Sujka, M. *Ultrason. Sonochem.* **2017**, *37*, 424-429. DOI: <https://doi.org/10.1016/j.ultsonch.2017.02.001>.
34. Vishal, Banyal, S.; Shukla, A. K.; Kumari, A.; Kumar, A.; Khatak, A.; Luthra, A.; Sunil; Kumar, M. *Waste Biomass Valorization.* **2023**, *14*, 1597-1610. DOI: <https://doi.org/10.1007/s12649-022-01945-0>.
35. Swami, S.B.; Kalse, S. B. *Bioact. Mol. Plant. Foods.* **2018**, 1-23.
36. Sulaiman, W. M. A. *Food Res.* **2019**, *3*, 546-555. DOI: [https://doi.org/10.26656/fr.2017.3\(5\).095](https://doi.org/10.26656/fr.2017.3(5).095).
37. Kushwaha, R.; Fatima, N. T.; Singh, M.; Singh, V.; Kaur, S. Puranik, V.; Kumar, R.; Kaur, D. *J. Food Process. Preserv.* **2021**, *45*, 15146. DOI: <https://ifst.onlinelibrary.wiley.com/doi/10.1111/jfpp.15146>.
38. Marta, H.; Tensiska, T. *KnE Life Sci.* **2017**, 689-700. DOI: <https://doi.org/10.18502/kls.v2i6.1091>.
39. Babu, S.A.; Parimalavalli, R. *Ann.Univ. Dunarea de Jos of Galati. Fascicle VI-Food Technol.* **2014**, *38*, 48-63. DOI: <https://www.gup.ugal.ro/ugaljournals/index.php/food/article/view/1733>.
40. Iheagwara, M. C. *J. Food Process. Technol.* **2013**, *4*. DOI: <https://doi.org/10.4172/2157-7110.1000198>.
41. Zia-ud-Din, Xiong, H.; Fei, P. *Crit. Rev. Food Sci. Nutr.* **2017**, *57*, 2691-2705. DOI: <https://doi.org/10.1080/10408398.2015.1087379>.
42. Mahajan, H.S.; Kelkar, Y. V. *J. Drug Deliv. Sci. Technol.* **2017**, *41*, 310-316. DOI: <https://doi.org/10.1016/j.jddst.2017.07.023>.
43. Widodo, R.T.; Hassan, A. *Powder Technol.* **2015**, *269*, 15-21. DOI: <https://doi.org/10.1016/j.powtec.2014.08.039>.

44. Wang, Y.; Li, Y.; Liu, Y.; Chen, X.; Wei, X. *Int. J. Biol. Macromol.* **2015**, 77, 76-84. DOI: <https://doi.org/10.1016/j.ijbiomac.2015.02.052>.
45. Zheng, Y.; Liu, R.; Hou, X.; Zhuang, X.; Wu, H.; Yin, D.; Yang, Y. *J. Drug Deliv. Sci. Technol.* **2023** 84, 104452. DOI: <https://doi.org/10.1016/j.jddst.2023.104452>.
46. Wang, D.; Sun, S.Q.; Wu, W.Z.; Yang, S.L.; Tan, J.M. *Carbohydr. Polym.* **2014**, 105, 127-134. DOI: <https://doi.org/10.1016/j.carbpol.2013.12.085>.
47. Archana, G.; Sabina, K.; Babuskin, S.; Radhakrishnan, K.; Fayidh, M.A.; Babu, P.A.S.; Sivarajan, M.; Sukumar, M. *Carbohydr. Polym.* **2013**, 98, 89-94. DOI: <https://doi.org/10.1016/j.carbpol.2013.04.062>.
48. Zhang, C. H.; Yu, Y.; Liang, Y. Z.; Chen, X. Q. *Int. J. Biol. Macromol.* **2015**, 79, 681-686. DOI: <https://doi.org/10.1016/j.ijbiomac.2015.05.060>.
49. Xie, J.H.; Zhang, F.; Wang, Z.J.; Shen, M.Y.; Nie, S.P.; Xie, M.Y. *Carbohydr. Polym.* **2015**, 133, 596-604. DOI: <https://doi.org/10.1016/j.carbpol.2015.07.031>.
50. Chaurasia, S.; Pandey, A. *Russ. J. Bioorg. Chem.* **2023**, 1-34. DOI: <https://doi.org/10.1134/S1068162023030081>.

## Biosynthesis of Silver Nanoparticles Mediated by *Lippia graveolens* Aqueous Extract

---

Karen M. Soto<sup>1</sup>, Montserrat Hernández-Iturriaga<sup>2</sup>, Arely Cárdenas<sup>3</sup>, Sandra Mendoza<sup>2\*</sup>

<sup>1</sup>Centro de Investigaciones y de Estudios Avanzados del I.P.N. Unidad Querétaro, Querétaro, Querétaro, C.P. 76230, Mexico.

<sup>2</sup>Departamento de Investigación y Posgrado en Alimentos, Facultad de Química, Universidad Autónoma de Querétaro. Querétaro, Qro 76010, México.

<sup>3</sup>Consejo Nacional De Ciencia y Tecnología (CONACYT)- Centro de Investigación en Química para la Economía Circular, CIQEC, Facultad de Química, Universidad Autónoma de Querétaro. Querétaro, Qro 76010, México.

\*Corresponding author: Sandra Mendoza, email: [smendoza@uaq.mx](mailto:smendoza@uaq.mx)

Received May 27<sup>th</sup>, 2023; Accepted October 10<sup>th</sup>, 2023.

DOI: <http://dx.doi.org/10.29356/jmcs.v68i3.2070>

**Abstract.** The synthesis of silver nanoparticles (AgNPs) with plant extracts has acquired a lot of interest in recent years, due to its different applications in areas such as medicine, optics, food, pharmaceutical, among others. The aim of this work was to evaluate aqueous extracts of Mexican oregano (*Lippia graveolens*), rich in antioxidant compounds, to synthesize AgNPs. *L. graveolens* extract was characterized by HPLC and the antioxidant capacity was evaluated by ABTS, DPPH and CUPRAC. The effect of factors such as pH, concentration of precursor and temperature on the synthesis of AgNPs was studied. The particles were characterized by SEM, TEM, FTIR and their stability was evaluated with respect to time. The AgNPs showed a spherical shape with an average diameter of 2.4 nm, and antimicrobial activity against *S. aureus*, *L. monocytogenes* and *E. coli*. After 30 days of storage, the AgNPs agglomerated to form dendritic structures.

**Keywords:** Silver nanoparticles; Mexican oregano; antimicrobial activity; green synthesis.

**Resumen.** La síntesis de nanopartículas de plata (AgNPs) mediante extractos de plantas ha adquirido interés en años recientes debido a los diversos campos donde pueden usarse, como la medicina, óptica, alimentos, farmacéutica, entre otras. El objetivo de esta investigación fue evaluar la capacidad de extractos acuosos del orégano mexicano (*Lippia graveolens*), rico en compuestos antioxidantes, para sintetizar AgNPs. El extracto de *L. graveolens* fue caracterizado por HPLC y la actividad antioxidante fue evaluada mediante los ensayos de ABTS, DPPH y CUPRAC. Se estudió el efecto del pH, concentraciones de precursor, y temperatura en la síntesis de AgNPs. Las partículas fueron caracterizadas mediante SEM, TEM, FTIR y su estabilidad con respecto al tiempo fue evaluada. Las AgNPs presentaron una forma esférica con diámetro promedio de 2.4 nm, y actividad antimicrobiana contra *S. aureus*, *L. monocytogenes* and *E. coli*. Después de 30 días de almacenaje, las AgNPs se aglomeraron formando estructuras dendríticas.

**Palabras clave:** Nanopartículas de plata; orégano mexicano; actividad antimicrobiana; síntesis verde.

---

## Introduction

Metallic nanoparticles in a nano size scale show unique characteristics with extensive applications in diverse fields such as agriculture, cosmetics, pharmaceuticals, medicine, textiles, and food industry [1]. Silver is the metal of first choice to produce nanoparticles due to its high antimicrobial activity against a wide range of bacteria and fungi as well as its catalytic properties [2,3]. Physical and chemical methods have been used to synthesize NPs but they are environmentally hazardous, technically laborious, and expensive [4]. To overcome these limitations, green synthesis methods have been proposed to obtain silver and gold nanoparticles (AgNPs, AuNPs) where antioxidants, plant extracts and microorganisms are used as reductant reagents [5]. The use of plant extracts has the advantages of being scalable and less expensive than the methods based on microbial processes; on the other hand, the rate of reduction of metal ions using plants has been found to be much faster as compared to microorganisms affording stable metal nanoparticles [6,7]. Several reviews highlight the synthesis, characterization, and application of plant-based metallic nanoparticles [8-10]. The secondary metabolites of plants (terpenoids, phenolic acids and flavonoids) act as reducing and stabilizing agents in the synthesis of metal nanoparticles, then the source of the plant extract and the extraction process influence the characteristics of the NPs [11,12].

Most of the aromatic oregano plants belong to the genus *Origanum* (Lamiaceae) and *Lippia* (Verbenaceae). Among the aromatic plants used to produce AgNPs, *Origanum vulgare* better known as European oregano, has been reported to generate spherical AgNPs sizes of 136 nm [13] and 1 to 50 nm [14]. *Lippia graveolens* KHB, commonly known as Mexican oregano, is used as condiment of many traditional Mexican dishes as well as raw material to produce cosmetics, drugs, and liquors. In Latin America, *L. graveolens* is used as antiseptic, antipyretic, analgesic, antispasmodic, antioxidant and antimicrobial agent [15]. The aqueous extract of *L. graveolens* has many secondary metabolites being the most abundant flavonoids and terpenoids which are responsible of the observed antioxidant activity [16-18]. The reducing power of *L. graveolens* extracts can mediate the synthesis of metallic nanoparticles. In the present study, AgNPs were obtained by an aqueous extract of *Lippia graveolens*, the effect of extract concentration, reaction time, temperature and pH of the reaction medium was analyzed. The obtained nanoparticles were physicochemical characterized, and the antimicrobial activity was tested against food pathogens.

## Methodology

### Materials

2,2'-azinobis-3-ethylbenzothiazoline-6-sulfonic acid (ABTS), potassium persulfate, Trolox, 1,1-diphenyl-2-picrylhydrazyl (DPPH), Folin & Ciocalteu's reagent and HPLC standards were obtained from Sigma Chemical Co. (St. Louis MO, U.S.A.). Agar (TSA), and Tryptic soy broth (TSB) were purchased from Becton-Dickinson (New Jersey, USA). All solvents, and silver nitrate were obtained from Baker (Mallinckrodt Baker, Inc., Phillipsburg, NJ, USA). Ammonium acetate, copper (II) chloride, sodium hydroxide, sodium carbonate, copper (II) sulfate, potassium persulfate, methanol, sodium potassium tartrate and 96% EtOH were obtained from Merck (Darmstadt, Germany).

### *Lippia graveolens* extract preparation and characterization

10 g of the dried plant were taken and mixed with 100 mL of deionized water and heated at 60 °C for 10 min. After cooling at room temperature, the mixture was filtered with a Whatman No.1 filter paper and the aqueous filtrate was lyophilized and stored for future use. The antioxidant activity of the extract was evaluated by the DPPH, ABTS and electrochemical CUPRAC (cupric ion reducing antioxidant capacity) assays according to reported procedures [19-21] and the results were expressed as IC<sub>50</sub> in mg/L. The total phenolic content of the extract was determined by Folin-Ciocalteu colorimetric method [22] expressing the results as mg of gallic acid equivalents per g dried sample (mg GA/g dw). The HPLC-DAD method reported by Ramírez-Jiménez *et al.* [23] was used to obtain the phenolic profile of the extract. The external standard method was used to quantify

the secondary metabolites in an Agilent 2100 Series HPLC system (Agilent Technologies, Palo Alto, CA, USA) using a Sorbax Eclipse XDB-C18 column (Agilent Technologies, 9.4 x 250 mm, 5.0  $\mu\text{m}$ ).

### Biosynthesis of silver nanoparticles

To study the effect of pH (2, 5, 8, 10), temperature (20, 60, 80 °C) and reaction time (5, 10, 15, 20 min) on the AgNPs formation, solutions containing 20 mg of lyophilized oregano aqueous extract and  $\text{AgNO}_3$  1mM were used. Values of pH were adjusted by using 0.1 N NaOH and 0.1 N HCl after the addition of the extract. The temperature used for pH experiments was 20 °C and for reaction time 80 °C. The AgNPs formation was monitored by UV-Vis spectrophotometry (200-800 nm) (Spectra Max Tunable Microplate Reader, Molecular Devices Co., Sunnyvale, CA, USA). The colloidal suspensions were centrifuged at 15,000 rpm, washed three times with distilled water and dried at 60 °C, the powder was kept for further characterization.

### Silver nanoparticle characterization

Infrared absorption spectra of dried AgNPs and dried extracts were recorded by DRIFT with 4  $\text{cm}^{-1}$  of resolution (Spectrum GX spectrophotometer, Perkin Elmer, Massachusetts, USA with a diffuse reflectance accessory, Pike Technology model). The morphology and size of AgNPs were obtained from a JEOL (Japan) high-resolution transmission electron microscope (JEM-1010) and a Carl Zeiss (Jena, Germany) high-resolution scanning electron microscope (EVO-50). Image J software was used to calculate the diameters of the NPs (average of 50 NPs).

### Stability of silver nanoparticles

The colloidal solutions obtained after biosynthesis of silver nanoparticles (pH 5, 80 °C, 5 min), were stored at room temperature for 30 days. Every five days UV-Visible spectra was recorded, and at the end of the experiment the AgNPs solution was characterized by TEM.

### Antimicrobial activity

To evaluate the antimicrobial activity of the AgNPs, the agar well diffusion technique was used against *Escherichia coli* (ATCC 25922), *Listeria monocytogenes* (ATCC 35152) and *Staphylococcus aureus* (ATCC 6538). The methodology described by Soto et al. [24] was followed. Briefly, five  $\mu\text{L}$  ( $10^5$  CFU/mL) of each microorganism culture were suspended in 6 mL of ST agar tempered at 45 °C, mixed and immediately poured into a Petri dish. Once agar solidified, 10  $\mu\text{L}$  of AgNPs solution (20, 40, 60, 70, 80, 90 and 100  $\mu\text{g/mL}$ ) were placed on the agar surface, then incubated for 48 h at 30 °C and the zone of growth inhibition was measured. Oregano lyophilized extract (100  $\mu\text{g/mL}$ ) and chloramphenicol (500  $\mu\text{g/mL}$ ) were used as control.

## Results and discussion

### Characterization of Lippia graveolens extract

Table 1 shows the identified compounds by HPLC-DAD of lyophilized *L. graveolens* extract. Rosmarinic, gallic and ellagic acids, kaempferol and thymol were the major components among the identified secondary metabolites, this result is similar to the reported data by Herrera-Rodríguez *et al.* [25] who evaluated the phenolic compounds in the essential oil of *L. graveolens* by GC/MS analysis. Thymol was detected in a higher concentration than Greek oregano (10.6  $\mu\text{g/g}$ ) under similar extraction conditions [26]. The antioxidant activity of the aqueous extract was evaluated by ABTS, DPPH and CUPRAC techniques, the first two methods are based on electron transfer from the secondary metabolites of the extracts to the radicals while the last one evaluates the electron-donating capacity of the extract to reduce a metal complex [27].  $\text{IC}_{50}$  values of  $229.4 \pm 10.5$  mg/L,  $290.1 \pm 12.7$  mg/L, and  $95.01 \pm 0.69$  mg/L for ABTS, DPPH and CUPRAC assays were obtained, respectively. The antioxidant activity of the extract was similar to the reported values ( $\text{IC}_{50}$  207 mg/L) for methanolic extracts from *L. graveolens* evaluated by the DPPH assay [15]. As expected, the antioxidant values were lower than the aqueous extracts from *O. vulgare* (26.7 mg/L) [28]. The total phenol content was  $330.5 \pm 1.7$  mg GAE/g dw, this value is higher than the reported values for several hydroethanolic extracts from *L.*

*graveolens* samples (95.74- 99.71mg GAE/g dw) [29]. Rosmarinic acid, thymol and kaempferol are the secondary metabolites that significantly contribute to the antioxidant capacity of the extract.

**Table 1.** Phenolic compounds in *Lippia graveolens* determined by HPLC-DAD

| Retention time (min)  | Compound            | Concentration mg/g dw | % Adjust |
|-----------------------|---------------------|-----------------------|----------|
| <i>Phenolic acids</i> |                     |                       |          |
| 3.22                  | Gallic acid         | 1.31 ± 0.39           | 93.9     |
| 3.97                  | Protocatechuic acid | 0.26 ± 0.02           | 97.9     |
| 5.44                  | Ellagic acid        | 1.86 ± 0.05           | 94.6     |
| 5.65                  | Coumaric acid       | 0.96 ± 0.07           | 96.5     |
| 5.76                  | Rosmarinic acid     | 2.46 ± 0.19           | 99       |
| 5.9                   | Ferulic acid        | 0.62 ± 0.03           | 99.8     |
| <i>Aldehyde</i>       |                     |                       |          |
| 6.16                  | Vanillin            | 0.87 ± 0.01           | 97.9     |
| <i>Flavonoids</i>     |                     |                       |          |
| 7.44                  | Quercetin           | 0.81 ± 0.09           | 99.7     |
| 14.69                 | Apigenin            | 0.63 ± 0.04           | 98.7     |
| 14.91                 | Kaempferol          | 5.76 ± 0.03           | 92.3     |
| 4.68                  | Naringenin          | 0.48 ± 0.05           | 98.3     |
| <i>Monoterpene</i>    |                     |                       |          |
| 15.22                 | Thymol              | 3.12 ± 0.06           | 93.7     |

Results reported as mean ± standard error of three replicates. The concentration is reported as mg/g of dried sample.

### Biosynthesis of silver nanoparticles in different conditions

The green synthesis of AgNPs with plant extracts is mediated by the compounds that have enough electrochemical potential to reduce silver ions, then the chemical state and concentration of the extract components affect the size and shape of the nanoparticles [30]. It has been demonstrated by several authors that green synthesis of AgNPs involves the reduction of  $\text{Ag}^+$  to  $\text{Ag}^0$  by antioxidant secondary metabolites, in this case mainly rosmarinic acid, thymol and kaempferol. Then nucleation and growth of  $\text{Ag}^0$  nanoparticles occur to finally be covered by the oxidized secondary metabolites, this final stage favours the stabilization of the NPs [8-10,24].

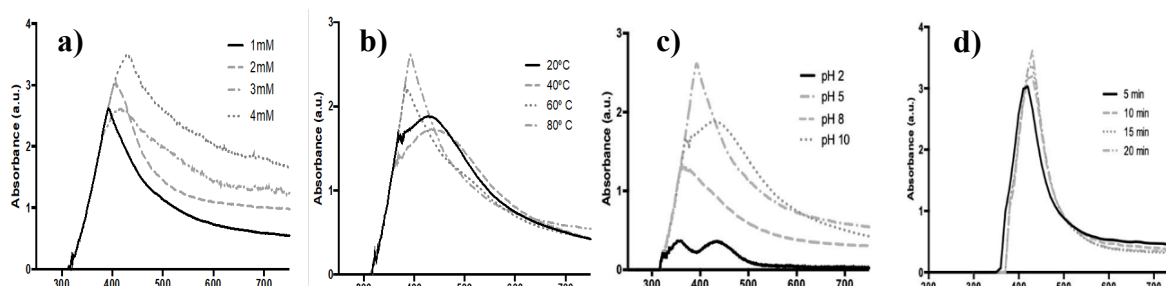
Here, colloidal solutions of AgNPs were prepared by adding different concentrations of  $\text{AgNO}_3$  to an aqueous solution of the oregano extract, the solutions changed their colour from transparent to dark yellow within minutes, indicating the presence of AgNPs. The effect of silver nitrate concentration is shown in Fig. 1(a), the characteristic AgNPs surface plasmon resonance (SPR) absorption band was observed at 357-400 nm. The band absorption increased, and the wavelength was shifted to the red as  $\text{AgNO}_3$  concentration increased from 1 mM to 4 mM. Similar results were reported for the obtention of AgNPs from an aqueous extract of *Oscillatoria limnetica*, addition of the silver nitrate concentration from 0.1 mM to 0.5 mM shifted the surface plasmon bands from 422 nm to 430 nm with gradual intensity increase (0.531-0.710) [31].



Considering the SPR response, further experiments were conducted using 1 mM AgNO<sub>3</sub>. Fig. 1(b) shows the absorption spectra of colloidal solutions at different temperatures (20-80 °C). With the increase of temperature, the reduction of silver salt is enhanced, as indicated by the rapid color change of the solution. The peak absorption wavelength shifted toward blue from 437 to 400 nm with the temperature increment. As reported, this displacement indicates that the size of the synthesized nanoparticles decreases with increasing temperature, which may be due to a faster reaction rate at higher temperature. It is generally accepted that high temperature promotes Ag nucleation while low temperature allows the growth of AgNPs, then smaller particles with uniform size distribution are formed at higher temperature [32,33].

The pH plays an important role in the nanoparticle's synthesis because the electron transfer from the secondary metabolites to the silver ions depends on the molecular ionization, also the charge of biomolecules might affect AgNPs capping as well as stabilizing properties [34]. Fig. 1(c) shows the spectra of AgNPs synthesized under different pH values at 80 °C, this temperature was chosen considering that smaller AgNPs were obtained. At pH 2 two absorption bands at 365 and 443 nm were observed. It has been reported that the AgNPs with nanocube morphology exhibit two dipole plasmonic peaks, one belongs to oscillating charges along longitudinal axis, and the other one belongs to oscillating charges along latitudinal axis [35]. For pH 5, 8 and 10 only one band was observed at 400, 375 and 442 nm, respectively. In basic pH values the synthesis of silver nanoparticles is faster than at acid pH, the change of color was observed immediately, but when the solution was heated precipitation was observed. Verma and Mehata [34] observed that at high pH values the particles became unstable and agglomerated, when kept overnight. For this study, AgNPs synthesis at pH 5 shows the major absorbance and the more defined band at lower wavelength which is related to small nanoparticles and homogeneous distribution of the particle size [36]. In other studies, it was reported that basic pH promotes the synthesis of silver nanoparticles due to deprotonation of organic acids such as citric and malic acid [37].

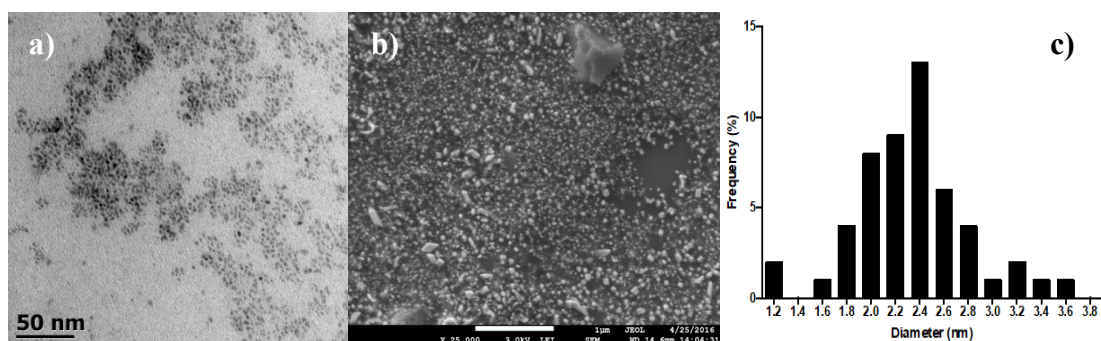
The effect of time reaction was evaluated using AgNO<sub>3</sub> 1mM, pH 5 and 80 °C. Fig. 1(d) shows the spectra of AgNPs at different reaction times, after ten minutes of reaction no SPR wavelength displacements were observed. The increment of the SPR absorption band indicates an enhancement in the formation of AgNPs. The reaction was completed at 30 min and a precipitate was obtained.



**Fig. 1.** UV-Visible spectra of synthesized AgNPs using aqueous extract of *L. graveolens* at different parameters. (a) AgNO<sub>3</sub> concentration, (b) 1 mM AgNO<sub>3</sub> at different temperatures, (c) 1 mM AgNO<sub>3</sub> at different pH and (d) 1 mM AgNO<sub>3</sub> at different reaction time.

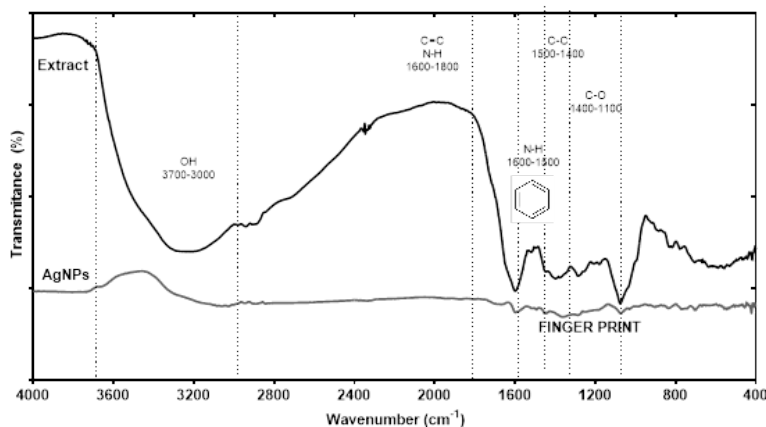
### Characterization of AgNPs

The synthesis of AgNPs was conducted in the optimal conditions established in the previous experiment (AgNO<sub>3</sub> 1mM, pH 5, 80 °C and 10 min). Fig. 2 shows the morphology of nanoparticles obtained by SEM and TEM, the AgNPs were spherical with diameters between 1-4 nm. Several plant extracts have been used to synthesize spherical AgNPs with sizes ranging from 0.5 nm to 100 nm [8-10]. The oregano AgNPs obtained here are smaller than those obtained from European oregano (*Origanum vulgare*) aqueous extract (136 nm) [18], and ethanolic extract (30-58 nm) [19]. Similar size was reported for AgNPs obtained from *Polygonatum graminifolium* (3-15 nm) [38], *Coriandrum sativum* (6.95 nm) [39], *Sida cardifolia* (3-8 nm) [40], *Piper retrofractum* (1-5 nm) [41], and *Allium sativum* (3-6 nm) [42].



**Fig. 2.** (a) TEM and (b) SEM images of AgNPs and (c) size distribution.

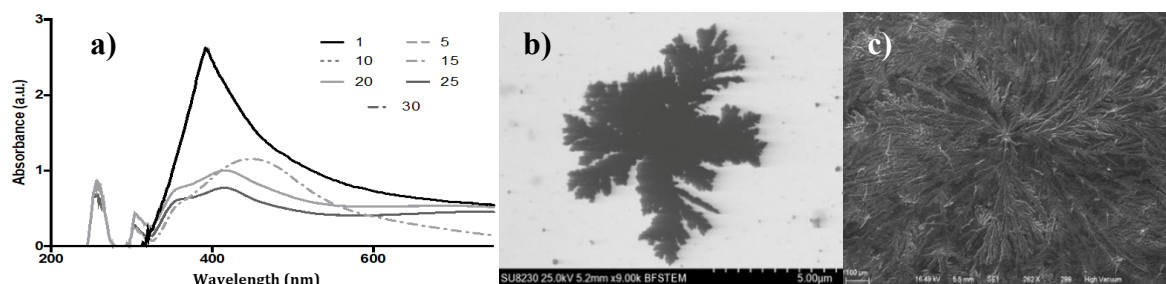
Fig. 3 shows the DRIFT spectra for the dried extract, where the typical fingerprint region from 800 to 1800  $\text{cm}^{-1}$  attributed to the stretching and bending vibrations characteristic of the *L. graveolens* secondary metabolites is observed [43]. This region included the signals at 1100-1400  $\text{cm}^{-1}$  corresponding to C-O of hydroxyl groups, bands at 1400-1500  $\text{cm}^{-1}$  corresponding to C-O and C-C stretching vibrations specific to phenyl groups, signals at 1500-1600  $\text{cm}^{-1}$  corresponding to aromatic domain and N-H bending, and the region at 1600-1800  $\text{cm}^{-1}$  corresponding to bending N-H, C=O stretching's signals assigned to aldehydes, ketones, and esters [43,44]. Other important band observed was at 3000-3700  $\text{cm}^{-1}$  corresponding to O-H stretching vibrations. The spectra of the dried AgNPs displayed most of the DRIFT bands of the extract, which confirm that the secondary metabolites play the role of capping and stabilizing agents in the synthesis of AgNPs. Some displacements were observed for some bands that represent the interactions of functional groups with AgNPs surface [45].



**Fig. 3.** DRIFT of lyophilized *L. graveolens* extract and dried AgNps.

### Stability of AgNPs

Fig. 4(a) shows the UV-Vis spectra of AgNPs at different times of storage. After fifteen days of storage at room temperature, the AgNPs SPR signal changed drastically, and after a month under storage, the colour of the AgNPs solution turned dark- gray and a sediment was formed. As storage time increase, the SPR signal gets wider and shifted to higher wave numbers, confirming changes of shape and size of the nanoparticles. After one month of storage, the SEM and TEM images (Fig. 4(b)-(c)) evidenced AgNPs clustering with a morphology which has been denominaded flower-like [46]. It has been proposed that the formation of the dendritic structures involves the aggregation of NPs to form micrometric worm-like structures that serve as template for the growth of multi-branched structures [47]. These dendritic structures can be used in catalysis, and antimicrobial metallic coatings, among other applications [48,49].



**Fig. 4.** (a) UV-Vis spectra of AgNPs at different days of storage. (b) TEM image after 30 days of storage, and (c) SEM image after 30 days of storage.

### Antimicrobial activity

Table 2 shows the diameter of growth inhibition zones produced by oregano extract and AgNPs against three food pathogens, *S. aureus*, *L. monocytogenes* and *E. coli*. For all tested microorganism, the AgNPs antimicrobial activity was concentration dependent, and the results revealed that the AgNPs displayed significant inhibition activity against all the tested pathogens. Although, *L. monocytogenes* and *S. aureus* are Gram positive with a thicker membrane cell compared to Gram negative microorganism such as *E. coli*, both demonstrated sensitivity to the antimicrobial effect of AgNPs. Similar results were reported by Ruíz-Baltazar et al. [50] where AgNPs synthesized with *Melissa officinalis* leaf extract, at 15 and 20 mM exhibited growth inhibition diameters of 12.5 and 11.5 mm against *S. aureus* and *E. coli*, respectively. Sankar et al. [13] evaluated the antimicrobial activity of AgNPs (30 µL) obtained from *O. vulgare* extract against *E. coli* obtaining a 10 mm growth inhibition diameter. Several factors are to be considered regarding AgNPs antimicrobial activity, the electronic effect produced by the interaction of silver with bacterial membrane surface, the chemical structure of secondary metabolites that stabilized the AgNPs when synthesized by plant extracts, and the shape and size of NPs [7,51]. All the evaluated AgNPs concentrations showed higher antimicrobial activity compared with *L. graveolens* extract [52,53]. The antimicrobial activity of the Mexican oregano has been mainly attributed to the terpenes like thymol and eugenol as well as phenolic acids like rosmarinic acid (15,29,52). As expected, the antimicrobial activity of the AgNPs were higher than the extract, since the antimicrobial activity produce by the release of Ag<sup>+</sup> ions is added to the antimicrobial activity of the secondary metabolites that surrounded the NPs (8-10). At the maximum AgNPs concentration (100 µg/mL), the antimicrobial effect against *E. coli* and *S. aureus* was higher than chloramphenicol.

**Table 2.** Diameter of growth inhibition zone of AgNPs against *S. aureus*, *E. coli* and *L. monocytogenes*.

| Concentration (µg/mL)       | <i>S. aureus</i><br>Diameter (mm) | <i>L. monocytogenes</i><br>Diameter (mm) | <i>E. coli</i><br>Diameter (mm) |
|-----------------------------|-----------------------------------|------------------------------------------|---------------------------------|
| 20                          | 9.36 ± 0.15 <sup>c</sup>          | 8.52 ± 0.06 <sup>f</sup>                 | 9.46 ± 0.11 <sup>f</sup>        |
| 40                          | 10.16 ± 0.19 <sup>dc</sup>        | 9.64 ± 0.12 <sup>c</sup>                 | 10.27 ± 0.09 <sup>c</sup>       |
| 60                          | 11.06 ± 0.11 <sup>d</sup>         | 10.89 ± 0.04 <sup>d</sup>                | 10.71 ± 0.07 <sup>dc</sup>      |
| 70                          | 12.60 ± 0.16 <sup>c</sup>         | 11.15 ± 0.09 <sup>d</sup>                | 11.63 ± 0.11 <sup>c</sup>       |
| 80                          | 13.53 ± 0.17 <sup>bc</sup>        | 11.59 ± 0.05 <sup>c</sup>                | 13.38 ± 0.03 <sup>b</sup>       |
| 100                         | 14.87 ± 0.45 <sup>a</sup>         | 12.58 ± 0.10 <sup>b</sup>                | 13.95 ± 0.06 <sup>a</sup>       |
| Extract (100 µg/mL)         | 7.56 ± 0.14 <sup>f</sup>          | 7.90 ± 0.05 <sup>g</sup>                 | 7.5 ± 0.11                      |
| Chloramphenicol (500 µg/mL) | 13.95 ± 0.39 <sup>ab</sup>        | 14.80 ± 0.05 <sup>a</sup>                | 10.80 ± 0.08 <sup>d</sup>       |

Results reported as mean ± standard error of three replicates. Different letters in the same column represent significance difference (P<0.05) according to the Tukey test n=3.

## Conclusions

Silver nanoparticles have been successfully synthesized using *L. graveolens* extract, the AgNPs are spherical and exhibit a high energy SPR band around 400 nm. According to the FTIR analysis, the compounds present in *L. graveolens* extract play an important role in the reduction and stabilization of metal nanoparticles. The obtained AgNPs are stable in colloidal solution for 15 days, after which the nanoparticles agglomerated and formed dendritic structures, meaning that the use of oregano AgNPs on liquid products that need to be stored for more than 15 days is not recommended. The AgNPs antimicrobial activity is dependent on the concentration and has better activity against *S. aureus* and *E. coli*. The obtained AgNPs can be used in different applications due to its biological activity and morphology.

## References

1. Ahmad, S.; Munir, S.; Zeb, N.; Ullah, A.; Khan, B.; Ali, J.; Bilal, M.; Omer, M.; Alamzeb, M.; Salman, S. M.; Ali, S. *Int. J. Nanomedicine*. **2019**, *14*, 5087–5107. DOI: <https://doi.org/10.2147/IJN.S200254>.
2. Saha, J.; Begum, A.; Mukherjee, A.; Kumar, S. *Sustain. Environ. Res.* **2017**, *27*, 245–250. DOI: <https://doi.org/10.1016/j.serj.2017.04.003>.
3. Sharma, V.; Kaushik, S.; Pandit, P.; Dhull, D.; Yadav, J. P.; Kaushik, S. *Appl. Microbiol. Biotechnol.* **2019**, *103*, 881–891. DOI: <https://doi.org/10.1007/s00253-018-9488-1>.
4. Pattanayak, S.; Rahaman, M.; Maity, D.; Chakraborty, S.; Kumar, S.; Chattopadhyay, S. *J. Saudi Chem. Soc.* **2017**, *21*, 673–684. DOI: <https://doi.org/10.1016/j.jscs.2015.11.004>.
5. Sudha, A.; Jeyakanthan, J.; Srinivasan, P. *Resource-Efficient Technologies*. **2017**, *3*, 506–515. DOI: <https://doi.org/10.1016/j.reffit.2017.07.002>.
6. Castillo-Henríquez, L.; Alfaro-Aguilar, K.; Ugalde-álvarez, J.; Vega-Fernández, L.; de Oca-Vásquez, G. M.; Vega-Baudrit, J. R. *Nanomater.* **2020**, *10*, 1–24.
7. Kumar, A.; Chisti, Y.; Chand, U. *Biotechnol. Adv.* **2013**, *31*, 346–356. DOI: <https://doi.org/10.1016/j.biotechadv.2013.01.003>.
8. Alshameri, A.W.; Owais, M. *OpenNano*. **2022**, *8*, 100077. DOI: <https://doi.org/10.1016/j.onano.2022.100077>.
9. Hasan, K. M.; Xiaoyi, L.; Shaoqin, Z.; Horváth, P. G.; Bak, M.; Bejó, L.; Sipos, G.; Alpár, T. *Heliyon*. **2022**, *8*, e12322. DOI: <https://doi.org/10.1016/j.heliyon.2022.e12322>.
10. Nadaf, S.J.; Jadhav, N. R.; Naikwadi, H. S.; Savekar, P. L.; Sapkal, I.D.; Kambli, M.M.; Desai, I. A. *OpenNano*. **2022**, *8*, 100076. DOI: <https://doi.org/10.1016/j.onano.2022.100076>.
11. Gopinath, K.; Venkatesh, K. S.; Ilangovan, R.; Sankaranarayanan, K.; Arumugam, A. *Ind. Crops Produ.* **2013**, *50*, 737–742. DOI: <https://doi.org/10.1016/j.indcrop.2013.08.060>.
12. Sulaiman, G. M.; Mohammed, W. H.; Marzoog, T. R.; Al-, A. A. A.; Kadhum, A. A. H.; Mohamad, A. B. *Asian Pac. J. Trop. Biomed.* **2013**, *3*, 58–63. DOI: [https://doi.org/10.1016/S2221-1691\(13\)60024-6](https://doi.org/10.1016/S2221-1691(13)60024-6).
13. Sankar, R.; Karthik, A.; Prabu, A.; Karthik, S.; Subramanian, K.; Ravikumar, V. *Colloids Surf. B: Biointerfaces*, **2013**, *108*, 80–84. DOI: <https://doi.org/10.1016/j.colsurfb.2013.02.033>.
14. Hambardzumyan, S.; Sahakyan, N.; Petrosyan, M.; Nasim, M. J.; Jacob, C.; Trchounian, A. *AMB Express*. **2020**, *10*. DOI: <https://doi.org/10.1186/s13568-020-01100-9>.
15. Martínez-Rocha, A.; Puga, R.; Hernández-Sandoval, L.; Loarca-Piña, G.; Mendoza, S. *Plant Foods Hum. Nutr.* **2008**, *63*, 1–5 DOI: <https://doi.org/10.1007/s11130-007-0061-9>.
16. González-Fuentes, F.; López-Gil, M.A.; Mendoza S.; Escarpa A. *Electroanalysis*. **2011**, *9*, 2212–2216. DOI: <https://doi.org/10.1002/elan.201100245>.
17. Cortés-Chitala, M. D. C.; Flores-Martínez, H.; Orozco-Ávila, I.; León-Campos, C.; Suárez-Jacobo, Á.; Estarrón-Espinosa, M.; López-Muraira, I. *Molecules*. **2021**, *26*. DOI: <https://doi.org/10.3390/molecules26030702>.

18. Soto-Domínguez, A.; García-Garza, R.; Ramírez-Casas, Y.; Morán-Martínez, J.; Serrano-Gallardo, L. B. *Int. J. Morphol.* **2012**, *30*, 937–944. DOI: <https://doi.org/10.4067/S0717-95022012000300029>.
19. Cárdenas, A.; Gómez, M.; Frontana, C. *Electrochim. Acta.* **2014**, *128*, 113–118. DOI: <https://doi.org/10.1016/j.electacta.2013.10.191>.
20. Fukumoto, L. R.; Mazza, G. *J. Agric. Food Chem.* **2000**, *48*, 3597–3604. DOI: <https://doi.org/10.1021/jf000220w>.
21. Nenadis, N.; Wang, L. F.; Tsimidou, M.; Zhang, H. Y. *J. Agric. Food Chem.* **2004**, *52*, 4669–4674. DOI: <https://doi.org/10.1021/jf0400056>.
22. Rodríguez, B. A.; Mendoza, S.; Iturriga, M. H.; Castaño-Tostado, E. *J. Food Sci.* **2012**, *77*, C121–C1217. DOI: <https://doi.org/10.1111/j.1750-3841.2011.02487.x>.
23. Ramírez-Jiménez, A. K.; Reynoso-Camacho, R.; Mendoza-Díaz, S.; Loarca-Piña, G. *Food Chem.* **2014**, *161*, 254–260. DOI: <https://doi.org/10.1016/j.foodchem.2014.04.008>.
24. Soto, K.M.; Quezada-Cervantes, C.T.; Hernández-Iturriga, M.; Luna-Bárceñas, G.; Vazquez-Duhalt, R.; Mendoza, S. *LWT - Food Sci. Technol.* **2019**, *103*, 293–300. DOI: <https://doi.org/10.1016/j.lwt.2019.01.023>.
25. Herrera-Rodríguez, S. E.; López-Rivera, R. J.; García-Márquez, E.; Estarrón-Espinosa, M.; Espinosa-Andrews, H. *Food Sci. Biotechnol.* **2019**, *28*, 441–448. DOI: <https://doi.org/10.1007/s10068-018-0499-6>.
26. Skendi, A.; Irakli, M.; Chatzopoulou, P. *J. Appl. Res. Med. Aromat. Plants.* **2017**, *6*, 62–69. DOI: <https://doi.org/10.1016/j.jarmap.2017.02.001>.
27. Bendini, A.; Dell, V.; Antiossidante, A.; Foglie, D. I.; Origano, D. I. *Biol. Nyssana.* **2016**, *7*, 131–139. DOI: <https://doi.org/10.5281/zenodo.200410>.
28. Boroski, M.; Giroux, H.J.; Sabik, H.; Petit, H.V.; Visentainer, J.V.; Matumoto-Pintro, P.T.; Britten, M. *LWT - Food Sci. Technol.* **2012**, *47*, 167–174. DOI: <https://doi.org/10.1016/j.lwt.2011.12.018>.
29. Cortés-Chilata, M. C.; Flores-Martínez, H.; Orozco-Ávila, I.; León-Campos, C.; Suárez-Jacobo, A.; Estarrón-Espinosa, M.; López-Muraira, I. *Molecules* **2021**, *26*, 702. DOI: <https://doi.org/10.3390/molecules26030702>.
30. Heydari, R.; Rashidipour, M. *Int. J. Breast Cancer.* **2015**, *1*. DOI: <https://doi.org/10.1155/2015/846743>.
31. Hamouda, R. A.; Hussein, M. H.; Abo-Elmagd, R. A.; Bawazir, S. S. *Sci. Rep.* **2019**, *9*, 1–17. DOI: <https://doi.org/10.1038/s41598-019-49444-y>.
32. Kumar, M.; Bansal, K.; Gondil, V. S.; Sharma, S.; Jain, D. V. S.; Chhibber, S.; Sharma, R. K.; Wangoo, N. *J. Mol. Liq.* **2018**, *249*, 1145–1150. DOI: <https://doi.org/10.1016/j.molliq.2017.11.143>.
33. Liu, H.; Zhang, H.; Wang, J.; Wei, J. *Arab. J. Chem.* **2017**, *13*, 1011–1019. DOI: <https://doi.org/10.1016/j.arabjc.2017.09.004>.
34. Verma, A.; Mehata, M. S. *J. Radiat. Res. Appl. Sci.* **2016**, *9*, 109–115. DOI: <https://doi.org/10.1016/j.jrras.2015.11.001>.
35. Ashkarran, A.; Bayat, A. *Int. Nano Lett.* **2013**, *3*, 50. DOI: <https://doi.org/10.1186/2228-5326-3-50>.
36. Huang, X.; El-Sayed, M. A. *J. Adv. Res.* **2010**, *1*, 13–28. DOI: <https://doi.org/10.1016/j.jare.2010.02.002>.
37. Marciniak, L.; Nowak, M.; Trojanowska, A.; Tylkowski, B.; Jastrzab, R. *Materials.* **2020**, *13*, 1–12. DOI: <https://doi.org/10.3390/ma13235444>.
38. Rawat, V.; Sharma, A.; Bhatt, V.P.; Singh, R.P.; Maurya, I.K. *Mater. Today Proc.* **2020**, *29*, 911–916. DOI: <https://doi.org/10.1016/j.matpr.2020.05.274>.
39. Khan, M.; Tareq, F.; Hossen, M.A.; Roki, M.N.A.M. *J. Eng. Sci. Technol.* **2018**, *13*, 158–166.
40. Pallela, P.N.V.K.; Ummey, S.; Ruddaraju, L.K.; Pammi, S.V.N.; Yoon, S.G. *Microb. Pathog.* **2018**, *124*, 63–69. DOI: <https://doi.org/10.1016/j.micpath.2018.08.026>.
41. Amaliyah, S.; Sabarudin, A.; Masruri, M.; Sumitro, S.B. *Appl. Pharm. Sci.* **2022**, *12*, 103–114. DOI: <https://doi.org/10.7324/JAPS.2022.120311>.



42. Otunola, G.; Afolayan, A.; Ajayi, E.; Odeyemi, S. *Pharmacogn. Mag.* **2017**, *13*, 201. DOI: [https://doi.org/10.4103/pm.pm\\_430\\_16](https://doi.org/10.4103/pm.pm_430_16).
43. Black, C.; Haughey, S. A.; Chevallier, O. P.; Galvin-King, P.; Elliott, C. T. *Food Chem.* **2016**, *210*, 551–557. DOI: <https://doi.org/10.1016/j.foodchem.2016.05.004>.
44. Barbieri, N.; Sanchez-Contreras, A.; Canto, A.; Cauich-Rodriguez, J. V.; Vargas-Coronado, R.; Calvo-Irabien, L. M. *Ind. Crops Prod.* **2018**, *121*, 114–123. DOI: <https://doi.org/10.1016/j.indcrop.2018.04.081>.
45. Li, R.; Chen, Z.; Ren, N.; Wang, Y.; Wang, Y.; Yu, F. *J. Photochem. Photobiol. B: Biol.* **2019**, *199*, 111593. DOI: <https://doi.org/10.1016/j.jphotobiol.2019.111593>.
46. Zhang, X.; Gao, C.; Lü, S.; Duan, H.; Jing, N.; Dong, D.; Shi, C.; Liu, M. *J. Mater. Chem. B*, **2014**, *2*, 5452–5460. DOI: <https://doi.org/10.1039/c4tb00905c>.
47. Nersisyan, H. H.; Lee, Y. J.; Joo, S. H.; Han, S. K.; Lee, T. H.; Lee, J. S.; An, Y. S.; Lee, J. H. *Cryst. Eng. Comm.* **2015**, *17*, 7535–7542. DOI: <https://doi.org/10.1039/c5ce01367d>.
48. Carbone, K.; Paliotta, M.; Micheli, L.; Mazzuca, C.; Cacciotti, I.; Nocente, F.; Ciampa, A.; Dell'Abate, M. T. *Arab. J. Chem.* **2019**, *12*, 597–609. DOI: <https://doi.org/10.1016/j.arabjc.2018.08.001>.
49. Vimbela, G. V.; Ngo, S. M.; Frazee, C.; Yang, L.; Stout, D. A. *Int. J. Nanomed.* **2017**, *12*, 3941–3965. DOI: <https://doi.org/10.2147/IJN.S134526>.
50. Ruíz-Baltazar, Á. D. J.; Reyes-lópez, S. Y.; Larrañaga, D.; Estévez, M.; Pérez, R. *Results Phys.* **2017**, *7*, 2639–2643. DOI: <https://doi.org/10.1016/j.rinp.2017.07.044>.
51. Abbaszadegan, A.; Ghahramani, Y.; Gholami, A.; Hemmateenejad, B.; Dorostkar, S.; Nabavizadeh, M.; Sharghi, H. *J. Nanomater.* **2015**, *1*. DOI: <https://doi.org/10.1155/2015/720654>.
52. Arana-Sánchez, A.; Estarrón-Espinosa, M.; Obledo-Vázquez, E. N.; Padilla-Camberos, E.; Silva-Vázquez, R.; Lugo-Cervantes, E. *Lett. Appl. Microbiol.* **2010**, *50*, 585–590. DOI: <https://doi.org/10.1111/j.1472-765X.2010.02837.x>.
53. Rueda, E.; Juvera, J.; Romo, I.; Holguín, R. *Rev. Mexicana Cienc. Agri.* **2018**, *20*, 4251–4261.

## Chemical Constituents, Antimicrobial Activity and Nitric Oxide Production Inhibitory Activity of Essential Oil from the Leaves of *Croton kongensis* Gagnep. Collected from Two Different Locations in Vietnam

Le D. Chac<sup>1,\*</sup>, Hoang V. Chinh<sup>1</sup>, Nguyen T. M. Hong<sup>2</sup>, Bui B. Think<sup>1,3\*</sup>

<sup>1</sup>Faculty of Natural Sciences, Hong Duc University, Thanh Hoa, 40130, Vietnam.

<sup>2</sup>Faculty of Agriculture Forestry and Fisheries, Hong Duc University, Thanh Hoa, 40130, Vietnam.

<sup>3</sup>Cracow University of Technology, Warszawska 24, 31-155 Cracow, Poland.

\*Corresponding author: Le D. Chac, email: [ledinhchac@hdu.edu.vn](mailto:ledinhchac@hdu.edu.vn); Bui B. Think, email: [buibaothinh9595@gmail.com](mailto:buibaothinh9595@gmail.com)

Received May 14<sup>th</sup>, 2023; Accepted June 25<sup>th</sup>, 2023.

DOI: <http://dx.doi.org/10.29356/jmcs.v68i3.2065>

**Abstract.** In this study, essential oil from the leaves of *Croton kongensis* Gagnep. from two different locations in Thanh Hoa province, Vietnam, were obtained by hydrodistillation in a Clevenger-type apparatus and characterized by GC/MS analyses. The Nhu Xuan essential oil sample contained sabinene (52.17 %), (*E*)-caryophyllene (7.23 %), and linalool (6.33 %) as major components, while the Thuong Xuan essential oil sample contained sabinene (12.96 %), camphene (9.45 %), linalool (8.43 %), bornyl acetate (7.99 %), (*E*)-nerolidol (7.07 %), and (*E*)-caryophyllene (6.53 %). Both essential oil samples showed promising antimicrobial activity against four bacterial and four fungal strains using the broth microdilution method, with minimum inhibitory concentrations (MICs)  $\leq$  200  $\mu\text{g/mL}$ . However, the Thuong Xuan essential oil sample exhibited a broader spectrum of antimicrobial activity than the Nhu Xuan essential oil sample. Furthermore, the anti-inflammatory potential study showed that the Thuong Xuan essential oil sample exhibited better inhibition of nitric oxide production induced by lipopolysaccharide in RAW 264.7 cells than the Nhu Xuan essential oil sample, which has IC<sub>50</sub> values of 97.32 and 172.67  $\mu\text{g/mL}$ , respectively. These findings provide a theoretical foundation for further investigation and use of the essential oil from *C. kongensis* leaves in the pharmaceutical and food industries.

**Keywords:** *Croton kongensis*; anti-inflammatory; antimicrobial; chemical composition; volatile oils.

**Resumen.** En este estudio, el aceite esencial de las hojas de dos poblaciones de *Croton kongensis* Gagnep. colectadas en la provincia Thanh Hoa en Vietnam, fue obtenido por hidrodestilación mediante un aparato Clevenger, y las muestras fueron caracterizadas mediante el análisis de CG/EM. La muestra del aceite esencial proveniente de Nhu Xuan contenía sabineno (52.17%), (*E*)-cariofileno (7.23%), y linalool (6.33%) como constituyentes mayoritarios, mientras que la muestra proveniente de Thuong Xuan contenía sabineno (12.96%), canfeno (9.45%), linalool (8.43%), acetato de bornilo (7.99%), (*E*)-nerolidol (7.07%), y (*E*)-cariofileno (6.53%). Ambas muestras mostraron actividad antimicrobiana promisorio contra cuatro cepas bacterianas y cuatro cepas fúngicas, usando el método de microdilución del caldo, obteniendo concentraciones mínimas inhibitorias (MICs)  $\leq$  200  $\mu\text{g/mL}$ , respectivamente. No obstante, el aceite esencial proveniente de Thuong Xuan mostró un espectro más amplio de actividad antimicrobiana con respecto a la muestra de Nhu Xuan. Además, el estudio del potencial anti-inflamatorio de los aceites esenciales indicó que la muestra de Thuong Xuan exhibió mejor inhibición de la producción de óxido nítrico inducida por lipopolisacáridos en células RAW264.7, con respecto a la muestra de Nhu Xuan, con valores de CI<sub>50</sub> de 97.32 y 172.67, respectivamente. Estos hallazgos proporcionan un argumento teórico para investigaciones adicionales y para el uso del aceite esencial de las hojas de *C. kongensis* en las industrias farmacéutica y de alimentos.

**Palabras clave:** *Croton kongensis*; anti-inflamatorios; antimicrobianos; composición química; aceites volátiles.

## Introduction

The rise of antimicrobial resistance has generated a huge concern in the health system in recent decades [1]. This is a phenomenon in which microorganisms, such as bacteria, viruses, fungi, and parasites, evolve to become resistant to antimicrobial drugs. This has increased the risk of treatment failure, prolonged illness, and the spread of infections [1]. Furthermore, steroidal, and non-steroidal anti-inflammatory drugs are commonly used to treat inflammatory diseases, but they also have side effects and limitations [2]. Non-steroidal anti-inflammatory drugs can cause digestive problems, kidney damage, and increased risk of heart disease, while long-term use of steroids can result in osteoporosis, diabetes, and immunosuppression. Additionally, some inflammatory conditions can become resistant to these drugs over time, reducing their efficacy. In this context, essential oils, with their low toxicity and potential antimicrobial and anti-inflammatory properties as well as accompanied by reduced side effects, have attracted renewed attention as an alternative to conventional antimicrobial and anti-inflammatory drugs [3,4].

*Croton* L. is a genus of plants in the Euphorbiaceae family, with about 1300 species distributed in tropical and subtropical regions [5]. The plants are known for their bright and diversely coloured leaves and their use in traditional medicine to treat various ailments such as stomachache, abscesses, sore throat, and malaria [6,7]. *Croton* species have been found to contain phytochemicals such as diterpenes, triterpenes, sesquiterpenes, alkaloids, and flavonoids, which are thought to contribute to their medicinal properties [8-11]. Some *Croton* species have been found to possess anti-inflammatory, antimicrobial, antimalarial, anticancer, and antioxidant activities [8-11].

*Croton kongensis* Gagnep. (Synonym: *Croton tonkinensis* Gagnep.) is a species of plant in the genus *Croton*, native to China [12,13]. It is known for its medicinal properties and has been traditionally used for various purposes, including the treatment of skin conditions, diarrhea, stomach aches, and dysmenorrhoea [14, 15]. In terms of pharmacology, various parts of *C. kongensis* have been studied for their biological activities and potential medicinal properties. For example, the leaves and stems of *C. kongensis* have been found to possess antimicrobial and antimalarial activities [13,16]. The plant is also a rich source of diterpenoids, which are known to promote various beneficial biological activities [16-21]. Moreover, the authors have acknowledged the existence of two previously published studies on the chemical compositions of essential oils derived from *C. kongensis* [22,23]. The results of these studies demonstrated that the primary compounds found in the essential oil of *C. kongensis* were  $\beta$ -caryophyllene (10.1 %),  $\beta$ -bisabolene (9.6 %), bicycloelemene (8.0%), linalool (7.8 %),  $\alpha$ -humulene (7.1 %), and  $\beta$ -sesquiphellandrene (6.9 %) in the leaves [22], as well as benzyl benzoate (12.7 %),  $\beta$ -selinene (9.8 %), bulnesol (8.0 %) and 5,6,7,8-tetrahydroquinoxaline (7.4 %) in the stems [23]. In addition, the chemical constituents and biological properties of essential oils extracted from other species of *Croton* have been extensively investigated [24-34]. Nevertheless, it is worth noting that the information available on the antimicrobial and anti-inflammatory activities of *C. kongensis* essential oil is limited, and the qualitative and quantitative profiles of essential oils can be affected by environmental factors, as evidenced by previous studies [35-37]. As a result, this current research aims to explore the chemical constituents, antimicrobial activity, and nitric oxide (NO) production inhibitory activity of essential oil obtained from *C. kongensis* leaves collected from two distinct regions in Thanh Hoa province, Vietnam, namely Nhu Xuan and Thuong Xuan.

## Materials and methods

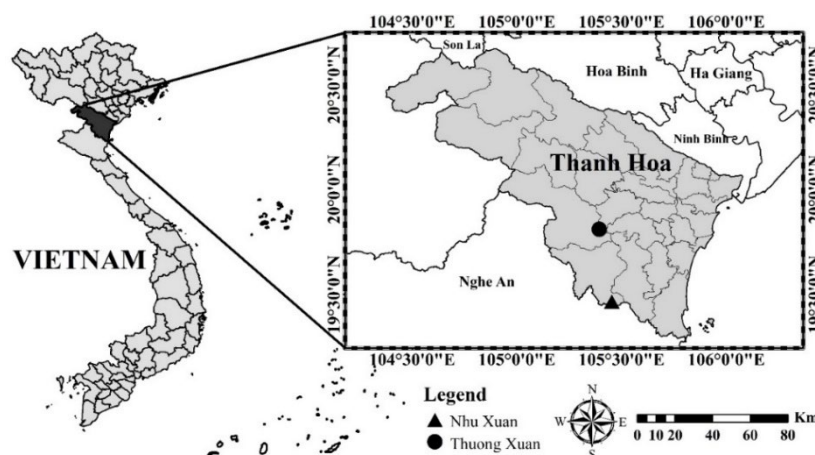
### Plant material

The Fresh leaves of *Croton kongensis* growing wild in Nhu Xuan (sample 1) and Thuong Xuan (sample 2) of Thanh Hoa province, Vietnam were randomly collected in February 2022 (Table 1 and Fig. 1). Geographic positions (latitude and longitude), altitude, locations, and key meteorological data (total rainfall, average minimum and maximum temperatures) of each collection site are presented in Table 1. The voucher specimens, NXTH-2022 for the Nhu Xuan sample and TXTH-2022 for the Thuong Xuan sample were identified by Dr. Le Dinh Chac, from Hong Duc University, Vietnam, and deposited in the herbarium of that university.



**Table 1.** Geographic positions and climatic data of the locations.

| Site N° | Localities             | Latitude     | Longitude     | Altitude (m) | Temperature (°C) |      | Rainfall (mm) |
|---------|------------------------|--------------|---------------|--------------|------------------|------|---------------|
|         |                        |              |               |              | Max.             | Min. |               |
| 1       | Nhu Xuan, Thanh Hoa    | 19°27'56.4"N | 105°27'10.5"E | 165          | 33.0             | 13.0 | 1095.7        |
| 2       | Thuong Xuan, Thanh Hoa | 19°48'36.2"N | 105°23'35.0"E | 47           | 35.0             | 13.0 | 1054.5        |

**Fig. 1.** Collection site of *Croton kongensis* from two different locations in Thanh Hoa province, Vietnam. (▲) Nhu Xuan; (●) Thuong Xuan.

### Extraction of the essential oil

The leaves of *C. kongensis* were prepared for essential oil extraction by cutting them into small pieces and subjecting them to hydrodistillation using a Clevenger-type apparatus. The extraction process was carried out for a duration of 4 h, following the methodology recommended by the Vietnamese Pharmacopoeia [38], and as described in earlier publications [39,40]. The experiments were conducted in triplicate. The resulting essential oils were then dried using anhydrous sodium sulfate, filtered, and stored at 4 °C until they were ready for testing and analysis.

### Gas chromatography/mass spectrometry (GC/MS)

The GC/MS analysis was conducted to identify the chemical components of the essential oil samples obtained from the leaves of *C. kongensis*. The analysis was performed using an Agilent 7890A gas chromatograph, which was coupled with a 5975C Mass Spectrometer detector and equipped with a DB-XLB capillary column (60 m x 0.25 mm i.d., 0.25 μm film thickness). Helium was used as the carrier gas, with a flow rate of 1.0 mL/min. A volume of 1.0 μL of essential oil was injected into the column, with a split ratio of 100:1. The column temperature was maintained at 40 °C for 1 min, followed by a gradual increase to 270 °C at a rate of 4 °C/min, and held at 270 °C for 5 min. The inlet and ion source temperatures were set at 250 °C and 230 °C, respectively. The ionization voltage applied was 70 electron volts (eV), and the mass range was set between 35 and 450 atomic mass units (amu). Identification of the constituents was performed on the basis of their retention time, Kovats retention indices (relative to C<sub>7</sub>–C<sub>30</sub> n-alkanes, under the same experimental conditions), and computer matching with the NIST Mass Spectral Database for GC-MS as well as comparisons of their mass spectra with those of authentic samples or with data already available in the literature [41,42]. The quantitative analysis was performed by integrating the peak areas.

### Antimicrobial assay

The antimicrobial activity of essential oil samples from *C. kongensis* leaves was evaluated against eight microorganisms obtained from the American Type Culture Collection (ATCC, Manassas, USA). These included two Gram-positive bacteria (*Bacillus subtilis* ATCC 6633 and *Staphylococcus aureus* ATCC 6538), two Gram-negative bacteria (*Escherichia coli* ATCC 8739 and *Pseudomonas aeruginosa* ATCC 9027), two filamentous fungi (*Aspergillus niger* ATCC 9763 and *Fusarium oxysporum* ATCC 48112), and two yeasts (*Candida albicans* ATCC 10231 and *Saccharomyces cerevisiae* ATCC 16404). The broth microdilution method with minor modifications to a previous protocol was used to determine the minimum inhibitory concentration (MIC) of the tested oil samples [43,44]. The microorganisms were grown on Tryptic Soy Agar (TSA) and Sabouraud Dextrose Agar (SDA) for bacteria and fungi, respectively. The essential oil samples, dissolved in 10 % dimethylsulfoxide (DMSO), were added to 96-well microtiter plates in concentrations ranging from 200 to 12.5 µg/mL. The microorganisms were inoculated into each well at a concentration of  $150 \times 10^6$  CFU/mL, and the plates were incubated at 37 °C for 24 h for bacteria and 48 h at 30 °C for fungi. The lowest concentration of essential oil that inhibited the visible growth of a microorganism after overnight incubation was defined as the MIC [44]. All the tests were repeated in triplicate. Streptomycin, tetracycline, and nystatin were used as positive controls for Gram-positive bacteria, Gram-negative bacteria, and fungi, respectively, while NaCl 0.9 % was used as a negative control.

### Nitric oxide production inhibitory assay

The NO inhibitory activity assay was used to evaluate the anti-inflammatory potential of essential oil samples extracted from *C. kongensis* leaves, as previously described with minor modifications [45]. The assay was conducted on RAW 264.7 macrophage cells that were stimulated with lipopolysaccharide (LPS). The cells were obtained from the American Type Culture Collection (ATCC) and cultured in Dulbecco's Modified Eagle Medium (DMEM) supplemented with 10 % fetal bovine serum (FBS), 100 µg/mL streptomycin, and 100 U/mL penicillin, under 5 % CO<sub>2</sub> at 37 °C for 48 h. The cells were then seeded at a density of  $2.5 \times 10^5$  cells/well in 96-well plates and treated with 1 µg/mL of LPS for 24 h. The quantity of nitrite in the culture medium was measured using the Griess reaction and quantified spectrophotometrically at 570 nm on an Infinite F50 microplate reader (Tecan, Männedorf, Switzerland). All the tests were repeated in triplicate. The 50 % inhibition concentration (IC<sub>50</sub>) was calculated using the program Table Curve Version 4.0.

To determine cell viability, the MTT assay was performed according to the protocol previously described [45]. After cell culture, the supernatants were collected for NO measurement. Next, 100 µL of 0.5 % w/v MTT, dissolved in phosphate buffer saline, was added to each well and incubated for an additional 4 h at 37 °C in a 5 % CO<sub>2</sub> incubator. After incubation, the insoluble formazan product was dissolved in DMSO, and the degree of MTT reduction was measured by analyzing the absorbance at 540 nm on an Infinite F50 microplate reader (Tecan, Männedorf, Switzerland). All the tests were repeated in triplicate.

### Statistical analysis

The experiments were conducted in triplicate, and their mean value was calculated. The results were presented as mean ± standard deviation, which was calculated using Microsoft Office Excel 2010. Statistical analysis was performed by Student's t-test. Differences were considered significant at  $p \leq 0.05$ .

## Results and discussion

### Chemical composition of the essential oil

Hydrodistillation of the leaves of *C. kongensis* collected from the two different locations yielded  $0.13 \% \pm 0.01$  and  $0.15 \% \pm 0.01$  pale yellowish oils for Nhu Xuan (sample 1) and Thuong Xuan (sample 2), respectively. Both essential oil samples from the leaves of *C. kongensis* were analyzed by GC/MS. The compositions of two samples of *C. kongensis* are displayed in Table 2, where constituents are listed in order of their elution on the DB-XLB column. A total of 54 components were detected, 42 and 50 of which were identified, accounting for 99.60 % and 97.55 % of the oil of Nhu Xuan and Thuong Xuan samples, respectively.

As can be seen from Table 2, the essential oil sample of Nhu Xuan was characterized by significantly larger amounts of monoterpenes (69.29 %) than sesquiterpenes (27.31 %), while the Thuong Xuan oil sample had a less different content of monoterpenes (54.79 %) and sesquiterpenes (38.42 %). The main composition of the oil of Nhu Xuan was characterized by its high content of sabinene (52.17 %). (*E*)-Caryophyllene and linalool were also found to be abundant in the Nhu Xuan oil sample with 7.23 % and 6.33 %, respectively. In the oil of Thuong Xuan, the most abundant composition was sabinene with 12.96 %, lower than that of the Nhu Xuan sample. Camphene (9.45 %), linalool (8.43 %), bornyl acetate (7.99 %), (*E*)-nerolidol (7.07 %), and (*E*)-caryophyllene (6.53 %) were also found to be abundant in the essential oil of Thuong Xuan. However, most of these compounds occurred in a lower content in the Nhu Xuan oil sample. In addition, our results also demonstrated that the composition was different not only quantitatively but also qualitatively. For instance, geraniol and borneol, which accounted for 0.29 % and 0.43 % of the volatile oil of the Thuong Xuan sample, respectively, were not identified in the Nhu Xuan sample. Two of the identified chemical compounds in the Nhu Xuan sample such as *ar*-curcumene and germacrene D, which accounted for 0.17 % and 0.15 %, respectively, were not detected in the Thuong Xuan sample.

**Table 2.** Chemical compositions of essential oil from the leaves of *Croton kongensis* from two different locations.

| No. | Compound <sup>a</sup>                | RI <sup>b</sup> | RI <sup>c</sup> | Relative peak area (%) |             |
|-----|--------------------------------------|-----------------|-----------------|------------------------|-------------|
|     |                                      |                 |                 | Nhu Xuan               | Thuong Xuan |
| 1.  | Tricyclene                           | 928             | 921             | - <sup>d</sup>         | 0.29        |
| 2.  | $\alpha$ -Thujene                    | 929             | 924             | 0.60                   | 0.36        |
| 3.  | $\alpha$ -Pinene                     | 938             | 932             | 1.50                   | 4.76        |
| 4.  | Camphene                             | 955             | 946             | 0.58                   | 9.45        |
| 5.  | Sabinene                             | 979             | 969             | 52.17                  | 12.96       |
| 6.  | $\beta$ -Pinene                      | 984             | 974             | 0.89                   | 0.38        |
| 7.  | Myrcene                              | 991             | 988             | 0.55                   | 0.23        |
| 8.  | $\alpha$ -Terpinene                  | 1021            | 1014            | 0.67                   | 0.39        |
| 9.  | <i>o</i> -Cymene                     | 1029            | 1022            | 0.11                   | 0.20        |
| 10. | Limonene                             | 1033            | 1024            | 0.41                   | 1.12        |
| 11. | 1,8-Cineole                          | 1037            | 1026            | 2.78                   | 4.09        |
| 12. | 2-Heptyl acetate                     | 1039            | 1038            | 3.00                   | 4.34        |
| 13. | $\gamma$ -Terpinene                  | 1063            | 1054            | 1.08                   | 0.73        |
| 14. | <i>cis</i> -Sabinene hydrate         | 1072            | 1065            | 0.18                   | -           |
| 15. | Terpinolene                          | 1094            | 1086            | 0.29                   | 0.32        |
| 16. | Linalool                             | 1101            | 1095            | 6.33                   | 8.43        |
| 17. | Borneol (= <i>endo</i> -Borneol)     | 1175            | 1173            | -                      | 0.43        |
| 18. | Terpinen-4-ol                        | 1185            | 1174            | 0.63                   | 1.00        |
| 19. | $\alpha$ -Terpineol                  | 1197            | 1186            | 0.25                   | 0.73        |
| 20. | Geraniol                             | 1256            | 1249            | -                      | 0.29        |
| 21. | Linalyl acetate (= Linalool acetate) | 1257            | 1254            | -                      | 0.23        |
| 22. | Bornyl acetate                       | 1294            | 1287            | 0.27                   | 7.99        |

| No. | Compound <sup>a</sup>                                 | RI <sup>b</sup> | RI <sup>c</sup> | Relative peak area (%) |             |
|-----|-------------------------------------------------------|-----------------|-----------------|------------------------|-------------|
|     |                                                       |                 |                 | Nhu Xuan               | Thuong Xuan |
| 23. | Methyl geranate                                       | 1326            | 1320            | -                      | 0.24        |
| 24. | $\delta$ -Elemene                                     | 1348            | 1335            | 0.19                   | 0.15        |
| 25. | $\alpha$ -Terpinyl acetate                            | 1356            | 1346            | -                      | 0.17        |
| 26. | Cyclosativene                                         | 1382            | 1372            | -                      | 0.12        |
| 27. | $\alpha$ -Copaene                                     | 1389            | 1374            | 0.20                   | 0.12        |
| 28. | Daucene                                               | 1392            | 1385            | 0.53                   | 0.60        |
| 29. | Cyperene                                              | 1418            | 1398            | 0.13                   | 0.71        |
| 30. | ( <i>E</i> )-Caryophyllene (= $\beta$ -Caryophyllene) | 1437            | 1417            | 7.23                   | 6.53        |
| 31. | <i>trans</i> - $\alpha$ -Bergamotene                  | 1446            | 1432            | 0.13                   | -           |
| 32. | ( <i>E</i> )- $\beta$ -Farnesene                      | 1465            | 1443            | 0.19                   | 0.17        |
| 33. | $\alpha$ -Humulene                                    | 1471            | 1452            | 2.06                   | 2.27        |
| 34. | 9- <i>epi</i> -( <i>E</i> )-Caryophyllene             | 1479            | 1464            | 0.62                   | 0.47        |
| 35. | $\gamma$ -Curcumene                                   | 1488            | 1470            | 0.33                   | 0.19        |
| 36. | $\gamma$ -Muuroolene                                  | 1490            | 1476            | -                      | 0.16        |
| 37. | <i>ar</i> -Curcumene                                  | 1491            | 1482            | 0.17                   | -           |
| 38. | Germacrene D                                          | 1498            | 1484            | 0.15                   | -           |
| 39. | <i>trans</i> -Muurolo-4(14),5-diene                   | 1511            | 1498            | -                      | 0.35        |
| 40. | Bicyclogermacrene                                     | 1514            | 1500            | 5.11                   | 4.38        |
| 41. | $\beta$ -Bisabolene                                   | 1517            | 1507            | 1.69                   | 2.82        |
| 42. | $\beta$ -Sesquiphellandrene                           | 1534            | 1526            | 2.60                   | 2.37        |
| 43. | $\delta$ -Cadinene                                    | 1537            | 1528            | 0.23                   | 0.30        |
| 44. | <i>trans</i> -Dauca-4(11),8-diene                     | 1547            | 1534            | 0.46                   | 0.79        |
| 45. | ( <i>E</i> )-Nerolidol                                | 1569            | 1561            | 3.50                   | 7.07        |
| 46. | 4 $\alpha$ -Hydroxygermacra-1(10),5-diene             | 1593            | 1575            | 0.23                   | 0.42        |
| 47. | Spathulenol                                           | 1597            | 1577            | 0.43                   | 1.51        |
| 48. | Caryophyllene oxide                                   | 1605            | 1582            | 0.43                   | 2.73        |
| 49. | Humulene epoxide I                                    | 1620            | 1600            | -                      | 0.18        |
| 50. | Ledol                                                 | 1625            | 1602            | 0.23                   | 0.66        |
| 51. | Humulene epoxide II                                   | 1632            | 1608            | -                      | 1.07        |
| 52. | <i>epi</i> - $\alpha$ -Cadinol (= $\tau$ -Cadinol)    | 1658            | 1638            | 0.31                   | 1.28        |
| 53. | $\alpha$ -Cadinol                                     | 1672            | 1652            | 0.16                   | 0.75        |
| 54. | ( <i>E,E</i> )-Farnesol                               | 1728            | 1719            | -                      | 0.25        |

| No. | Compound <sup>a</sup>             | RI <sup>b</sup> | RI <sup>c</sup> | Relative peak area (%) |              |
|-----|-----------------------------------|-----------------|-----------------|------------------------|--------------|
|     |                                   |                 |                 | Nhu Xuan               | Thuong Xuan  |
|     | <b>Monoterpene hydrocarbons</b>   |                 |                 | <b>58.85</b>           | <b>31.19</b> |
|     | <b>Oxygenated monoterpenes</b>    |                 |                 | <b>10.44</b>           | <b>23.60</b> |
|     | <b>Sesquiterpene hydrocarbons</b> |                 |                 | <b>22.02</b>           | <b>22.50</b> |
|     | <b>Oxygenated sesquiterpenes</b>  |                 |                 | <b>5.29</b>            | <b>15.92</b> |
|     | <b>Others</b>                     |                 |                 | <b>3.00</b>            | <b>4.34</b>  |
|     | <b>Total identified</b>           |                 |                 | <b>99.60</b>           | <b>97.55</b> |

Note: <sup>a</sup>Elution order on the DB-XLB column; <sup>b</sup>Calculated Kovats retention index on the DB-XLB column; <sup>c</sup>Literature retention index; <sup>d</sup>not detected.

It is noteworthy that two prior studies have been conducted to investigate the composition of essential oil from *C. kongensis*. Dai *et al.* [22] reported the major components of essential oil from *C. kongensis* leaves as  $\beta$ -caryophyllene (10.1 %),  $\beta$ -bisabolene (9.6 %), bicycloelemene (8.0 %), linalool (7.8 %),  $\alpha$ -humulene (7.1 %), and  $\beta$ -sesquiphellandrene (6.9 %). Apparently, both samples of essential oil from *C. kongensis* leaves obtained in the present study presented discrepancies when compared with data reported by Dai *et al.* [22]. Indeed, although bicycloelemene was one of the main components in Dai *et al.*'s study, this component was not detected in both oil samples of the present study. In addition, sabinene was found in high amounts in both oil samples of the present study (Table 2), while this component was in lower amounts in Dai *et al.*'s study [22]. Furthermore, the components in both oil samples of this study were significantly different from the essential oil of *C. kongensis* stems reported by Chau *et al.* [23]. Chau *et al.* [23] found that the major compounds in the essential oil of *C. kongensis* stems were benzyl benzoate (12.7 %),  $\beta$ -selinene (9.8 %), bulnesol (8.0 %), and 5,6,7,8-tetrahydroquinoxaline (7.4 %). Therefore, the essential oil composition of *C. kongensis* may vary depending on the part of the plant studied and environmental conditions.

Although there is little information available specifically about *C. kongensis*, there have been many studies on the essential oil compositions of other *Croton* species, particularly their leaves. For instance, previous studies have found that the major constituents of leaf essential oil from *C. cajucara* were linalool (41.2 %), (*E*)-nerolidol (12.6 %), and  $\beta$ -caryophyllene (6.9 %) [26], whereas in *C. matourensis*,  $\beta$ -caryophyllene was the most abundant compound [28]. Phenylpropanoid compounds were the main components of leaf essential oil of *C. grewoides*, which consisted mainly of (*E*)-anethole (65.5 %), eugenol (10.6 %), and (*E*)-methyl isoeugenol (4.7 %) [31]. In a study on *C. campestris*, caryophyllene oxide (29.9 %) and humulene oxide II (8.0 %) were the major components in leaf essential oil [34]. These findings indicate that the chemical variability of essential oils from *Croton* leaves depends largely on the species being studied.

The observed differences in essential oil compositions may be attributed to various factors, such as environmental conditions, genetic factors, season and harvest period, and other factors [37,46,47]. Additionally, there have been studies investigating the variation in essential oil compositions of *Croton* species collected from different locations. For instance, GC-MS analysis showed significant differences in essential oil compositions of *C. rhamnifolioides* samples collected from three different locations in the semi-arid region of the state of Pernambuco, Brazil [36]. Similarly, essential oil compositions extracted from leaves of *C. jimenezii* collected from two locations in Costa Rica were found to vary significantly [35]. These findings support our results that environmental factors are important contributors to the variation in chemical components of essential oil from *C. kongensis* leaves across different geographical locations.

### Antimicrobial activity

The present study tested the antimicrobial activity of essential oil extracted from *C. kongensis* leaves collected from two different locations. The findings are outlined in Table 3 using the broth microdilution method, which analyzed eight microorganisms. The essential oil from Nhu Xuan demonstrated inhibitory

effects against *S. aureus*, *A. niger*, *C. albicans*, and *S. cerevisiae* with a MIC of 200 µg/mL. However, it did not suppress the growth of *B. subtilis*, *E. coli*, *P. aeruginosa*, and *F. oxysporum*. On the other hand, the essential oil sample from Thuong Xuan showed antimicrobial activity against almost all the tested microorganisms, except *F. oxysporum*. The most significant antimicrobial activity was observed in the essential oil sample from Thuong Xuan against *C. albicans* with a MIC of 150 µg/mL. In addition, the essential oil sample from Thuong Xuan inhibited the growth of *B. subtilis*, *S. aureus*, *E. coli*, *P. aeruginosa*, *A. niger*, and *S. cerevisiae* with a MIC of 200 µg/mL. Therefore, it can be concluded that the essential oil sample from Thuong Xuan demonstrated more effective antimicrobial activity than that from Nhu Xuan. This variance in activity could be due to the presence of distinct chemical compounds or differences in predominant compounds in the essential oils [46,47]. These research results align with prior studies examining the antimicrobial properties of essential oils from *Croton* plants, which selectively inhibited the growth of various microorganisms [29,30,33,34]. It is crucial to note that natural products with MIC values below 500 µg/mL are considered potent inhibitors, those with MIC values ranging from 600 to 1500 µg/mL are considered moderate inhibitors, and those with MIC values above 1600 µg/mL are considered weak inhibitors [48,49]. Based on these guidelines, both essential oils from *C. kongensis* leaves demonstrated potent antimicrobial activity and may represent a promising new source of antimicrobial agents.

**Table 3.** Antimicrobial activity of essential oil from the leaves of *Croton kongensis* from two different locations.

| Microorganisms                  | MIC           |             |              |              |          |
|---------------------------------|---------------|-------------|--------------|--------------|----------|
|                                 | Essential oil |             | Streptomycin | Tetracycline | Nystatin |
|                                 | Nhu Xuan      | Thuong Xuan |              |              |          |
| <i>Bacillus subtilis</i>        | ND            | 200         | 6.25         | NA           | NA       |
| <i>Staphylococcus aureus</i>    | 200           | 200         | 6.25         | NA           | NA       |
| <i>Escherichia coli</i>         | ND            | 200         | NA           | 6.25         | NA       |
| <i>Pseudomonas aeruginosa</i>   | ND            | 200         | NA           | 12.5         | NA       |
| <i>Aspergillus niger</i>        | 200           | 200         | NA           | NA           | 12.5     |
| <i>Fusarium oxysporum</i>       | ND            | ND          | NA           | NA           | 25.0     |
| <i>Candida albicans</i>         | 200           | 150         | NA           | NA           | 6.25     |
| <i>Saccharomyces cerevisiae</i> | 200           | 200         | NA           | NA           | 12.5     |

Note: MIC: minimum inhibitory concentration (µg/mL); ND: not determined; NA: not applicable.

The antimicrobial activity of both essential oil samples could be attributed to their chemical composition. Indeed, several investigations have shown that sabinene, linalool, and (*E*)-caryophyllene were major components in both essential oils with broadly antimicrobial [50-52]. Camphene, bornyl acetate, and (*E*)-nerolidol were abundant components in the essential oil sample of Thuong Xuan also known for their well-known antimicrobial properties [53-55]. However, the antimicrobial activity of essential oils may also be due to an additive or synergistic effect of the major constituents with the minor components [47,56]. This means that the overall activity of the oil is likely the result of a combination of compounds rather than a single compound. Therefore, minor components in two essential oil samples such as  $\alpha$ -pinene, 1,8-cineole,  $\alpha$ -humulene, and bicyclogermacrene, can be other possible factors affecting this antimicrobial activity [57-60]. These compounds can interact with the microorganism cell membrane and alter its permeability, leading to the leakage of cell contents and the death of the microorganism [61].

In general, the mechanism of action of essential oils against microorganisms is difficult to describe due to the complexity of their composition. However, one of the advantages of using essential oils is that the wide variety of chemical compounds present in the oil can interact with different targets in the microorganism and inhibit its growth and survival [61,62]. This multi-target effect can make it more difficult for the microorganism to develop resistance, as it would need to evolve multiple resistance mechanisms at the same time [61]. Therefore, using essential oils may be a way to decrease the likelihood of microorganism resistance.

### Nitric oxide production inhibitory activity

Innate immune cells produce NO, a molecule that can be potentially harmful [63]. Immune cells such as macrophages release NO as part of the inflammatory response when the body experiences infection or injury. This NO can damage surrounding tissue, leading to chronic inflammation [64]. The measurement of NO production in response to stimuli, like LPS, in cells such as macrophages can help evaluate the anti-inflammatory effects of plant extracts. A reduction in NO production would indicate an anti-inflammatory effect.

In this study, the essential oil extracted from *C. kongensis* leaves collected from two locations was evaluated for its ability to inhibit NO production in LPS-stimulated RAW 264.7 macrophage cells. Both essential oil samples were effective in inhibiting NO production at all tested concentrations (25, 50, 100, and 200  $\mu\text{g/mL}$ ), as shown in Table 4. The 200  $\mu\text{g/mL}$  concentration of Nhu Xuan and Thuong Xuan oil samples was found to inhibit NO production by 56.76 % and 78.51 %, respectively. Furthermore, the inhibition by both essential oil samples was found to be dose dependent. The  $\text{IC}_{50}$  values of Nhu Xuan and Thuong Xuan oil samples were 172.67 and 97.32  $\mu\text{g/mL}$ , respectively. The MTT assay revealed that concentrations up to 100  $\mu\text{g/mL}$  did not decrease the cell viability of RAW 264.7 cells treated with essential oils. Additionally, essential oil treatments with concentrations below 100  $\mu\text{g/mL}$  were found to slightly increase the number of RAW 264.7 cells. However, when the concentration of both essential oil samples was increased to 200  $\mu\text{g/mL}$ , the viability of RAW 264.7 cells decreased slightly. These results suggest that the Thuong Xuan essential oil sample exhibited a greater inhibitory effect on NO production in LPS-stimulated RAW 264.7 macrophages than the Nhu Xuan sample. The varying chemical compositions of the two essential oil samples may account for their different effects on NO production in LPS-stimulated RAW 264.7 macrophages. Each essential oil sample may have a unique combination of chemical compounds in its essential oil, which could have different abilities to interact with cellular signaling pathways involved in NO production [64]. Furthermore, the different concentrations of the same compounds in the essential oils of both samples could also contribute to the observed differences in NO inhibition.

**Table 4.** Inhibitory effects of essential oil of *Croton kongensis* leaves from two different locations on nitric oxide (NO) production and cell viability in LPS-stimulated RAW 264.7 macrophage cells.

| Concentration<br>( $\mu\text{g/mL}$ ) | Nhu Xuan         |                   | Thuong Xuan      |                   |
|---------------------------------------|------------------|-------------------|------------------|-------------------|
|                                       | % Inhibition NO  | % Cell viability  | % Inhibition NO  | % Cell viability  |
| 200                                   | 56.76 $\pm$ 0.98 | 87.05 $\pm$ 0.74  | 78.51 $\pm$ 0.61 | 86.74 $\pm$ 0.14  |
| 100                                   | 31.81 $\pm$ 0.73 | 101.95 $\pm$ 1.36 | 51.79 $\pm$ 0.53 | 99.64 $\pm$ 0.18  |
| 50                                    | 16.34 $\pm$ 1.04 | 103.75 $\pm$ 0.61 | 42.74 $\pm$ 0.72 | 105.17 $\pm$ 0.09 |
| 25                                    | 8.76 $\pm$ 0.83  | 115.66 $\pm$ 0.32 | 22.79 $\pm$ 0.68 | 106.13 $\pm$ 0.05 |

Note: Values are expressed as mean  $\pm$  standard deviation (SD) (n = 3).

Overall, the inhibitory effects of two essential oil samples on NO production in LPS-stimulated RAW 264.7 macrophage cells could be explained by the presence of their abundant components such as sabinene, linalool, camphene, bornyl acetate, (*E*)-nerolidol, and (*E*)-caryophyllene. These compounds have been studied for their potential anti-inflammatory effects, including the inhibition of NO production in LPS-stimulated RAW

264.7 macrophages [64-67]. Sabinene has been shown to may inhibit the activity of inducible nitric oxide synthase (iNOS), the enzyme responsible for the production of NO in macrophages, by blocking the phosphorylation of iNOS [68,69]. Camphene and (*E*)-nerolidol may inhibit the activity of iNOS by decreasing the expression of the iNOS gene [70,71]. Furthermore, linalool, bornyl acetate, and (*E*)-caryophyllene may inhibit the activity of iNOS and the expression of pro-inflammatory cytokines such as TNF- $\alpha$  and IL-1 $\beta$  which are involved in the production of NO [64-67]. In addition, (*E*)-caryophyllene can also act as a selective activator of the Peroxisome Proliferator-Activated Receptor (PPAR- $\gamma$ ) which regulates the production of pro-inflammatory cytokines and the expression of iNOS [67]. However, we also hypothesize that the reduction of NO production by the two essential oil samples could be due to the effect of the minor components present in the essential oil as well as a synergism between the major and minor components [64,68].

## Conclusions

In conclusion, both essential oil samples from the leaves of *C. kongensis* examined in the current study had different chemical compositions. The main compounds in the essential oil sample of Nhu Xuan were sabinene (52.17 %), (*E*)-caryophyllene (7.23 %), and linalool (6.33 %), while sabinene (12.96 %), camphene (9.45 %), linalool (8.43 %), bornyl acetate (7.99 %), (*E*)-nerolidol (7.07 %), and (*E*)-caryophyllene (6.53 %) were the main constituents in the essential oil sample of Thuong Xuan. Furthermore, the antimicrobial activity and production inhibitory activity of both essential oil samples were examined. The test results showed that the essential oil sample of Thuong Xuan had better antimicrobial and production inhibitory activities than the Nhu Xuan sample. These differences could be explained by different environmental parameters such as climatic conditions.

## References

1. Abushaheen, M. A.; Fatani, A. J.; Alosaimi, M.; Mansy, W.; George, M.; Acharya, S.; Rathod, S.; Divakar, D. D.; Jhugroo, C.; Vellappally, S.; Khan, A. A.; Shaik, J.; Jhugroo, P. *Dis. Mon.* **2020**, *66*, 100971. DOI: <https://doi.org/10.1016/j.disamonth.2020.100971>.
2. Xiao, S.; Yu, H.; Xie, Y.; Guo, Y.; Fan, J.; Yao, W. *J. Ethnopharmacol.* **2021**, *267*, 113516. DOI: <https://doi.org/10.1016/j.jep.2020.113516>.
3. Bakkali, F.; Averbeck, S.; Averbeck, D.; Idaomar, M. *Food Chem. Toxicol.* **2008**, *46*, 446-475. DOI: <https://doi.org/10.1016/j.fct.2007.09.106>.
4. Thin, D. B.; Thinh, B. B.; Igoli, J. O. *Chem. Nat. Compd.* **2023**, *59*, 584-586. DOI: <https://doi.org/10.1007/s10600-023-04061-0>.
5. Webster, G. L. *Ann. Mo. Bot. Gard.* **1994**, *81*, 3-32. DOI: <https://doi.org/10.2307/2399908>.
6. Barrera, C. A. C.; Gómez, D. C.; Castiblanco, F. A. *Rev. Cuba Plantas Med.* **2016**, *21*, 234-247.
7. Salatino, A.; Salatino, M. L. F.; Negri, G. *J. Braz. Chem. Soc.* **2007**, *18*, 11-33. DOI: <https://doi.org/10.1590/S0103-50532007000100002>.
8. Xu, W. H.; Liu, W. Y.; Liang, Q. *Molecules.* **2018**, *23*, 2333. DOI: <https://doi.org/10.3390/molecules23092333>.
9. Moremi, M. P.; Makolo, F.; Viljoen, A. M.; Kamatou, G. P. *J. Ethnopharmacol.* **2021**, *280*, 114416. DOI: <https://doi.org/10.1016/j.jep.2021.114416>.
10. Junior, J. I. G.; Ferreira, M. R. A.; de Oliveira, A. M.; Soares, L. A. L. *Res. Soc. Dev.* **2022**, *11*, e57311225306. DOI: <https://doi.org/10.33448/rsd-v11i2.25306>.
11. Bezerra, F. W.; do N Bezerra, P.; de Oliveira, M. S.; da Costa, W. A.; Ferreira, G. C.; de Carvalho, R. N. *Curr. Bioact. Compd.* **2020**, *16*, 383-393. DOI: <https://doi.org/10.2174/1573407215666181122103511>.



12. Shi, S. Q.; Fan, Y. Y.; Xu, C. H.; Ding, J.; Wang, G. W.; Yue, J. M. *J. Asian Nat. Prod. Res.* **2018**, *20*, 920-927. DOI: <https://doi.org/10.1080/10286020.2017.1373100>.
13. Wang, M. J.; Wang, M.; Zhan, X. Q.; Liu, L.; Wu, Q.; An, F. L.; Lu, Y. B.; Guo, L. L.; Zhang, Z. X.; Fei, D. Q. *Fitoterapia.* **2023**, *164*, 105350. DOI: <https://doi.org/10.1016/j.fitote.2022.105350>.
14. Chi, V. V. in: *The Dictionary of Vietnamese Medicinal Plants*. Medical Publishing House, Hanoi, Vietnam, **2012**.
15. Loi, D. T. in: *The Vietnamese Medicinal Plants and Ingredients*. Medical Publishing House, Hanoi, Vietnam, **2012**.
16. Thongtan, J.; Kittakoop, P.; Ruangrunsi, N.; Saenboonrueng, J.; Thebtaranonth, Y. *J. Nat. Prod.* **2003**, *66*, 868-870. DOI: <https://doi.org/10.1021/np030067a>.
17. Fan, Y. Y.; Shi, S. Q.; Deng, G. Z.; Liu, H. C.; Xu, C. H.; Ding, J.; Wang, G. W.; Yue, J. M. *Org. Lett.* **2020**, *22*, 929-933. DOI: <https://doi.org/10.1021/acs.orglett.9b04484>.
18. Chen, W.; Yang, X. D.; Zhao, J. F.; Zhang, H. B.; Li, L. *Helv. Chim. Acta.* **2007**, *90*, 1554-1558. DOI: <https://doi.org/10.1002/hlca.200790162>.
19. Sun, L.; Meng, Z.; Li, Z.; Yang, B.; Wang, Z.; Ding, G.; Xiao, W. *Nat. Prod. Res.* **2014**, *28*, 563-567. DOI: <https://doi.org/10.1080/14786419.2013.867856>.
20. Yang, X.; Chen, W.; Zhao, J.; Yang, L.; Zhang, H.; Li, L. *Biochem. Syst. Ecol.* **2009**, *37*, 237-240. DOI: <https://doi.org/10.1016/j.bse.2009.03.007>.
21. Chen, W.; Yang, X. D.; Zhao, J. F.; Yang, J. H.; Zhang, H. B.; Li, Z. Y.; Li, L. *Helv. Chim. Acta.* **2006**, *89*, 537-541. DOI: <https://doi.org/10.1002/hlca.200690057>.
22. Dai, D. N.; Huong, L. T.; Thang, T. D.; Ogunwande, I. A. *Chem. Nat. Compd.* **2014**, *50*, 155-157. DOI: <https://doi.org/10.1007/s10600-014-0898-8>.
23. Chau, L. T. M.; Thang, T. D.; Diep, L. V.; Tu, N. T.; Ogunwande, I. A. *Am. J. Plant Sci.* **2014**, *5*, 43926. DOI: <https://doi.org/10.4236/ajps.2014.55090>.
24. Bracho, R.; Crowley, K. J. *Phytochemistry.* **1966**, *5*, 921-926. DOI: [https://doi.org/10.1016/S0031-9422\(00\)82788-0](https://doi.org/10.1016/S0031-9422(00)82788-0).
25. Boyom, F. F.; Keumedjio, F.; Dongmo, P. M. J.; Ngadjui, B. T.; Zollo, P. H. A.; Menut, C.; Bessiere, J. M. *Flavour. Fragr. J.* **2002**, *17*, 215-217. DOI: <https://doi.org/10.1002/ffj.1081>.
26. Lopes, D.; Blzzo, H. R.; Sá Sobrinho, A. F.; Pereira, M. V. *J. Essent. Oil Res.* **2000**, *12*, 705-708. DOI: <https://doi.org/10.1080/10412905.2000.9712196>.
27. Radulović, N.; Mananjarasoa, E.; Harinantenaina, L.; Yoshinori, A. *Biochem. Syst. Ecol.* **2006**, *8*, 648-653. DOI: <https://doi.org/10.1016/j.bse.2006.02.005>.
28. Lima, E. J. D.; Alves, R. G.; D' Elia, G. M.; Anunciação, T. A. D.; Silva, V. R.; Santos, L. D. S.; Soares, M. B. P.; Cardozo, N. M. D.; Costa, E. V.; da Silva, F. M. A.; Koolen, H. H. F.; Bezerra, D. P. *Molecules.* **2018**, *23*, 2974. DOI: <https://doi.org/10.3390/molecules23112974>.
29. Athikomkulchai, S.; Tadtong, S.; Ruangrunsi, N.; Hongratanaworakit, T. *Nat. Prod. Commun.* **2015**, *10*, 1459-1460. DOI: <https://doi.org/10.1177/1934578X1501000836>.
30. De Heluani, C. S.; De Lampasona, M. P.; Vega, M. I.; Catalan, C. A. *J. Essent. Oil Res.* **2005**, *17*, 351-353. DOI: <https://doi.org/10.1080/10412905.2005.9698927>.
31. Silva, C. G.; Zago, H. B.; Júnior, H. J.; da Camara, C. A.; de Oliveira, J. V.; Barros, R.; Schwartz, M. O. E.; Lucena, M. F. A. *J. Essent. Oil Res.* **2008**, *20*, 179-182. DOI: <https://doi.org/10.1080/10412905.2008.9699985>.
32. Setzer, W. N.; Stokes, S. L.; Bansal, A.; Haber, W. A.; Caffrey, C. R.; Hansell, E.; McKerrow, J. H. *Nat. Prod. Commun.* **2007**, *2*, 685-689. DOI: <https://doi.org/10.1177/1934578X0700200613>.
33. Miranda, F. M.; Junior, B. B. D. N.; Aguiar, R. M.; Pereira, R. S.; Teixeira, A. D. O.; Oliveira, D. M. D.; Lima, E. D. O.; Oigman, S. S.; de Rezende, C. M.; Froidi, G. *J. Essent. Oil Res.* **2019**, *31*, 223-227. DOI: <https://doi.org/10.1080/10412905.2018.1539416>.
34. Babili, F. E.; Fouraste, I.; Moulis, C.; Bessiere, J. M.; Roques, C.; Haddioui, L. *J. Essent. Oil Res.* **2009**, *21*, 272-275. DOI: <https://doi.org/10.1080/10412905.2009.9700168>.

35. Ciccio, J. F.; Segnini, M. *J. Essent. Oil Res.* **2002**, *14*, 357-360. DOI: <https://doi.org/10.1080/10412905.2002.9699883>.
36. da Camara, C. A.; de Moraes, M. M.; de Melo, J. P.; da Silva, M. M. *J. Essent. Oil Bearing Plants.* **2017**, *20*, 1434-1449. DOI: <https://doi.org/10.1080/0972060X.2017.1416677>.
37. Mehalaine, S.; Chenchouni, H. *Arab J. Geosci.* **2021**, *14*, 1257. DOI: <https://doi.org/10.1007/s12517-021-07582-6>.
38. Ministry of Health. *Vietnamese Pharmacopoeia*. Medical Publishing House, Hanoi, Vietnam, 2009.
39. Thinh, B. B.; Khoi, N. T.; Doudkin, R. V.; Thin, D. B.; Ogunwande, I. A. *Nat. Prod. Res.* **2023**, *37*, 1625-1631. DOI: <https://doi.org/10.1080/14786419.2022.2103698>.
40. Chac, L. D.; Hoi, Q. V.; Thinh, B. B. *Chem. Nat. Compd.* **2023**, *59*, 597-599. DOI: <https://doi.org/10.1007/s10600-023-04065-w>.
41. National Institute of Science and Technology. *NIST Chemistry Webbook*. Data from NIST Standard Reference Database 69, **2018**.
42. Adams, R. P. in: *Identification of essential oil components by gas chromatography/mass spectroscopy*. Allured Publishing Corporation, Carol Stream, **2007**.
43. Thinh, B. B.; Hanh, D. H.; Hung, N.; Thin, D. B. *Moscow Univ. Chem. Bull.* **2022**, *77*, 300-305. DOI: <https://doi.org/10.3103/S0027131422050108>.
44. Thinh, B. B.; Thin, D. B. *J. Essent. Oil Bearing Plants.* **2023**, *26*, 653-663. DOI: <https://doi.org/10.1080/0972060X.2023.2234398>.
45. Loizzo, M. R.; Menichini, F.; Conforti, F.; Tundis, R.; Bonesi, M.; Saab, A. M.; Statti, G. A.; de Cindio, B.; Houghton, P. J.; Menichini, F.; Frega, N. G. *Food Chem.* **2009**, *117*, 174-180. DOI: <https://doi.org/10.1016/j.foodchem.2009.03.095>.
46. Ersoy, E.; Ozkan, E. E.; Karahan, S.; Şahin, H.; Cinar, E.; Canturk, Y. Y.; Kara, E. M.; Zengin, G.; Boga, M. S. *Afr. J. Bot.* **2023**, *153*, 124-135. DOI: <https://doi.org/10.1016/j.sajb.2022.12.020>.
47. Huong, L. T.; Dai, D. N.; Thin, D. B.; Hung, N. H.; Thinh, B. B. *Nat. Prod. Commun.* **2023**, *18*, 1-10. DOI: <https://doi.org/10.1177/1934578X231193541>.
48. Pereira, M. L.; Santos, D. C. P.; Soares Júnior, C. A. M.; Bazan, T. A. X. N.; Bezerra Filho, C. M.; Silva, M. V. D.; Correia, M. T. D. S.; Cardenas, A. F. M.; de Siqueira, F. S. F.; Carvalho, E. M.; Fronza, B. M.; André, C. B.; da Silva, L. C. N.; Galvão, L. C. D. C. *J. Funct. Biomater.* **2022**, *13*, 149. DOI: <https://doi.org/10.3390/jfb13030149>.
49. Galvão, L. C. D. C.; Furletti, V. F.; Bersan, S. M. F.; da Cunha, M. G.; Ruiz, A. L. T. G.; de Carvalho, J. E.; Sartoratto, A.; Rehder, L. G. R.; Figueira, G. M.; Duarte, M. C. T.; Ikegaki, M.; de Alencar, S. M.; Rosalen, P. L. *Evid. Based Complement Altern. Med.* **2012**, *2012*, 751435. DOI: <https://doi.org/10.1155/2012/751435>.
50. Arunkumar, R.; Nair, S. A.; Rameshkumar, K. B.; Subramoniam, A. *Rec. Nat. Prod.* **2014**, *8*, 385-393.
51. Herman, A.; Tambor, K.; Herman, A. *Curr. Microbiol.* **2016**, *72*, 165-172. DOI: <https://doi.org/10.1007/s00284-015-0933-4>.
52. Sabulal, B.; Dan, M.; Kurup, R.; Pradeep, N. S.; Valsamma, R. K.; George, V. *Phytochemistry.* **2006**, *67*, 2469-2473. DOI: <https://doi.org/10.1016/j.phytochem.2006.08.003>.
53. Badr, M. M.; Badawy, M. E.; Taktak, N. E. *J. Drug Deliv. Sci. Technol.* **2021**, *65*, 102732. DOI: <https://doi.org/10.1016/j.jddst.2021.102732>.
54. Rabib, H.; Elagdi, C.; Hsaine, M.; Fougrach, H.; Koussa, T.; Badri, W. *Biochem. Res. Int.* **2020**, *2020*, 9638548. DOI: <https://doi.org/10.1155/2020/9638548>.
55. Krist, S.; Banovac, D.; Tabanca, N.; Wedge, D. E.; Gochev, V. K.; Wanner, J.; Schmidt, E.; Jirovetz, L. *Nat. Prod. Commun.* **2015**, *10*, 143-148. DOI: <https://doi.org/10.1177/1934578X1501000133>.
56. Thin, D. B.; Korneeva, A. A.; Thinh, B. B.; Ogunwande, I. A. *Russ. J. Bioorg. Chem.* **2023**, *49*, 815-822. DOI: <https://doi.org/10.1134/S1068162023040209>.
57. da Silva Rivas, A. C.; Lopes, P. M.; de Azevedo Barros, M. M.; Costa Machado, D. C.; Alviano, C. S.; Alviano, D. S. *Molecules.* **2012**, *17*, 6305-6316. DOI: <https://doi.org/10.3390/molecules17066305>.

58. Morcia, C.; Malnati, M.; Terzi, V. *Food Addit. Contam.* **2012**, *29*, 415-422. DOI: <https://doi.org/10.1080/19440049.2011.643458>.
59. de Lacerda Leite, G. M.; de Oliveira Barbosa, M.; Lopes, M. J. P.; de Araújo Delmondes, G.; Bezerra, D. S.; Araújo, I. M.; de Alencar, C. D. C.; Coutinho, H. D. M.; Peixoto, L. R.; Barbosa-Filho, J. M.; Felipe, C. F. B.; Barbosa, R.; de Menezes, I. R. A.; Kerntof, M. R. *Trends Food Sci. Technol.* **2021**, *115*, 255-274. DOI: <https://doi.org/10.1016/j.tifs.2021.06.049>.
60. Duarte, A. E.; De Menezes, I. R. A.; Bezerra Moraes Braga, M. F.; Leite, N. F.; Barros, L. M.; Waczuk, E. P.; da Silva, M. A. P.; Boligon, A.; Rocha, J. B. T.; Souza, D. O.; Kamdem, J. P.; Coutinho, H. D. M.; Burger, M. E. *Molecules*. **2016**, *21*, 743. DOI: <https://doi.org/10.3390/molecules21060743>.
61. Nazzaro, F.; Fratianni, F.; De Martino, L.; Coppola, R.; De Feo, V. *Pharmaceuticals*. **2013**, *6*, 1451-1474. DOI: <https://doi.org/10.3390/ph6121451>.
62. Huong, L. T.; Thinh, B. B.; Hung, N. H.; Phu, H. V.; Hieu, N. C.; Dai, D. N. *Braz. J. Biol.* **2024**, *84*, e270967. DOI: <https://doi.org/10.1590/1519-6984.270967>.
63. Sharma, J. N.; Al-Omran, A.; Parvathy, S. S. *Inflammopharmacology*. **2007**, *15*, 252-259. DOI: <https://doi.org/10.1007/s10787-007-0013-x>.
64. Miguel, M. G. *Molecules*. **2010**, *15*, 9252-9287. DOI: <https://doi.org/10.3390/molecules15129252>.
65. de Cássia da Silveira e Sá, R.; Andrade, L. N.; de Sousa, D. P. *Molecules*. **2013**, *18*, 1227-1254. DOI: <https://doi.org/10.3390/molecules18011227>.
66. de Cássia Da Silveira e Sá, R.; Andrade, L. N.; de Sousa, D. P. *Nat. Prod. Commun.* **2015**, *10*, 1767-1774. DOI: <https://doi.org/10.1177/1934578X1501001033>.
67. Francomano, F.; Caruso, A.; Barbarossa, A.; Fazio, A.; La Torre, C.; Ceramella, J.; Mallamaci, R.; Saturnino, C.; Lacopetta, D.; Sinicropi, M. S. *Appl. Sci.* **2019**, *9*, 5420. DOI: <https://doi.org/10.3390/app9245420>.
68. Valente, J.; Zuzarte, M.; Gonçalves, M. J.; Lopes, M. C.; Cavaleiro, C.; Salgueiro, L.; Cruz, M. T. *Food Chem. Toxicol.* **2013**, *62*, 349-54. DOI: <https://doi.org/10.1016/j.fct.2013.08.083>.
69. Yoon, W. J.; Moon, J. Y.; Kang, J. Y.; Kim, G. O.; Lee, N. H.; Hyun, C. G. *Nat. Prod. Commun.* **2010**, *5*, 1311-1316. DOI: <https://doi.org/10.1177/1934578X1000500835>.
70. Hachlafi, N. E.; Aanniz, T.; Menyiy, N. E.; Baaboua, A. E.; Omari, N. E.; Balahbib, A.; Shariati, M. A.; Zengin, G.; Fikri-Benbrahim, K.; Bouyahya, A. *Food Rev. Int.* **2023**, *39*, 1799-1826. DOI: <https://doi.org/10.1080/87559129.2021.1936007>.
71. Chen, S. P.; Su, C. H.; Huang-Liu, R.; Lee, M. W.; Chiang, C. Y.; Chen, W. Y.; Chen, C. J.; Wu, S. W.; Kuan, Y. H. *J. Funct. Foods*. **2020**, *69*, 103943. DOI: <https://doi.org/10.1016/j.jff.2020.103943>.

## Novel and Reusable Magnetic Zinc Ferrites Modified SBA-15 Supported Ionic Liquids for Sustainable and Efficient Cycloaddition of CO<sub>2</sub> and Epoxides to Cyclic Carbonates

---

Yu Lin Hu<sup>1\*</sup>, Zhi Guo Sun<sup>1</sup>, Xiao Bing Liu<sup>2</sup>

<sup>1</sup>College of Chemistry and Chemical Engineering, Anshun University, Anshun 561000, P. R. China.

<sup>2</sup>College of Chemistry and Chemical Engineering, Jinggangshan University, Ji'an 343009, P. R. China.

\*Corresponding author: Yu Lin Hu, email: [huyulin1982@163.com](mailto:huyulin1982@163.com)

Received June 27<sup>th</sup>, 2022; Accepted July 7<sup>th</sup>, 2023.

DOI: <http://dx.doi.org/10.29356/jmcs.v68i3.1824>

**Abstract.** A type of magnetic zinc ferrites modified SBA-15 supported ionic liquids have been synthesized and evaluated as effective catalysts for the synthesis of cyclic carbonates from epoxides and CO<sub>2</sub>. The effects of catalysts, CO<sub>2</sub> pressure, reaction temperature, and catalyst stability have also been investigated, the catalyst ZnFe<sub>2</sub>O<sub>4</sub>@SBA-15-ILVO<sub>3</sub> exhibited excellent activity in high to excellent yields (87~98 %) with excellent selectivities (98~99.7 %). Moreover, the catalyst exhibited excellent stability and could be easily recovered and reused for five times without a considerable decrease in catalytic activity. This work provides a sustainable and efficient strategy for the chemical fixation of carbon dioxide into valuable cyclic carbonates.

**Keywords:** Supported ionic liquid; magnetic zinc ferrites modified SBA-15; cycloaddition; cyclic carbonates; carbon dioxide.

**Resumen.** Se sintetizó y evaluó un líquido iónico soportado tipo ferrita de zinc magnética modificada SBA-15 como un catalizador efectivo para la síntesis de carbonatos cíclicos a partir de epóxidos y CO<sub>2</sub>. Se investigaron los efectos del catalizador, el CO<sub>2</sub>, la presión, la temperatura de reacción y la estabilidad del catalizador; el catalizador ZnFe<sub>2</sub>O<sub>4</sub>@SBA-15-ILVO<sub>3</sub> mostró una excelente actividad con rendimientos de altos a excelentes (87~98 %), así como excelentes selectividades. Adicionalmente, el catalizador mostró tener una excelente estabilidad, y se logró recuperar y reutilizar fácilmente en cinco ocasiones sin mostrar un decremento importante en su actividad catalítica. Este trabajo proporciona una estrategia sostenible y eficiente para la transformación química de dióxido de carbono en carbonatos cíclicos de alto valor.

**Palabras clave:** Líquidos iónicos soportados; ferritas de zinc magnéticas modificadas SBA-15; cicloadición; carbonatos cíclicos; dióxido de carbono.

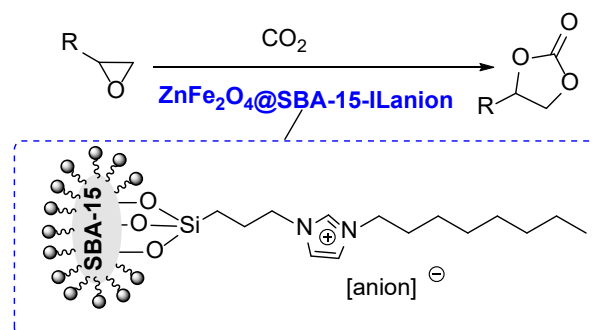
---

### Introduction

Chemical fixation of CO<sub>2</sub> into value-added products was one of the promising strategies for CO<sub>2</sub> capture and storage, which play important roles towards the clean environment [1-4]. As a promising way for CO<sub>2</sub> chemical utilization, the cycloaddition reaction of CO<sub>2</sub> with epoxides is promising due to both the view of 100% atomic economy and the wide applications of cyclic carbonates products in fine chemistry and industry [5,6]. However, due to the thermodynamic stability and kinetic inertness of CO<sub>2</sub>, considerable efforts have been devoted to develop efficient catalytic systems for the CO<sub>2</sub> sustainable transformation. Recently, a wide range

of catalytic systems have been successfully developed for the synthesis of cyclic carbonates, including metal complexes [7-9], metal-organic frameworks [10-12], covalent organic frameworks [13,14],  $\text{InBr}_3/\text{NBu}_4\text{Br}$  [15],  $\text{Ag}/\text{TUD-1}$  [16], organocatalysts [17-19],  $\text{Zn-Zr}$  bimetallic oxide [20], and others [21-23]. Despite these advances, the development of a green and sustainable strategy for the chemical fixation of  $\text{CO}_2$  into cyclic carbonates via the cycloaddition with epoxides remains a challenge for chemists.

Ionic liquids (ILs) have found numerous applications in various areas of reaction solvents and catalysis due to their negligible vapour pressure, thermal and chemical stability, non-flammable, nonvolatile, low toxicity and strong structural design prospects [24-28]. Through the functional design of anions and cations of ionic liquids, the use of ILs as catalysts in the efficient synthesis of cyclic carbonates via the cycloaddition of  $\text{CO}_2$  and epoxides have been developed [29-31]. However, the isolation of pure ILs from products and reusability has been the major issue in these processes in view of eco-sustainability. Immobilization of ILs onto solid supports could alleviate these issues, not only reduce cost, and enhance catalytic efficiency, but also facilitate catalyst separation and reutilization [32-35]. Amongst the available supports, magnetic mesoporous materials such as the inactive mesoporous silica materials modified by different magnetic active metal oxides have become as exceptional and significant solid supports due to the unique properties of high specific surface area, easy functionalization, well-defined size, controlled pore size distribution, innocuity and high biocompatibility, good hydrothermal stability as well as easy separation and reusability [36-46]. Herein, a type of magnetic zinc ferrites modified SBA-15 supported ionic liquids via the immobilization of different amounts of functional ionic liquids onto active magnetic zinc ferrites modified SBA-15 supports have been designed to investigate their catalytic performance in the synthesis of cyclic carbonates via the cycloaddition of  $\text{CO}_2$  and epoxides under mild conditions (Scheme 1). In addition, catalyst reusability was also carried out to assess the stability of the catalytic system.



**Scheme 1.** Catalytic synthesis of cyclic carbonates with magnetic supported ionic liquids.

## Experimental

### Materials and apparatus

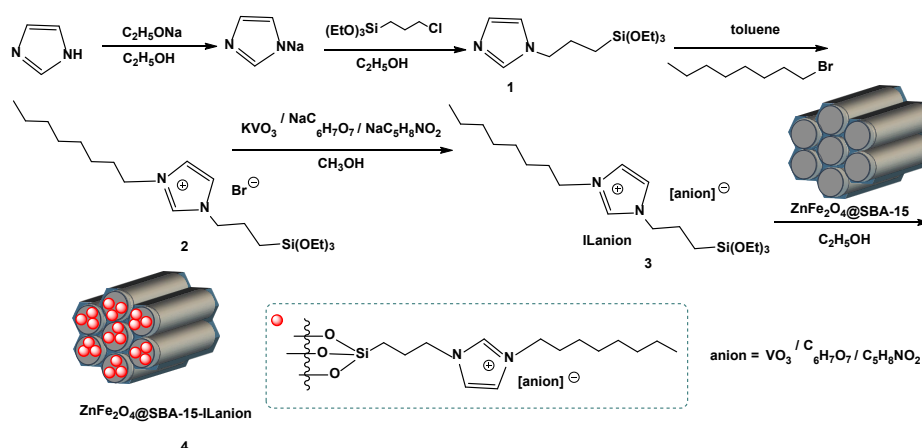
Pluronic 123 ( $\text{EO}_{20}\text{PO}_{70}\text{EO}_{20}$ ) was purchased from Sigma-Aldrich, and other reagents are of analytical grade and used directly without further purification. Scanning electron microscopy (SEM) and energy dispersive X-ray spectroscopy (EDX) were recorded with a JSM-7500F electron microscope. FT-IR spectra were conducted on a PE Fourier Transform spectrometer in a range from  $4000$  to  $400\text{ cm}^{-1}$ . Powder X-ray diffraction patterns were recorded on an Ultima IV diffractometer using  $\text{Cu K}\alpha$  radiation ( $\lambda = 1.5405\text{ \AA}$ ), with a scan speed of  $4^\circ/\text{min}$ . Thermogravimetric analysis (TGA) was performed on a NETZSCH STA 449 F5 with a heating rate of  $10\text{ }^\circ\text{C min}^{-1}$  under nitrogen. UV-Vis spectra were obtained on a Shimadzu UV-2450 spectrophotometer. The BET surface area and pore volume distributions of the catalysts were determined with  $\text{N}_2$  adsorption-desorption isotherms using a BELSORP-max instrument. Pore size distribution curves were calculated from the analysis of desorption branch of the isotherm by the BJH (Barrett-Joyner-Halenda). Magnetic properties were carried out using a vibrating sample magnetometer (PPMS-9T, Quantum Design, USA) in the magnetic field range of  $-10000$  to  $10000\text{ Oe}$  at room temperature.  $^1\text{H}$  NMR spectra were recorded



on a Bruker Avance 400 MHz spectrometer in DMSO- $d_6$  or  $CDCl_3$  with tetramethylsilane (TMS) as an internal reference. Elemental analysis were obtained on a Vario Micro cube Elemental Analyzer. Melting points were measured by an electro-thermal IA 9100 apparatus.

### Synthesis of magnetic supported ionic liquids

Magnetic zinc ferrites functionalized SBA-15 support  $ZnFe_2O_4@SBA-15$  was synthesized following the previously reported methods [42-44]. The supported ionic liquids were prepared according to the similar procedures described in literatures (Scheme 2) [25-29, 36-39]. To a round-bottomed flask were added sodium ethoxide (0.3 mol), imidazole (0.3 mol) and ethanol (150 mL). The mixture was vigorously stirred at 70 °C for 8 h, then (3-chloropropyl) triethoxysilane (0.3 mol) was added into the solution gradually and stirred at 80 °C for 12 h. After filtering the slurry and evaporating the ethanol solvent to give **1**. Next, 1-bromo-octan (0.2 mol) and **1** (0.2 mol) were dispersed in 120 mL of toluene, and the resulting mixture was stirred under nitrogen at 110 °C for 24 h. After this procedure, the excess solvent was isolated by liquid-liquid separation and the residue was dried under vacuum at 70 °C to give **2**. Then, **2** (0.1 mol), potassium metavanadate (0.1 mol) or sodium dihydrogen citrate (0.1 mol) or sodium proline (0.1 mol), and methanol (60 mL) were refluxed under vigorous stirring for 24 h. The suspension was filtered, washed with ethanol and dried at 50 °C to give the anionic functionalized ionic liquids ILanion **3**. Finally, the magnetic supported ionic liquids **4** were synthesized using a post-synthesis grafting method. A mixture of the as-prepared  $ZnFe_2O_4@SBA-15$  (2.0 g), ILanion **3** (1.2 g), and ethanol (80 mL) was refluxed for 24 h. The resulting precipitates were centrifugalized, washed three times with dichloromethane and dried at 50 °C overnight to obtain  $ZnFe_2O_4@SBA-15$ -ILanion **4**.



**Scheme 2.** Synthesis of magnetic supported ionic liquids.

### Catalytic synthesis of cyclic carbonates

The cycloaddition reactions of  $CO_2$  and epoxides were conducted in a stainless-steel autoclave. Typically, the reaction autoclave was replaced with  $CO_2$ , then epoxide (10 mmol) and  $ZnFe_2O_4@SBA-15$ - $ILVO_3$  (0.15 g) were added into the autoclave under stirring. The reaction mixture was stirred at 90 °C for a desired time under a fixed pressure. The reaction progress was monitored by GC. After completion of the reaction, the catalyst was easily separated by an external magnet and then washed three times with  $CH_2Cl_2$  for the recycling experiments, fresh substrates were added and recycled under identical reaction conditions. All target products are known and commercial, thus were verified by comparison with those of standard compounds or by  $^1H$  NMR and Elemental analysis.

### Spectroscopic data for products

**1,3-Dioxolan-2-one** (Table 2, entry 1).  $^1H$  NMR (400 MHz,  $CDCl_3$ ) ( $\delta$ /ppm): 4.53 (s,  $CH_2$ , 2H). Elemental analysis for  $C_3H_4O_3$ : C, 40.84; H, 4.53; O, 54.44. Found: C, 40.92; H, 4.58; O, 54.50.

**Propylene carbonate** (Table 2, entry 2).  $^1\text{H}$  NMR (400 MHz,  $\text{CDCl}_3$ ) ( $\delta/\text{ppm}$ ): 1.47 (dd,  $\text{CH}_3$ , 3H), 3.95 (t, CH, 1H), 4.53 (t, CH, 1H), 4.82 (m, CH, 1H); Elemental analysis for  $\text{C}_4\text{H}_6\text{O}_3$ : C, 47.01; H, 5.86; O, 46.97. Found C, 47.06; H, 5.92; O, 47.01.

**(Chloromethyl)ethylene carbonate** (Table 2, entry 3).  $^1\text{H}$  NMR (400 MHz,  $\text{CDCl}_3$ ) ( $\delta/\text{ppm}$ ): 3.75 (dd,  $\text{CH}_2$ , 2H), 4.32 (t,  $\text{CH}_2$ , 1H), 4.59 (t,  $\text{CH}_2$ , 1H), 4.93 (m, CH, 1H); Elemental analysis for  $\text{C}_4\text{H}_5\text{ClO}_3$ : C, 35.14; Cl, 25.92; O, 35.11. Found C, 35.19; Cl, 25.96; O, 35.15.

**4-(Hydroxymethyl)-1,3-dioxolan-2-one** (Table 2, entry 4).  $^1\text{H}$  NMR (400 MHz,  $\text{CDCl}_3$ ) ( $\delta/\text{ppm}$ ): 3.56 (t,  $\text{CH}_2$ , 2H), 4.28-4.50 (dd,  $\text{CH}_2$ , 2H), 4.76 (m, CH, 1H), 5.25 (t, OH, 1H). Elemental analysis for  $\text{C}_4\text{H}_6\text{O}_4$ : C, 40.64; H, 5.07; O, 54.15. Found: C, 40.68; H, 5.12; O, 54.19.

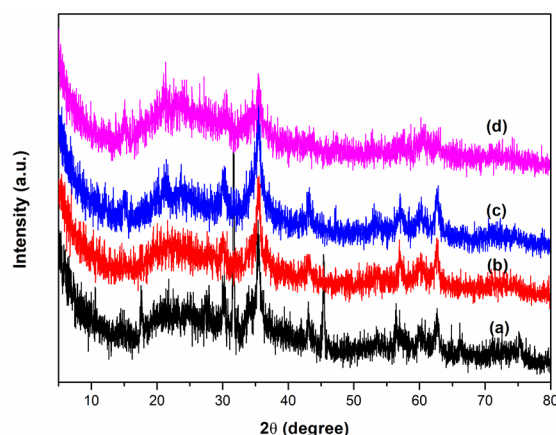
**1,2-Butylene glycol carbonate** (Table 2, entry 5).  $^1\text{H}$  NMR (400 MHz,  $\text{CDCl}_3$ ) ( $\delta/\text{ppm}$ ): 0.93 (t,  $\text{CH}_3$ , 3H), 1.57-1.61 (m,  $\text{CH}_2$ , 2H), 4.06 (t,  $\text{CH}_2$ , 2H); 4.42 (d,  $\text{CH}_2$ , 1H); 4.64 (m, CH, 1H); Elemental analysis for  $\text{C}_5\text{H}_8\text{O}_3$ : C, 51.68; H, 6.90; O, 41.32. Found: C, 51.72; H, 6.94; O, 41.34.

**Hexahydrobenzo[d][1,3]dioxol-2-one** (Table 2, entry 6).  $^1\text{H}$  NMR (400 MHz,  $\text{CDCl}_3$ ) ( $\delta/\text{ppm}$ ): 1.37-1.42 (m,  $\text{CH}_2\text{CH}_2$ , 4H), 1.74-1.80 (m,  $2\text{CH}_2$ , 4H), 4.61 (t,  $2\text{CH}$ , 2H); Elemental analysis for  $\text{C}_7\text{H}_{10}\text{O}_3$ : C, 59.11; H, 7.05; O, 33.71. Found C, 59.15; H, 7.09; O, 33.76.

**Styrene carbonate** (Table 2, entry 7).  $^1\text{H}$  NMR (400 MHz,  $\text{CDCl}_3$ ) ( $\delta/\text{ppm}$ ): 4.30 (t,  $\text{CH}_2$ , 1H), 4.72 (t,  $\text{CH}_2$ , 1H), 5.67 (t,  $\text{CH}_2$ , 1H), 7.29-7.37 (m, Ar-H, 5H); Elemental analysis for  $\text{C}_9\text{H}_8\text{O}_3$ : C, 65.80; H, 4.86; O, 29.21. Found C, 65.85; H, 4.91; O, 29.24.

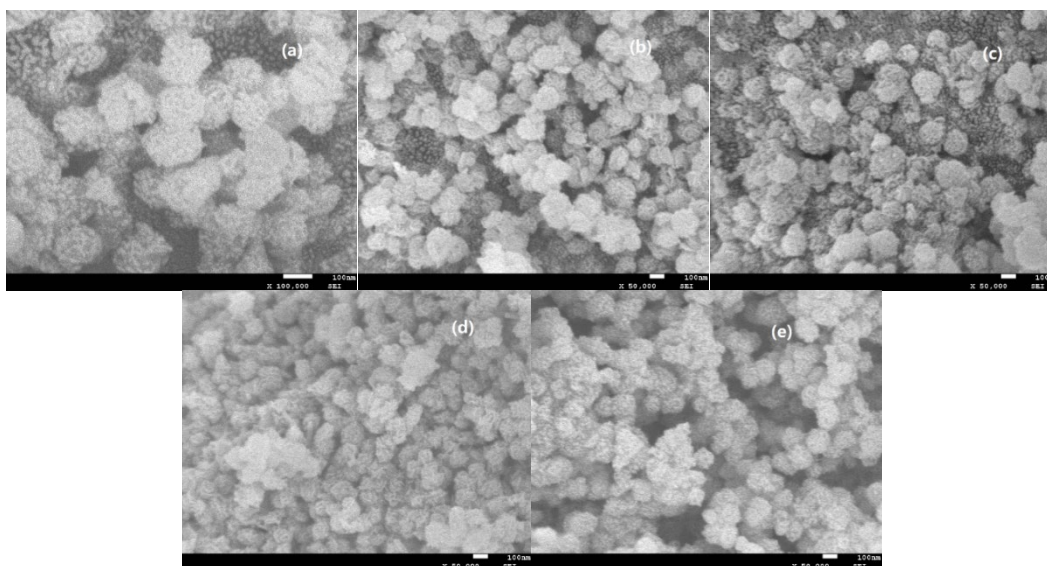
## Results and discussion

X-ray diffraction (XRD) was performed to investigate the structure of the supported ionic liquids. As can be seen from the Fig. 1, all the samples exhibited a broad diffraction peak between  $2\theta = 20\text{--}25^\circ$ , which are assigned to the characteristic peak of mesoporous silica [42-45], suggesting the basic crystalline structure of ordered mesoporous materials. The characterization peaks at  $2\theta = 30.3^\circ, 35.4^\circ, 42.8^\circ, 53.6^\circ, 56.5^\circ, 62.4^\circ$  assigned to the  $\text{ZnFe}_2\text{O}_4$  crystal planes (220), (311), (400), (422), (511), (440), respectively (JCPDS card No. 221012). In addition, no obvious peaks about the ionic liquid species were observed, indicating a well dispersion on the support framework.

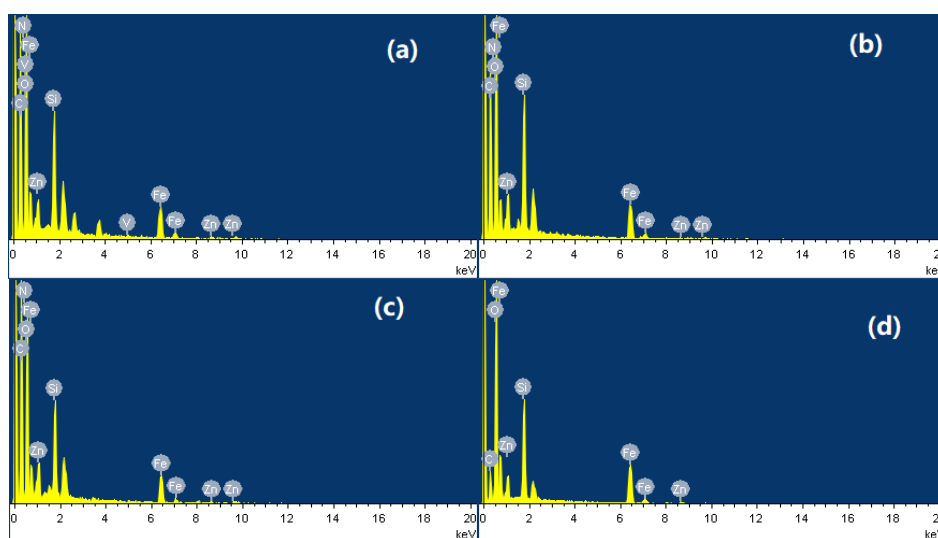


**Fig. 1.** XRD diffractograms of  $\text{ZnFe}_2\text{O}_4@\text{SBA-15-ILVO}_3$  (a),  $\text{ZnFe}_2\text{O}_4@\text{SBA-15-ILC}_6\text{H}_7\text{O}_7$  (b),  $\text{ZnFe}_2\text{O}_4@\text{SBA-15-ILC}_5\text{H}_8\text{NO}_2$  (c), and  $\text{ZnFe}_2\text{O}_4@\text{SBA-15}$  (d).

The surface morphologies of samples are evaluated by SEM analysis. As shown in Fig. 2(d),  $\text{ZnFe}_2\text{O}_4@SBA-15$  presents an irregular shape consisting of some spherical agglomerates with wrinkled nano-sized particles. Fig. 2(a-c) display the SEM images of the magnetic supported ionic liquids. After the immobilization of ionic liquid on the  $\text{ZnFe}_2\text{O}_4@SBA-15$  support, the whole morphologies are retained, pointing to the preservation of the well-ordered structure in these supported ionic liquids. Comparatively, the typical aggregated small and irregular particles are clearly seen in these samples, which are attributed to the IL immobilization results. The EDX analysis revealed the presence of the corresponding elemental signals including C, Si, O, N, V, Fe, Zn in these supported ionic liquids (Fig. 3), indicating the successful immobilization of ionic liquid moieties on the support framework.



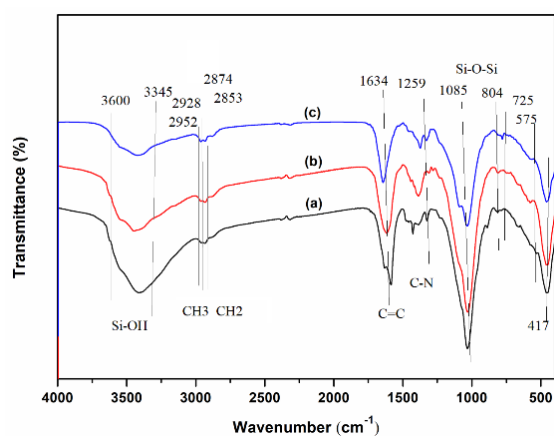
**Fig. 2.** SEM images of  $\text{ZnFe}_2\text{O}_4@SBA-15-ILVO3$  (a),  $\text{ZnFe}_2\text{O}_4@SBA-15-ILC6H7O7$  (b),  $\text{ZnFe}_2\text{O}_4@SBA-15-ILC5H8NO2$  (c), and  $\text{ZnFe}_2\text{O}_4@SBA-15$  (d), five times recycled  $\text{ZnFe}_2\text{O}_4@SBA-15-ILVO3$  (e).



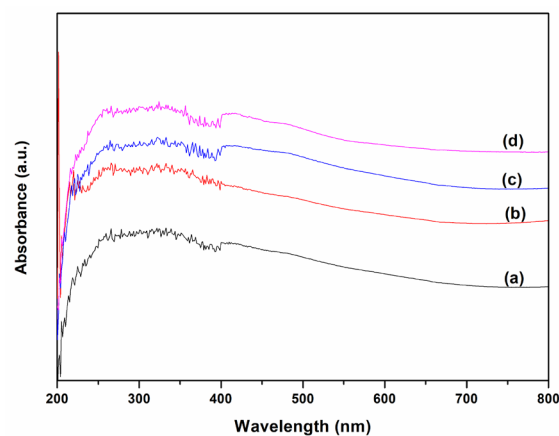
**Fig. 3.** EDX images of  $\text{ZnFe}_2\text{O}_4@SBA-15-ILVO3$  (a),  $\text{ZnFe}_2\text{O}_4@SBA-15-ILC6H7O7$  (b),  $\text{ZnFe}_2\text{O}_4@SBA-15-ILC5H8NO2$  (c), and  $\text{ZnFe}_2\text{O}_4@SBA-15$  (d).



To validate and characterize the functional groups of the supported ionic liquids, FT-IR spectra of the samples are taken. As shown in Fig. 4, the peak around  $3600\text{--}3345\text{ cm}^{-1}$  was accounted for the characteristic band of hydroxyl stretching vibration. The peaks at around  $2952\text{--}2853\text{ cm}^{-1}$  are attributed to the C-H stretching vibration of  $\text{CH}_3$  and  $\text{CH}_2$ . The characteristic peaks at around  $1085\text{ cm}^{-1}$  and  $804\text{ cm}^{-1}$  are attributed to the Si-O-Si stretching vibration. The absorption peaks around  $1634\text{ cm}^{-1}$ , and  $1259\text{ cm}^{-1}$  are assigned to C=C, and C-N stretching vibrations of imidazole ring [25-27]. Also, the peak at around  $725\text{ cm}^{-1}$  is attributed to bending vibration of  $\text{CH}_2$  units. Furthermore, the peaks at about  $575\text{ cm}^{-1}$ , and  $417\text{ cm}^{-1}$  were assigned to the lattice vibration modes of  $\text{ZnFe}_2\text{O}_4$  [41-43]. The above results indicated that the existence of mainly characteristic groups and the successful immobilization of ionic liquid on the support. The UV-vis spectra of the samples are shown in Fig. 5. For the supported catalysts, three major adsorption peaks could be observed in the region of 210-450 nm, the absorption peaks centered at around 227 nm is attributed to Si-O transition, other absorption weak peaks located at around 398 nm and 439 nm are probably assigned to the absorption of zinc ferrite particles of  $\text{ZnFe}_2\text{O}_4$  [38-41]. At the same time, no remarkable peaks of ionic liquid are found on the UV-vis spectra of the supported ionic liquids, which might be due to their low loading and good dispersion on the support framework.

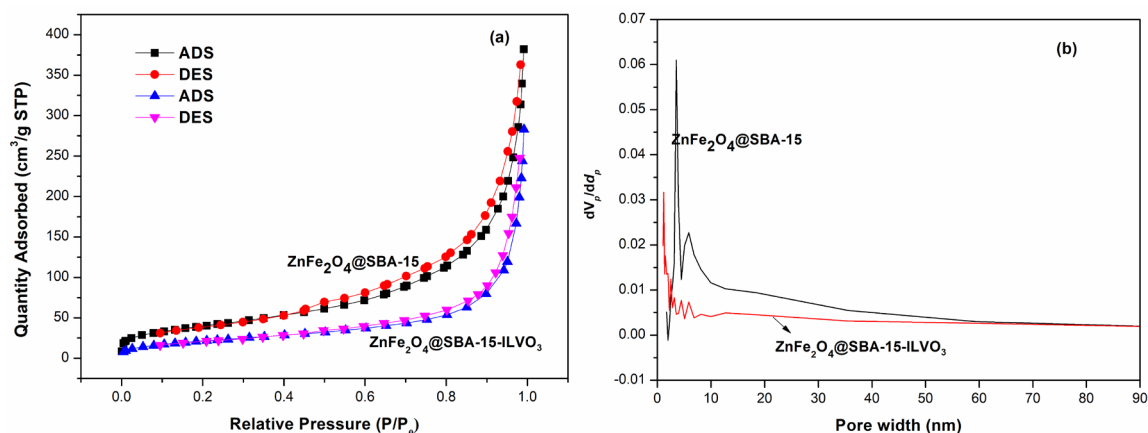


**Fig. 4.** FT-IR spectras of  $\text{ZnFe}_2\text{O}_4@\text{SBA-15-ILVO3}$  (a),  $\text{ZnFe}_2\text{O}_4@\text{SBA-15-ILC6H7O7}$  (b),  $\text{ZnFe}_2\text{O}_4@\text{SBA-15-ILC5H8NO2}$  (c).



**Fig. 5.** UV-Vis spectras of  $\text{ZnFe}_2\text{O}_4@\text{SBA-15-ILVO3}$  (a),  $\text{ZnFe}_2\text{O}_4@\text{SBA-15-ILC6H7O7}$  (b),  $\text{ZnFe}_2\text{O}_4@\text{SBA-15-ILC5H8NO2}$  (c), and  $\text{ZnFe}_2\text{O}_4@\text{SBA-15}$  (d).

The structural characteristics of the superior supported catalysts  $\text{ZnFe}_2\text{O}_4@\text{SBA-15-ILVO}_3$ , and  $\text{ZnFe}_2\text{O}_4@\text{SBA-15}$  are accomplished by a  $\text{N}_2$  adsorption-desorption isotherms and BJH pore size distribution analysis. As shown in Fig. 6, these samples exhibit the type IV isotherms with H1 hysteresis loop at relative pressure ( $P/P_0$ ) = 0.5-0.7, indicating their typical mesoporous structures. It is clearly found that the surface area and pore volume are significantly decreased from 145.7  $\text{m}^2/\text{g}$ , 0.59  $\text{cm}^3/\text{g}$  for  $\text{ZnFe}_2\text{O}_4@\text{SBA-15}$ , 80.2  $\text{m}^2/\text{g}$ , 0.42  $\text{cm}^3/\text{g}$  for  $\text{ZnFe}_2\text{O}_4@\text{SBA-15-ILVO}_3$ , respectively. The reduced surface area and pore volume may be due to the successful immobilization of ionic liquid on the support. Compared with the pure  $\text{ZnFe}_2\text{O}_4@\text{SBA-15}$  support, the supported catalyst  $\text{ZnFe}_2\text{O}_4@\text{SBA-15-ILVO}_3$  displayed no obvious change in terms of the pore size distribution (12.5 nm for  $\text{ZnFe}_2\text{O}_4@\text{SBA-15}$ , 12.8 nm for  $\text{ZnFe}_2\text{O}_4@\text{SBA-15-ILVO}_3$ ). It is worth noting that after the loading of ionic liquid, the mesoporous structure of the catalyst can be well remained.



**Fig. 6.** (a)  $\text{N}_2$  adsorption-desorption isotherms and (b) pore size distributions of  $\text{ZnFe}_2\text{O}_4@\text{SBA-15}$ , and  $\text{ZnFe}_2\text{O}_4@\text{SBA-15-ILVO}_3$ .

Initially, the catalytic performance of the magnetic supported ionic liquids was investigated employing the cycloaddition of  $\text{CO}_2$  and propylene oxide with as the model reaction, and the results were summarized in Table 1. In a first set of experiments, the reaction was carried out in the presence of the three supported ionic liquids catalysts of  $\text{ZnFe}_2\text{O}_4@\text{SBA-15-ILC}_6\text{H}_7\text{O}_7$ ,  $\text{ZnFe}_2\text{O}_4@\text{SBA-15-ILC}_5\text{H}_8\text{NO}_2$  and  $\text{ZnFe}_2\text{O}_4@\text{SBA-15-ILVO}_3$  (Table 1, entries 1-3). It was observed that  $\text{ZnFe}_2\text{O}_4@\text{SBA-15-ILVO}_3$  achieved the best outcome, in terms of 98 % yield of propylene carbonate with 99.5 % selectivity (Table 1, entry 3). For comparison, bare magnetic support  $\text{ZnFe}_2\text{O}_4@\text{SBA-15}$  or bulk ionic liquids as catalysts in the cycloaddition gave much low product yields (48~75 %) and selectivities (90.5~93.7 %) (Table 1, entries 4-7). Besides these, no product was obtained when the reaction in the absence any catalyst (Table 1, entry 8). The influence of the amount of suitable catalyst  $\text{ZnFe}_2\text{O}_4@\text{SBA-15-ILVO}_3$  on the cycloaddition was also studied. It can be seen that the product yield increased with increasing the amount of catalyst from 0.05 g to 0.15 g (Table 1, entries 9, 10 and 3). No significant enhancement in the yield was observed with further increasing the catalyst amount to 0.3 g (Table 1, entries 11 and 12). Thus, the optimum catalyst amount was 0.15 g.

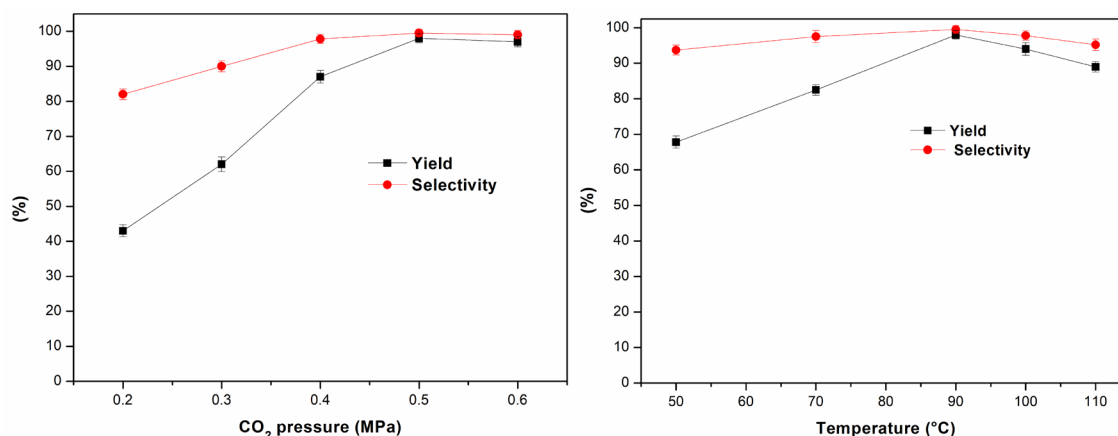
**Table 1.** Catalyst screening for the cycloaddition of propylene oxide with  $\text{CO}_2$ .<sup>a</sup>

| Entry | Catalyst                                                           | Catalyst (g) | Time (h) | Yield (%) <sup>b</sup> | Selectivity (%) <sup>c</sup> |
|-------|--------------------------------------------------------------------|--------------|----------|------------------------|------------------------------|
| 1     | $\text{ZnFe}_2\text{O}_4@\text{SBA-15-ILC}_6\text{H}_7\text{O}_7$  | 0.15         | 3        | 84                     | 97.2                         |
| 2     | $\text{ZnFe}_2\text{O}_4@\text{SBA-15-ILC}_5\text{H}_8\text{NO}_2$ | 0.15         | 3        | 90                     | 98.7                         |
| 3     | $\text{ZnFe}_2\text{O}_4@\text{SBA-15-ILVO}_3$                     | 0.15         | 3        | 98                     | 99.5                         |

|    |                                                            |      |    |       |      |
|----|------------------------------------------------------------|------|----|-------|------|
| 4  | ILC <sub>6</sub> H <sub>7</sub> O <sub>7</sub>             | 0.2  | 8  | 57    | 90.5 |
| 5  | ILC <sub>5</sub> H <sub>8</sub> NO <sub>2</sub>            | 0.2  | 8  | 69    | 92.1 |
| 6  | ILVO <sub>3</sub>                                          | 0.2  | 8  | 75    | 93.0 |
| 7  | ZnFe <sub>2</sub> O <sub>4</sub> @SBA-15                   | 0.4  | 8  | 48    | 93.7 |
| 8  | -                                                          | -    | 24 | trace | -    |
| 9  | ZnFe <sub>2</sub> O <sub>4</sub> @SBA-15-ILVO <sub>3</sub> | 0.05 | 5  | 51    | 98.7 |
| 10 | ZnFe <sub>2</sub> O <sub>4</sub> @SBA-15-ILVO <sub>3</sub> | 0.1  | 3  | 82    | 99.1 |
| 11 | ZnFe <sub>2</sub> O <sub>4</sub> @SBA-15-ILVO <sub>3</sub> | 0.2  | 3  | 98    | 99.4 |
| 12 | ZnFe <sub>2</sub> O <sub>4</sub> @SBA-15-ILVO <sub>3</sub> | 0.3  | 3  | 97    | 99.2 |

<sup>a</sup>Reaction conditions: propylene oxide (10 mmol), CO<sub>2</sub> (0.5 MPa), 90 °C. <sup>b</sup>Isolated yield. <sup>c</sup>GC analysis.

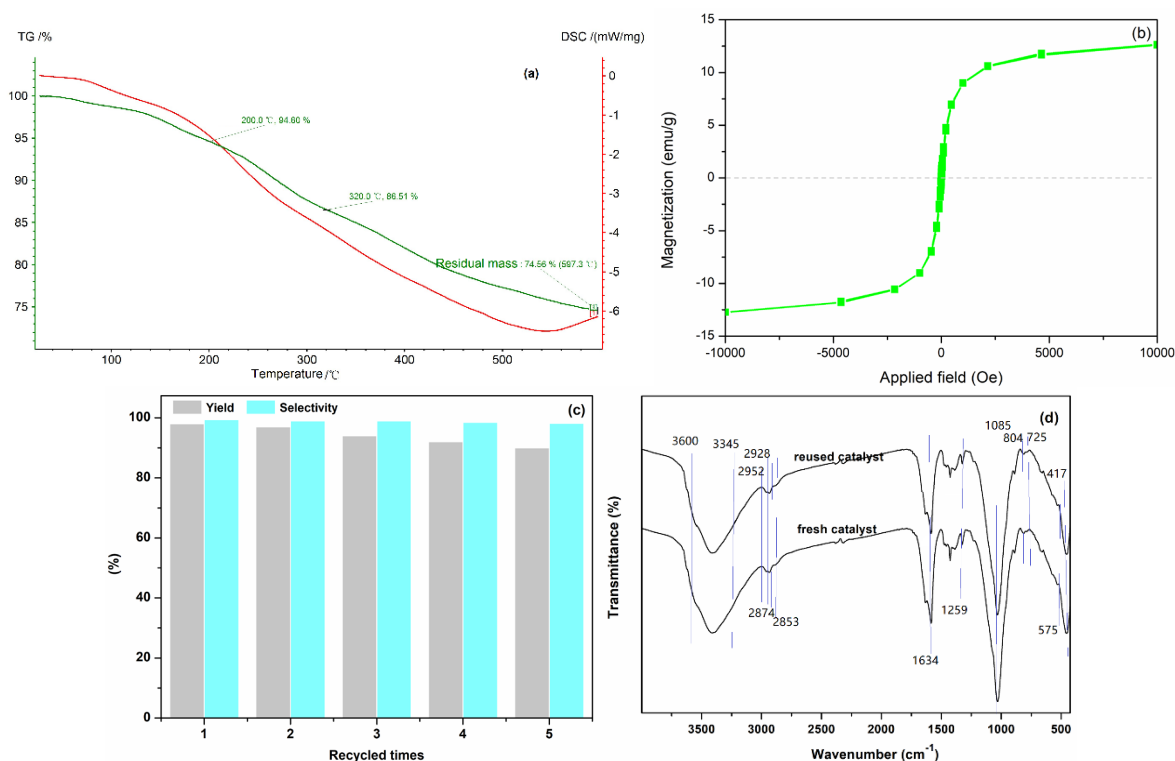
Then the influence of CO<sub>2</sub> pressure on the cycloaddition was also studied (Fig. 7(a)). It can be seen that the product yield and selectivity increased with increasing the CO<sub>2</sub> pressure from 0.2 MPa to 0.5 MPa. These results were related to the favorable diffusion between substrates and ZnFe<sub>2</sub>O<sub>4</sub>@SBA-15-ILVO<sub>3</sub> at the higher CO<sub>2</sub> pressures, resulting in more mass transfer and increasing the cycloaddition efficiency. No significant enhancement in the yield and selectivity was observed with further increasing the CO<sub>2</sub> pressure to 1.0 MPa. Excessive CO<sub>2</sub> pressure may reduce the concentration of propylene oxide, resulting in the slightly reduced product yield and selectivity. Thus, the optimum CO<sub>2</sub> pressure was 0.5 MPa. Moreover, reaction temperature was an important factor to affect the cycloaddition (Fig. 7(b)). It can be seen that the yield was increased in the reaction temperature up to 90 °C. Nevertheless, use of higher temperature beyond 90 °C would lead to a decreased yield and selectivity, which was due to the side reactions of isomerization and ring opening occurred at overly high temperatures (GC analysis). Accordingly, the appropriate temperature is 90 °C.



**Fig. 7.** (a) Influence of CO<sub>2</sub> pressure on the cycloaddition (10 mmol propylene oxide, 0.15 g ZnFe<sub>2</sub>O<sub>4</sub>@SBA-15-ILVO<sub>3</sub>, 90 °C, 3 h), (b) influence of reaction temperature on the cycloaddition (10 mmol propylene oxide, 0.15 g ZnFe<sub>2</sub>O<sub>4</sub>@SBA-15-ILVO<sub>3</sub>, 0.5 MPa CO<sub>2</sub>, 3 h).

Furthermore, the thermal stability catalyst of ZnFe<sub>2</sub>O<sub>4</sub>@SBA-15-ILVO<sub>3</sub> was evaluated by thermogravimetric analysis (TGA) (Fig. 8(a)). The first weight loss of 5.4 % below 200 °C was attributed to the elimination of adsorbed water and solvent. The second weight loss of 20.06 % from 200 °C to 600 °C was


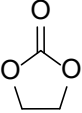

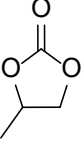
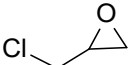
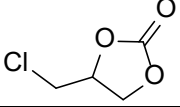
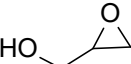
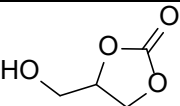
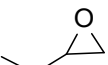
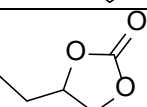
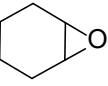
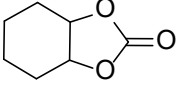
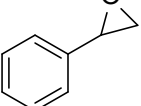
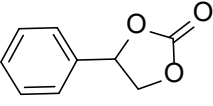
due to the elimination and decomposition of the ionic liquid moieties. This analysis strongly confirmed that the catalyst possessed superior thermal stability ( $\leq 200$  °C), which is beneficial to maintain its catalytic activity. Magnetic property of  $\text{ZnFe}_2\text{O}_4@\text{SBA-15-ILVO}_3$  catalyst was evaluated by using a VSM curve (Fig. 8(b)). The catalyst exhibited a superparamagnetic property with magnetic saturation 12.6 emu/g, which can be easily separated from the reaction mixture via an external magnet. In order to further expand the practicability of the protocol, the reusability of the novel catalyst was then examined for the benchmark reaction under the optimal conditions (Fig. 8(c)). After completion of the reaction, the catalyst could be easily separated and collected from the reaction mixture with an external magnet, washed three times with  $\text{CH}_2\text{Cl}_2$  and subjected to the next cycle. The catalyst could be reused five times for the reaction without considerable loss of catalytic activity, indicating that the catalyst had a good catalytic recyclability. In addition, the surface appearance features of the catalyst after five cycles is similar to that of the fresh one (SEM, Fig. 2(e)) and the structural features of the catalyst not changed after five cycles (FT-IR, Fig. 8(d)), which suggested that the magnetic catalyst has excellent product performance and stability.



**Fig. 8.** (a) TG analysis, (b) magnetization curve, (c) recyclability study, and (d) FT-IR analysis of catalyst  $\text{ZnFe}_2\text{O}_4@\text{SBA-15-ILVO}_3$  after five times use.

To demonstrate the generality of this approach for the cycloaddition, a range of epoxides were then investigated (Table 2). The epoxides containing electron-donating or electron-withdrawing groups could be successfully converted into the corresponding cyclic carbonates in high to excellent yields (87~98 %) with excellent selectivities (98~99.7 %) under the optimal reaction conditions. Interestingly, 2-(chloromethyl)oxirane was the most reactive substrate and converted into 4-(chloromethyl)-1,3-dioxolan-2-one within 1.5 h (Table 2, entry 3). Furthermore, the carboxylation of 7-oxabicyclo[4.1.0]heptane required a long time of 4 h to obtain a high yield of 87 % (Table 2, entry 6), which may be due to the high steric hindrance during the reaction. These results indicated that the designed catalyst could be widely and efficiently used for the synthesis of cyclic carbonates through cycloaddition of  $\text{CO}_2$  and epoxides.

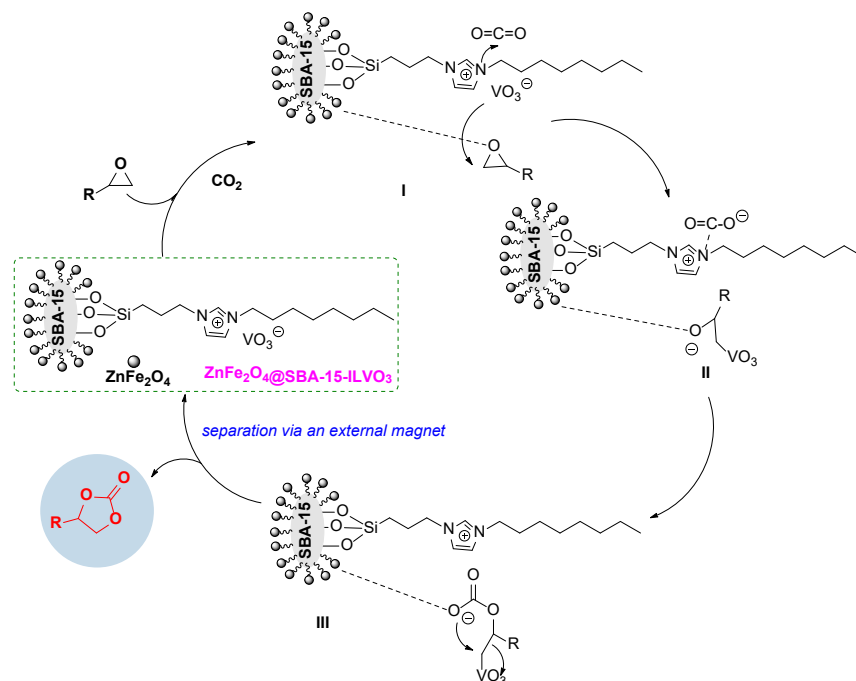
**Table 2.** Catalytic synthesis of cyclic carbonates from epoxides and CO<sub>2</sub>.<sup>a</sup>

| Entry | Epoxide                                                                             | Product                                                                             | Time (h) | Yield (%) <sup>b</sup> | Selectivity (%) <sup>c</sup> |
|-------|-------------------------------------------------------------------------------------|-------------------------------------------------------------------------------------|----------|------------------------|------------------------------|
| 1     |    |    | 3        | 91                     | 99.3                         |
| 2     |    |    | 3        | 98                     | 99.5                         |
| 3     |    |    | 1.5      | 98                     | 99.7                         |
| 4     |    |    | 3        | 95                     | 99.2                         |
| 5     |    |    | 3        | 96                     | 99.3                         |
| 6     |   |   | 4        | 87                     | 98                           |
| 7     |  |  | 3        | 92                     | 99.1                         |

<sup>a</sup>Reaction conditions: epoxide (10 mmol), CO<sub>2</sub> (0.5 MPa), ZnFe<sub>2</sub>O<sub>4</sub>@SBA-15-ILVO<sub>3</sub> (0.15 g), 90 °C.

<sup>b</sup>Isolated yield. <sup>c</sup>GC analysis.

Based on the above experimental results and previous studies [15-20, 29-31], a possible reaction pathway for the catalytic synthesis of cyclic carbonates from the cycloaddition of CO<sub>2</sub> with epoxides was proposed (Scheme 3). The catalyst ZnFe<sub>2</sub>O<sub>4</sub>@SBA-15-ILVO<sub>3</sub> provides a synergistic microenvironment, which could be more favorable to active CO<sub>2</sub> and epoxides. Initially, the substrate epoxide could be activated via the coordination interaction with the metal sites of ZnFe<sub>2</sub>O<sub>4</sub>@SBA-15 support to form an intermediate **I**, together with the adsorption and activation of CO<sub>2</sub> by the imidazolium cation to form carbonate species. Simultaneously, the VO<sub>3</sub> anion adds to the less sterically hindered C atom of epoxide via the nucleophilic attack for the formation of intermediate **II**. Next, there is nucleophilic interaction between the oxygen anion of intermediate **II** and CO<sub>2</sub>, thus stimulates the formation of the intermediate acyclic carbonate **III**. Subsequently, intermediate **III** could be converted into the corresponding product via intramolecular nucleophilic substitution. The regeneration of the catalyst ZnFe<sub>2</sub>O<sub>4</sub>@SBA-15-ILVO<sub>3</sub> was used for the next cycle. The presence of intramolecular synergy of ternary active sites (metal sites of ZnFe<sub>2</sub>O<sub>4</sub>@SBA-15, VO<sub>3</sub> anion, and imidazolium cation) on the CO<sub>2</sub> cycloaddition significantly enhanced the activities of the catalyst in this reaction system. The combination of ionic liquid and magnetic zinc ferrites modified SBA-15 provides superior advantages in the separation of cyclic carbonates products, recovery, and reusability of catalyst via an external magnet under identical conditions.



**Scheme 3.** Possible reaction pathway for the synthesis of cyclic carbonates.

## Conclusions

In conclusion, a type of magnetic zinc ferrites modified SBA-15 supported ionic liquids were designed and synthesized and used as effective and heterogeneous catalysts for the synthesis of cyclic carbonates from epoxides and  $\text{CO}_2$ . The results showed that a range of epoxides with  $\text{CO}_2$  employed in the presence of the catalyst  $\text{ZnFe}_2\text{O}_4@SBA-15-ILVO_3$  leading to the corresponding products in high to excellent yields and excellent selectivities under mild conditions. Moreover, the catalyst could be easily recovered and reused for five times without a considerable decrease in catalytic activity. This procedure offers additional advantages in terms of ease work-up, feasibility, cleaner reaction profile, sustainable and stable recyclability of catalyst. This protocol provides a green and promising strategy for the synthesis of cyclic carbonates toward catalytic cycloaddition of  $\text{CO}_2$  to epoxides.

## Acknowledgements

We gratefully acknowledge the Jiangxi Provincial Natural Science Foundation (20202BABL203023).

## References

1. Ji, Y.; Xu J.; Sun H.; Liu, J. *Chem. Res. Chin. Univ.* **2022**, 38, 688-697.
2. Kassim, M. A.; Meng, T. K. *Sci. Total Environ.* **2017**, 584-585, 1121-1129.
3. Wang, B.; Liu, J.; Yao, S.; Liu, F.; Li, Y.; He, J.; Lin, Z.; Huang, F.; Liu, C.; Wang, M. *J. Mater. Chem. A* **2021**, 9, 17143-17172.

4. Jelmy, E. J.; Thomas, N.; Mathew, D. T.; Louis, J.; Padmanabhan, N. T.; Kumaravel, V.; John, H.; Pillai, S. C. *React. Chem. Eng.* **2021**, *6*, 1701-1738.
5. Sable, D. A.; Vadagaonkar, K. S.; Kapdi, A. R.; Bhanage, B. M. *Org. Biomol. Chem.* **2021**, *19*, 5725-5757.
6. Lopes, E. J. C.; Ribeiro, A. P. C.; Martins, L. M.D.R.S. *Catalysts*. **2020**, *10*, 479.
7. Zhou, F.; Deng, Q.; Huang, N.; Zhou, W.; Deng, W. *ChemistrySelect*. **2020**, *5*, 10516-10520.
8. İköz, M.; İspir, E.; Aytar, E.; Ulusoy, M.; Karabuğa, Ş.; Aslantaş, M.; Çelik, Ö. *New J. Chem.* **2015**, *39*, 7786-7796.
9. Muthuramalingam, S.; Velusamy, M.; Mayilmurugan, R. *Dalton Trans.* **2021**, *50*, 7984-7994.
10. Guo, F.; Zhang, X. *Dalton Trans.* **2020**, *49*, 9935-9947.
11. Beyzavi, M. H.; Stephenson, C. J.; Liu, Y.; Karagiari, O.; Hupp, J. T.; Farha, O. K. *Front. Energy Res.* **2015**, *2*, 1-10.
12. Nguyen, P. T. K.; Nguyen, H. T. D.; Nguyen, H. N.; Trickett, C. A.; Ton, Q. T.; Gutierrez-Puebla, E.; Monge, M. Á.; Cordova, K. E.; Gándara, F. *ACS Appl. Mater. Interf.* **2018**, *10*, 733-744.
13. Luo, R.; Yang, Y.; Chen, K.; Liu, X.; Chen, M.; Xu, W.; Liu, B.; Ji, H.; Fang, Y. *J. Mater. Chem. A* **2021**, *9*, 20941-20956.
14. Zhi, Y.; Shao, P.; Feng, X.; Xia, H.; Zhang, Y.; Shi, Z.; Mu, Y.; Liu, X. *J. Mater. Chem. A* **2018**, *6*, 374-382.
15. Baalbaki, H. A.; Roshandel, H.; Hein, J. E.; Mehrkhodavandi, P. *Catal. Sci. Technol.* **2021**, *11*, 2119-2129.
16. Keshri, K. S.; Bhattacharjee, S.; Singha, A.; Bhaumik, A.; Chowdhury, B. *Mol. Catal.* **2022**, *522*, 112234.
17. Guo, C. H.; Liang, M.; Jiao, H. *Catal. Sci. Technol.* **2021**, *11*, 2529-2539.
18. Takaishi, K.; Okuyama, T.; Kadosaki, S.; Uchiyama, M.; Ema, T. *Org. Lett.* **2019**, *21*, 1397-1401.
19. Tong, H.; Qu, Y.; Li, Z.; He, J.; Zou, X.; Zhou, Y.; Duan, T.; Liu, B.; Sun, J.; Guo, K. *Chem. Eng. J.* **2022**, *444*, 135478.
20. More, G. S.; Srivastava, R. *Sustain. Energy Fuels*. **2021**, *5*, 1498-1510.
21. Valenzuela, M. L.; MacLeod-Carey, D.; Marfull, C. S.; León-Baeza, J.; Martínez, J.; Antiñolo, A.; Carrillo, F. *J. Inorg. Organomet. Polym. Mater.* **2022**, *32*, 1724-1735.
22. Song, Q. W.; He, L. N.; Wang, J. Q.; Yasuda, H.; Sakakura, T. *Green Chem.* **2013**, *15*, 110-115.
23. Schoepff, L.; Monnereau, L.; Durot, S.; Jenni, S.; Gourlaouen, C.; Heitz, V. *ChemCatChem*. **2020**, *12*, 5826-5833.
24. Haq, I. U.; Qasim, A.; Lall, B.; Zaini, D. B.; Foo, K. S.; Mubashir, M.; Khoo, K. S.; Vo, D. V. N.; Leroy, E.; Show, P. L. *Environ. Chem. Lett.* **2022**, *20*, 2165-2188.
25. Fabre, E.; Murshed, S. M. S. *J. Mater. Chem. A* **2021**, *9*, 15861-15879.
26. Yan, J.; Mangolini, F. *RSC Adv.* **2021**, *11*, 36273-36288.
27. Portillo-Castillo, O. J.; Castro-Ríos, R.; Chávez-Montes, A.; González-Horta, A.; Cavazos-Rocha, N.; Granados-Guzmán, G.; de Torres, N. W.; Garza-Tapia, M. *J. Mex. Chem. Soc.* **2022**, *66*, 198-220.
28. Martínez-Palou, R. *J. Mex. Chem. Soc.* **2007**, *51*, 252-264.
29. Yan, R.; Chen, K.; Li, Z.; Qu, Y.; Gao, L.; Tong, H.; Li, Y.; Li, J.; Hu, Y.; Guo, K. *ChemSusChem*. **2021**, *14*, 738-744.
30. Zhang, J.; Li, X.; Zhu, Z.; Chang, T.; Fu, X.; Hao, Y.; Meng, X.; Panchal, B.; Qin, S. *Adv. Sustain. Syst.* **2021**, *5*, 2000133.
31. Ebrahimi, A.; Rezazadeh, M.; Khosravi, H.; Rostami, A.; Al-Harrasi, A. *ChemPlusChem*. **2020**, *85*, 1587-1595.
32. Logemann, M.; Marinkovic, J. M.; Schörner, M.; García-Suárez, E. J.; Hecht, C.; Franke, R.; Wessling, M.; Riisager, A.; Fehrmann, R.; Haumann, M. *Green Chem.* **2020**, *22*, 5691-5700.
33. Selvam, T.; Machoke, A.; Schwieger, W. *Appl. Catal. A: Gen.* **2012**, *445-446*, 92-101.
34. Cao, Y.; Zhou, H.; Li, J. *Renew. Sustain. Energy Rev.* **2016**, *58*, 871-875.

35. Xia, S. P.; Ding, G. R.; Zhang, R.; Han, L. J.; Xu, B. H.; Zhang, S. J. *Green Chem.* **2021**, 23, 3073-3080.
36. Gandhi, S.; Sethuraman, S.; Krishnan, U. M. *Dalton Trans.* **2012**, 41, 12530-12537.
37. Mdlovu, N. V.; Lin, K. S.; Weng, M. T.; Hsieh, C. C.; Lin, Y. S.; Espinoza, M. J. C. *J. Ind. Eng. Chem.* **2021**, 102, 1-16.
38. Ehsanimehr, S.; Moghadam, P. N.; Dehaen, W.; Shafiei-Irannejad, V. *Colloid. Surface. A.* **2021**, 615, 126302.
39. Laskowska, M.; Bałanda, M.; Fitta, M.; Dulski, M.; Zubko, M.; Pawlik, P.; Laskowski, Ł. *J. Magnet. Mater.* **2019**, 478, 20-27.
40. Karimi, B.; Tavakolian, M.; Akbari, M.; Mansouri, F. *ChemCatChem.* **2018**, 10, 3173-3205.
41. Arora, G.; Yadav, M.; Gaur, R.; Gupta, R.; Yadav, P.; Dixit, R.; Sharma, R. K. *Nanoscale.* **2021**, 13, 10967-11003.
42. Liu, S.; Yue, B.; Jiao, K.; Zhou, Y.; He, H. *Mater. Lett.* **2006**, 60, 154-158.
43. Sang, C.; Jin, S.; Li, G.; Luo, Y. *J. Sol-Gel Sci. Technol.* **2021**, 98, 559-567.
44. Zhao, Q.; Long, M.; Li, H.; Wen, Q.; Li, D. *New J. Chem.* **2022**, 46, 1144-1157.
45. Chen, X.; Wang, P.; Xu, J.; Han, Y.; Jin, H.; Jin, D.; Peng, X.; Hong, B.; Li, J.; Yang, Y.; Ge, H.; Wang, X. *Adv. Powder Technol.* **2017**, 28, 2087-2093.
46. Jiang, H.; Xu, X.; Zhang, R.; Zhang, Y.; Chen, J.; Yang, F. *RSC Adv.* **2020**, 10, 5116-5128.



## The Influence of Additives Upon the Energetic Parameters and Physicochemical Properties of Environmentally Friendly Biomass Pellets

---

Daniela Gheorghe, Ana Neacsu \*

Institute of Physical Chemistry, Ilie Murgulescu”, 202 Spl. Independentei, 060021, Bucharest, Romania.

\*Corresponding author: Ana Neacsu, email: [anna\\_matache@yahoo.com](mailto:anna_matache@yahoo.com); Phone: (004)021 318 85 95; Fax: (004)021 312 11 47.

Received March 28<sup>th</sup>, 2023; Accepted December 22<sup>nd</sup>, 2023.

DOI: <http://dx.doi.org/10.29356/jmcs.v68i3.2032>

**Abstract.** Solid biomass fuels are economical and practical renewable energy sources. Exploitation of agricultural biomass as a fuel offers considerable advantages in different domains as energy supply as far as the climate is involved. In this study we intended to investigate the feasibility of alternative agricultural residues of grape pomace and corn cob pellets with addition of sawdust, starch, and waste rapeseed oil and to examine how these additives affects the calorific powers and pellets physical properties. Sawdust, starch, and waste rapeseed oil addition was 10 %. Pellets were produced by a manual single pellet press. The calorific powers of the biomass samples were experimentally determined using an oxygen bomb calorimeter (model 6200 adiabatic calorimeter Parr Instruments). The results show that waste rapeseed oil addition significantly increases the calorific powers in grape pomace and corn cob pellets. The highest calorific value was obtained for the grape pomace pellets containing 10 % waste rapeseed oil, 22.14 MJ/kg, compared to grape pomace control pellets, of 21.35 MJ/kg. The calorific values of corn cob control pellets were also increased when adding 10 % waste rapeseed oil, from 17.29 MJ/kg to 19.76 MJ/kg.

The results obtained in this work, related to calorific powers, moisture, ash, volatile, sulphur and nitrogen content, fixed carbon, bulk density, fuel value index, energy density and combustion efficiency, revealed that depending on additives used and their dosage, an acceptable fuel pellet could be produced.

**Keywords:** Biomass pellets; raw materials; combustion calorimetry; additives dosage.

**Resumen.** Los combustibles de biomasa sólida son fuentes de energía renovables económicas y prácticas. Al tomar en consideración el clima, la explotación de la biomasa proveniente de la agricultura como combustible ofrece ventajas considerables como fuente de energía en diferentes ámbitos. En este trabajo estudiamos la factibilidad utilizar residuos agrícolas de pastillas de orujo de uva y elote adicionándole aserrín, almidón y desperdicio de canola para analizar como estos aditivos afectan el potencial calórico y las propiedades físicas de las pastillas. El aserrín, almidón y canola se agregaron al 10%. Las pastillas se obtuvieron en una pastilladora manual. Experimentalmente, las potencias calóricas de las muestras de biomasa se determinaron con una bomba calorimétrica de oxígeno (calorímetro adiabático Parr Instruments modelo 6200). Los resultados muestran que la adición de canola incrementa significativamente la potencia calórica de las pastillas de orujo y elote. El valor calórico más alto se obtuvo con las pastillas de orujo a las que se les adicionó un 10% de canola, y fue de 22.14 MJ/kg, comparado con el control de pastillas de orujo que tiene un valor de 21.35 MJ/kg. Las potencias calóricas de las pastillas de control de elote también se incrementaron al adicionar 10% de canola, pasando de 17.29 MJ/kg a 19.76 MJ/kg.

Los resultados de este trabajo relacionados con las potencias calóricas, humedad, contenido de cenizas, volátiles, contenido de azufre y nitrógeno, carbono, densidad de bulto, índice de valor del combustible, densidad de energía

y eficiencia a la combustión revelan que se puede obtener una pastilla de combustible aceptable dependiendo de utilizar los aditivos y las dosis adecuadas.

**Palabras clave:** Pastillas de biomasa; materias primas; calorimetría de combustión; dosis de aditivos.

---

## Introduction

A solid fuel based on plant biomass could be a substitute to coal, which in comparison to this fossil fuel, is generated in nature. The expression “biomass” suggests here a diversity of plant constituents, as well as their residues and wastes [1].

In order to produce energy, biomass can be good enough for being considered an option as sustainable and carbon-neutral raw material. In the energy sector, all over the world, there is a need for a fundamental transformation, due to the changing climate circumstances and growing emissions of greenhouse gases. Consequently, biomass gained noticeable attention as a feasible stockpile. Energy from biomass is dependent on various supplies: agricultural and house-hold waste, forest wastes and energy crops. There are two classes of biomass energy production: biofuels (liquid fuels obtained from biomass, replacing petroleum production) and biopower (electricity and heat are obtained using biomass).

In Romania, a high potential is considered to have the production of biofuels and biogas. According to the Romanian National Institute of Statistics the unused technical energy production potential from renewables is of around 8000 Ktonnes, which includes 47 % biomass and biogas, 19 % solar, 19 % wind, 14 % hydro and 2% geothermal energy [2].

Romania is the second country after France regarding the agriculture sector, for both the cultivated area and production of corn [3].

The pellet market is developing constantly, the EU being directly a leader in this area. In Europe, an essential role will have the pelleted solid biofuels in achieving renewable energy objectives, as stated by European Commission. All this reveal furthermore extension in pellet manufacturing and requirement for employment of new, low-cost, substitute raw materials. Alternative supplies of notable concern are residues and by-products from agriculture and food/feed processing. Biomass constituents with high- and low-energy can be mixed in convenient amounts. Constituents generating excessive quantity of ash can be combined with constituents that produce a small amount of ash in order to obtain a good-quality pellet. Choosing the appropriate constituents and combine them in suitable ratio customize the calorific value, moisture and ash content. In order to enhance the quality parameters, biomass can be combined with constituents, such as wood or coal dust [4].

In this study grape pomace and corn cob were chosen as raw materials for obtaining alternative biofuel pellets. The demand to develop the quality of the pellets has become progressively significant. The quality of pellets is established by the end-user’s specification on the combustion systems and the handling characteristics [5].

According to Grover et al [6] the first and most relevant step in the analysis into the employment of fuels obtained from waste for energy targets is the achieving of calorific values. Compressed biofuels are performed for improving the fuel properties of residues. Compressed biofuels derived from solid biomass residues, briquettes or pellets, will accomplish a better fuel homogenization, lower moisture content and a higher energy density [7].

Grape pomace is a powerful source of biomass, being the most abundant waste from wine production [8]. The most outspread crops are grapevine, representing 50 million tonnes of grapes per year of which more than 20 million tonnes are assumed by European producers [9]. Romania recorded an increase of the grapes production since 2014, this great potential is due to its geographical position, climatic condition and sandy soils [10]. The waste that comes from wine processing (seeds, skins, leaves and stems) obtained by the winemaking industry, turn into an ecological and economic difficulty, thus, utilisation within power sector is financially reasonable and technically justified in both small and large wineries [11].

Corn cobs are a ratio of the corn residues (corn stover), besides stalks, leaves (including tassels) and husks [12]. The capacity of corn stover for energy production are expressive since corn is one of the most expanded grown field crops worldwide [13].

Correlating to further crop residues, corn cobs have more favourable combustion properties. Hence, this fuel is a challenge to woody fuels, intending to diminish undesirable consequences after combustion. Corn cob has a heating value of about 19.14 MJ/kg, thus might be employed as an alternative for coal or mixture with coal to decrease hazardous emissions which contaminate the environment. In Romania, the areas cultivated for corn and sunflower are placed in the top four along with France, Germany, and Spain. Our country was second after France for both the cultivated area and production of corn [3]. A method to handle these agricultural residues from industrial processing is to use it for solid combustion as a solid fuel in blends with various additives, due to the inconveniences with pelletization as well as with emissions of undesired by-products during combustion. This is the argument why the additives with good densification characteristics seems encouraging for preparing pellets with enhanced quality.

In the literature, there was implemented a wide range of calorimetric measurements of combustion heat and caloric power of grape marc in its original state, grape marc after seed separation (assumption of oil pressing usage), and in seeds themselves. The results indicate that the heating power varies between 16.07-21.14 MJ/kg [14]. Although many biomass feedstocks possess natural binders, they do not have enough strength due to the limitations of binding between particles. The most used additives can be coal, lignosulphonate, starch, sawdust and sugar, dolomite, corn or potato flour, and some vegetable oils [15-16]. Additives are added to improve the combustion properties, improve durability, or to reduce wear on the pellet die. The additives and binding agents influence all the main features of the biomass pellets. Each additive has consequences in distinct physical and thermal properties when used with various biomass materials. The additives act as a lubricant and raise the production rate and lower the energy use per unit output of wood pellets. In the literature is specified that 0.5 % assay of motor oil and vegetable oil raise the calorific values and 0.5 % corn starch additive decreases calorific values by about 0.5 MJ/kg [16].

Gageanu et al. performed a series of experimental research conducted on pellets obtained from agricultural biomass, namely, wheat straws, rapeseed stalks, corn stalks as received and with additives (paraffin 5 %, paraffin 1.5 % + corn starch 5 % and dolomite 5 %). The authors demonstrated that the pellets obtained after combining different types of materials and those obtained by using additives showed good results, both during the production process as well as in terms of the quality parameters [17].

Starch is already used on some markets to achieve reduced operating costs and better durability. Obernberger and Thek found that 7 of 23 producers of pellets (mostly in Austria) used starch as a biological binding agent to reduce the operating cost and achieve higher abrasion resistance [18]. Nielsen showed by laboratory measurements that, when 5 % of potato starch was added, the strength of the pellets increased [19].

Corn starch was the most effective of the starch binders; the tensile strength of the pellets improved with up to 10 wt %. Further additions of the three starches, up to 20 wt%, made the pellets deteriorate in terms of tensile strength, even though density increased [20].

According to Demir et al., starch may function as an adhesive agent. Additives of 2.5 %, 5 %, 7.5 %, 10 % (wt/wt) starch to pellet materials were examined. Their results showed an improvement on pellet processing, calorific values and physical properties with increasing starch content [21].

Falemara et al. studied the physical and combustion properties of briquettes produced from agricultural wastes (groundnut shells and corn cobs), wood residues (*Anogeissus leiocarpus*), and mixture of the particles at 15 %, 20 %, and 25 % starch levels (binder). The authors concluded that briquettes containing 25 % starch level had better quality in terms of density and combustion properties, thus being suitable as feasible alternative energy source [22].

Rice husk and coconut shell have been proposed as alternative energy sources by Yuliah et al. The basic ingredients were briquettes prepared from rice husk and coconut shell charcoal with varying composition and addition of tapioca starch gradually as adhesive material to obtain briquettes in solid with the maximum heat energy content. After going through pressing and drying process, the briquettes with 50:50 percent of composition and the 6 % addition of adhesive was found to have the highest heat energy content, equal to 4966 cal/g [23].

In the literature, studies regarding the effects of additives on the pelletization of raw and torrefied food waste were performed using three binders; starch, lignin, and vegetable oil, at various compositions of 10 %, 15 %, and 20 % in order to obtain the raw and torrefied food waste pellets [24].

Potato starch is another common binder that can reduce the energy needed for pellet formation, increasing the moisture content, and decreasing the lower heating value [25,26]. Concentrations of 10 %, 20 %, and 30% provided ash content of 1.45 %, 1.50 %, and 1.59 % and calorific value of 18.2, 18.1, and 18.0 MJ/kg, respectively.

The effects of paraffin, corn starch, and dolomite on the quality of wheat straw pellets were investigated by Gageanu et al. [17,27] founding beneficial effects of these binders on the pellet length, surface, shape, bulk density, and ash content.

Vegetable oils are referred in literature as additives which decrease die wall friction and reduce energy consuming for pelleting procedure as a result of lubrication effect, however there is no systemic research about the impact of oil on pelletability and physical characteristics of pellets.

Waste cooking oils (WCO) are classified among used vegetable oils (UVO), which, according to the Waste Catalogue Regulation of the Minister of Environment dated 27 September 2001, constitute waste hazardous for the environment [28].

Waste vegetable oil is disposed by restaurants, food manufactures, households since it cannot be furthermore utilized in human or animal dietary. Improper removal of waste vegetable oil can be ecologically harmful; hence its furthermore usage is preferred. Waste vegetable oil has an appreciable capacity as a constituent of pelleted biofuels due to the fact that it is non-fossil oil, possess high calorific value and does not necessitate any preliminary treatment. Oil inclusion can enhance wood fuel characteristics, but compaction of wood with adding oil could be more complex. Utilization of oil can decrease dust generation during pelleting and afterward throughout pellet manipulation [29].

Misljenovic et al. added waste vegetable oil in two different amounts in spruce sawdust, which has been pelletized in a single pellet press under four compacting pressures. Their results led to the conclusion that oil addition significantly increases energy content in biofuel, make material less compressible, reduce pellet strength and reduce friction on the pellet – die contact area. The most important change caused by waste vegetable oil addition is reflected in increasing energy content [30-31]. Emadi et al. used plastic wastes as additives in the pelletizing process of wheat straw and barley straw. The result showed that the higher heating value and tensile strength were increased [32]. Similar results were reported by Saletnik et al. modifying the energy parameters of wood pellets using waste cooking oil. The waste cooking oil was applied at the rates of 2 %, 4 %, 6 %, 8 %, 10 % and 12 % relative to the weight of pellets, increasing the calorific value of the pellets without decreasing their durability. The highest dose of the modifier (12 %) on average led to a 12–16 % increase in calorific value. In each case, the addition of sunflower oil resulted in decreased contents of ash in the pellets; on average a decrease of 16–38 % was reported in the samples treated with the highest dose of the modifier [33].

In literature, experiments concerning fast pyrolysis of corn cob (CC) and waste cooking oil (WCO) were conducted in a fixed-bed reactor, using CC/WCO ratios (1:0.1; 1:0.5; 1:0.87; 1:1 in mass). CC/WCO ratio of 1:1 was found to be the optimum considering high bio-oil yields (68.6 wt.%) and good bio-oil properties (HHV of 32.78 MJ/kg) [34].

The benefit of oil palm and para-rubber residues, and the potential of these residues as biomass were examined by Wattana et al [35]. The biomass pellets were prepared from oil palm leaves (PL) and frond (PF), para-rubber leaves litter (PAL) and branch (PB) and their blend (mixing of 50 wt.% of two materials). These samples were the waste in the local plantation in Pathiu District, Chumphon Province, Thailand. The authors demonstrated that the characteristics of mixed biomass pellets differed from pure biomass pellets which contributed to the further improve its quality.

Waste engine oil is a type of artificial organic additive. The waste engine oil was recycled as an additive in wheat straw pelletizing process. Wang et al. focused on the reuse of wheat straw and waste engine oil by producing pellets with mixtures of the two products. The engine oil content was 5 %, 10 %, 15 % and 20 % included in biomass pellet. The higher heating value was only affected in this case by the additive content and increased linearly as the oil content increased [36].

In our study, we have demonstrated that 10 % content of starch, sawdust and waste vegetable oil applied to grape pomace and corn cob biomass, are suitable for obtaining pellets with good characteristics in term of combustion. Proximate analysis, namely, moisture content, volatile matter, ash content, and fixed carbon was performed. Combustion calorimetry method was applied for obtaining the calorific values of the studied species.

The obtained results will complete the existing databases concerning the properties of solid biofuels from biomass containing the mentioned additives. Our investigations clearly indicate that the type of biomass used in the process has an important effect on the energy parameters.

The achieved data are helpful for both improving the value of characterized biomass pellets and for the recycling of used rapeseed oil.

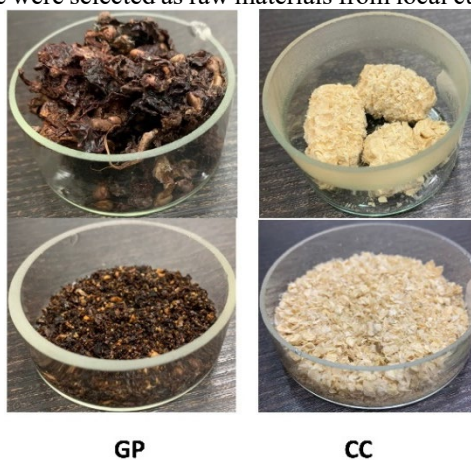
## Experimental

### Material

#### Samples description

The biomass pellets resulted from grape pomace and corn cob and their mixture with 10 % waste rapeseed oil, sawdust and starch were used. The rapeseed oil was acquired from household, starch and sawdust were used from the market.

Corn cobs and grape pomace were selected as raw materials from local cultivators, in September 2021.



**Fig. 1.** Biomass grape pomace (GP) and corn cob (CC) before and after grinding.

### Method and equipments

The pelletisation process consists of certain subprocesses such as grinding, drying, milling and pelleting. The process of pelletization is affected by the material's moisture content, particle size, density, fibre strength, lubricating characteristics and natural binders [37].

Prior to the pelleting, the samples were dried at 105 °C in the laboratory oven, until constant mass [38]. It is known that moisture content affects the energy yield of the process.

In the pelletisation process, pretreatment mainly consists of two different processes: drying and grinding. Drying is usually required to decrease the moisture content of biomass which in many cases exceeds an appropriate value for pelletisation (between around 6 and 18% moisture content). Milling is also required in order to transform the feedstock into a more uniform material. The material after milling process consists of particles which are of equal size and similar moisture content. This homogeneity makes the pellets more durable [39]. Furthermore, milling brings size reduction which in turn leads to an increase in particle surface area facilitating interparticle bonding [40].

In raw state, up to 70-80 % mass of grape residues is water. It is necessary to dry it first to guarantee effective utilisation within most of power technologies.

According to Burg et al., to reduce a moisture content of grape pomace from 60 % to 8 %, approximately 1.5 GJ of heat need to be utilised. However, that value may be covered by renewable energy streams (solar, geothermal) or waste heat (from fumes) in integrated driers [41]. Comprehensive drying of grape pomace is essential to be introduced also for reasons of the periodicity of the grape pomace generation

(harvesting takes place between September and October). When having a lot of water, aerobic biodegradation during storage contributes would deteriorate quality as a fuel [42].

The moisture content is determined by weighing of the sample before and after drying, the obtained difference in weight being considered for calculation, according to o EN 13183-1:2004 standard. [43].

The different blends of corn cob and grape pomace containing 10 % starch, sawdust and used rapeseed oil were prepared in appropriate proportions, weighting in dry basis and, by means of a mechanical blender, thoroughly mixed in order to ensure optimal homogenization that guaranteed the right composition of mixtures. The purpose was to obtain pellets that would meet the specifications established for industrial pellets. The proportion of biomass samples for each blend was configured, taking into account the N, S and ash contents of each biomass sample, since these parameters could restrict the quantity of biomass permitted in the mixture with respect to pellet quality specifications. After mixing, there have been obtained stable pellets by using a Parr 2811 Pellet Press. This pellet press provides a convenient means for compressing powdered materials into pellet or tablet form, being a compact, hand-operated press producing uniform pellets in a polished stainless-steel die and ejecting them smoothly into a stainless receiver without danger of contamination. This system is designed to provide a steadily increasing mechanical advantage up to a ratio of approximately 50 to 1 at the end of the stroke. Thus, a force of 20 pounds applied to the lever develops approximately 1000 pounds on the punch, which is adequate to produce firm pellets from most powdered materials. The obtained pellets are cylindrical in shape with flat ends and have ½ inch diameter [44]. The calorific values for all the blends studied were higher than 16.5 MJ/kg, which is the minimum value required for the industrial pellet qualities.

The calorific energy values were measured using an isoperibolic Parr Instruments 6200 Combustion Calorimeter, previously described [45]. Proximate analysis was performed to establish the standards quality of the pellets produced.

The calorific values using Parr Instruments 6200 Combustion Calorimeter were calculated following ASTM D5865 standard test for gross calorific value [46] and standard operating procedure of the calorimeter [47]. The method was detailed in previous papers [45,48]. The nitrogen was calculated from the nitric acid formed [45]. Sulphur content was performed by adding in the resulted solution of the calorimeter bomb after combustion, a diluted sodium hydroxide to convert sulphur to sulphates [49]. The obtained results are crucial in the estimating of the emission of gas contaminants generated during combustion (dioxins, furans, NO<sub>x</sub>, SO<sub>x</sub>, or HCN), corrosion problems in heaters and bad operation in boilers.

Bulk densities have a major impact on shipping and storage charges [50-51] and were calculated using an analytical balance Mettler Toledo, model XP6.

Volatile matter is a characteristic feature of solid fuels, which is standardized when assessing energy biomass [52-54]; biomass is characterized by a high content of volatile matter [53] which includes gaseous products and vapours produced during the thermal decomposition of solid fuel under anaerobic conditions. The amount of volatile components essential to the assessment of the energy suitability of solid fuels decreases as the degree of carbonization increases. Volatile matter content (%) is an important parameter which has a considerable influence on the combustion process [55]. Data from the literature indicate that biomass contains up to 2.5 times more volatile matter than coal, which has a significant impact on the conditions under which it is ignited and combusted [56].

The presence of volatile compounds can change the behaviour of the fuel in generating boilers, variations in efficiency and severe operational problems. Volatile matter content was calculated according EN ISO 18123:2015 standard and following the procedure stated in the literature [57].

Fixed carbon [58-59] is the mass left after the release of volatile compounds, excluding ash and moisture. This may be calculated using some of the data obtained previously in the proximate analysis. The higher the percentage of fixed carbon in a solid fuel, the higher the calorific value and consequently, the fuel is better.

The ash content (AshC, %) was derived from the difference in the weights of the bomb crucible before and after combustion. To obtain accurate results the measurements were performed in triplicate, in accordance with the protocols of the literature [60]. Similar to hard coal and lignite, biomass combustion produces solid waste, mainly in the form of bottom ash. The quantity of this waste is largely dependent on the type of biomass used [56]. Typically, biofuels have much lower ash content after combustion than fossil fuels such as coal or lignite. This has certain operational benefits, i.e., longer periods between ash disposal.

The energy density ( $\text{MJ/m}^3$ ) was derived from the bulk density and calorific value of the biomass raw materials [61-62].

The analysis of the fuel value index (FVI,  $\text{GJ/m}^3$ ) shows that the materials are applicable to the energy product, a threshold value for application as fuel being  $100 \text{ GJ/m}^3$  [63]. The procedure was previously described [64]. Each test was carried out in triplicate. The aim of the knowledge of each property under investigation is to certify the solid fuel derived from biomass in accordance with European standards for solid biofuels CEN/TS 14961/ 2005.

Combustion efficiency is a measure of how well the fuel is being burned and the main parameter to describe the performance of a biomass furnace. Essentially, it is the percentage of the energy of a fuel that has been used up in the burning process. While complete combustion (100 percent combustion efficiency) is theoretically possible, in reality it is not, mostly due to heat losses [65].

In literature, a method for calculation of the combustion efficiency is presented. The method is based on the combustion reaction and can be applied to every biofuel with given composition. The following equation is proposed [66-67]:

$$\text{Combustion efficiency (\%)} = 1 - \left[ \frac{\text{unburned fuel in bottom solids}}{\text{initial fuel placed in burner}} \right] \times 100 \quad (1)$$

The statistical analysis of the obtained data was performed using Minitab 18 program [68]. The median of the survey and the standard deviation was determined as the main statistical parameters of tendency and dispersion, for each group of values. The entire statistical analysis was carried out with a confidence interval of 95 % and an alpha error of 0.05.

## Results and discussion

Extensive knowledge of all the parameters presented above is essential for characterizing a biomass sample as a potential fuel resource. Calorimetry may be the most influential of all because it provides precise data on the heating value of each of the samples studied; data that when combined with market prices for each fuel, enable consumers to compare the energy and financial yield of each one.

Grape husk (pomace) obtained from a winery in native state cannot be used efficiently due to its size, biodegradability, and low weight. The grape raw materials has a very good caloric power, comparable with the one of fire wood and pellets obtained from beech or resinous sawdust, thus obtaining pellets of good quality from this raw material, especially when additives are used is of great interest. As other researchers stated before, the more sugar the higher calorific value will be [69].

Due to their high calorific value the corn cob cores are often used as fuel, and the by-products of the combustion process are also used. The products of the corn cob core combustion process, i.e., ash, can be used as partial substitutes in cement production [70].

Starch-based and sawdust binders offer numerous advantages that are both ecologically and economically beneficial, including improving durability, reducing abrasion and dust formation, lowering the energy consumption of the pelleting plant and reducing maintenance and wear costs [71]. The possibility of using used vegetable oil in a valuable way, combined with the advantage of avoiding its dispersion into the environment and its very high availability, has encouraged scientists to look for a way to reuse waste. The most common uses of used vegetable oil are the production of bio-lubricants or fuel as animal feed, or as additives for asphalts and for energy production [28]. In Fig. 2 are shown the obtained higher heating values and moisture content for the studied samples. Moisture content is known to be one of the most important parameters for determining the quality of biopellets. The low water content will facilitate the ignition of the biopellet and extend the shelf life. High moisture levels can result in mould growth during storage [72]. From Fig. 2 it can be ascertained that single additive waste rapeseed oil has the highest heating value ( $40.21 \text{ MJ/Kg}$ ) and the lowest moisture content (1.32 %). The grape pomace pellets containing 10 % waste rapeseed oil have the highest heating value ( $22.14 \text{ MJ/kg}$ ) and the lowest moisture content (2.81 %) from the analysed samples containing

additives, thus being in agreement with literature statements [72]. Authors demonstrated that increasing dosages of wheat and maize starch further reduces the final wood pellet moisture content [16].

An important aspect to take in consideration for obtaining good quality pellets is the method of pellet refining. Densification by means of pelletisation is considered to be a proven technology to improve biomass properties for its conversion into heat and power. Also, the torrefaction process upgrades the biomass and produce solid fuels with better quality. Torrefaction is helpful in enhancing biomass for its use in wider applications. A major advantage of torrefaction is that it can break down the fibrous character of biomass and reduce the formation of soot [73].

Torrefaction is a fast-developed technology to produce solid biofuel (biochar) or sustainable materials for several applications, but the problem induced by tar, one of the by-products formed from biomass torrefaction, is an important challenge that needs to be solved, especially in industrial systems. The torrefaction process increases the ash content in final products, and this limits the applications of combustion and gasification from torrefied biomass. Comparing the raw and torrefied biomass higher heating values (HHV) results that torrefied biomass values ranges between 16-29 MJkg<sup>-1</sup>, higher than raw biomass values of 15-20 MJkg<sup>-1</sup> [74].

An alternative process for the production of biopellets is a combination of torrefaction with pelletisation and is called the TOP process for the production of TOP pellets. The TOP process integrates the advantages of both processes with respect to the quality of the biopellet, having a net calorific value of 19 to 22 MJ/kg as received. This results in an energy density of 14 to 18.5 GJ/m<sup>3</sup>, significantly higher than conventional biopellets produced from softwood (sawdust: 7.8 to 10.5 GJ/m<sup>3</sup>) [75].

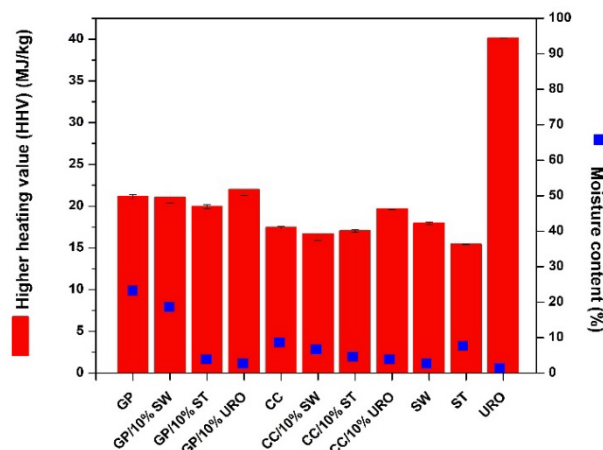
In Table 1 are presented a summary of various biomass combustion technologies.

**Table 1.** Summary of various biomass combustion technologies.

| Species                                       | HHV (MJ/Kg) | LHV (MJ/Kg) | Moisture content (%) | Technologies                                    |
|-----------------------------------------------|-------------|-------------|----------------------|-------------------------------------------------|
| <b>Grape pomace (our exp.)</b>                | 21.35       | 21.14       | 23.28                | combustion calorimetry                          |
| <b>Grape seeds (lit.)</b>                     | 20.83       | 20.03       | 19.2                 | combustion calorimetry [76]                     |
| <b>Corn cob (our exp.)</b>                    | 17.66       | 17.42       | 8.63                 | combustion calorimetry                          |
| <b>Corn cob (lit.)</b>                        | 18.7        | 18.3        | 7                    | torrefaction in tubular furnace [77]            |
| <b>Maize Stalks (Corn Cobs) (lit.)</b>        | 15.46       | 15.06       | 6.9                  | torrefaction technique / pyrolyzed samples [73] |
| <b>Corn stover (lit.)</b>                     | 17.6        | 17.2        | 8.1                  | combustion calorimetry [78]                     |
| <b>All wood fuels and most biomass (lit.)</b> | 17.9        | 17.5        | 5-60                 | moving grate furnaces [79]                      |
| <b>Sorghum (lit.)</b>                         | 15.8        | 14.4        | 5-60                 | bubbling fluidized bed [79-80]                  |
| <b>Sorghum (lit.)</b>                         | 17.1        | 15.8        | 5-60                 | circulating fluidized bed [79-80]               |
| <b>Sawdust (our exp.)</b>                     | 18.17       | 17.94       | 2.82                 | combustion calorimetry                          |
| <b>Sawdust (lit.)</b>                         | 19.47       | 19.3        | 3.2                  | briquetting [81]                                |
| <b>Starch (our exp.)</b>                      | 15.45       | 15.42       | 7.66                 | combustion calorimetry                          |
| <b>Starch (lit.)</b>                          | 19.43       | 19.22       | 2.67                 | combustion calorimetry [82]                     |
| <b>Waste rapeseed oil (our exp.)</b>          | 40.22       | 40.11       | 1.32                 | combustion calorimetry                          |
| <b>Sunflower husks (lit.)</b>                 | 18.83       | 18.44       | 4                    | combustion calorimetry [76]                     |



Compared with other method of biomass energy fortification like torrefaction, the addition of 10 % oil increased the final energy content similarly as torrefaction at 225 °C. This way of increasing the energy content is definitely easier and less energy demanding compared to torrefaction [83].



**Fig. 2.** Plot of the higher heating values and moisture content for the studied samples. (GP=grape pomace; CC=corn cob; SW=sawdust; ST=starch; URO=used rapeseed oil; GP/10%SW=grape pomace containing 10 % sawdust; GP/10%ST=grape pomace containing 10 % starch; GP/10 %URO= grape pomace containing 10 % used rapeseed oil; CC/10%SW=corn cob containing 10 % sawdust; CC/10%ST=corn cob containing 10 % starch; CC/10%URO=corn cob containing 10 % used rapeseed oil).

Our values for high heating value of control grape pomace (21.35 MJ/kg) and corn cob (17.29 MJ/kg) are close to the values reported for bamboo biomass ranging from 18 to 21 MJ/kg. These values are higher than other commonly used biomass such as sugarcane bagasse (16.60 MJ/kg), corn cob (16.90 MJ/kg), barley straw (16.81 MJ/kg), rice straw (16.78 MJ/kg), pine wood chips (16.81 MJ/kg), lignite (16.16 MJ/kg) and palm kernel shell (19.82 MJ/kg) [84-85].

The values of the higher heating value for control grape pomace (21.35 MJ/kg) calculated in this work are greater than the values reported by Annamalai et al [86], of about 20.34 MJ/kg. It is obvious that grape pomace is a material with a very good calorific value, surpassing the values of wood (14.6 MJ/kg) and cereals (18.00 MJ/kg) [14, 87]. The high heating values are caused by wastage of sugars. According to the literature, it is very possible to use waste corn cob as fuel in the power plant due to its calorific value of about 16.92 MJ/kg [88], close to the results reported in this study, of 17.29 MJ/kg.

Analysing the obtained results, it can be ascertained that samples containing 10 % starch present a lower heating value than the control sample (see Fig. 2), a higher value being observed for samples with 10% waste rapeseed oil. Nosek et al [89] reported for the wood pellets that a 0.5 % dosage of motor oil and vegetable oil increases calorific values, and 0.5 % corn starch additive decreases calorific values by about 0.5 MJ/kg.

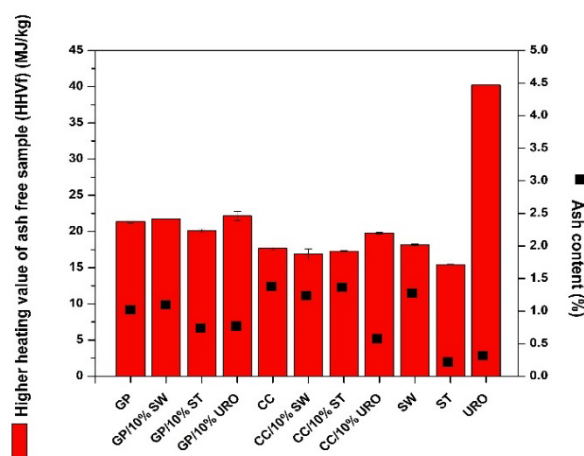
The moisture content obtained in this study for grape pomace is 23.28 % and for corn cob samples 8.63 % without using additives. Adding the mentioned additives, these values decrease ranging between 2.81 % and 6.65 %, the lowest value being obtained by adding 10 % waste rapeseed oil (Fig.2). These results indicated that additives are beneficial for decreasing moisture and keeping it under 10 %, the desired value for optimal storage and use, the same behaviour being highlighted by Gageanu et al. in their study concerning wheat straws, rapeseed stalks, corn stalks and their mixtures with paraffin 5 %, paraffin 1.5 % + corn starch 5 % and dolomite 5 %. Their moisture values ranged between 8.25 % and 11.65 % for pellets obtained without using additives and between 7.48 % and 9.25 % for pellets obtained using additives [17]. Li and Liu reported that a good quality pellet has a moisture content ranging between 6 % and 12 % [90].

Kumar et al. investigated the effect of combining dry leaves, rice husk and sawdust in different proportions and concluded that the dry leaves can be used as potential source for the production of briquettes

in India. Their higher heating value of 20.03 MJ/kg indicates that the briquette could supplement the traditional wood fuel for cooking and other purposes. Sawdust was added in proportion of 20 %, 40 % and 50 % respectively. Briquette made from equal proportions of sawdust and rice husk had the lowest heating value, of 16.52 MJ/kg, thus resulting that blending of biomass materials will not always produce higher quality briquettes [91].

Our results indicated an increase of the higher heating value by adding 10% sawdust in grape pomace and corncob samples, from 21.35 MJ/kg (control grape pomace) to 21.72 MJ/kg and from 17.29 MJ/kg (control corncob) to 17.39 MJ/kg, respectively.

Greinert et al. in their study evidenced that pellets prepared from a mixture of 80 % of straw and 20 % of wood had a low ash generation value amounting to 2.34 % and a calorific value of 18.95 MJ/kg. The pellets prepared from a mixture of 70 % of straw, 27 % of wood and 3 % of lime had a calorific value of 18.83 MJ·kg<sup>-1</sup> and an ash generation amounted to 2.98 % [92]. The amount of ash generated from biomass is described as variable, depending on the origin of the material. For pure wood, it is within 0.4–1.8 %; for wood bark, it is within 6.3–10.4 %; for energy plants, it is within 2.4–7.7 %; for agricultural biomass, it is within 6.9–9.2 %; for agri-food industry wastes, it is within 1.1–9.2 % [93]. From Fig. 3 we can conclude that our ash values for corn cob and grape pomace are in agreement with the above-mentioned intervals.



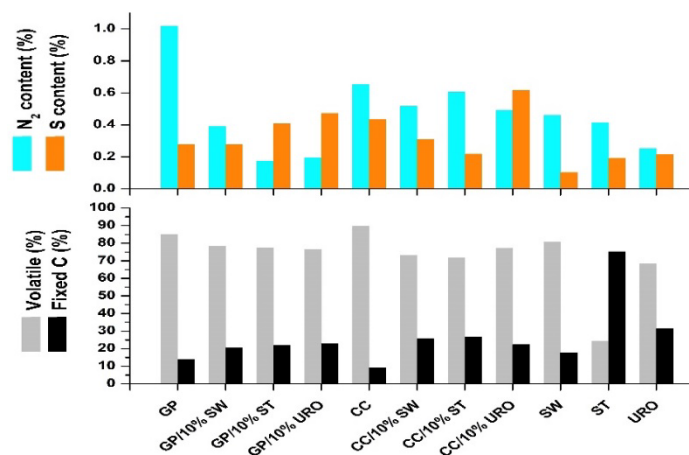
**Fig. 3.** Plot of the higher heating values and ash content for the studied samples.

(GP=grape pomace; CC=corn cob; SW=sawdust; ST=starch; URO=used rapeseed oil; GP/10%SW=grape pomace containing 10 % sawdust; GP/10 %ST=grape pomace containing 10 % starch; GP/10%URO= grape pomace containing 10% used rapeseed oil; CC/10%SW=corn cob containing 10 % sawdust; CC/10%ST=corn cob containing 10 % starch; CC/10%URO=corn cob containing 10 % used rapeseed oil).

In order to guarantee a combination of efficiency and comfort for the consumer of pellets in the home heating sector, a high ash content should be avoided, as this would eliminate the necessity of emptying the ash box at regular intervals, minimize the risk of slag formation in the furnace and lower soot emissions [18]. Taking these risks into account, the 10 % waste of rapeseed oil corn cob samples seems to be the most suitable raw materials for pellet production, with an ash content of 0.578 %. The low ash content indicates the good quality of the pellets, the values obtained from this study are less than 4 % (Fig. 3), considered as the tolerance level for the ash content in the fuel [94]. Ebeling et al. reported 1.4 % ash content for corn cob, which is lower than for other agricultural biomasses., e.g. the corn stover has 6.7 % ash content and the wheat straw 5.7 %, but higher than the woody biomass with an average ash content of 0.9 % to 1.2 % [95]. The control grape pomace sample has an ash content of 1.017 % and corn cob 1.374 %. The lowest content of ash was calculated for pellets containing 10 % waste rapeseed oil, grape pomace (0.77 %) and corn cob (0.578 %) respectively. In literature it was demonstrated by Saletnik et al that addition of waste cooking oil, even at a rate of 2 %, resulted in a statistically significant decrease in ash contents in beech wood pellet from the Pomorskie Region, in

coniferous wood pellet from the Swietokrzyskie Region and in coniferous and deciduous wood pellet from the Podkarpackie Region [33].

Regarding the wood pellets, Kuokkanen et al. found that a supplement of 1 % potato flour does not affect ash content, but 2 % dosage of the same additive increases ash content from 0.5 % (native wood) to 0.6 % [96].



**Fig. 4.** Plot of the fixed carbon (%), volatile matter (%), sulphur and nitrogen content (%) for the investigated sample.

(GP=grape pomace; CC=corn cob; SW=sawdust; ST=starch; URO=used rapeseed oil; GP/10%SW=grape pomace containing 10% sawdust; GP/10%ST=grape pomace containing 10% starch; GP/10%URO=grape pomace containing 10% used rapeseed oil; CC/10%SW=corn cob containing 10% sawdust; CC/10%ST=corn cob containing 10% starch; CC/10%URO=corn cob containing 10% used rapeseed oil).

Grape pomace and corn cob have very low nitrogen and sulphur levels compared to coal (nitrogen 0.8-1.9 % and sulphur 0.7-1.2 %) [97]. In this study, control grape pomace has a nitrogen level of 0.517 %, the lowest level being obtained for grape pomace with 10 % starch, about 0.172 %. Corn cob presents a nitrogen level of 0.653 %. Knowing the nitrogen content of biomass is important to assess nitrogen oxides (NO<sub>x</sub>) that are air pollutants. From Fig. 4 it can be ascertained that the presence of additives of 10 % results in decreasing the nitrogen content of the investigated samples.

Malat'ák et al in their study on white and red grape pomace as well as grape stems, added straw of *Miscanthus sinensis* (in proportion of 25 %, 50 % and 75 %) in order to verify the possibility of a reduction in emissions of NO<sub>x</sub>. In their study, NO<sub>x</sub> concentrations decreased significantly in stems and gradually in pomaces. The mixtures with 50 % and 25 % red grape pomace indicate the effect of addition of cleanly burning biomass on the emissions of CO and NO. With an increasing proportion of *Miscanthus* straw, the emission concentrations of nitrogen oxides decreased [7].

The sulphur levels for control samples are lower compared to coal, this making them emit less sulphur oxides (SO<sub>x</sub>) than fossil fuels. Control grape pomace sample has 0.279 % sulphur content and control corncob 0.436 %. Greinert et al. reported a low content of sulphur for the studied mixtures of straw and wood, about 0.3 % comparing with our mentioned results. The authors stated that the content of biomass components is strongly related to the species of energy plants and particular parts of these plants [92].

Sulphur is a major problem because of the accumulation of sulphates on the heat transfer surfaces of the combustion chamber [98]. Research has demonstrated that the biomass tested contains a quantity of sulphur that meets the standards for wood pellets. Moreover, the presence of sulphur is a natural consequence of the sulphur content of vegetable proteins, which is a building material for the biomass tested.

The percentage of fixed carbon content in pellets is a critical factor in determining the calorific value of the fuel [99]. From Fig. 4 it can be seen that the samples containing additives have a high level of fixed carbon than the control samples, thus a high calorific value, which is in agreement to literature statements [50].

The approach of volatile matter assigns the components released when fuel is heated at a high temperature, eliminating moisture, being part combustible gases ( $C_xH_y$  gases, CO or  $H_2$ ) and part incombustible ( $CO_2$ ,  $SO_2$  or  $NO_x$ ). Usually, biomass has a very high volatile level, with common biomass values at about 75 %, but they may increase to 90 %, depending on the sample [100]. The lowest volatile sample should have the highest energy content. Corn cob pellets without additives have the highest volatile content of 89.6 %; this means that more energy will be needed to burn the volatile matter before releasing its thermal energy. By comparing the volatile matter content of the samples containing 10 % starch with pristine ones, results that this additive produces the decreasing of the volatile matter content. This is caused by the presence of volatile substances contained by an adhesive, such as CO,  $CO_2$ ,  $H_2$  and  $CH_4$  [23]. The most volatile matter is contained by pristine samples of corn cobs and grape pomace as it can be observed from Fig. 4.

For comparison, Maj et al. [101] indicated that the volatile content in the corn cobs cores from seed production was 69.24 %, below than the values reported in the analyses performed in this study. On the other hand, Lu et al. [54] carried out studies on the volatile matter content in 66 types of biomasses and stated that their levels range between 70.39 % - 83.92 %. This analysis shows that the volatile components reported in the literature are typically lower than the values obtained in the experiments performed in this work.

The high heating value (HHV) was found to be ranged between 16-21 MJ/kg for the two types of biomasses studied. Among the used additives, the waste rapeseed oil presented the highest HHV values (40.21 MJ/Kg), which indicated that it would be the most appropriate additive for improving the combustion characteristics of biomass. It should be pointed out that the calorific value of pellets obtained from agricultural biomass is extremely important for professional energetics because this index affects the price of the product delivered.

The combustion efficiencies for all types of the studied pellets were calculated using equation (1) and ranged between 98 up to 99.91 % (see Table 2). Our results in terms of combustion efficiencies are close to the values obtained by Chen et al. for pellets made from wood and coal residues at various ratios (0, 25, 50, 75, and 100 % wood, and 50 % wood-plus-limestone). The authors stated that the obtained combustion efficiencies, ranging from 96 to 100 % of all types of investigated pellets were excellent [67].

Well-designed pellet-fired systems can achieve efficiencies of over 80 per cent. Many pellet stoves operate with a very high excess air level, which reduces their efficiency to 50–60 per cent. Technology to reduce emissions and improve combustion efficiency is being developed continuously. Thus, the negative environmental impacts of biomass combustion that exist today will be reduced in future plants [102].

**Table 2.** Determination of bulk densities and energetic features of grape pomace and corn cob with different additives.

| Species                   | Bulk density (kg/m <sup>3</sup> ) | FVI (J/cm <sup>3</sup> ) | Energy density (MJ/m <sup>3</sup> ) | Combustion efficiency (%) |
|---------------------------|-----------------------------------|--------------------------|-------------------------------------|---------------------------|
| <b>Grape pomace (GP)</b>  | 431.5                             | 388.9                    | 9212.5                              | 99.07                     |
| <b>10% sawdust-GP</b>     | 382.4                             | 396.9                    | 8121.11                             | 98.71                     |
| <b>10%starch-GP</b>       | 462.8                             | 3266.5                   | 9293.5                              | 99.27                     |
| <b>10% waste oil-GP</b>   | 422.5                             | 4317.9                   | 9354.7                              | 99.05                     |
| <b>Corncob (CC)</b>       | 217.2                             | 438.05                   | 5194.3                              | 98.45                     |
| <b>10% sawdust-CC</b>     | 159.24                            | 326.66                   | 4687.17                             | 98.59                     |
| <b>10% starch-CC</b>      | 294.13                            | 587.87                   | 5755.38                             | 98.96                     |
| <b>10%waste oil-CC</b>    | 191.4                             | 1681.08                  | 5784.0                              | 99.30                     |
| <b>sawdust</b>            | 175.2                             | 882.13                   | 3183.03                             | 98.76                     |
| <b>starch</b>             | 640.8                             | 5874.8                   | 9900.3                              | 99.76                     |
| <b>Waste rapeseed oil</b> | 939                               | 75707.3                  | 33977                               | 99.91                     |

From Table 2 it can be observed that the studied biomass has low bulk density, which consists of pieces of different shapes and sizes. For this reason, the low energy density was increased by converting the free biomass to dense pellets. The pellet bulk density was increased when 10 % starch was added, from 431.5 kg/m<sup>3</sup> to 462.8 kg/m<sup>3</sup> (grape pomace) and from 217.2 kg/m<sup>3</sup> to 294.13 kg/m<sup>3</sup> (corn cob), although that required by the ENPlus Bquality (600 kg/m<sup>3</sup>) was not reached. It was demonstrated that other additives, such as lignosulphonate and different types of starch, also decrease the moisture content of wood pellets, thereby increasing the bulk density of the product [16].

Stahl M. et al investigated how white sugar, molasses and spent sulphite liquor additives affect the energy needed by the pellet press, the durability and oxidation of the produced pellets. They found that using sugar additive, the bulk density (7 to 15 %) and durability (10 to 20 %) of the pellets were increased [103].

The FVI is a relevant parameter for the screening of biomass species, and it can be concluded that the samples with the highest FVI possesses better biofuel properties [104].

The amount of heat that can be "pulled" through the combustion of biomass is referred to as the energy density. Different fuels have different levels of energy density, which can be calculated using the equivalent energy released during combustion. The amount of energy that can be released by a specific mass or volume of fuel is known as its energy density. The quality of the fuel increases with increasing energy density. From Table 2 it can be ascertained that the samples with the highest energy density and fuel value index were 10 % waste rapeseed oil-grape pomace and 10 % waste rapeseed oil-corn cob, demonstrating that waste rapeseed oil is the best additive for enhancing the quality of the pellets. Pellets made from 10% waste rapeseed oil-grape pomace and 10 % waste rapeseed-oil corn cob appear to be particularly well suited for a clean and effective combustion. We were able to draw conclusions concerning energy efficiency and measures for environmental protection thanks to the analysis of additive properties.

## Conclusions

To improve the quality of the pellets made from grape pomace and corncob and to lower the concentration of harmful emissions, three additives, namely, sawdust, starch and used rapeseed oil in addition of 10 % in dry solids, were used. In comparison to most types of wood, the results of proximate analysis and their calorific values are significantly higher. In comparison to pristine grape pomace and corncob, the nitrogen and sulphur content decreases when 10 % sawdust, starch, and waste rapeseed oil are added. Addition of waste rapeseed oil (from cooking) applied at a rate of 10 % relative to the weight of the pellets, increased their calorific value. Each time, the pellets ash contents decreased when the waste rapeseed oil was added. The biomass pellets from this study have a calorific value ranged between 16 to 22 MJ/kg. Pellets made from agricultural waste are some of the most popular biofuels. Scientists started looking for novel solutions to make it possible to improve pellets heating value because of the rising interest in them and the need to increase their efficiency. In this study, the most favourable effect upon the investigated parameters was obtained when waste rapeseed oil was added. The method of pellet refining suggested in this study may be competitive in comparison to other technologies available, according to the obtained results.

## Acknowledgements

This contribution is carried out within the research program "Chemical Thermodynamics" of the "Ilie Murgulescu" Institute of Physical Chemistry of the Romanian Academy. Support of the EU (ERDF) and Romanian Government, for the acquisition of the research infrastructure under Project INFRANANO-CHEM-No.19/01.03.2009 is gratefully acknowledged.

## References

1. Saidur, R.; Abdelaziz, E.A.; Demirbas, A.; Hossain, M.S.; Mekhilef, S. *Renew. Sust. Energy Rev.* **2011**, *15*, 2262-2289. DOI: <https://doi.org/10.1016/j.rser.2011.02.015>.
2. <https://market-entry-romania.blogspot.ro/2017/02/waste-to-energy-potential-in-romania.html>, accessed in January 2023.
3. Radu, L. in: *The agricultural crops production of Romania, Ovidius University Annals, Economic Sciences Series*, **2018**, *XVIII*.
4. Smaga, M.; Wielgosiński, G.; Kochański, A.; Korczak, K. *Acta Innovations*. **2018**, *26*, 81-92. DOI: 10.32933/ActaInnovations.26.9.
5. Lehtikangas, P. *Biomass Bioenerg.* **2001**, *20*, 301-360. DOI: [https://doi.org/10.1016/S0961-9534\(00\)00092-1](https://doi.org/10.1016/S0961-9534(00)00092-1).
6. Grover, V.; Hogland, W. in: *Recovering energy from waste-various aspects*, Science Publishers, Inc Enfield (NH), USA, Plymouth, UK, 338 pages, ISBN 1-57808-200-5.
7. Malat'ák, J.; Velebil, J.; Malat'áková, J.; Passian, L.; Bradna, J.; Tamelová, B.; Gendek, A.; Aniszewska, M. *Materials*. **2022**, *15*, 7288-7302.
8. Spinei, M.; Oroian, M. *Foods*. **2021**, *10*, 867-872.
9. Scoma, A.; Rebecchi, S.; Bertin, L.; Fava, F. *Crit. Rev. Biotechnol.* **2016**, *36*, 175-189. DOI: <https://doi.org/10.3109/07388551.2014.947238>.
10. [www.statista.com/statistic/Romania-production-of-grapes/](http://www.statista.com/statistic/Romania-production-of-grapes/), accessed in February 2023.
11. Chowdhary, P.; Gupta, A.; Gnansounou, E.; Pandey, A.; Chaturvedi, P. *Environ. Pollut.* **2021**, *278*, 116796. DOI: <https://doi.org/10.1016/j.envpol.2021.116796>.
12. Golub, M. in: *Agricultural mechanization in Asia, Africa and Latin America*. **2012**, *43*, 72-79.
13. Kim, S.; Dale, B.E. *Biomass Bioenerg.* **2004**, *26*, 361-375. DOI: <https://doi.org/10.1016/j.biombioe.2003.08.002>.
14. Burg, P.; Masan, V.; Ludin, D. *Eng. for Rural Development*. **2017**, 1333-1338.
15. Jindaporn, J.; Charoenporn, L. *Energ. Procedia*. **2017**, *138*, 1147-1152. DOI: <https://doi.org/10.1016/j.egypro.2017.10.223>.
16. Tarasov, D.; Shahi, C.; Leitch, M. *ISRN Forestry*, **2013**, 1-6, Hindawi Publishing Corporation, Article ID 876939.
17. Gageanu, I.; Cujbescu, D.; Persu, C.; Voicu, G. *Eng. Rural Dev.* **2018**, *17*, 1632-1638.
18. Obernberger, I.; Thek, G. *Biomass Bioenergy*. **2004**, *27*, 653-669. DOI: <https://doi.org/10.1016/j.biombioe.2003.07.006>.
19. Nielsen, N. P. K. Ph.D. Thesis, University of Copenhagen, Copenhagen, Denmark, 2009.
20. Stahl, M.; Berghel, J.; Frodeson, S.; Granström, K.; Renström, R. *Energy Fuels*. **2012**, *26*, 1937-1945.
21. Demir, V. G.; Yaman, P.; Efe, M.O.; Yuksel, H. ICOEST, International Conference on Environmental Science and Technology, 28 september-2 october **2016**.
22. Falemara, B.C.; Joshua, V.I.; Aina, O.O.; Nuhu, R.D. *Recycling*. **2018**, *3*, 37-42. DOI: <https://doi.org/10.3390/recycling3030037>.
23. Yuliah, Y.; Kartawidjaja, M.; Suryaningsih, S.; Ulfi, K. International Conference on Biomass: Technology, Application, and Sustainable Development IOP Publishing IOP Conf. Series: Earth and Environmental Science. **2017**, *65*, 1-8.
24. Rasid, R. A.; Elamparithy, G.; Ismail, M.; Harun, N. *J. Chem. Eng. Ind. Biotech.* **2021**, *07*, 1 - 6.
25. Obidzinski, S.; Piekut, J.; Dec, D. *Renew. Energy*. **2016**, *87*, 289-297. DOI: <https://doi.org/10.1016/j.renene.2015.10.025>.
26. Obidzinski, S.; Dołzynska, M.; Kowczyk-Sadowy, M.; Jadwisieniczak, K.; Sobczak, P. *Energies*. **2019**, *12*, 4687-4691. DOI: <https://doi.org/10.3390/en12244687>.
27. Gageanu, I.; Persu, C.; Cujbescu, D.; Gheorghe, G.; Voicu, G. *Eng. Rural Dev.* **2019**, *18*, 362-367.



28. Mannu, A.; Garroni, S.; Porras, J.I.; Mele, A. *Recycling Processes*. **2020**, *8*, 366-370. DOI: <https://doi.org/10.3390/pr8030366>.
29. Demirbas, A. *Energy Convers. Manage.* **2009**, *50*, 923-927. DOI: <https://doi.org/10.1016/j.enconman.2008.12.023>.
30. Misljenovic, N.; Mosbye, J.; Schüller, R.B.; Lekang, O. I.; Bringas, C. S. *Ann. Trans. Nordic Rheology Soc.* **2014**, *22*, 211-218.
31. Misljenovic, N.; Mosbye, J.; Schuller, R.B.; Lekang, O.I.; Salas-Bringas, C. *Fuel Process. Technol.* **2015**, *134*, 214-222. DOI: <https://doi.org/10.1016/j.fuproc.2015.01.037>.
32. Emadi, B.; Iroba, K.L.; Tabil, L.G. *Appl. Energ.* **2018**, *198*, 312-319. DOI: <https://doi.org/10.1016/j.apenergy.2016.12.027>.
33. Saletnik, A.; Saletnik, B.; Puchalski, C. *Energies*. **2021**, *14*, 6486-6492.
34. Chen, G.; Liu, C.; Ma, W.; Zhang, X.; Li, Y.; Yan, B.; Zhou, W. *Biores. Technol.* **2014**, *166*, 500-507.
35. Wattana, W.; Phetklung, S.; Jakaew, W.; Chumuthai, S.; Sriam, P.; Chanurair, N. in: *International Conference on Alternative Energy in Developing Countries and Emerging Economies 2017*, AEDCEE, Bangkok, Thailand.
36. Wang, Y.; Sun, Y.; Wu, K. *BioRes.* **2019**, *14*, 537-553.
37. Samson, R.; Duxbury, P. in: *Assessment of pelletized biofuels*, **2000**, Resource efficient agricultural production Canada. DOI: <http://dx.doi.org/10.13140/RG.2.2.20841.70248>.
38. ASTM D3173-03 *Standard test method for moisture in the analysis sample of coal and coke*. **2008**.
39. Chen, Q.; Swithenbank, J.; Sharifi, V.N. in: *Review of biomass and solid recovered fuel (SRF) pelletisation technologies*, **2008**, EPSRC Supergen bioenergy theme 4 (heat and power), SUWIC, Sheffield University.
40. Sokhansanj, S.; Cushman, J.; Wright, L. *CIGR Electronic Journal*. **2003**, *5*, 1-21.
41. Burg, P.; Ludin, D.; Rutkowski, K.; Krakowiak-Bal, A.; Trávníček, P.; Zemánek, P.; Turan, J.; Višacki, V. *Int. Agrophys.* **2016**, *30*, 261-265. DOI: <https://doi.org/10.1515/intag-2015-0082>.
42. Malik, B.; Pirzadah, T.B.; Islam, S. T.; Tahir, I.; Kumar, M.; Rehman, R. in: *Agricultural biomass based potential materials*. **2015**, Springer International Publishing Switzerland K. R. Hakeem et al. (eds.).
43. Gendek, A.; Aniszewska, M.; Malatak, J.; Velebil, J. *Biomass Bioenerg.* **2018**, *117*, 173-179. DOI: <https://doi.org/10.1016/j.biombioe.2018.07.025>.
44. [www.parrinst.com](http://www.parrinst.com), *Bulletin 2811*, 1-4, accessed in November 2023.
45. Gheorghe, D.; Neacsu, A. *Rev. Roum. Chim.* **2019**, *64*, 633-639. DOI: <https://doi.org/10.33224/rch%2F2019.64.7.10>.
46. ASTM D5865, Standard Test Method for Gross Calorific Value of coal and coke, **2013**, [www.astm.org](http://www.astm.org), accessed in January 2023.
47. Parr Instrument Company, *6200 Isoperibolic Calorimeter*, **2014**, <http://www.parrinst.com/products/oxygenbomb-calorimeters/6200isoperibolcalorimeter>, accessed in February 2023.
48. Neacsu, A.; Gheorghe, D. *Rev. Roum. Chim.* **2021**, *66*, 321-329. DOI: 10.33224/rch.2021.66.4.02.
49. Parr Analytical Methods for Oxygen Bombs No 207M, accessed in January 2023
50. Onukak, I. E.; Mohammed-Dabo, I.A.; Ameh, A.O.; Okoduwa, I.D.S.I.R.; Fasanya, O.O. *Recycling*. **2017**, *2*, 1-19. DOI: <https://doi.org/10.3390/recycling2040017>.
51. Villanueva, M.; Proupin, J.; Rodriguez-Anon, J.A.; Fraga-Grueiro, L.; Salgado, J.; Barros, N. *J Therm. Anal. Calorim.* **2011**, *104*, 61-67. DOI: <https://doi.org/10.1007/s10973-010-1177-y>.
52. Miao, M.; Kong, H.; Deng, B.; Chen, L.; Yang, H.; Lyu, J.; Zhang, M. *Fuel Process. Technol.* **2020**, *208*, 106517. DOI: <https://doi.org/10.1016/j.fuproc.2020.106517>.
53. Wang, T.; Yang, Q.; Wang, Y.; Wang, J.; Zhang, Y.; Pan, W.P. *Biores. Technol.* **2020**, *297*, 122388. DOI: <https://doi.org/10.1016/j.biortech.2019.122388>.

54. Lu, Z.; Chen, X.; Yao, S.; Qin, H.; Zhang, L.; Yao, X.; Yu, Z.; Lu, J. *Fuel*. **2019**, 258, 116150. DOI: <https://doi.org/10.1016/j.fuel.2019.116150>.
55. Sadiku, N.A.; Oluyeye, A.O.; Sadiku, I.B. *Lignocellulose*. **2016**, 5, 34–49.
56. Holtmeyer, M.L.; Li, G.; Kumfer, B.M.; Li, S.; Axelbaum, R.L. *Energy Fuels*. **2013**, 27, 7762–7771. DOI: <https://doi.org/10.1021/ef4013505>.
57. Ivanova, T.; Muntean, A.; Havrland, B.; Hutla, P. *BIO Web of Conferences 10*. <https://doi.org/10.1051/bioconf/20181002007>, *Contemporary Research Trends in Agricultural Engineering*. **2018**.
58. ASTM D3174-04 Standard test method for ash in the analysis sample of coal and coke from coal. **2003**, [www.astm.org](http://www.astm.org), accessed January 2023.
59. ISO 1171:2010 Solid mineral fuels-determination of ash.
60. Ivanova, T.; Muntean, A.; Titei, V.; Havrland, B.; Kolarikova, M. *Agronomy Res.* **2015**, 13, 311-317.
61. Vijayanand, C.; Kamaraj, S.; Karthikeyan, S.; Sriramajayam, S. *Intl. J. Agric. Sci.* **2016**, 8, 2124-2127.
62. Lunguleasa, A.; Dobrev, T.; Fotin, A. *Pro Ligno*. **2015**, 11, 686-691.
63. Mierzwa-Hersztek, M.; Gondek, K.; Jewiarz, M.; Dziedzic, K. *J. Mater. Cycles*. **2019**, 21, 786-800. DOI: <https://doi.org/10.1007/s10163-019-00832-6>.
64. Neacusu, A.; Gheorghe, D. *J. Mex.Chem.Soc.* **2022**, 66, 408-420. DOI: <https://doi.org/10.29356/jmcs.v66i4.1739>.
65. Sadaka, S.; Johnson, D.M. *Technical Report*. **2010**, Agriculture and Natural Resources, University of Arkansas System.
66. Nussbaumer, T.; Good, J. *Biomass for Energy and Industry*. **1998**, 10th European Conference and Technology Exhibition, Würzburg (Germany).
67. Chen, Y.S.; Workman, E.C. Jr. *Wood and Fiber Sci.* **1990**, 22, 378-387.
68. Minitab Statistical Software <https://www.minitab.com/en-us/products/minitab/>, accessed in November 2023.
69. Spîrchez, C.; Lunguleasa, A. *Wood Res.* **2019**, 64, 549-556.
70. Wojcieszak, D.; Przybył, J.; Czajkowski, L.; Majka, J.; Pawłowski, A. *Materials*. **2022**, 15, 2831-2836.
71. Yunita, L.; Irmaya, A.I. *IOP Conf. Ser.: Earth Environ. Sci.* **2018**, 212, 012079, DOI: <https://doi.org/10.1088/1755-1315/212/1/012079>.
72. Sofyan Munawar, S.; Subiyanto, B. *Proc. Environm. Sci.* **2014**, 20, 336-341. DOI: <https://doi.org/10.1016/j.proenv.2014.03.042>.
73. Akhtar, J.; Imran, M.; Ali, A.M.; Nawaz, Z.; Muhammad, A.; Butt, K.R.; Jillani, M.S.; Naeem, H.A. *Energies*. **2021**, 14, 4218-4231.
74. Chen, W. H.; Lin, B. J.; Lin, Y. Y.; Chu, Y. S.; Show, A.; Ong, H. C.; Chang, J. S.; Ho, S.H.; Culaba, A. B.; Pétrissans, A.; Pétrissans, M. *Prog. Energy Combust. Sci.* **2021**, 82-87. DOI: <https://doi.org/10.1016/j.peccs.2020.100887>.
75. Wang, L.; Riva, L.; Skreiberg, O.; Khalil, R.; Bartocci, P.; Yang, Q.; Yang, H.; Wang, X.; Chen, D.; Rudolfsson, M.; Nielsen, H.K. *Energy Fuels*. **2020**, 34, 15343-15354. DOI: <https://doi.org/10.1021/acs.energyfuels.0c02671>.
76. Gravalos, I.; Xyradakis, P.; Kateris, D.; Gialamas, T.; Bartzialis, D.; Giannoulis, K. *Nat. Resour.* **2016**, 7, 57-68. DOI: <https://doi.org/10.4236/nr.2016.71006>.
77. Tian, X.; Dai, L.; Wang, Y.; Zeng, Z.; Zhang, S.; Jiang, L.; Yang, X.; Yue, L.; Liu, Y.; Ruan, R. *Bioresour. Technol.* **2020**, 297, 122490. DOI: <https://doi.org/10.1016/j.biortech.2019.122490>.
78. [www.extension.psu.edu/manufacturing-fuel-pellets-from-biomass](http://www.extension.psu.edu/manufacturing-fuel-pellets-from-biomass), accessed in November 2023.
79. Saracoglu, N.; Gunduz, G. *Energy Sources. Part A*, **2009**, 31, 1708–1718. DOI: <https://doi.org/10.1080/15567030802459677>.
80. Lalak, J.; Martyniak, D.; Kasprzycka, A.; Żurek, G.; Moroń, W.; Chmielewska, M.; Wiącek, D.; Tys, J. *Int. Agrophys.* **2016**, 30, 475-482. DOI: <https://doi.org/10.1515/intag-2016-0021>.
81. [www.ecostan.com](http://www.ecostan.com), accessed in November 2023.



82. Hasan, E.S.; Mashuni, M.J.; Ilmawati, W.; Wati, W.; Sudiana, N. *J. Phys.: Conf. Series*. **2017**, *846*, 012022.
83. Misljenovic, N.; Bach, Q.V.; Tran, K.Q.; Bringas, C. S.; Skreiberg, O. *Energy Fuels*. **2014**, *28*, 2554-2561. DOI: <https://doi.org/10.1021/ef4023674>.
84. Shah, K.; Yusop, N. A. K. A.; Rohani, M. Z. M.; Fadil, J. M.; Manaf, N. A.; Hartono, N.A.; Tuyen, B.; Masaki, N.D.; Ahmad, T.; Ramli, A.S. *Chem. Eng. Trans.* **2021**, *89*, 127–132.
85. Dhyani, V.; Bhaskar, T. *Renew. Energy*. **2018**, *129*, 695–716. DOI: <https://doi.org/10.1016/j.renene.2017.04.035>.
86. Annamalai, K.; Sweeten, J.M.; Ramalingam, S.C. *Trans. Asae*. **1987**, *30*, 1205-1208.
87. Dumitrascu, R.; Lunguleasa, A.; Spirchez, C. *Bioresurces*. **2018**, *13*, 6985-7001.
88. Muhamad, A.; Farid Nasir, A.; Ab Saman Makhрани, K. *Adv. Sci. Lett.* **2017**, *23*, 4184-4187. DOI: <https://doi.org/10.1166/asl.2017.8242>.
89. Holubcik, M.; Nosek, R.; Jnadacka, J. *Intl. J. Energ. Optim. Energ.* **2012**, *1*, 20-40. DOI: <https://doi.org/10.4018/ijeoc.2012040102>.
90. Li, Y.; Liu, H. *Biomass Bioenergy*. **2000**, *19*, 177–186. DOI: [https://doi.org/10.1016/S0961-9534\(00\)00026-X](https://doi.org/10.1016/S0961-9534(00)00026-X).
91. Ajith Kumar, T.T.; Mech, N.; Ramesh, S.T.; Gandhimathi, R. *J. Cleaner Prod.* **2022**, *350*, 131312. DOI: <https://doi.org/10.1016/j.jclepro.2022.131312>.
92. Greinert, A.; Mrówczyńska, M.; Grech, R.; Szefner, W. *Energies*. **2020**, *13*, 463-468.
93. Zajac, G.; Szyszlak-Bargłowicz, J.; Golebiowski, W.; Szczepanik, M. *Energies*. **2018**, *11*, 2885-2889.
94. Grover, P.D. *Proceedings of the International Workshop on Biomass Briquetting*. Bangkok, april, 1996, <http://www.rwedp.org>, accessed in November 2023.
95. Ebeling, J.M.; Jenkins, B.M. *ASAE*. **1985**, *28*, 898-902.
96. Kuokkanen, M.; Kuokkanen, T.; Pohjonen, V. **2009**, *Energ. Res. University of Oulu. Proced. of the EnePro Conf. June 3rd, 2009, University of Oulu, Finland. Kalevaprint, Oulu, ISBN 978-951-42-9154-8. 36-40.*
97. Lesego, M.; Mohlala, M.; Bodunrin, O.; Ayotunde, A.; Awosusi, M.; Daramola, O.; Nonhlanhla, P.; Cele, P.; Olubambi, A. *Alexandria Eng. J.* **2016**, *55*, 3025-3036. DOI: <https://doi.org/10.1016/j.aej.2016.05.014>.
98. Demirbas, A. *Energy Convers. Manage.* **2001**, *42*, 183–188. DOI: [https://doi.org/10.1016/S0196-8904\(00\)00050-9](https://doi.org/10.1016/S0196-8904(00)00050-9).
99. Thabout, M.; Pagketanang, T.; Panyacharoen, K.; Mongkuta, P.; Wongwicha, P. *Energy Procedia*. **2015**, *79*, 890-895.
100. Khan, A.A.; De Jong, W.; Jansens, P.J.; Spliethoff, H. *Fuel Process. Technol.* **2009**, *90*, 21–50. DOI: <https://doi.org/10.1016/J.FUPROC.2008.07.012>.
101. Maj, G.; Szyszlak-Bargłowicz, J.; Zajac, G.; Słowik, T.; Krzaczek, P.; Piekarski, W. *Energies*. **2019**, *12*, 4383-4390.
102. Loo, S.; Koppejan, J. *The Handbook of Biomass Combustion and Co-firing*, 2008, 134-173. <https://www.researchgate.net/publication/237079687>, accessed in November 2023.
103. Stahl, M.; Berghel, J.; Granstrom, K. *BioResources*. **2016**, *11*, 3373-3383.
104. Abbot, P.G.; Lowore, J. D. *For. Ecol. Management*. **1999**, *11*, 111–121.

## A DFT Study of the Hydrogen Storage Potentials and Properties of Ca, Fe, and Ti Deposited NaSi<sub>20</sub> Fullerenes

Huixi Yang<sup>1</sup>, Bin Liu<sup>1\*</sup>, Hongjiang Ren<sup>2\*</sup>

<sup>1</sup>Xi'an Key Laboratory of Textile Chemical Engineering Auxiliaries, School of Environmental and Chemical Engineering, Xi'an Polytechnic University, Xi'an 710600, PR China.

<sup>2</sup>School of Chemical Engineering, Xi'an University, Xi'an 710065, PR China.

\*Corresponding author: Bin Liu; Hongjiang Ren, email: [hjren@xawl.edu.cn](mailto:hjren@xawl.edu.cn)

Received May 30<sup>th</sup>, 2023; Accepted December 22<sup>nd</sup>, 2023.

DOI: <http://dx.doi.org/10.29356/jmcs.v68i3.2073>

**Abstract.** In this work, the hydrogen storage materials of Ca, Fe, and Ti deposited NaSi<sub>20</sub> clusters were investigated utilizing DFT methods (B3LYP and M06-2X) combined with the 6-311++G(*d*, *p*) basis set. The results show that Ca, Fe, and Ti atoms tend to bind with two adjacent Si atoms. The Ca@NaSi<sub>20</sub>, Fe@NaSi<sub>20</sub>, and Ti@NaSi<sub>20</sub> can adsorb up to three, four, and six hydrogen molecules, respectively. The adsorption energy ( $E_{ads}$ ) per hydrogen molecule meets the United States Department of Energy (DOE) target for hydrogen storage materials for  $nH_2$ -Ti@NaSi<sub>20</sub> ( $n = 2-6$ ) and  $nH_2$ -Fe@NaSi<sub>20</sub> ( $n = 1-4$ ), implying that NaSi<sub>20</sub> fullerene could be a potentially suitable material for hydrogen storage.

**Keywords:** NaSi<sub>20</sub> fullerenes; DFT methods; hydrogen storage.

**Resumen.** Utilizando métodos de la DFT (B3LYP y M06-2X) combinados con las bases 6-311++G(*d*, *p*), en este trabajo se investigaron materiales para el almacenamiento de hidrógeno a base de Ca, Fe, y Ti depositados en cúmulos de NaSi<sub>20</sub>. Los resultados muestran que los átomos de Ca, Fe, y Ti tienden a unirse a dos átomos adyacentes de Si. Los cúmulos Ca@NaSi<sub>20</sub>, Fe@NaSi<sub>20</sub>, y Ti@NaSi<sub>20</sub> pueden adsorber hasta tres, cuatro y seis moléculas de hidrógeno, respectivamente. Las energías de adsorción por molécula de hidrógeno ( $E_{ads}$ ) de  $nH_2$ -Ti@NaSi<sub>20</sub> ( $n = 2-6$ ) y  $nH_2$ -Fe@NaSi<sub>20</sub> ( $n = 1-4$ ) cumplen con el objetivo del Departamento de Energía de los Estados Unidos (DOE) lo que implica que el fullereno NaSi<sub>20</sub> puede ser un material potencialmente adecuado para el almacenamiento de hidrógeno.

**Palabras clave:** NaSi<sub>20</sub> fullerenos; métodos de la DFT; almacenamiento de hidrógeno.

### Introduction

With the growth of the world population and rapid economic development, as well as the shortage of fossil fuels and global environmental problems that threaten the peaceful existence of mankind and stimulate people's determination to find new energy sources [1,2]. Hydrogen as a renewable and clean energy source has several ideal characteristics, for example, it contains the maximum energy per unit weight, is abundant in the natural environment, and its combustion products do not pollute the environment like sulfur oxidation and aromatic hydrocarbon oxides [3,4]. The U. S. Department of Energy (DOE) system has identified goals for hydrogen storage materials, the average adsorption energy per H<sub>2</sub> (average adsorption energy per H<sub>2</sub>,  $E_{ad}/H_2$ ) in

an ideal hydrogen storage material should be between chemisorption and physical adsorption (0.1 - 0.8 eV) to meet the hydrogen storage reversibility of the material [5].

Currently, there are many types of hydrogen storage materials. Carbon-based and chemically active hydrogen storage materials include fullerene, graphene, carbon nanotubes, etc [6,7]. Nano-structured magnesium and magnesium-based hydrides can also be used to store hydrogen through adsorption [8]. In recent years, the semiconductor cluster has become one of the research objects in cluster science and the silicon cluster is the most widely used technology in the semiconductor cluster [9-13].

Silicon is not only rich in content but is also one of the most important materials in the modern industry [11-13]. It has a wide range of applications in various areas of life, such as metallurgy, electronic manufacturing, the military industry, medical, etc [10-12]. But at the same time, the disadvantages of silicon materials are also very obvious. For example, the hollow structure of silicon and the lack of unsaturated bonds in silicon valence electrons with  $sp^2$  hybridization deliver unstable fullerene cages (silicon nanotubes and silicon fullerenes) [10]. However, studies over the years have shown that their structures can be improved by various chemical modifications, such as encapsulating metal atoms in clusters [11] or using H adsorption to enhance the  $sp^3$  bonding between Si atoms to improve stability [12]. Meanwhile, Ryou *et al.* found that the binding energy of hydrogen molecules to silicon nanotubes is less than 0.1 eV even in stable structures through DFT calculations, and then pure silicon nanotubes are not suitable for hydrogen storage [13]. Kumar *et al.* found that metal doping enhanced the stability and size selectivity of silicon clusters [14]. Sporea *et al.* stabilized silicon clusters by encapsulating alkali metal atoms Na, K, and Li inside  $Si_{20}$ , which can provide regular shapes for  $Si_{20}$  clusters [15]. Moreover, Ammar *et al.* investigated the hydrogen storage properties of  $KSi_{20}$  and  $Ti@KSi_{20}$  using the DFT-based B3LYP and M06-2X methods. The adsorption energy values ( $\bar{E}_{ads}$ ) per hydrogen molecule satisfy the U.S. DOE targets for hydrogen storage materials [16].

According to our knowledge,  $NaSi_{20}$  should have similar hydrogen storage properties to  $KSi_{20}$ . However, the hydrogen storage performance of  $NaSi_{20}$  has not been reported. And more importantly, as previously reported by researchers, Ca, Fe, and Ti metal atoms were often considered and performed well in the previous studies of modified carbon-based and boron-based hydrogen storage materials [17-19]. Meanwhile, Ca is one of the most active atoms in alkaline earth metals, Fe is the transition metal atom with more outer electrons, and Ti is the transition metal atom with fewer outer electrons. To the best of our knowledge,  $NaSi_{20}$  deposited with Ca, Fe, and Ti atoms has not been previously investigated as hydrogen storage materials. In this work, the storage characteristics of  $H_2$  on Na-encapsulated  $Si_{20}$  ( $NaSi_{20}$ ) clusters deposited in Ca, Fe, and Ti were investigated by performing DFT calculations at the theoretical level of B3LYP and M06-2X combined with the 6-311++G( $d, p$ ) basis set. The effect of electron properties on  $NaSi_{20}$  fullerenes deposited in Ti, Ca, and Fe was studied. Then the adsorption of  $n$  hydrogen molecules ( $n = 1-6$ ) on  $Ca@NaSi_{20}$ ,  $Fe@NaSi_{20}$ , and  $Ti@NaSi_{20}$  is discussed.

## Computational methods

To investigate the storage properties of  $H_2$  molecules on  $Ca@NaSi_{20}$ ,  $Fe@NaSi_{20}$ , and  $Ti@NaSi_{20}$  fullerenes, DFT calculations [20] were performed at the B3LYP/6-311++G( $d, p$ ) and M06-2X/6-311++G( $d, p$ ) levels of theory for the non-metallic atoms (H, Si) and an effective for the effective pseudopotential basis set LANL2DZ of Na, Ca, Fe and Ti atoms, respectively [20]. Full geometric optimizations were carried out at two levels for free  $H_2$  molecules,  $Si_{20}$ ,  $NaSi_{20}$ ,  $Ca@NaSi_{20}$ ,  $Fe@NaSi_{20}$ , and  $Ti@NaSi_{20}$  substrates as well as  $nH_2$ - $Ca@NaSi_{20}$  ( $n = 1-3$ ),  $nH_2$ - $Fe@NaSi_{20}$  ( $n = 1-4$ ), and  $nH_2$ - $Ti@NaSi_{20}$  ( $n = 1-6$ ) complexes. Because silicon is the most readily available semiconductor in nature, hydrogen can be adsorbed on silicon in both crystalline and amorphous forms and can be desorbed again. Several experimental and theoretical studies have been conducted by Mao WL and Mao HK to investigate whether porous silicon is capable of conducting hydrogen storage [21]. All the calculations were calculated using the Gaussian 09 program [22].

The ionization potential (IP), electron affinity (EA), and chemical hardness ( $\eta$ ) can be expressed in equations 1-3, where  $E(N-1)$ ,  $E(N)$ , and  $E(N+1)$  are total energies when the system has  $N-1$ ,  $N$  and  $N+1$  electrons, respectively.

$$IP = E(N-1) - E(N) \quad (1)$$

$$EA = E(N) - E(N+1) \quad (2)$$

$$\eta \approx \frac{1}{2}(IP-EA) \quad (3)$$

The average binding energy ( $\bar{E}_b$ ) of per atom for Si<sub>20</sub>, NaSi<sub>20</sub>, Ca@NaSi<sub>20</sub>, Fe@NaSi<sub>20</sub>, and Ti@NaSi<sub>20</sub> is calculated by equation (4),

$$\bar{E}_b = \frac{E_{\text{cluster}} - \sum E_{\text{atom}}}{n} \quad (4)$$

where  $E_{\text{cluster}}$  is the energy of the optimized cluster,  $\sum E_{\text{atom}}$  is the sum of the energies of the free atoms of the cluster and  $n$  is total number of the cluster atoms. The binding energies ( $E_{\text{bind}}$ ) of Ca, Fe, and Ti atoms on NaSi<sub>20</sub> substrate clusters are calculated by equation (5).  $n\text{H}_2$  molecule ( $n = 1-6$ ) adsorption energies ( $E_{\text{ads}}$ ) and the average adsorption energy of per hydrogen molecule ( $\bar{E}_{\text{ads}}$ ) on M@NaSi<sub>20</sub> fullerenes (M = Ca, Fe and Ti) are calculated by equations (6) and (7), respectively.

$$E_{\text{bind}} = E_{\text{M@NaSi}_{20}} - (E_{\text{NaSi}_{20}} + E_{\text{M}}) \quad (5)$$

$$E_{\text{ads}} = E_{n\text{H}_2\text{-M@NaSi}_{20}} - (nE_{\text{H}_2} + E_{\text{M@NaSi}_{20}}) \quad (6)$$

$$\bar{E}_{\text{ads}} = \frac{1}{n} [E_{n\text{H}_2\text{-M@NaSi}_{20}} - (nE_{\text{H}_2} + E_{\text{M@NaSi}_{20}})] \quad (7)$$

where  $E_{\text{M@NaSi}_{20}}$  is the energy of the optimized Ca@NaSi<sub>20</sub>, Fe@NaSi<sub>20</sub>, and Ti@NaSi<sub>20</sub> complexes,  $E_{\text{M@NaSi}_{20}}$  is the energy of the corresponding optimized NaSi<sub>20</sub> substrate clusters,  $E_{\text{M}}$  is the atomic energy of the free M (M = Ca, Fe, and Ti) atoms, and  $E_{n\text{H}_2\text{-M@NaSi}_{20}}$  is the total energy of the optimized  $n\text{H}_2\text{-M@NaSi}_{20}$  (M = Ca, Fe, and Ti).

The enthalpy difference ( $\Delta H^\ominus$ ) and free energy difference ( $\Delta G^\ominus$ ) of  $n\text{H}_2\text{-M@NaSi}_{20}$  (M = Ca, Fe, and Ti) complexes are calculated by equations (8) and (9), respectively [23].

$$\Delta H^\ominus = \left[ H^\ominus_{n\text{H}_2\text{-M@NaSi}_{20}} - (nH^\ominus_{\text{H}_2} + H^\ominus_{\text{M@NaSi}_{20}}) \right] / n \quad (8)$$

where,  $H^\ominus_{n\text{H}_2\text{-M@NaSi}_{20}}$ ,  $H^\ominus_{\text{M@NaSi}_{20}}$ , and  $H^\ominus_{\text{H}_2}$  are the enthalpies for  $n\text{H}_2\text{-M@NaSi}_{20}$ , M@NaSi<sub>20</sub> and H<sub>2</sub> molecules, respectively.

$$\Delta G^\ominus = \left[ G^\ominus_{n\text{H}_2\text{-M@NaSi}_{20}} - (nG^\ominus_{\text{H}_2} + G^\ominus_{\text{M@NaSi}_{20}}) \right] / n \quad (9)$$

where  $G^\ominus_{n\text{H}_2\text{-M@NaSi}_{20}}$ ,  $G^\ominus_{\text{M@NaSi}_{20}}$  and  $G^\ominus_{\text{H}_2}$  are the free energies of  $n\text{H}_2\text{-M@NaSi}_{20}$ , M@NaSi<sub>20</sub>, and H<sub>2</sub> molecules, respectively.

For testing the stability of the wave function of our investigated systems, the keywords of UB3LYP, stable and nosymm are used in the examples for both  $4\text{H}_2/\text{Ti}@\text{NaSi}_{20}$  and  $4\text{H}_2/\text{Fe}@\text{NaSi}_{20}$  complexes and the results show that the wave functions are stable under the perturbations considered. The corresponding figure is given in Supplement 1.

## Results and discussion

### Geometric structure and electronic properties of $\text{Ca}@\text{NaSi}_{20}$ , $\text{Fe}@\text{NaSi}_{20}$ , and $\text{Ti}@\text{NaSi}_{20}$ clusters

Fig. 1 shows the optimized structures of  $\text{Si}_{20}$  and  $\text{NaSi}_{20}$  fullerenes, as well as Ca, Fe, and Ti external doping  $\text{NaSi}_{20}$  fullerenes, named  $\text{Ca}@\text{NaSi}_{20}$ ,  $\text{Fe}@\text{NaSi}_{20}$ , and  $\text{Ti}@\text{NaSi}_{20}$  clusters. The geometrical and electronic properties of the investigated clusters are listed in Table 1. As can be seen from Fig. 1(a), the  $\text{Si}_{20}$  fullerene cluster is a distorted cage with the shortest Si-Si bond length ( $d_{\text{Si-Si}}$ ) of 2.279 Å and dipole moments of 1.198 Debye at the B3LYP level, and the shortest Si-Si bond length ( $d_{\text{Si-Si}}$ ) of 2.291 Å and dipole moments of 1.215 Debye at the M06-2X level. This is similar to the value of Si-Si bond length ( $d_{\text{Si-Si}}$ ) calculated by Ammar *et al.*, which is 2.335 Å for Si-Si bond length ( $d_{\text{Si-Si}}$ ) calculated by B3LYP method and 2.381 Å for Si-Si bond length ( $d_{\text{Si-Si}}$ ) calculated by M06-2X method. After a Na atom is embedded in the  $\text{Si}_{20}$  cluster, the structure of the cluster has changed into a regular shape, as shown in Fig. 1(b). Compared with pure silicon clusters without internally doped metal atoms, the shape of  $\text{NaSi}_{20}$  clusters is more uniform. Under the B3LYP method, the Si-Si bond length ( $d_{\text{Si-Si}}$ ) is reduced to 2.777 Å, which is similar to the results previously reported by Borshch *et al.* [24]. The HOMO-LUMO gap ( $E_g$ ) decreased from 2.163 and 3.486 eV to 1.329 and 2.512 eV, respectively. Chemical hardness ( $\eta$ ) decreased by 38.63 % and 27.94 %, respectively, while the average binding energy between atoms ( $\bar{E}_b$ ) increased by 4.5 % and 5.2 %.

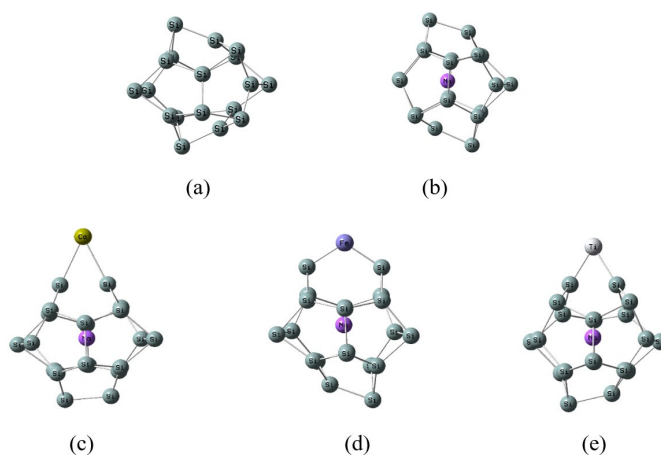
**Table 1.** Ionization potential (IP, eV), electron affinity (EA, eV), hardness ( $\eta$ , eV), HOMO and LUMO energy gap ( $E_g$ , eV), binding energy per atom ( $E_b$ , eV), dipole moment (D, Debye), bond length (d, Å), binding energy ( $E_{\text{bind}}$ , eV) of  $\text{Si}_{20}$ ,  $\text{NaSi}_{20}$ ,  $\text{Ca}@\text{NaSi}_{20}$ ,  $\text{Fe}@\text{NaSi}_{20}$  and  $\text{Ti}@\text{NaSi}_{20}$  as well as Mulliken charges ( $Q_M$ , e) of Ca, Fe, Ti atoms in the clusters.

|                                    | $\text{Si}_{20}$ |        | $\text{NaSi}_{20}$ |        | $\text{Ca}@\text{NaSi}_{20}$ |        | $\text{Fe}@\text{NaSi}_{20}$ |        | $\text{Ti}@\text{NaSi}_{20}$ |        |
|------------------------------------|------------------|--------|--------------------|--------|------------------------------|--------|------------------------------|--------|------------------------------|--------|
|                                    | B3LYP            | M06-2X | B3LYP              | M06-2X | B3LYP                        | M06-2X | B3LYP                        | M06-2X | B3LYP                        | M06-2X |
| IP                                 | 5.780            | 6.581  | 5.255              | 5.922  | 4.761                        | 5.485  | 5.372                        | 5.656  | 5.209                        | 5.391  |
| EA                                 | 3.616            | 3.095  | 3.926              | 3.410  | 3.776                        | 3.303  | 3.911                        | 3.831  | 3.795                        | 3.432  |
| $\eta$                             | 1.082            | 1.743  | 0.664              | 1.256  | 0.493                        | 1.091  | 0.730                        | 0.913  | 0.707                        | 0.979  |
| $E_g$                              | 2.163            | 3.486  | 1.329              | 2.512  | 0.986                        | 2.182  | 1.460                        | 1.825  | 1.414                        | 1.959  |
| $E_b$                              | -4.285           | -4.540 | -4.091             | -4.306 | -3.955                       | -4.155 | -4.137                       | -4.286 | -4.103                       | -4.250 |
| D                                  | 1.198            | 1.215  | 0.163              | 0.259  | 11.843                       | 11.489 | 2.966                        | 1.597  | 8.502                        | 9.983  |
| $d_{\text{Si-Si}}/d_{\text{M-Si}}$ | 2.279            | -      | 2.777              | -      | 3.013                        | -      | 2.367                        | -      | 2.502                        | -      |
| $E_{\text{bind}}$                  |                  |        |                    |        | -1.091                       | -0.992 | -5.109                       | -3.877 | -4.348                       | -3.069 |
| $Q_M$                              |                  |        |                    |        | 1.266                        | 1.042  | -0.184                       | -0.123 | 0.398                        | 0.466  |

We studied the external doping of Ca, Fe, and Ti atoms at different positions of  $\text{NaSi}_{20}$  fullerene. The structure with the most stable energy after optimization is shown in Fig. 1. The results show that Ca, Fe, and Ti

are bound to the NaSi<sub>20</sub> cluster by bonding with two adjacent silicon atoms, which is the same as the external doping mode of Ti atoms to the KSi<sub>20</sub> cluster in the cluster studied by Ammar et al. [14].

According to Baei's theory, the size of the energy gap ( $E_g$ ) value is closely related to the activity and stability of chemical reactions [25]. Under the density functional B3LYP method, the energy gap ( $E_g$ ) of the NaSi<sub>20</sub> cluster modified by Fe and Ti atoms is larger than that of the NaSi<sub>20</sub> cluster modified by Ca atoms, while the energy gap ( $E_g$ ) of the NaSi<sub>20</sub> cluster modified by Ca atoms is smaller than that of the NaSi<sub>20</sub> cluster. Similarly, with the B3LYP method, the chemical hardness ( $\eta$ ) of the Fe@NaSi<sub>20</sub> cluster and Ti@NaSi<sub>20</sub> cluster increases by 9.93 % and 6.48 %, respectively, while the chemical hardness ( $\eta$ ) of the Ca@NaSi<sub>20</sub> cluster decreases by 25.75 %. With the M06-2X method, the Ca@NaSi<sub>20</sub>, Fe@NaSi<sub>20</sub>, and Ti@NaSi<sub>20</sub> clusters have smaller energy gaps than the NaSi<sub>20</sub> clusters. The Ca@NaSi<sub>20</sub>, Fe@NaSi<sub>20</sub>, and Ti@NaSi<sub>20</sub> clusters also have smaller  $\eta$  values than the NaSi<sub>20</sub> clusters. Under the M06-2X method,  $\eta$  values of Ca@NaSi<sub>20</sub>, Fe@NaSi<sub>20</sub> and Ti@NaSi<sub>20</sub> are reduced by 22.05 %, 27.31 % and 13.14%, respectively. Since the density functional M06-2X method considers the weak interaction, it can well describe the weak interaction between metals and clusters. At the same time, the M06-2X method is effective in calculating the energy of the reactants, the isomerization process and the reaction energy barrier. The results showed that the chemical reactivity of Ca@NaSi<sub>20</sub>, Fe@NaSi<sub>20</sub>, and Ti@NaSi<sub>20</sub> clusters was better than that of NaSi<sub>20</sub> clusters. Compared with NaSi<sub>20</sub> clusters, the average binding energy ( $\bar{E}_b$ ) of NaSi<sub>20</sub> clusters modified by Ca, Fe, and Ti atoms increases by about 3.51 %, 0.47 %, and 1.31 %, respectively, under M06-2X method. However, the average binding energy ( $\bar{E}_b$ ) of NaSi<sub>20</sub> clusters modified by Fe and Ti atoms calculated by the B3LYP method decreases by 1.12 % and 1.20 %, respectively, and for Ca@NaSi<sub>20</sub>, the mean binding energy ( $\bar{E}_b$ ) increases by about 3.61 %. This is consistent with the changing trend of the binding energy of C<sub>20</sub> and KSi<sub>20</sub> clusters modified by Ti atoms reported by Ammar et al. [12]. It can be seen that the external doping of Ca, Fe and Ti atoms on the NaSi<sub>20</sub> cluster reduces the stability of NaSi<sub>20</sub> and increases the activity of the reaction.

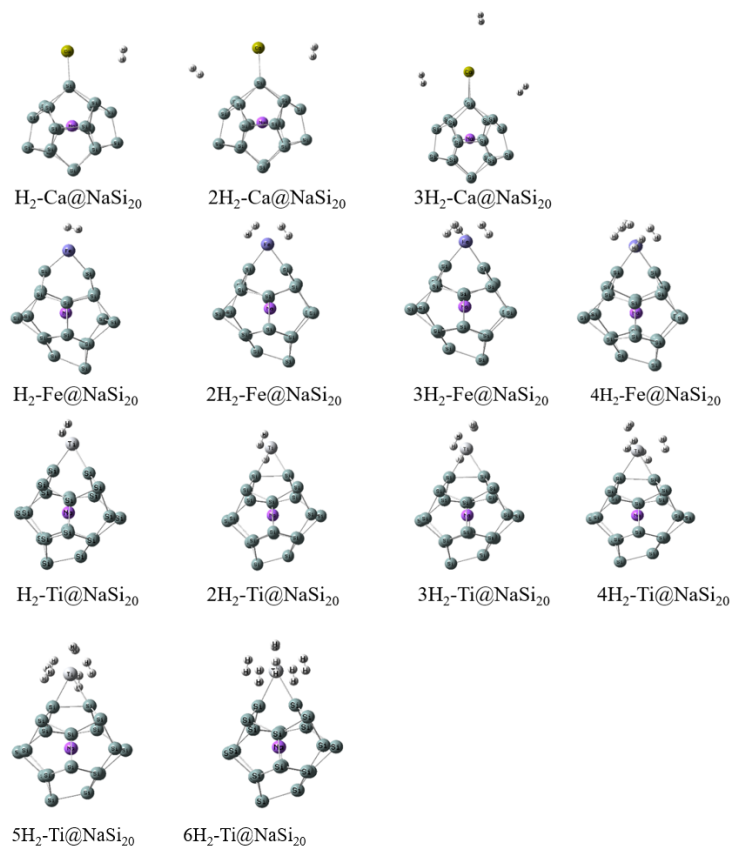


**Fig. 1.** The optimized structures of (a) Si<sub>20</sub>, (b) NaSi<sub>20</sub>, (c) Ca@NaSi<sub>20</sub>, (d) Fe@NaSi<sub>20</sub> and (e) Ti@NaSi<sub>20</sub> calculated at B3LYP method.

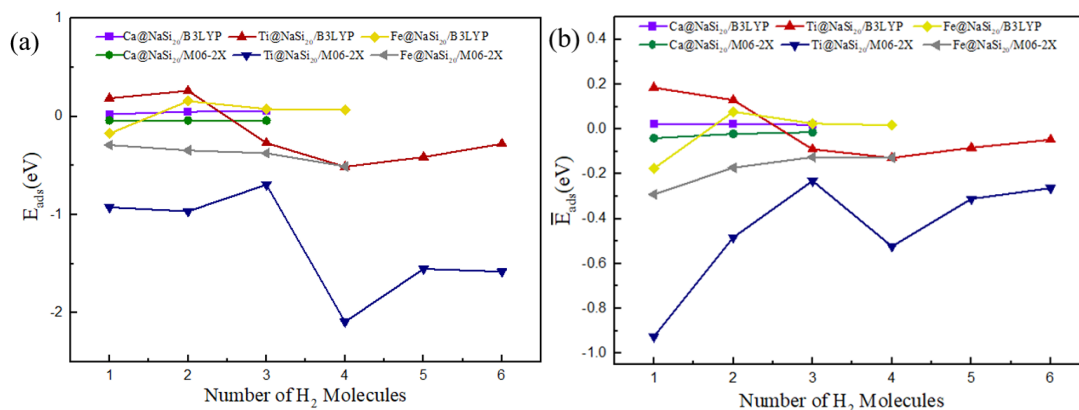
### Interaction of H<sub>2</sub> on Ca@NaSi<sub>20</sub>, Fe@NaSi<sub>20</sub>, and Ti@NaSi<sub>20</sub>

In this work, hydrogen molecules are stored on optimized Ca@NaSi<sub>20</sub>, Fe@NaSi<sub>20</sub>, and Ti@NaSi<sub>20</sub> clusters to characterize the properties of the selected hydrogen storage materials. Fig. 2 shows the geometry of  $n\text{H}_2\text{-Ca@NaSi}_{20}$ ,  $n\text{H}_2\text{-Fe@NaSi}_{20}$ , and  $n\text{H}_2\text{-Ti@NaSi}_{20}$  clusters and in order to explore the place of adsorption more clearly, the structure diagrams from different viewpoints for 4H<sub>2</sub>-Fe@NaSi<sub>20</sub> and 6H<sub>2</sub>-Ti@NaSi<sub>20</sub> as well as different direction of hydrogen attacking for Ti@NaSi<sub>20</sub> and Fe@NaSi<sub>20</sub> are given in Fig. 3. As can be seen from Fig. 2, the H-H bonds of all H<sub>2</sub> molecules are not broken, and they are all adsorbed by metal atoms in the form of molecules. Parameters such as dipole moment, bond length and Mulliken charge of adsorbed clusters are shown

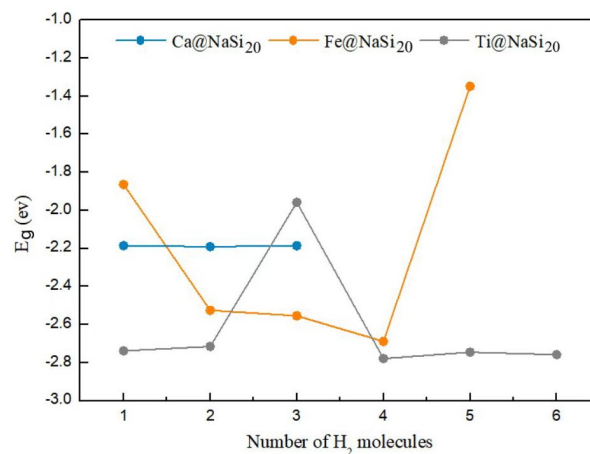
in Tables 2-4, respectively. Equations (6) and (7) were used to calculate the adsorption energy of hydrogen storage materials and the average adsorption energy data of each hydrogen molecule, as shown in Fig. 4(a) and 4(b), respectively. Density functional methods of B3LYP and M06-2X were used to optimize the structure of the H<sub>2</sub> molecule, and the results showed that the H-H bond lengths were 0.744 Å and 0.740 Å, respectively.



**Fig. 2.** The optimized structures for  $n\text{H}_2\text{-Ca@NaSi}_{20}$ ,  $n\text{H}_2\text{-Fe@NaSi}_{20}$  and  $n\text{H}_2\text{-Ti@NaSi}_{20}$  calculated at B3LYP method.



**Fig. 3.** (a) The adsorption energy ( $E_{\text{ads}}$ ) and (b) the average adsorption energy per hydrogen molecule ( $\bar{E}_{\text{ads}}$ ) for  $n\text{H}_2\text{-Ca@NaSi}_{20}$ ,  $n\text{H}_2\text{-Fe@NaSi}_{20}$  and  $n\text{H}_2\text{-Ti@NaSi}_{20}$  at B3LYP and M06-2X methods.



**Fig. 4.** The energy gap ( $E_g$ ) for  $n\text{H}_2\text{-Ca@NaSi}_{20}$ ,  $n\text{H}_2\text{-Fe@NaSi}_{20}$  and  $n\text{H}_2\text{-Ti@NaSi}_{20}$  at M06-2X method.

#### Adsorption of H<sub>2</sub> on Ca@NaSi<sub>20</sub>

This section focuses on the interaction between H<sub>2</sub> and Ca@NaSi<sub>20</sub> clusters. As can be seen from Table 2, under the B3LYP and M06-2X methods, the interaction between a single H<sub>2</sub> molecule and the Ca@NaSi<sub>20</sub> cluster results in an increase of 0.023 eV and a decrease of 0.040 eV, respectively. According

to Mulliken charge analysis, it can be found that the H<sub>2</sub> molecule ( $Q_{\text{H}_2}$ ) gains a negative charge of 0.017e, the positive charge ( $Q_{\text{Ca}}$ ) on the Ca atom decreases by 0.246e, and the charge ( $Q_{\text{Na}}$ ) on Na atom remains basically unchanged under the B3LYP method. This indicates that there is a transfer of charge between the Ca atom and the H<sub>2</sub> molecule. The average adsorption energy of  $n\text{H}_2\text{-Ca@NaSi}_{20}$  cluster is in the range of 0.019 - 0.024 eV, and the average adsorption the energy of the third H<sub>2</sub> molecule is not different from that of the second H<sub>2</sub> molecule. Under the density functional method of M06-2X, the adsorption energy ( $E_{\text{ads}}$ ) increases from -0.040 eV to - 0.014 eV, and the absolute value of the adsorption energy ( $E_{\text{ads}}$ ) decreases gradually when the H<sub>2</sub> molecules adsorbed by Ca@NaSi<sub>20</sub> cluster increase from the first H<sub>2</sub> molecule to the third H<sub>2</sub> molecule. As can be seen from Table 2, under the B3LYP method, when the second H<sub>2</sub> molecule is adsorbed by Ca@NaSi<sub>20</sub> cluster, the Ca-Si atomic bond length ( $d_{\text{Ca-Si}}$ ) is 3.009 Å, and this Ca-Si atomic bond length ( $d_{\text{Ca-Si}}$ ) is the same as the third H<sub>2</sub> adsorbed by the Ca@NaSi<sub>20</sub> cluster. Meanwhile, as shown in Table 2, when the third H<sub>2</sub> molecule is adsorbed by the Ca@NaSi<sub>20</sub> cluster, the distance ( $d_{\text{Ca-H}}$ ) between the H<sub>2</sub> molecule and the Ca@NaSi<sub>20</sub> cluster increases to 6.259 Å, and the H-H bond length ( $d_{\text{H-H}}$ ) of the adsorbed third H<sub>2</sub> molecule is the same as that of a single H<sub>2</sub> molecule, both being 0.744 Å, that is, Ca@NaSi<sub>20</sub> cluster did not complete the adsorption of the third H<sub>2</sub> molecule. From the energy range analysis, it can also be seen from Table 2 and Fig. 4 that for the  $n\text{H}_2\text{-Ca@NaSi}_{20}$  cluster, the absolute value of adsorption energy ( $E_{\text{ads}}$ ) of the Ca@NaSi<sub>20</sub> cluster also increases with the increase of the H<sub>2</sub> molecule. When the Ca@NaSi<sub>20</sub> cluster adsorbs the third H<sub>2</sub> molecule, the absolute value of the adsorption energy ( $E_{\text{ads}}$ ) is less than that of the second H<sub>2</sub> molecule ( $E_{\text{ads}}$ ), which means that the third H<sub>2</sub> molecule is not adsorbed by the Ca@NaSi<sub>20</sub> cluster, indicating that the Ca@NaSi<sub>20</sub> cluster is saturated at the adsorption of the second H<sub>2</sub> molecule. Therefore, although Ca doped NaSi<sub>20</sub> clusters can effectively adsorb 2 H<sub>2</sub> molecules, the hydrogen storage capacity is weak, which is lower than the minimum value of reversible adsorption 0.1eV, and the system is unstable after adsorption, so it is not a relatively ideal hydrogen storage material.



**Table 2** The dipole moment (D, Debye), bond length (d, Å), adsorption energy ( $E_{ads}$ , eV) and Mulliken charges (Q, e) of Ca@NaSi<sub>20</sub>.

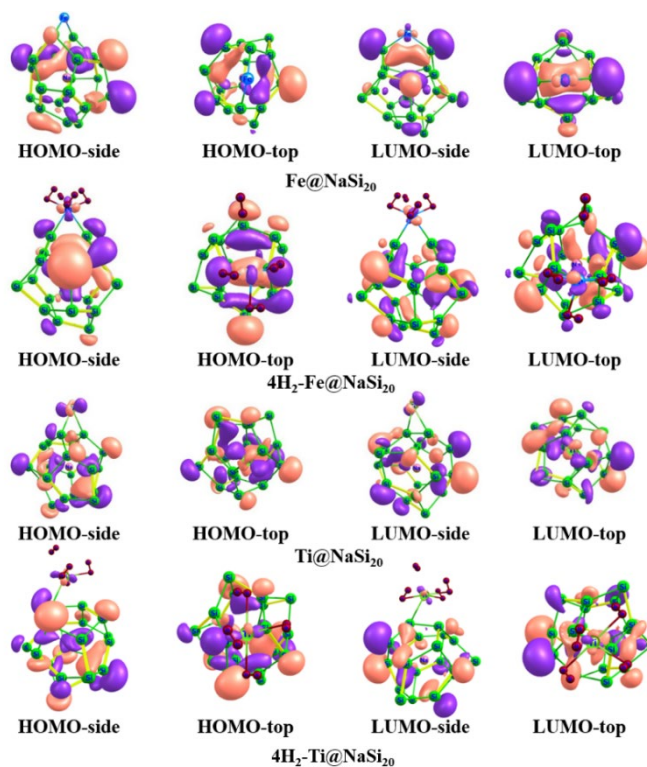
|                                        | D      | d <sub>Ca-Si</sub> | d <sub>Ca-H</sub> | d <sub>H-H</sub> | $E_{ads}$ |        | $\bar{E}_{ads}$ | $Q_{Na}$ |        | $Q_{Ca}$ | $Q_{H_2}$ |
|----------------------------------------|--------|--------------------|-------------------|------------------|-----------|--------|-----------------|----------|--------|----------|-----------|
|                                        | B3LYP  | B3LYP              | B3LYP             | B3LYP            | B3LYP     | M06-2X | B3LYP           | M06-2X   | B3LYP  | B3LYP    | B3LYP     |
| H <sub>2</sub> -Ca@NaSi <sub>20</sub>  | 11.881 | 3.012              | 4.054             | 0.745            | 0.023     | -0.040 | 0.023           | -0.040   | -0.311 | 1.020    | -0.017    |
| 2H <sub>2</sub> -Ca@NaSi <sub>20</sub> | 11.816 | 3.009              | 4.133             | 0.745            | 0.048     | -0.041 | 0.024           | -0.021   | -0.323 | 1.029    | 0.005     |
|                                        |        |                    | 5.552             | 0.745            |           |        |                 |          |        |          | -0.019    |
| 3H <sub>2</sub> -Ca@NaSi <sub>20</sub> | 11.857 | 3.009              | 4.107             | 0.745            | 0.057     | -0.042 | 0.019           | -0.014   | -0.321 | 1.030    | 0.005     |
|                                        |        |                    | 5.411             | 0.745            |           |        |                 |          |        |          | -0.021    |
|                                        |        |                    | 6.259             | 0.744            |           |        |                 |          |        |          | -0.001    |

### Adsorption of H<sub>2</sub> on Fe@NaSi<sub>20</sub>

This section concerns the interaction of the H<sub>2</sub> molecules with the Fe@NaSi<sub>20</sub> cluster. As can be seen from Table 3, the bond length of the H<sub>2</sub> molecule increases from 0.744 Å to 0.802 Å for a single H<sub>2</sub> molecule after adsorption, increasing by 0.058 Å. After the adsorption of one H<sub>2</sub> molecule, the bond length of the Si-Fe atom (d<sub>Fe-Si</sub>) in the Fe@NaSi<sub>20</sub> cluster is 2.320 Å under the B3LYP method, which is 0.047 Å shorter than the Fe@NaSi<sub>20</sub> cluster without adsorption of the H<sub>2</sub> molecule. The increasing of hydrogen molecular bond length (d<sub>H-H</sub>) and the shortening of Si-Fe atom bond length (d<sub>Fe-Si</sub>) indicate that the H<sub>2</sub> molecule is successfully adsorbed by the Fe@NaSi<sub>20</sub> cluster. In terms of energy range, when the number of adsorbed H<sub>2</sub> molecules increases from 1 to 4, the absolute value of adsorption energy ( $E_{ads}$ ) calculated by the M06-2X method gradually increases from 0.291 eV to 0.508 eV, and the absolute value of average adsorption energy ( $\bar{E}_{ads}$ ) gradually decreases from 0.291 eV to 0.127 eV. The average absolute adsorption energy of all hydrogen molecules adsorbed by clusters is greater than 0.1eV, which is within the reversible adsorption energy range of 0.1 - 0.8eV. Meanwhile, as can be seen from Fig. 5, the absolute value of the energy gap ( $E_g$ ) increases with the increase in the number of H<sub>2</sub> molecules adsorbed by the Fe@NaSi<sub>20</sub> cluster. When the fourth H<sub>2</sub> molecule is adsorbed, the energy gap ( $E_g$ ) reaches saturation. When the fifth H<sub>2</sub> molecule is adsorbed by the Fe@NaSi<sub>20</sub> cluster, the absolute value of the energy gap ( $E_g$ ) becomes smaller and increases from -2.689 eV to -1.348 eV. It can be concluded that the maximum number of H<sub>2</sub> molecules adsorbed by Fe@NaSi<sub>20</sub> is 4. From the discussion of the energy gap, adsorption energy and average adsorption energy, it can be seen that the Fe@NaSi<sub>20</sub> cluster cannot effectively adsorb the fifth H<sub>2</sub> molecule. As can be seen from the Mulliken charge  $Q_{Fe}$  of the Fe atom in Table 3, the negative charge density of Fe atom increases gradually during the adsorption of the H<sub>2</sub> molecule, while the charge density  $Q_{Na}$  of the metal atom remains basically unchanged, and the charge density reaches saturation when the fourth H<sub>2</sub> molecule is adsorbed. Therefore, it can be seen that the Fe@NaSi<sub>20</sub> cluster increases the negative charge density in the outermost orbital of the Fe atom through charge transfer between the Fe atom and H<sub>2</sub> molecule in the adsorption process of H<sub>2</sub>, so that Fe atom cannot store the fifth H<sub>2</sub> molecule, and the main hydrogen storage role in the system is determined by Fe atom. Therefore, Fe modified NaSi<sub>20</sub> cluster has strong hydrogen storage performance. Fe atoms in the Fe@NaSi<sub>20</sub> cluster can store up to 4 H<sub>2</sub> molecules, and the absolute value of average adsorption energy is within 0.1 - 0.8 eV. Fe@NaSi<sub>20</sub> cluster can realize a reversible cycle of hydrogen storage performance. Compared with the calculation results of the Ca@NaSi<sub>20</sub> cluster, Fe@NaSi<sub>20</sub> has better hydrogen storage performance.

**Table 3** The dipole moment (D, Debye), bond length (d, Å), adsorption energy ( $E_{\text{ads}}$ , eV) and Mulliken charges (Q, e) of Fe@NaSi<sub>20</sub>.

|                                            | D     | d <sub>FeSi</sub> | d <sub>FeH</sub> | d <sub>HH</sub> | $E_{\text{ads}}$ |        | $\bar{E}_{\text{ads}}$ |        | Q <sub>Na</sub> | Q <sub>Fe</sub> | Q <sub>H<sub>2</sub></sub> |
|--------------------------------------------|-------|-------------------|------------------|-----------------|------------------|--------|------------------------|--------|-----------------|-----------------|----------------------------|
|                                            | B3LYP | B3LYP             | B3LYP            | B3LYP           | B3LYP            | M06-2X | B3LYP                  | M06-2X | B3LYP           | B3LYP           | B3LYP                      |
| <b>H<sub>2</sub>-Fe@NaSi<sub>20</sub></b>  | 3.359 | 2.320             | 1.771            | 0.802           | -0.175           | -0.291 | -0.175                 | -0.291 | -0.408          | -0.298          | 0.119                      |
| <b>2H<sub>2</sub>-Fe@NaSi<sub>20</sub></b> | 3.397 | 2.260             | 1.629            | 0.851           | 0.156            | -0.345 | 0.078                  | -0.172 | -0.346          | -0.434          | 0.296                      |
|                                            |       |                   | 1.635            | 0.845           |                  |        |                        |        |                 |                 | 0.265                      |
| <b>3H<sub>2</sub>-Fe@NaSi<sub>20</sub></b> | 3.020 | 2.275             | 1.637            | 0.838           | 0.076            | -0.374 | 0.025                  | -0.125 | -0.344          | -0.614          | 0.250                      |
|                                            |       |                   | 1.635            | 0.842           |                  |        |                        |        |                 |                 | 0.230                      |
|                                            |       |                   | 1.756            | 0.796           |                  |        |                        |        |                 |                 | 0.126                      |
| <b>4H<sub>2</sub>-Fe@NaSi<sub>20</sub></b> | 3.083 | 2.289             | 1.636            | 0.843           | 0.067            | -0.508 | 0.017                  | -0.127 | -0.368          | -0.630          | 0.257                      |
|                                            |       |                   | 1.637            | 0.839           |                  |        |                        |        |                 |                 | 0.255                      |
|                                            |       |                   | 1.769            | 0.793           |                  |        |                        |        |                 |                 | 0.005                      |
|                                            |       |                   | 3.387            | 0.744           |                  |        |                        |        |                 |                 | -0.023                     |

**Fig. 5.** Frontier molecular orbitals of 4H<sub>2</sub>-Fe@NaSi<sub>20</sub> (the top row) and 4H<sub>2</sub>-Ti@NaSi<sub>20</sub> (the bottom row).

### Adsorption of H<sub>2</sub> on Ti@NaSi<sub>20</sub>

This section discusses the interaction of H<sub>2</sub> molecules with Ti@NaSi<sub>20</sub> clusters. Table 4 shows the geometric parameters of the optimized  $n\text{H}_2\text{-Ti@NaSi}_{20}$  ( $n = 6$ ) cluster. Under the B3LYP method, the bond length ( $d_{\text{H-H}}$ ) of the adsorbed H<sub>2</sub> molecule increases from 0.744 Å to 0.846 Å, and as can be seen from Fig. 2, there is no break in the hydrogen bond of all H<sub>2</sub> molecules adsorbed by  $n\text{H}_2\text{-Ti@NaSi}_{20}$  ( $n = 6$ ) system. It indicates that H<sub>2</sub> molecules are adsorbed on the cluster in molecular form. The Ti-Si atomic bond length ( $d_{\text{Ti-Si}}$ ) increases with the number of H<sub>2</sub> adsorbed. When the sixth hydrogen molecule is adsorbed, the maximum value of the Ti-Si atomic bond length ( $d_{\text{Ti-Si}}$ ) is 2.656 Å. When the seventh molecule is adsorbed by the Ti@NaSi<sub>20</sub> cluster, the Ti-Si bond is broken. That is, the Ti-Si atomic bond length ( $d_{\text{Ti-Si}}$ ) reaches the maximum value when the sixth H<sub>2</sub> molecule is adsorbed. Therefore, the Ti@NaSi<sub>20</sub> system can adsorb up to 6 H<sub>2</sub> molecules according to the bond length analysis. Under the B3LYP method, the dipole moment of the H<sub>2</sub>-Ti@NaSi<sub>20</sub> system is 0.250 Debye smaller than that of Ti@NaSi<sub>20</sub>, and under the M06-2X method the dipole moment of the H<sub>2</sub>-Ti@NaSi<sub>20</sub> system is 1.022 Debye smaller than that of Ti@NaSi<sub>20</sub>, with the decrease of dipole moment the stability of the clusters is decreased and the activity is increased. Meanwhile, Mulliken charge analysis results show that from the analysis of the charge  $Q_{\text{Ti}}$  on the Ti atom, due to the charge transfer and redistribution around the metal atoms and H<sub>2</sub> molecules, compared with the Ti@NaSi<sub>20</sub> cluster, the positive charge of the Ti atom in H<sub>2</sub>-Ti@NaSi<sub>20</sub> system decreases by 0.045 e, and  $Q_{\text{Ti}}$  gradually decreases as the number of H<sub>2</sub> molecules adsorbs increases, and reaches the minimum value at the adsorption of the sixth H<sub>2</sub> molecule. In addition, Ti atoms have fewer electrons in their outermost shell and can accept more electrons than Fe atoms, which is one reason why Ti@NaSi<sub>20</sub> can attach more H<sub>2</sub> molecules than Fe@NaSi<sub>20</sub> clusters. The absolute values of the adsorption energy ( $E_{\text{ads}}$ ) of the first H<sub>2</sub> molecule adsorbed by the Ti@NaSi<sub>20</sub> cluster were 0.185 and 0.925 eV, respectively, calculated by the B3LYP and M06-2X methods. With the number of adsorbed H<sub>2</sub> molecules gradually increasing to 6, the absolute value of adsorption energy ( $E_{\text{ads}}$ ) first increases and then decreases, and the absolute value of average adsorption energy ( $\bar{E}_{\text{ads}}$ ) first decreases, then increases and subsequently decreases with the increase of the adsorbed H<sub>2</sub> molecules, presenting an irregular change, which is related to the types of doped atoms and the types of atoms covered by silicon clusters [1]. But it's within the normal range. When the Ti@NaSi<sub>20</sub> cluster adsorbs the fourth hydrogen molecule, the absolute values of adsorption energy ( $E_{\text{ads}}$ ) and average adsorption energy ( $\bar{E}_{\text{ads}}$ ) reach the maximum value under the calculation of B3LYP and M06-2X, and the absolute values of adsorption energy ( $E_{\text{ads}}$ ) are 0.512 eV and 2.091 eV, respectively. The absolute values of average adsorption energy ( $\bar{E}_{\text{ads}}$ ) are 0.128 eV and 0.523 eV, respectively. In this case, the Ti@NaSi<sub>20</sub> cluster has the best adsorption effect on H<sub>2</sub> molecules, the system is the most stable and can realize reversible storage of H<sub>2</sub> molecules. The energy gap ( $E_{\text{g}}$ ) of the system is observed to change. The energy gap ( $E_{\text{g}}$ ) and mean adsorption energy ( $\bar{E}_{\text{ads}}$ ) of the system change in the same trend, reaching the maximum value when the fourth H<sub>2</sub> molecule is adsorbed, and the value is basically unchanged when the sixth H<sub>2</sub> molecule is adsorbed. In summary, the analysis of charge density, adsorption energy, mean adsorption energy, and energy gap of the Ti@NaSi<sub>20</sub> cluster shows that the Ti@NaSi<sub>20</sub> cluster reaches the maximum value of mean adsorption energy ( $\bar{E}_{\text{ads}}$ ) when it adsorbs 4 H<sub>2</sub> molecules, and the saturation state of H<sub>2</sub> molecular adsorption when it adsorbs 6 H<sub>2</sub> molecules. In addition, under the calculation of M06-2X, the mean adsorption energy ( $\bar{E}_{\text{ads}}$ ) of Ti@NaSi<sub>20</sub> clusters for each hydrogen molecule is within the range of 0.1- 0.8 eV, which can realize reversible adsorption of hydrogen. It is also proved that Ti@NaSi<sub>20</sub> clusters have a better storage effect on H<sub>2</sub> molecules than Ca@NaSi<sub>20</sub> and Fe@NaSi<sub>20</sub> clusters.

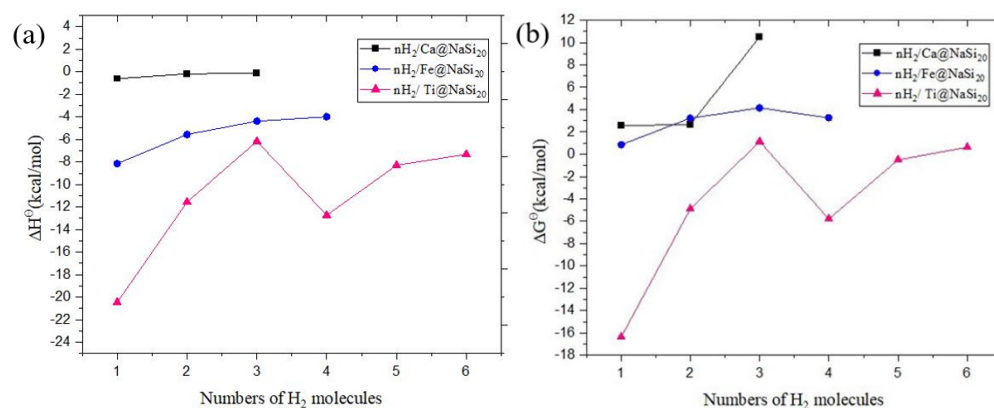
**Table 4** The dipole moment (D, Debye), bond length (d, Å), adsorption energy ( $E_{\text{ads}}$ , eV) and Mulliken charges (Q, e) of Ti@NaSi<sub>20</sub>.

|                                            | D     | d <sub>Ti-Si</sub> | d <sub>Ti-H</sub> | d <sub>H-H</sub> | $E_{\text{ads}}$ |        | $\bar{E}_{\text{ads}}$ |        | $Q_{\text{Na}}$ | $Q_{\text{Ti}}$ | $Q_{\text{H}_2}$ |
|--------------------------------------------|-------|--------------------|-------------------|------------------|------------------|--------|------------------------|--------|-----------------|-----------------|------------------|
|                                            | B3LYP | B3LYP              | B3LYP             | B3LYP            | B3LYP            | M06-2X | B3LYP                  | M06-2X | B3LYP           | B3LYP           | B3LYP            |
| <b>H<sub>2</sub>-Ti@NaSi<sub>20</sub></b>  | 8.252 | 2.465              | 1.957             | 0.791            | 0.185            | -0.925 | 0.185                  | -0.925 | -0.344          | 0.353           | -0.155           |
| <b>2H<sub>2</sub>-Ti@NaSi<sub>20</sub></b> | 7.850 | 2.452              | 1.870             | 0.824            | 0.261            | -0.966 | 0.130                  | -0.483 | -0.347          | 0.297           | -0.131           |
|                                            |       |                    | 1.855             | 0.825            |                  |        |                        |        |                 |                 | -0.118           |
| <b>3H<sub>2</sub>-Ti@NaSi<sub>20</sub></b> | 6.133 | 2.470              | 1.856             | 0.826            | -0.270           | -0.694 | -0.090                 | -0.231 | -0.353          | 0.252           | -0.026           |
|                                            |       |                    | 1.855             | 0.840            |                  |        |                        |        |                 |                 | -0.007           |
|                                            |       |                    | 1.866             | 0.826            |                  |        |                        |        |                 |                 | 0.095            |
| <b>4H<sub>2</sub>-Ti@NaSi<sub>20</sub></b> | 9.268 | 2.546              | 2.020             | 0.776            | -0.512           | -2.091 | -0.128                 | -0.523 | -0.366          | 0.279           | -0.036           |
|                                            |       |                    | 2.120             | 0.768            |                  |        |                        |        |                 |                 | -0.054           |
|                                            |       |                    | 2.028             | 0.775            |                  |        |                        |        |                 |                 | 0.094            |
|                                            |       |                    | 1.980             | 0.798            |                  |        |                        |        |                 |                 | 0.305            |
| <b>5H<sub>2</sub>-Ti@NaSi<sub>20</sub></b> | 6.426 | 2.535              | 1.912             | 0.814            | -0.413           | -1.552 | -0.083                 | -0.311 | -0.404          | 0.220           | -0.021           |
|                                            |       |                    | 1.907             | 0.816            |                  |        |                        |        |                 |                 | 0.008            |
|                                            |       |                    | 2.014             | 0.793            |                  |        |                        |        |                 |                 | 0.101            |
|                                            |       |                    | 1.875             | 0.818            |                  |        |                        |        |                 |                 | 0.149            |
|                                            |       |                    | 1.844             | 0.836            |                  |        |                        |        |                 |                 | 0.190            |
| <b>6H<sub>2</sub>-Ti@NaSi<sub>20</sub></b> | 7.089 | 2.656              | 1.818             | 0.846            | -0.279           | -1.580 | -0.047                 | -0.263 | -0.390          | 0.240           | -0.020           |
|                                            |       |                    | 1.916             | 0.811            |                  |        |                        |        |                 |                 | 0.041            |
|                                            |       |                    | 1.970             | 0.803            |                  |        |                        |        |                 |                 | 0.103            |
|                                            |       |                    | 1.917             | 0.803            |                  |        |                        |        |                 |                 | 0.204            |
|                                            |       |                    | 1.995             | 0.796            |                  |        |                        |        |                 |                 | 0.191            |
|                                            |       |                    | 1.921             | 0.810            |                  |        |                        |        |                 |                 | 0.161            |

### Orbital analysis

The two systems with the best adsorption performance were selected for the wave function analysis. Fig. 6 shows the distribution of the highest occupied molecular orbitals (HOMO) and the lowest unoccupied molecular orbitals (LUMO) in the Fe@NaSi<sub>20</sub>, Ti@NaSi<sub>20</sub>, 4H<sub>2</sub>-Fe@NaSi<sub>20</sub> and nH<sub>2</sub>-Ti@NaSi<sub>20</sub> (n=3-6) clusters, whose analysis can be used to guide the design and characterization of novel functional hydrogen storage fullerenes. The active points are the regions of high local charge density, in which the red and green colors represent the positive and negative wave functions, respectively. As can be seen from Fig. 6, in the Fe@NaSi<sub>20</sub> cluster the electron cloud contribution of the Fe atoms in HOMO-LUMO is almost zero. But after the cluster adsorbed 4 H<sub>2</sub> molecules, the electron cloud around Fe atom in the 4H<sub>2</sub>-Fe@NaSi<sub>20</sub> cluster increased

and HOMO distribution increased, which represents charge transfer between Fe atoms and H<sub>2</sub> molecules. This is consistent with the previous charge analysis of  $Q_{\text{Fe}}$  and  $Q_{\text{H}_2}$ . For the Ti@NaSi<sub>20</sub> cluster, HOMO and LUMO are partially distributed on Ti and partially distributed on the NaSi<sub>20</sub> cluster when there is no H<sub>2</sub> molecule adsorbed. With the increase of H<sub>2</sub> molecules from 3 to 6, the distribution of frontier orbitals on Ti gradually decreases. When four H<sub>2</sub> molecules are adsorbed, there are a few unoccupied orbitals around Ti atoms, indicating that they can still adsorb H<sub>2</sub> molecules, which is consistent with the previous analysis trend.



**Fig. 6.** (a) Enthalpy difference ( $\Delta H^{\ominus}$ ) and (b) free energy difference ( $\Delta G^{\ominus}$ ) for  $n\text{H}_2/\text{Ca}@Na\text{Si}_{20}$ ,  $n\text{H}_2/\text{Fe}@Na\text{Si}_{20}$  and  $n\text{H}_2/\text{Ti}@Na\text{Si}_{20}$  calculated at M06-2X method.

### Adsorbed H<sub>2</sub> prediction

Theoretically, the Effective Atomic Number Rule (EAN) can be used to calculate the maximum adsorption capacity of hydrogen atoms of hydrogen storage material with surface doped metal atoms [26]. The equation is as follows,

$$n_{\text{H}} = 18 - n_{\text{v}}^e - n_{\text{s}}^e - n_{\text{m}}^e \quad (10)$$

where  $n_{\text{v}}^e$  is the number of valence electrons of the metal atom,  $n_{\text{s}}^e$  is the bonding number of the metal to the substrate, and  $n_{\text{m}}^e$  is the bonding number between neighboring metal atoms. Considering the 3d orbitals of transition metal atoms Ti and Fe, the valence electron numbers ( $n_{\text{v}}^e$ ) of Ca, Fe, and Ti atoms are 2, 8, and 4, respectively. Since M is adsorbed above the Si-Si bond,  $n_{\text{s}}^e = 2$ , the  $n_{\text{H}}$  of  $M@NaSi_{20}$  (M = Ca, Fe, and Ti) is calculated to be 14, 8, and 12, respectively, which means that the maximum adsorption numbers of hydrogen molecules are 7, 4, and 6. Compared with the calculated results, it can be seen that the hydrogen storage performance of  $\text{Ca}@NaSi_{20}$  is less than the theoretical results, so the hydrogen storage performance is poor. The maximum hydrogen storage number of  $M@NaSi_{20}$  (M = Fe and Ti) is in accordance with the theoretical expectation, *i.e.*, the number of H<sub>2</sub> molecules that can be adsorbed is in accordance with EAN. At the same time, we tried to adsorb the third, 5th, and 7th H<sub>2</sub> molecules on  $\text{Ca}@NaSi_{20}$ ,  $\text{Fe}@NaSi_{20}$ , and  $\text{Ti}@NaSi_{20}$ , respectively. None of the results calculated by the density functional method can converge, which further indicates that  $\text{Ca}@NaSi_{20}$ ,  $\text{Fe}@NaSi_{20}$ , and  $\text{Ti}@NaSi_{20}$  can adsorb at most 2, 4, and 6 H<sub>2</sub> molecules.

### Thermodynamic analysis

The enthalpy difference ( $\Delta H^{\ominus}$ ) can express the strength of the interaction and the free energy difference ( $\Delta G^{\ominus}$ ) is a measure of the spontaneity of the reaction, which are the key thermodynamic parameters for the interaction between hydrogen and the sorbent materials.  $\Delta H^{\ominus}$  and  $\Delta G^{\ominus}$  are graphed in Fig. 7 as a function of the number of hydrogen molecules for  $n\text{H}_2\text{-Ca}@NaSi_{20}$ ,  $n\text{H}_2\text{-Fe}@NaSi_{20}$ , and  $n\text{H}_2\text{-Ti}@NaSi_{20}$  complexes. As

shown in Fig. 7a,  $\Delta H^\circ$  values are negative for all the considered structures, indicating exothermic reactions. For all the complexes of the  $n\text{H}_2\text{-Ti@NaSi}_{20}$  system only the free energy difference of  $1\text{H}_2\text{-Ti@NaSi}_{20}$ ,  $2\text{H}_2\text{-Ti@NaSi}_{20}$ ,  $4\text{H}_2\text{-Ti@NaSi}_{20}$ ,  $5\text{H}_2\text{-Ti@NaSi}_{20}$  is negative ( $\Delta G^\circ < 0$ ), which shows that they are spontaneous reactions. In the  $n\text{H}_2\text{-Ti@NaSi}_{20}$  system, when  $n = 1$  the absolute value of  $\Delta H^\circ$  decreases as the number of  $\text{H}_2$  molecules increases, and the absolute value of  $\Delta H^\circ$  is 20.45 kcal/mol. It can be seen from Fig. 7b, in all the complexes,  $3\text{H}_2\text{-Ca@NaSi}_{20}$  has the largest value of free energy difference ( $\Delta G^\circ$ ), which is 10.50 kcal/mol. As a negative  $\Delta H^\circ$  value indicates stronger stability, and a negative  $\Delta G^\circ$  value indicates stronger reversal ability of the reaction, with the increase of the number of hydrogen molecules, the stability decreases, the hydrogen storage capacity gradually reaches saturation, and the desorption ability of  $\text{H}_2$  molecules increases [27-29].

## Conclusions

In this work, the storage characteristics of  $\text{H}_2$  molecules on  $\text{NaSi}_{20}$  fullerenes deposited by Ca, Fe, and Ti were investigated at the theoretical level of the DFT-based B3LYP and M06-2X methods. The results show that the encapsulated Na atom into the  $\text{Si}_{20}$  cluster delivers the regular shape to the  $\text{NaSi}_{20}$ . The deposition of the Ca, Fe and Ti atoms on  $\text{NaSi}_{20}$  clusters decreases the ionization potential (IP), HOMO-LUMO energy gap ( $E_g$ ), and hardness ( $\eta$ ), and increases the dipole moment (D), which confirms that  $\text{Ca@NaSi}_{20}$ ,  $\text{Fe@NaSi}_{20}$ , and  $\text{Ti@NaSi}_{20}$  clusters are less stable and therefore more reactive than  $\text{NaSi}_{20}$  clusters.

Additionally, the  $\text{Ca@NaSi}_{20}$ ,  $\text{Fe@NaSi}_{20}$ , and  $\text{Ti@NaSi}_{20}$  clusters are saturated by two, four, and six  $\text{H}_2$  molecules, respectively. The adsorption energy values ( $E_{\text{ads}}$ ) per hydrogen molecule meet the U. S. DOE target for hydrogen storage materials for  $n\text{H}_2\text{-Ti@NaSi}_{20}$  ( $n = 2 - 6$ ) and  $n\text{H}_2\text{-Fe@NaSi}_{20}$  ( $n = 1-4$ ), which implies that  $\text{NaSi}_{20}$  fullerenes may be a potentially suitable material for hydrogen storage. The calculated enthalpy differences emphasize that some hydrogen molecules are physisorbed on the studied clusters with an effect greater than one.

## Acknowledgements

This study was financially supported by the Natural Science Basic Research Plan in Shaanxi Province of China (Program No. 2022JM-075) and the Three-year action plan project of Xi'an University (Program No. 21XJZZ0001-11) as well as the Youth Innovation Team of Shaanxi Universities (Environmental Pollution Monitoring and Control Innovation Team, 51).

## References

1. Hoel, M.; Kverndok, K. *Resour Energy Econ.* **1996**, 18, 115-136.
2. Kale, P. *Int J Hydrogen Energy.* **2012**, 37, 3741-3747.
3. Bailleux, C. *Int J Hydrogen Energy.* **1981**, 6, 461.
4. Mazloomi, K. *Renew Sust Energ Rev.* **2012**, 16, 3024-3033.
5. Anafcheh, M. *Int J Hydrogen Energy.* **2018**, 43, 12271-12277.
6. Xu, W. *Prog Chem.* **2006**, 18, 200-201.
7. Gong, J. M. *Natural Gas Chem. Indus.* **2010**, 5, 71.
8. Sahaym, U. *J Mater Sci.* **2008**, 43, 5395.
9. Wang, Q.; Sun, Q.; Jena, P.; Kawazoe, Y. *J Chem Theory Comput.* **2009**, 5, 374-379.
10. Zhang, D. J.; Ma, C.; Liu, C. B. *J Phys Chem C.* **2007**, 111, 17099.
11. Khanna, S. N.; Rao, B. K.; Jena, P. *Phys Rev Lett.* **2002**, 89, 016803.

12. Kumar, V.; Kawazoe, Y. *Phys Rev Lett.* **2003**, 90, 055502.
13. Ryou, J.; Hong, S.; Kim, G. *Solid State Commun.* **2008**, 148, 469-471.
14. Kumar, V.; Kawazoe, Y. *Phys Rev B.* **2007**, 75, 155425.
15. Sporea, C.; Rabilloud, F. *J Chem Phys.* **2007**, 127, 164306.
16. Ammar, H. Y.; Badran, H. M. *Int J Hydrogen Energy.* **2021**, 46, 14565-14580.
17. Williamson, A. J.; Reboredo, F. A.; Galli, G. *Appl Phys Lett.* **2004**, 85, 2917-2919.
18. Yoon, M.; Yang, S.Y.; Hicke, C.; Wang, E. *Phys Rev Lett.* **2008**, 100, 206806.
19. Wang, C. J.; Tang, C. M.; Zhang, Y. J.; Gao, F. Z. *Chem Res Chin Univ.* **2014**, 35, 2131-2137.
20. Kohn, W.; Sham, L. J. *Phys Rev.* **1965**, 140, 1133-1138.
21. Mao, W. L.; Mao, H. K. *Proc Natl Acad Sci USA.* **2004**, 101, 708-710.
22. Frisch, M. J. Gaussian 09, revision D.01, Wallingford, CT: Gaussian, Inc, 2009.
23. Guo, C.; Wang, C. *Int J Hydrogen Energy.* **2019**, 44, 10763-10769.
24. Borshch, N. A.; Pereslavytseva, N. S.; Kurganskiĭ, S. I. *Semiconductors.* **2006**, 40, 1457-1462.
25. Baei, M. T.; Koochi, M.; Shariati, M. *J Mol Struct.* **2018**, 1159, 118-134.
26. Kubas, G. J. *Kluwer Academic/Plenum Publishing.* 2001.
27. Padhee, S. P.; Roy, A.; Pati, S. *Int J Hydrogen Energy.* **2021**, 46, 906-921.
28. Liu, Z. C.; Ruan, Y. M.; Li, F.; Zhang, G. F.; Zhao, M. *Int J Hydrogen Energy.* **2021**, 46, 4201-4210.
29. Pluengphon, P.; Tsuppayakorn-ae, P.; Inceesungvorn, B. *Int J Hydrogen Energy.* **2020**, 45, 25065-25074.

## Experimental Studies to Optimize Process Parameters for the Removal of Cationic and Anionic Dyes by Natural Cypress Leaves

Oussama Larabi<sup>1</sup>, Afaf Amara-Rekkab<sup>1,2\*</sup>, Mohamed Amine Didi<sup>1</sup>, Amel Didi<sup>1</sup>, Souad Feddane<sup>1</sup>

<sup>1</sup>Laboratory of Separation and Purification Technologies, Department of Chemistry — Faculty of Sciences, Box 119, University of Tlemcen — 13000, Algeria.

<sup>2</sup>Institute of Science and Technology, Department of Hydraulics, University center of Maghnia, Zouia maghnia street— 13000, Algeria.

\*Corresponding author: Afaf Amara-Rekkab, email: [amarafaf@yahoo.fr](mailto:amarafaf@yahoo.fr); [afaf.amara@cumaghnia.dz](mailto:afaf.amara@cumaghnia.dz)

Received March 30<sup>th</sup>, 2023; Accepted January 23<sup>rd</sup>, 2024.

DOI: <http://dx.doi.org/10.29356/jmcs.v68i3.2037>

**Abstract.** In this study, cypress leaves were used for the preparation of a biosorbent to remove brilliant green (BG) and black lanasyn (LB) from aqueous solutions. The influence of several experimental factors, such as time of contact, pH, initial concentration, ionic strength, temperature, stirring speed, and particle size, on the adsorption of these dyes was studied. Contact time effect has showed that balance was reached at 30 min with adsorption capacities 9.24 and 4.08 mg/g and elimination rates of 95.97 % and 34 % for BG and LB, respectively. Moreover, the study has shown that the adsorption of the two dyes can be described by pseudo-second-order kinetics. The adsorption isotherms demonstrated that the Freundlich model was satisfactory compared with the Langmuir model for describing the process of adsorption of the two dyes on the cypress. The results showed that the adsorption process is spontaneous, feasible, and endothermic for BG and non-spontaneous and exothermic for LB. Multi-docking reflecting the biosorption of brilliant green and Lanasyn black on the adsorbant surface is proposed. On the fundamental plane, the fractional orthogonal Taguchi plane  $L_{16} (4^5)$  was used to optimize the conditions for brilliant green adsorption on the cypress. In conclusion, the results showed that cypress leaves could be advantageously used as a low-cost biosorbent for the removal of brilliant green and lanasyn black in wastewater treatment.

**Keywords:** Brilliant green; lanasyn black; cypress leaves; adsorption; Taguchi method.

**Resumen.** En este estudio se usaron hojas de ciprés para preparar un biosorbente que remueve los colorantes verde brillante (BG) y lanasyn negro (LB) de soluciones acuosas. En la adsorción de estos colorantes se estudió la influencia de varios factores experimentales como tiempo de contacto, pH, concentración inicial, fuerza iónica, temperatura, velocidad de agitación y tamaño de partícula. El efecto del tiempo de contacto mostró que el balance se alcanzó a los 30 min con capacidades de adsorción de 9.24 y 4.08 mg/g y velocidades de eliminación de 95.97 % y 34 % para BG y LB, respectivamente. El estudio mostró que la adsorción de los dos colorantes se puede describir por una cinética de pseudo segundo orden. Para describir el proceso de adsorción de los dos colorantes en las hojas de ciprés, las isothermas de adsorción demostraron que el modelo de Freundlich es satisfactorio comparado con el modelo de Langmuir. Los resultados muestran que el proceso de adsorción es espontáneo, factible y endotérmico para BG, y no espontáneo y exotérmico para LB. Se propone un acoplamiento múltiple reflejando la biosorción del verde brillante y el lanasyn negro sobre la superficie del adsorbente. En el aspecto fundamental, la fracción ortogonal del plano de Taguchi  $L_{16} (4^5)$  se utilizó para optimizar las condiciones de adsorción del verde brillante en las hojas de ciprés. En conclusión, los resultados muestran que las hojas de ciprés pueden utilizarse como biosorbentes de bajo costo para la remoción de verde brillante y lanasyn negro en el tratamiento de aguas residuales.



**Palabras clave:** Verde brillante; lanasyn negro; hojas de ciprés; adsorción; método de Taguchi.

---

## Introduction

The textile industry's need for various types of dyes used in clothing dye and paper printing is a main source of water pollution [1]. Although dyes are present in only small amounts, they are highly detectable and thereby capable of causing various problems.

In addition, dyes are widely used in the textile, paper, plastic, and leather industries. Effluents discharged from these industries generally contain high concentrations of waste dyes. In addition, synthetic dyes can cause enormous environmental pollution, and pose a serious threat to human health [2-3]. For example, they cause severe headaches, profuse sweating, and other similar risks [4]. Therefore, the removal of dyes from wastewater is widely practiced in the industrial environment.

They are the first pollutants detected visually; however, because of their synthetic origin and mainly complex aromatic molecules, they are among the most difficult to remove. Most dyes are not directly or extremely toxic to living organisms [5]. For instance, brilliant green dye is an important dye in the paper printing and textile industries. Wood and silk materials, in particular, are dyed brilliant green. Its effluents are also generated by the rubber and plastic industries. This dye is hazardous in the case of skin contact, eye contact, and ingestion. It is toxic to the lungs by inhalation. Repeated or prolonged exposure to this substance may cause damage to the target organ. During its decomposition, it can generate carbon dioxide, sulfur oxides, and nitrogen oxides. Therefore, it is more important to remove the brilliant green dye from the aqueous solution [6].

Lanasyn black is an acidic metal complex azo dye. It is considered to be one of the most widely used and difficult to remove in wastewater [7].

Various physical, chemical, and biological techniques have been developed and tested to treat wastewater containing dyes, such as coagulation and agglomeration [8], biodegradation [9-10], membrane filtration [11-13], chemical oxidation [14], ozone treatment [15], ion exchange [16], electrochemical processes [17-20], and adsorption [21-23]. However, these processes are expensive and generate large quantities of sludge or derivatives.

Adsorption techniques are the cheapest methods to remove dyes, and they have become the analytical method of choice due to their high ability to purify contaminated water, high efficiency, and ease of use [24]. Biosorbents are the most commonly used materials because of their low cost. However, literature on the optimization of Brilliant green and Lanasyn black removal from aqueous solutions by the selected adsorbent using the Taguchi method design is not available.

Our work is based on the extraction of two dyes ("Brilliant green" cationic dye and "Black lanasyn" anionic dye) by a natural biosorbent, namely cypress leaves. The extraction technique used is liquid–solid extraction. Note that the adsorption of brilliant green and lanasyn black on different materials has been extensively investigated [25-34].

The analysis method used was UV-visible spectroscopy. The following parameters, stirring time, concentration effect, pH, ionic strength, salts (NaCl, Na<sub>2</sub>SO<sub>4</sub>, KBr, KNO<sub>3</sub>), temperature, grain size, and stirring speed, were studied during this experiment to determine their influence on the extraction.

The effect of these experimental parameters on extraction was also studied by statistical treatment using the orthogonal array of L<sub>16</sub> (4<sup>5</sup>) of Taguchi modeling.

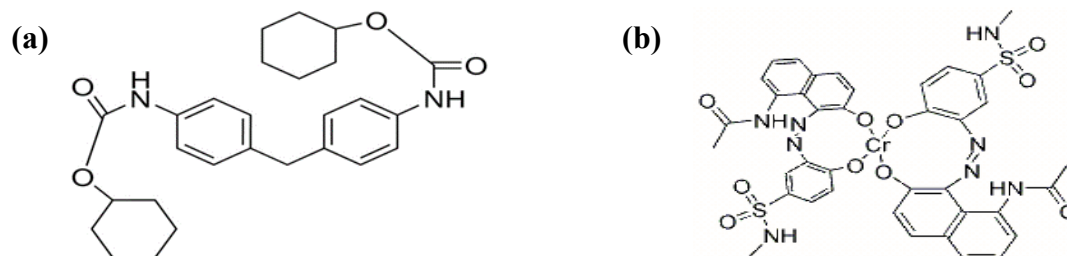
## Experimental

### Preparation of the biosorbent

After collecting the cypress leaves from the tree, we washed them well with distilled water and left them to dry in the sun and then in an oven for 24 h at 60°C. After washing and drying, our biosorbent was ground and sieved as well as possible to a diameter of less than 0.2 mm, ready for use.

## Dyes

Brilliant green (BG) and lanasyn black (LB) are used as dyes of analytical and practical grade, respectively. They were supplied to us by a textile factory (SOITEX) located in Tlemcen, Algeria. Their molecular structures are given in Scheme. 1.



**Scheme. 1.** Chemical structure of BG (a) and LB (b).

## Preparation of the solutions

In a 1000 mL volumetric flask, 0.1 g of the brilliant green dye was added. 20 mL of distilled water was added to dissolve the dye, and the mixture was filled up to the mark. In another 500-mL volumetric flask, 0.05 g of black was introduced and adjusted to the gauge mark. For both dyes, solutions were prepared at different concentrations, namely 10, 15, 20, 25, 30, 35, 40, 45, 50 ppm by dilution.

Solutions of HNO<sub>3</sub> and NaOH were prepared by diluting HNO<sub>3</sub> (69 %) (AnalaR NORMAPUR) and dissolving appropriate amounts of NaOH (CARLA ERBA) in distilled water, respectively.

Previously calculated quantities of the salts NaCl (PROLABO), Na<sub>2</sub>SO<sub>4</sub> (Sigma Aldrich), KNO<sub>3</sub> (Sigma Aldrich), and KBr (Sigma Aldrich) were dissolved in distilled water. The purity of all these compounds exceeds 99 %.

## Equipment used

UV-visible spectrophotometer (Analytik Jena Specord 210 plus), pH meter (Adwa AD1030), centrifuge (Sigma 2-6), analytical balance (Pioneer TM), oven (Binder), mechanical stirrer with a speed controller (Haier), heating and stirring plate (Yellow Line), and sieve shaker (Orto Alresa) were used in our study.

## Extraction procedure

The adsorption experiments were performed at different initial values of pH, temperature, and initial dye concentration. The tests were performed by shaking (at 250 rpm) 0.05 g of the cypress leaves in 10 mL of the synthetic solutions of the brilliant green and black dyes at concentrations varying from 10 to 50 ppm. The coloured solution was separated from the adsorbent by centrifugation at 4000 rpm for 10 min. The absorbance of the supernatant was measured using a UV/visible spectrometer at the wavelength that corresponds to the maximum absorbance of the BG ( $\lambda_{\text{max}} = 625$  nm) and LB ( $\lambda_{\text{max}} = 575$  nm). The residual dye concentration was determined using the calibration curve performed with a range of concentrations from 10 mg/L to 50 mg/L of BG and LB.

The adsorption capacity (Q) and adsorption yield of the dyes by the cypress leaves were calculated using Eq. (1) and (2):

$$Q \text{ (mg/g)} = \frac{(C_0 - C) \times V}{m} \quad (1)$$

$$\text{Biosorption yield (\%)} = \frac{C_0 - C}{C_0} \times 100 \quad (2)$$

where C<sub>0</sub>, C, V, and m are the initial concentration (ppm), equilibrium concentration (ppm), batch volume (L), and biosorbent mass, respectively.

## Results and discussion

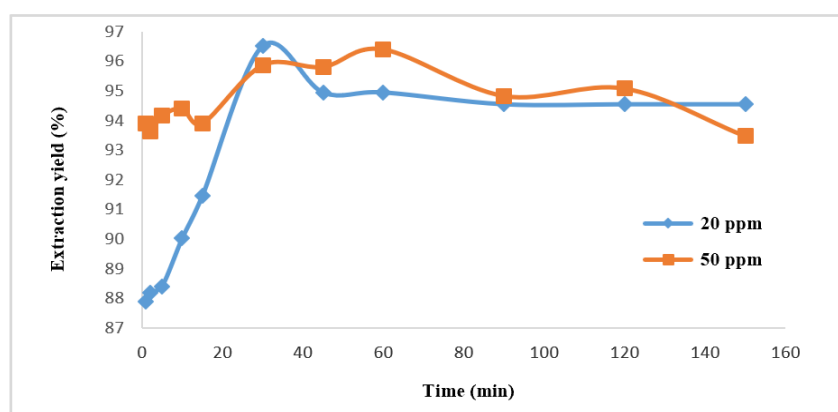
### Determination of the point of zero charge $\text{pH}_{\text{pzc}}$

50 mL of NaCl (0.1 M) is put in a series of polypropylene bottles where the pH has been adjusted to precise values of 1–12 by the addition of 1 M NaOH or HCl. Then, 0.1 g of the adsorbent was added to each vial. The suspensions were kept under constant stirring at ambient temperature for 24 h to determine the final pH. The point of zero charge (pzc) corresponds to the intersection of the curve  $\Delta\text{pH} = \text{pH}_f - \text{pH}_i$  as a function of  $\text{pH}_i$  with the abscissa axis.

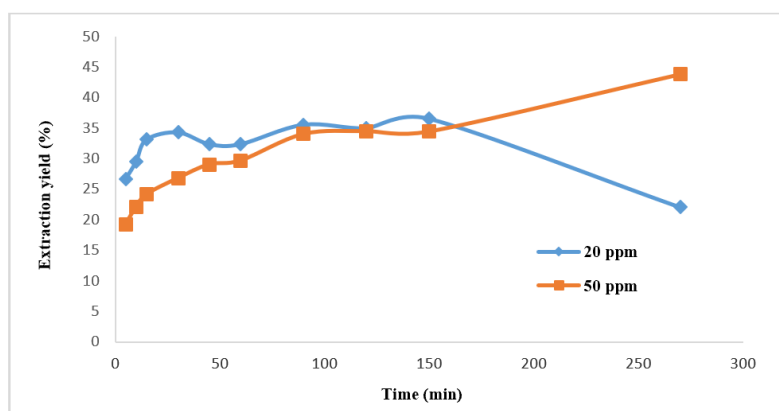
### Study of Adsorption

#### Effect of Agitation Time

Contact time is necessary to establish adsorption between the dye and the cypress biosorbent. This study was conducted to determine the fixed quantities of adsorbate dye from its first contact with the biosorbent until equilibrium is reached. For this, we followed the kinetics of adsorption of brilliant green and black lanasyn at initial concentrations of 20 and 50 ppm in contact with 0.1 g of cypress. The mixture was stirred at 25° C for varying durations ranging from 1 to 150 min. The yield curves of the adsorbed dyes as a function of time  $E(\%) = f(\text{Time})$  are presented in Figures 1 and 2.



**Fig. 1.** Effect of time on BG extraction by cypress leaves,  $\text{pH} = 6.3$ ,  $C_{\text{BG1}} = 20$  ppm,  $C_{\text{BG2}} = 50$  ppm, mass of biosorbent = 0.1g,  $V_{\text{solution}} = 10$  mL, and temperature = 18 °C.



**Fig. 2.** Effect of time on LB extraction by cypress leaves,  $\text{pH} = 3.3$ ,  $C_{\text{LB1}} = 20$  ppm,  $C_{\text{LB2}} = 50$  ppm, mass of biosorbent = 0.1 g,  $V_{\text{solution}} = 10$  mL, and temperature = 18 °C.

The study of the extraction yield as a function of the initial concentration, which is presented in Fig. 1, shows that the yield is better for the high concentration (50 ppm). It is observed that the increase in the initial concentration of BG causes a global increase in the adsorption of the dye. This is probably due to the saturation of cypress leaves active sites with the dye molecules, and consequently, the adsorption process decreased and finally reached equilibrium. The same observation was made in another research [24]. The opposite effect occurred in the case of LB adsorption, except for the high time of contact, Fig. 2.

Moreover, Fig. 1 shows that the adsorption is fast at the beginning of the process and becomes increasingly slow during the stirring time. The removal efficiency and adsorption capacity reached 95.97 % and 9.24 mg/g for a contact time of 30 min (equilibrium time), respectively.

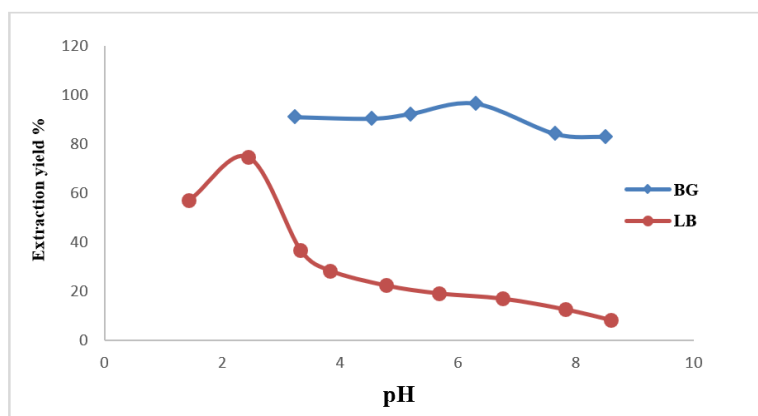
From Fig. 2, we can note that the yield of the LB dye increases with stirring time, and the time required to reach equilibrium is 150 min with a removal efficiency of 34 % and an adsorption capacity  $q$  of 4.08 mg/g.

These contact times were fixed for the different dyes in the rest of the experiments. The high speed of adsorption in the first minutes of the reaction can be explained by the fact that at the start of adsorption, the number of active sites available on the surface of the adsorbent is much greater than the sites remaining after some time. For high contact times, the molecules need time to diffuse inside the pores of the adsorbent. The remaining unabsorbed amount may be attributed to the saturation of the adsorbent surface [24].

### Effect of pH

The initial pH of the coloured solutions is a crucial factor in controlling the adsorption process of cationic and anionic organic compounds. To evaluate the effect of the initial pH on the adsorption of the dyes studied, we chose coloured solutions at a concentration of 20 ppm with pH varying from 1 to 8. Acidification was achieved by the addition of a few drops of nitric acid  $\text{HNO}_3$  1M. A solution of 1 M NaOH was used to make the medium basic.

Variations in the yield (%) of dye elimination as a function of the pH of the medium are presented in Fig. 3.



**Fig. 3.** Effect of pH on BG and LB extraction by cypress leaves, contact time: [30; 150 min],  $C_{BG} = C_{LB} = 20$  ppm, mass of biosorbent = 0.1g,  $V_{\text{solution}} = 10$  mL, and temperature = 18 °C.

The  $\text{pH}_{\text{pzc}}$  value of cypress leaves was 4.9. Consequently, at pH above the  $\text{pH}_{\text{pzc}}$  the adsorbent surface is negatively charged, favoring cation adsorption, anions adsorption is enhanced at pH below  $\text{pH}_{\text{pzc}}$ .

Fig. 3 highlights a slight increase in extraction yield when the pH is acidic. At pH 6, the BG adsorption yield reaches a maximum value of  $E$  equal to 96.52 %. We notice a strong decrease when the pH is strongly basic and higher than  $\text{pH}_{\text{pzc}}$  because of the repulsion between the negatively charged surface of the support and the molecules of the dye, which are also negatively charged. The biosorbent surface is slightly

acidic and positively charged when the pH of the solution is lower than  $\text{pH}_{\text{pzc}}$  and negatively charged when the pH of the solution is higher than  $\text{pH}_{\text{pzc}}$  [1]. In our case,  $\text{pH}_{\text{pzc}}$  is 4.9.

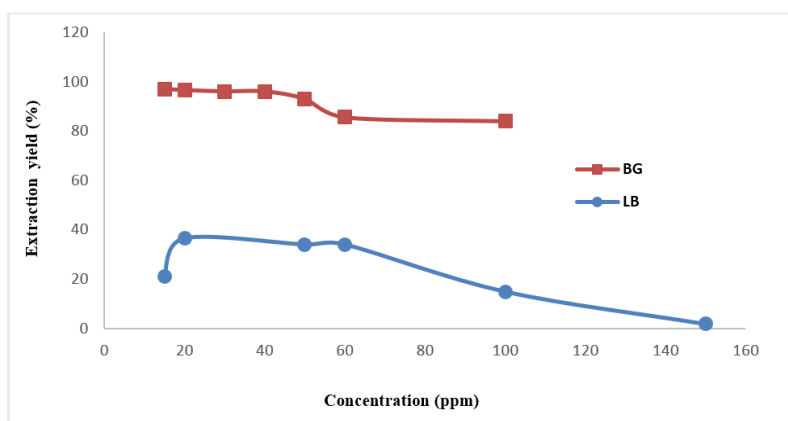
Concerning LB and from Fig. 3, we noticed that the extraction depends on the pH change of the aqueous phase. The extraction yield increases from 39.45 % to 78.45 % when the initial pH increases in parallel from 1.44 to 2.44. We notice also that the adsorption rate greatly decreased when the initial pH of the solution increased from 2.44 to 3.33. From the curve represented in Fig. 3, we can state that the best dye removal efficiency 78.45 % is obtained at pH equal to 2.44.

Finally, we can conclude that the variation in pH values reflects the effect of the chemical structure of the acid dye moieties on the adsorption process and their affinity for adsorption. The high affinity of the acid dye for the biosorbent is the result of ionic interactions between the anionic centers on the dye and the basic sites [35].

### Effect of initial concentration

The effect of the initial concentration of the dye on the adsorption capacity of the different dyes on the "cypress" biosorbent was studied because of the significant influence of this parameter.

The concentration values vary between 10 and 100 ppm at a fixed room temperature for a contact time of 30 to 150 min. The results obtained from this study are shown in Fig. 4.

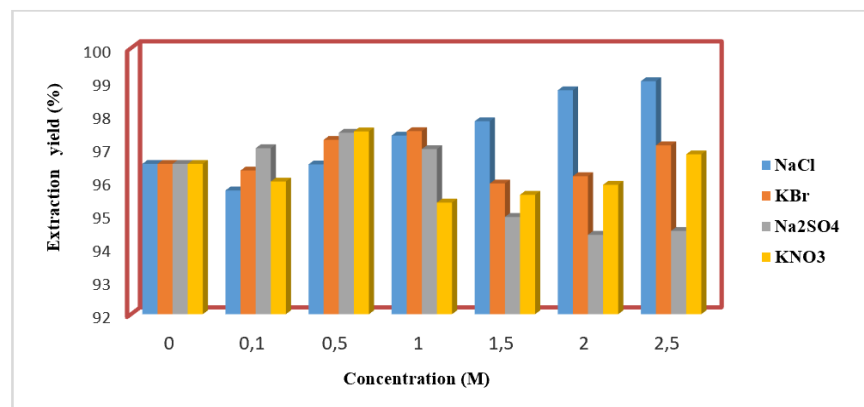


**Fig. 4.** Effect of initial concentration on BG and LB extraction by cypress leaves, contact time: [30; 150 min], pH= [6.3; 3.3], mass of biosorbent = 0.1 g,  $V_{\text{solution}} = 10$  mL, and temperature = 18 °C.

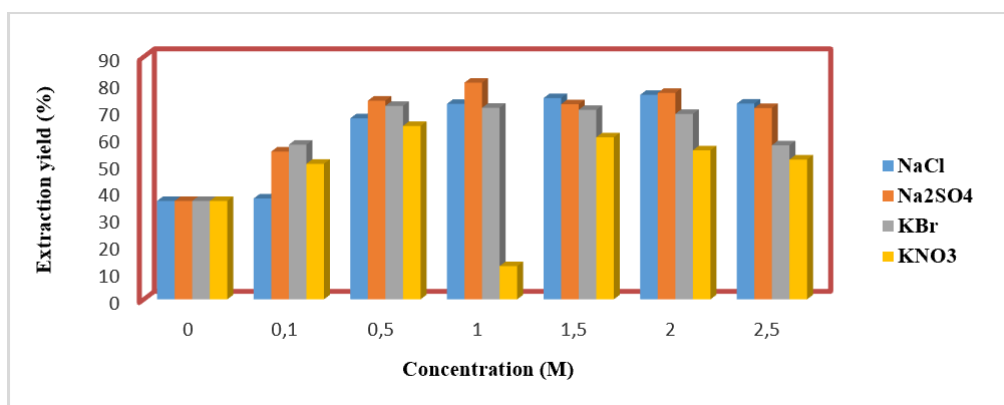
Fig. 4 shows that the LB adsorption capacity increases at low concentrations and reaches its maximum percentage at a concentration of 20 ppm, which corresponds to yields of 36.50 %, while the BG adsorption capacity decreases monotonously as the dye concentration increases. From these results, it can be concluded that the adsorption of dyes strongly depends on the initial concentration of the solution.

### Effect of the ionic strength

The effect of ionic strength was studied using solutions of the following salts: NaCl, KNO<sub>3</sub>, Na<sub>2</sub>SO<sub>4</sub>, and KBr at different concentrations. The results are shown in Figs. 5 and 6.



**Fig. 5.** Effect of ionic strength on BG extraction by cypress leaves, pH = 6.3,  $C_{BG} = 20$  ppm, mass of biosorbent = 0.1g,  $V_{\text{solution}} = 10$  mL, and temperature = 18°C.



**Fig. 6.** Effect of ionic strength on LB extraction by cypress leaves, pH = 3.3,  $C_{LB} = 20$  ppm, biosorbent mass = 0.1 g,  $V_{\text{solution}} = 10$  mL, and temperature = 18 °C.

As shown in Fig. 5, the addition of KBr and KNO<sub>3</sub> decreases the adsorbed amount of BG, whereas the presence of NaCl and Na<sub>2</sub>SO<sub>4</sub> promotes its adsorption.

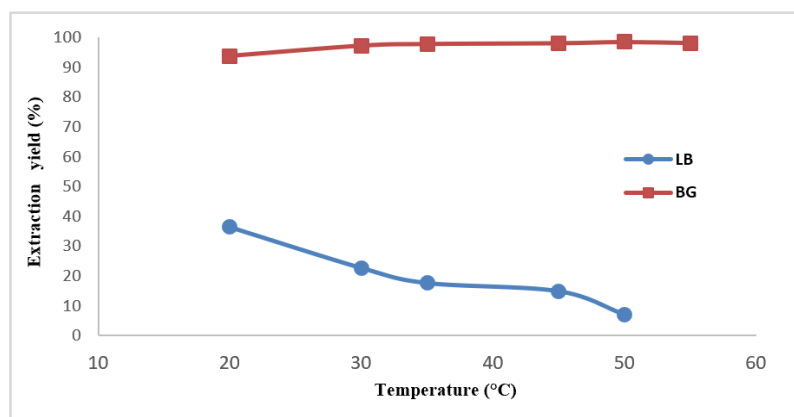
The increase in the adsorption of the dye on the biosorbents with the addition of NaCl and Na<sub>2</sub>SO<sub>4</sub> can then be attributed to the shielding of the repellent forces by the ionic force. This result is consistent with the literature that reports that when electrostatic forces are repulsive, an increase in ionic strength has a positive effect on adsorption [36]. We can also interpret these results using the Gouy Chapman theory on the double diffusion layer. This theory predicts that the thickness of this layer would be low with the ionic force, which facilitates the closeness of adsorbate molecules and particles. Furthermore, when NaCl is present in water, it dissolves easily. This results in a weakening of the bonds, so its hydrophobicity increases, which promotes dye adsorption [37].

Fig. 6 shows that the addition of the salts Na<sub>2</sub>SO<sub>4</sub> and NaCl in the aqueous phase leads to an increase in the percentage of elimination of black lanasyn when the concentration in the aqueous phase of Na<sub>2</sub>SO<sub>4</sub> and NaCl varies from 0 to 2.5 M, the extraction yield increases from 36.50 % to 80.39 % and from 36.50 % to 75.87 %, respectively. Therefore, the presence of Na<sup>+</sup> increases the extraction yield according to the Chatelier principle. Conversely, when adding KBr and KNO<sub>3</sub>, there is a decrease in the rate of adsorption.

This result can be explained by an ionic competition between the cation  $K^+$  and the anionic dye LB. This allows us to conclude that the salt that best promotes adsorption is indeed  $Na_2SO_4$ .

### Temperature influence

To study the effect of temperature on the adsorption of BG and LB on the biosorbent, experiments were conducted at different temperatures from 20°C to 55°C. Fig. 9 represents the results obtained.



**Fig. 7.** Temperature effect on BG and LB extraction by cypress leaves, contact time: [30; 150 min], pH= [6.3; 3.3],  $C_{LB} = 20$  ppm,  $C_{BG} = 20$  ppm, mass of biosorbent = 0.1 g,  $V_{solution} = 10$  mL.

For the BG, it is noted from Fig. 7 that the increase in temperature causes an increase in the yield, i.e., the adsorption capacity. In this case, the phenomenon is endothermic ( $\Delta H > 0$ ). The increase in adsorption with temperature is due to the increase in the solubility of the dye with the increase in temperature [37].

This figure also shows that an increase in the extraction temperature in the domain [20 °C – 50 °C] decreases the extraction yield of LB. This result can be attributed to the release of heat because  $\Delta H < 0$  in this case.

To determine the different thermodynamic parameters (enthalpy:  $\Delta H^\circ$ , entropy:  $\Delta S^\circ$  and free enthalpy:  $\Delta G^\circ$ ), we trace  $\ln K_d$  as a function of  $1/T$ :

$$\ln K_d = \frac{\Delta S^\circ}{R} - \frac{\Delta H^\circ}{RT} \quad (3)$$

This equation is drawn from the following equations:

$$\Delta G^\circ = \Delta H^\circ - T\Delta S^\circ \quad (4)$$

$$\Delta G^\circ = -RT \ln K_d \quad (5)$$

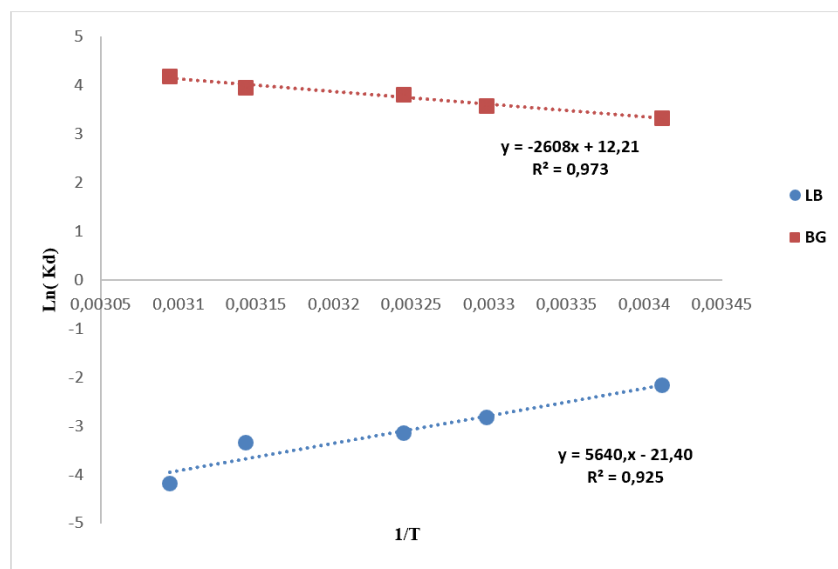
where R is the constant of perfect gases ( $R = 8.314 \text{ J}\cdot\text{mol}^{-1}\cdot\text{K}^{-1}$ ) and  $K_d$  is the distribution coefficient or partition coefficient of the two dyes BG and LB between the liquid and solid phases.

On the other hand,  $K_d$  is given by Eq. (6):

$$K_d = \frac{[C]}{[C]_{aq}} \quad (6)$$

where  $[C]$  and  $[C]_{aq}$  are the concentrations of the dyes BG and LB in both solid and the liquid phases at equilibrium, respectively.

The tracing of  $\ln K_d$  as a function of  $1/T$  allowed us to determine  $\Delta H^\circ$  and  $\Delta S^\circ$ .



**Fig. 8.** Evolution of  $\ln K_d$  as a function of  $1/T$  for BG and LB, contact time: [30; 150 min], pH= [6.3; 3.3],  $C_{BG} = C_{LB} = 20$  ppm, biosorbent mass = 0.1 g,  $V_{\text{Solution}} = 10$  mL,  $T = 18$  °C.

The values of the enthalpic  $\Delta H^\circ$  and  $\Delta S^\circ$  were determined from the slopes and the ordinate at the origin of the obtained straight lines according to Eq. (3), respectively.

**Table 1.** Summarizes the calculated values of  $\Delta H^\circ$  and  $\Delta S^\circ$ , and  $\Delta G^\circ$  at different temperatures.

| Dye             | $\Delta H^\circ$<br>(kJ/mol) | $\Delta S^\circ$<br>(J/mol.K) | $\Delta G^\circ$ (kJ/mol) |          |          |          |          |
|-----------------|------------------------------|-------------------------------|---------------------------|----------|----------|----------|----------|
|                 |                              |                               | 293.15 K                  | 303.15 K | 308.15 K | 318.15 K | 323.15 K |
| Brilliant green | 21.68                        | 999.45                        | -8.096                    | -9.010   | -9.763   | -10.432  | -11.242  |
| Lanasyn black   | -46.89                       | -177.94                       | 1.349                     | 3.083    | 3.945    | 4.607    | 6.907    |

The values of  $\Delta H^\circ$ ,  $\Delta S^\circ$ ,  $\Delta G^\circ$  allow us to perform a thermodynamic analysis.

Indeed, the inspection of table 1 enabled us to notice the following:

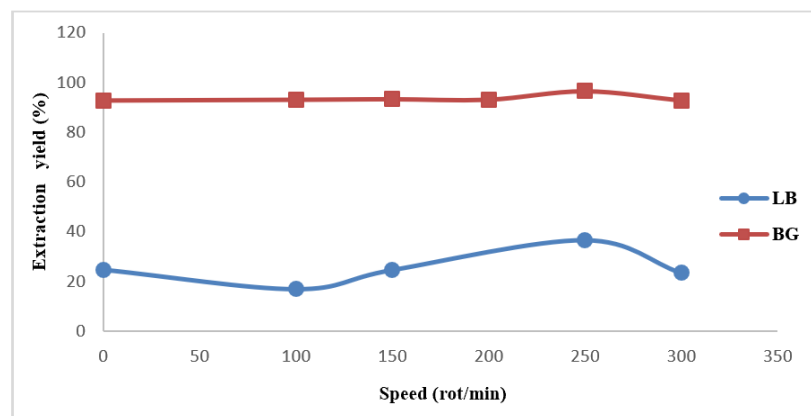
- For BG, the positive sign of the enthalpy of extraction reflects the endothermic nature of BG extraction. Moreover, the positive value of  $\Delta S^\circ$  indicates that the molecular disorder has increased, and the negative value of  $\Delta G^\circ$  indicates that the extraction is a spontaneous process.
- For LB, the negative sign of the enthalpy of extraction reflects the exothermic nature of LB extraction. Moreover, the negative value of  $\Delta S^\circ$  indicates an increase in order during adsorption. Randomness decreases at the solid-solution interface during this binding process. This can be explained by the redistribution of energy between the adsorbent and the adsorbate.



### Influence of stirring speed

To check the material transfer rate on the surface of the biosorbent, we tested different stirring rates, i.e.,  $w = 0, 100, 150, 200, 250,$  and  $300$  rpm.

In adsorption processes, the stirring rate plays a crucial role in ensuring a good distribution of the adsorbent in the total volume of the adsorbate [36]. The results obtained are shown in Fig. 9.



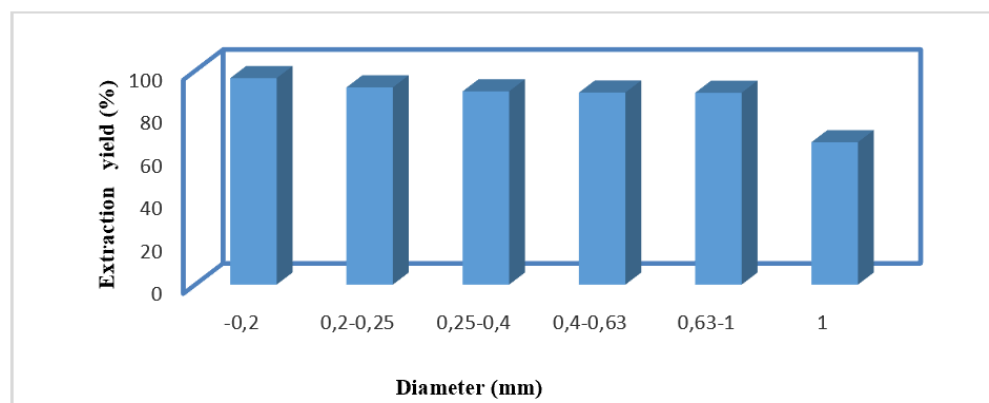
**Fig. 9.** Effect of stirring rate on BG and LB extraction by cypress leaves, contact time: [30; 150 min], pH= [6.3; 3.3],  $C_{BG} = C_{LB} = 20$  ppm, mass of biosorbent = 0.1 g,  $V_{\text{solution}} = 10$  mL.  $T = 18$  °C.

The results obtained from the study of the effect of the stirring rate on the adsorption of the two dyes on the cypress show that the maximum retention capacity is at a stirring speed of 250 rpm. Indeed, an average stirring speed of 250 rpm ensures good diffusion of the different dyes to the biosorbent used.

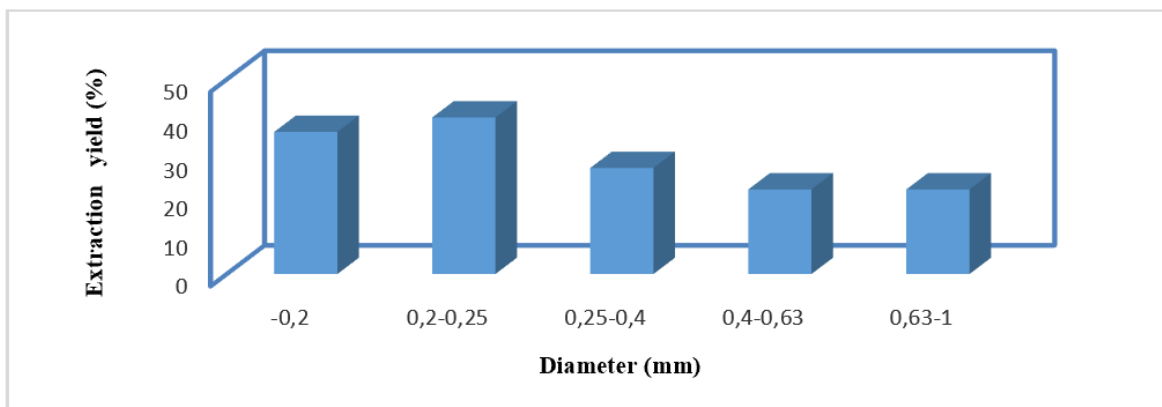
We can note that the homogenization of the mixture and a very high stirring rate reduce the contact between the dye and the support.

### Effect of particle size

This effect has a significant impact on the adsorption capacity. In our study, five types of cypress particle sizes were used to study their effects on the adsorption of different dyes. Figures. 10 and 11 show the results obtained.



**Fig. 10.** Particle size effect on BG extraction of by cypress leaves, contact time = 30 min, pH = 6.3,  $C_{BG} = 20$  ppm, biosorbent mass = 0.1 g,  $V_{\text{solution}} = 10$  mL, and temperature = 18 °C.



**Fig. 11.** Particle size effect on LB extraction by cypress leaves, contact time = 150 min, pH=3.3,  $C_{LB} = 20$  ppm, biosorbent mass = 0.1g,  $V_{\text{solution}} = 10$  mL, and temperature = 18 °C.

These figures demonstrate that adsorption is significant and rapid for small samples, particularly in the case of BG. This could be explained by the fact that adsorption depends on the outer surface of the particles; the smaller the particle size, the larger the exchange surface, favoring a high rate of transfer from the dye to the adsorbent. In our work, the extraction yield was better for particle sizes of the order of 0.2 mm.

### Models of kinetics

Several kinetic models were used to interpret the experimental data and provide essential information for the use of biosorbents in the adsorption domain. The most often used are pseudo-first-order and pseudo-second-order models [38].

#### Pseudo-first-order model

The expression is given by Lagergren:

$$\log (q_e - q_t) = \log (q_e) - (k_1 t / 2.303) \quad (7)$$

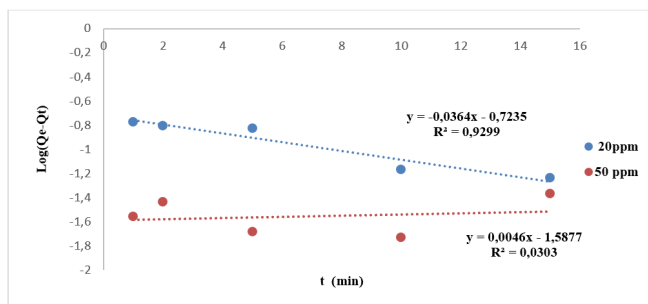
where  $k_1$  is the first-order reaction rate constant of the adsorption of BG or LB in (min),  $q_e$  is the amount of BG or LB adsorbed at equilibrium in (mg/g),  $q_t$  is the amount of BG or LB adsorbed at time  $t$  in (mg/g), and  $t$  is the contact time in (min).

#### Pseudo-second-order model

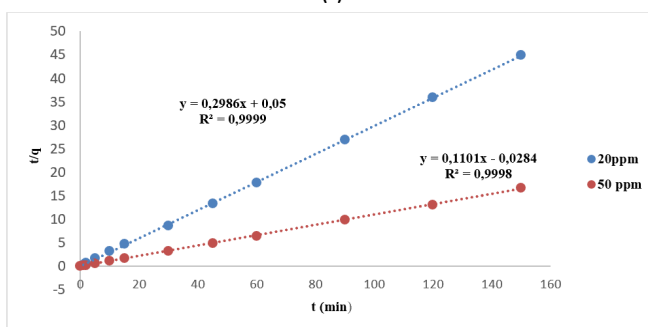
The pseudo-second-order model is given by the following expression [38]:

$$\frac{t}{q_t} = \frac{1}{k_2} * \frac{1}{q_e^2} + \frac{1}{q_e} * t \quad (8)$$

The results obtained for dye concentrations of 20 and 50 ppm are shown in Figs. 14 and 15:

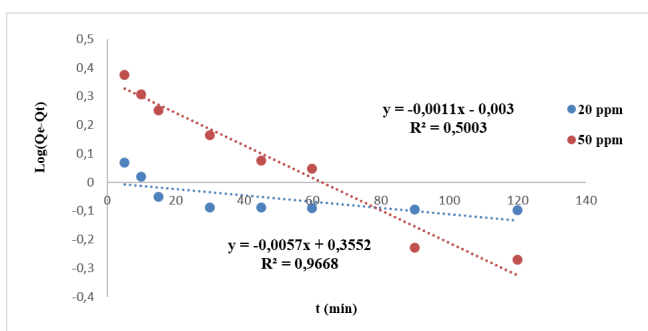


(a)

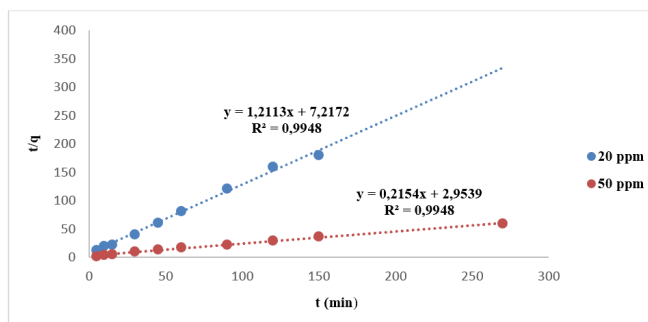


(b)

**Fig. 12.** (a) Pseudo-first-order, (b) pseudo-second-order kinetic modeling of BG adsorption on cypress leaves.



(a)



(b)

**Fig. 13.** (a) Pseudo-first-order, (b) pseudo-second-order kinetic modeling of LB adsorption on cypress leaves.

All parameters deduced from these figures and from the equation listed above are summarized in Table 2.

**Table 2.** Result of adsorption kinetics modeling for the two dyes.

|               | Brilliant green |        |        |              |        |        | Lanasyn black |        |        |              |        |        |
|---------------|-----------------|--------|--------|--------------|--------|--------|---------------|--------|--------|--------------|--------|--------|
|               | First order     |        |        | Second order |        |        | First order   |        |        | Second order |        |        |
|               | $q_e$           | $k_1$  | $R^2$  | $q_e$        | $k_2$  | $R^2$  | $q_e$         | $k_1$  | $R^2$  | $q_e$        | $k_2$  | $R^2$  |
| <b>20 ppm</b> | 0.485           | 0.0364 | 0.9299 | 3.3489       | 1.7833 | 0.9999 | 0.9931        | 0.0025 | 0.5003 | 0.8255       | 0.2033 | 0.9948 |
| <b>50 ppm</b> | 0.2043          | -0.004 | 0.0303 | 9.0744       | -0.362 | 0.9998 | 2.2656        | 0.0131 | 0.9668 | 4.6425       | 0.0157 | 0.9948 |

The results of the adsorption kinetics modeling for the dye BG mentioned in Table 2 show that the kinetic adsorption for the dye BG is of order 2, and that the adsorbed amount of the dye is better at a low concentration of 20 ppm. We also observe in Fig. 14 that for 20 ppm, the first and second orders are parallel to each other and stable over time, whereas for 50 ppm, the first and second orders differ slightly. Moreover, we note that the values of K decrease with increasing concentration.

Concerning LB, and according to the correlation values mentioned in Table 2 and Fig. 15, we can conclude that the 2<sup>nd</sup> order model is the most reliable and best for the concentration of 20 ppm. It is also observed that the value of K decreases with increasing concentration.

### Isotherms of adsorption

Adsorption isotherms are an important aspect of assessing the adsorption capacity of a biosorbent and demonstrating its efficacy [39].

Several adsorption isotherms have been proposed in the literature to express the equilibria of a solute on the surface of a solid. Among these models, the Freundlich and Langmuir models were chosen.

Equilibrium ( $C_e$ ) concentrations of BG and LB were quantified their adsorption mechanisms were elucidated using established nonlinear adsorption isotherms.

### Langmuir Model

Langmuir's linear equation is:

$$\frac{c_e}{q_e} = \frac{1}{q_{max} * k_l} + \frac{c_e}{q_{max}} \quad (9)$$

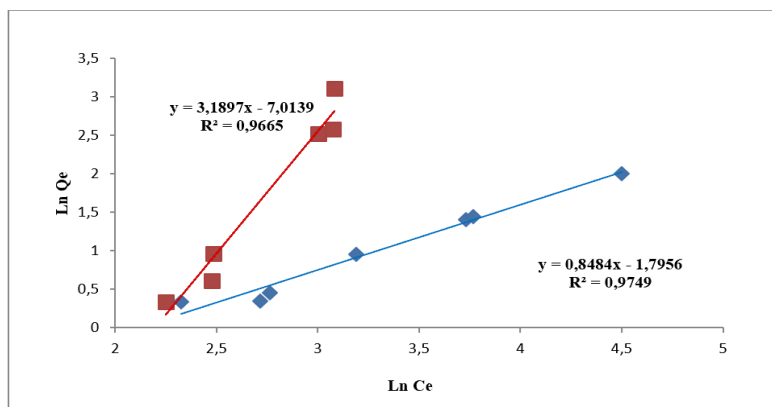
where  $C_e$  is the residual concentration of the solute in the equilibrium solution (mg/L).  $q_e$  is the equilibrium adsorption capacity (mg/g),  $q_{max}$  is the maximum adsorption capacity (mg/g), and  $k_L$  is the Langmuir adsorption coefficient (L/mg) [40].

### Freundlich model

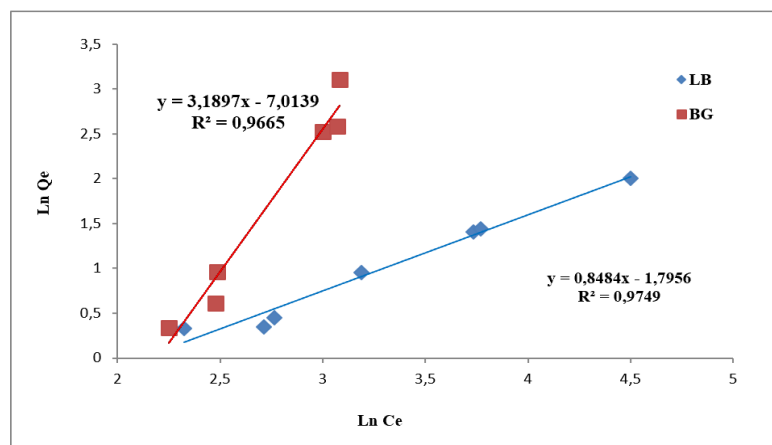
The linear form of the equation is:

$$\ln q_e = \ln k_f + \frac{1}{n} \ln c_e \quad (10)$$

where  $q_e$  is the equilibrium adsorption capacity (mg/g).  $k_f$  is the Freundlich adsorption coefficient (L/mg), and  $C_e$  is the residual concentration of the solute in the equilibrium (mg/L) [41].



**Fig. 14.** Langmuir isotherm for the adsorption of BG and LB on cypress leaves.



**Fig. 15.** Freundlich isotherm for the adsorption of BG and LB on cypress leaves.

The corresponding parameters are grouped in Table 3.

**Table 3.** Parameters of the Langmuir and Freundlich models for adsorption isotherm modeling of the two dyes on the biosorbent.

| Langmuir        |       |         |               |                      |         | Freundlich      |        |                      |               |        |       |
|-----------------|-------|---------|---------------|----------------------|---------|-----------------|--------|----------------------|---------------|--------|-------|
| Brilliant green |       |         | Lanasyn black |                      |         | Brilliant green |        |                      | Lanasyn black |        |       |
| $Q_m$           | $k_L$ | $R_L^2$ | $Q_m$         | $k_L$                | $R_L^2$ | $1/n$           | $R^2$  | $k_f$                | $1/n$         | $R^2$  | $K_f$ |
| 2.38            | 0.039 | 0.9387  | 37.593        | $2.82 \cdot 10^{-3}$ | 0.6412  | 3.1897          | 0.9665 | $8.99 \cdot 10^{-4}$ | 0.8484        | 0.9749 | 0.166 |

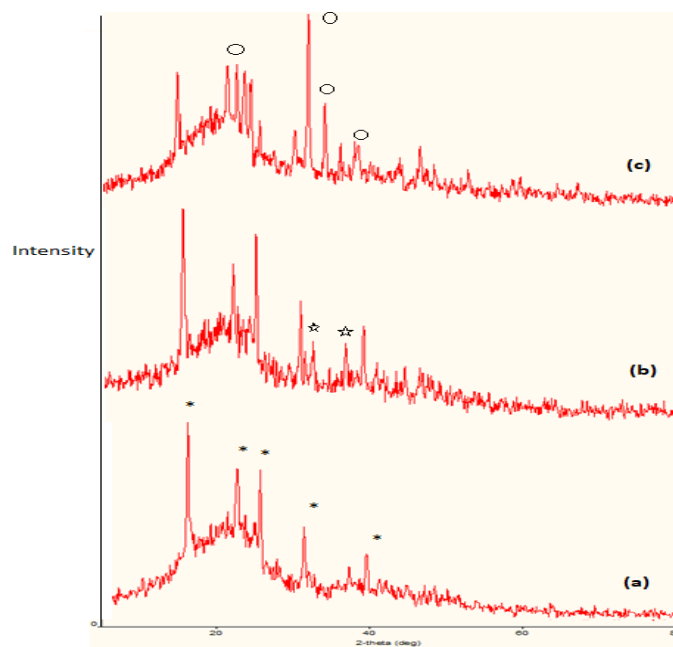
The results mentioned in Table 3 show that the modeling of adsorption isotherms at different concentrations of BG corroborates that the Freundlich model describes the experimental data of adsorption well.

For LB, the experimental values were adjusted for different isotherms such as Langmuir and Freundlich and are shown in Figs. 14 and 15. The different isotherm constants were evaluated, and the values of  $R^2$  were close to 1.0. In the case of the Freundlich model, the best fit of the experimental data is given by the Freundlich isotherm. The  $n$ -value of the Freundlich isotherm was found to be greater than unity ( $n = 1.17$ ). LB confirms the heterogeneity and greater affinity of LB toward the dye [42].

### Characterization of the biosorbent

#### XRD characterization

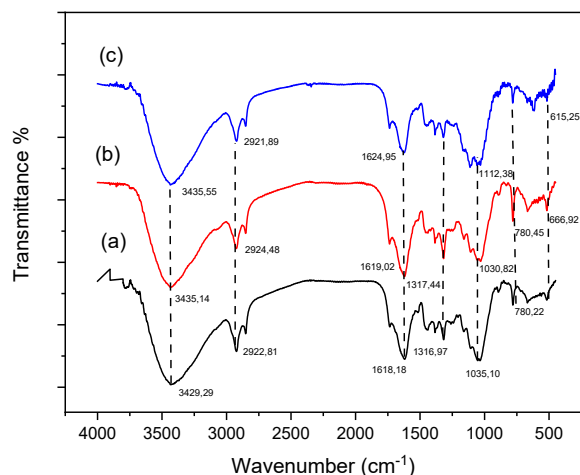
For the cypress leaves, an intense diffraction peak was observed at  $2\theta = 15.51^\circ$  and the other peaks were observed at  $2\theta = 21.93$  and  $24.94^\circ$  (Fig. 16 (a)). Diffraction peaks for BG were observed at  $2\theta = 15.45^\circ$  and  $24.91^\circ$ . For the LB, they were observed at  $2\theta = 15.50^\circ$ ,  $24.00^\circ$ ,  $32.453^\circ$ ,  $31^\circ$  and  $34.50^\circ$  as shown in Figs. 16 (b) and 16 (c). In comparing the latter with that of the cypress leaves composite, the peaks of cypress leaves-BG and cypress leaves-LB are moved toward the lower angles with the disappearance of the peak  $2\theta = 21.94$  for BG and the appearance of two new peaks for LB at  $2\theta = 32.453$  and  $34.50$ . This confirms that the adsorption of the dyes is successful.



**Fig. 16.** XRD of cypress leaves (a) before, (b) after brilliant green adsorption, and (c) after lanasyn black adsorption.

#### Fourier transform infrared spectroscopy

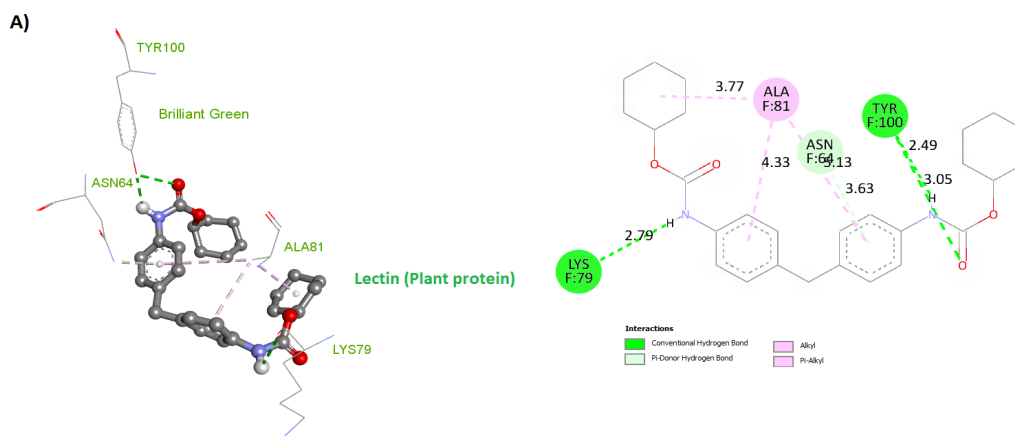
As can be observed in Fig. 17 (a), the strong and wide band with a maximum at  $3400\text{ cm}^{-1}$  can be assigned to the vibrations of the  $-\text{OH}$  group linked in cellulose and lignin molecules or by adsorbed water [43]. Stretching vibrations of C-H and C-O bonds were attributed to the bands at  $2922\text{ cm}^{-1}$  and  $1618\text{ cm}^{-1}$ , respectively. The band around  $1316\text{ cm}^{-1}$  was assigned to C-O stretching. The band at  $1035\text{ cm}^{-1}$  was assigned to C-O stretching of cellulose present in cypress leaves. The band around  $780\text{ cm}^{-1}$  was assigned to C-H bending. Furthermore, Fig.17 (b) and (c) show the spectra of BG-loaded and LB-loaded cypress leaves. A change is observed in the signal intensity of some bands and the displacement or appearance of other bands. These differences could be related to the possible involvement of specific functional groups on the cypress leaves surface during the adsorption process.

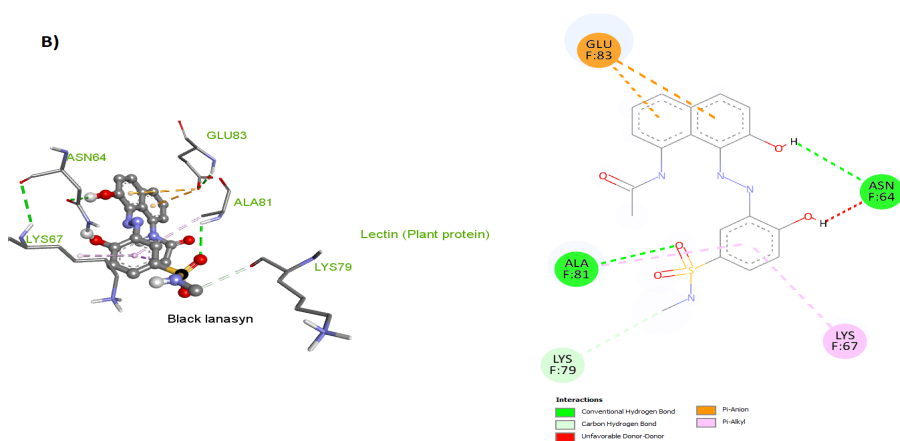


**Fig. 17.** FTIR spectra of cypress leaves (a) before, (b) after brilliant green adsorption, and (c) after lanasyn black adsorption.

### Docking analysis of brilliant green and lanasyn black

Molecular docking studies were carried out to validate the experimental findings and locate the credible binding interfaces of ligands with the active sites of the enzymes of our biosorbent cypress leaves. Lectins were synthesized in our biosorbent previously [44]. Docking studies were performed using the AUTODOCK 4.2 program [45-47]. The structure of lectins was retrieved from the Protein Data Bank (PDB: 5Y42): <https://www.rcsb.org/structure/5Y42> (Protein Plant). The 3D structures in PDB format of dyes were designed by Chemdraw data base and converted to PDB format using AutoDock Tools where the water molecules were removed, the polar hydrogen atoms were added to the amino acid residues. Then the protein in PDBQT format was used as an input for the AUTOGRID program. Rigid ligand docking was performed with using a blind docking. The results were shown using Discovery Studio Visualizer [46-48].





**Fig. 18.** 3D images of lectins of cypress leaves with (A) Brilliant green and (B) Lanasyn black.

Molecular docking allowed us to identify the different active sites of our biosorbent. Brilliant green complexed inside the active sites of lectins of cypress leaves, showing many important interactions, as presented in Fig. 18. It formed conventional hydrogen bonds with TRY 100 (2.49 and 3.05°A) and LYS 79 (2.79°A) amino acid residues of lectins. ASN 64 (3.63, 3.77 and 4.33°A) developed alkyl and pi-alkyl interactions with brilliant green. The ASN 64 residue stabilized the ligand by forming pi-donor hydrogen bond (3.13 °A) interactions.

Lanasyn black developed two converted hydrogen bonds: ASN 64 (4.59 °A), ALA 81 (3.74 °A), amino acid residues of the biosorbent. GLU 83 developed two  $\pi$ -anion (3.57 and 4.37°A) interaction with the lanasyn black. Pi-alkyl interaction was developed (LYS 67: 4.86 °A) and carbon hydrogen bond interaction (LYS 79: 5.71 °A) with our biosorbent. The least binding energies between lectins and brilliant green and lanasyn black were - 5.3 and - 5.6 Kcal/mol, respectively.

### Application of the Taguchi methodology

The adsorption process can be influenced by several variables, such as the initial pH of the solution, adsorbent dose, adsorbate concentration, contact time, temperature, stirring speed, and parameters related to the state of the adsorbate and the adsorbent. Therefore, to achieve maximum contaminant removal, it is important to adopt an experimental design and optimize the process conditions. In this part, it is a question of applying the statistical approach of Taguchi to optimize the parameters of the process of adsorption of brilliant green by the leaves of cypress. In the Taguchi method, word optimization implies the determination of the best controllable factor levels. The best levels of controllable factors are those that maximize the signal-to-noise (S/N) ratios [43]. Given that our results showed that cypress leaves adsorb brilliant green better than lanasyn black, we preferred to apply the Taguchi methodology only for brilliant green.

The orthogonal table  $L_{16} (4^5)$  was chosen for the extraction of brilliant green by the cypress leaves. It is a matrix of experiments with 5 columns (5 factors at 4 levels each) and 16 rows, i.e., 16 experiments to be carried out.

**Table 4.** Parameters examined and their levels for the brilliant green dye.

| Level | pH  | [BG] (ppm) | NaCl (M) | Granulometry (mm) | Time (min) |
|-------|-----|------------|----------|-------------------|------------|
| 1     | 3.3 | 20         | 0        | < 0.02            | 1          |
| 2     | 4.8 | 40         | 0.5      | 0.25-0.4          | 15         |
| 3     | 6.3 | 60         | 1.5      | 0.4-0.63          | 30         |
| 4     | 7.8 | 80         | 2.5      | 1                 | 60         |



### Analysis of the results of the extraction of Brilliant green dye

In this study, we will follow the evolution of the extraction yields of the brilliant green dye by the biosorbent "cypress leaves." The latter requires sixteen (16) experiments.

The signal-to-noise ratio (S/N) is a performance indicator used by Taguchi. Determining the combination of the main effects that are important and evaluating their influence on responses (extraction yield). This ratio simultaneously takes into account the desired objective (the signal) and the dispersion of this value (noise). It is determined differently depending on the nature of the criterion studied.

In this study, we seek to maximize the signal/noise (S/N) ratio. This is calculated as follows:

$$\frac{S}{N} = -10 \log \left( \frac{1}{n} \sum_{i=1}^n \frac{1}{E_i^2} \right) \quad (11)$$

where n denotes the number of duplicates in each experiment (3 times) and  $E_i$  denotes the extraction yield in each experiment. We calculated the S/N ratio to identify the control and noise parameters.

**Table 5.** Experimental results for the adsorption of brilliant green by cypress leaves.

|    | pH | [BG] (ppm) | NaCl (M) | Granulometry (mm) | Time (min) | R <sub>1</sub> (%) | R <sub>2</sub> (%) | R <sub>3</sub> (%) | R <sub>m</sub> (%) | S / N |
|----|----|------------|----------|-------------------|------------|--------------------|--------------------|--------------------|--------------------|-------|
| 1  | 1  | 1          | 1        | 1                 | 1          | 79.92              | 84.25              | 80.00              | 81.39              | 38.21 |
| 2  | 1  | 2          | 2        | 2                 | 2          | 61.00              | 75.41              | 71.73              | 69.38              | 36.82 |
| 3  | 1  | 3          | 3        | 3                 | 3          | 76.30              | 69.42              | 72.60              | 72.78              | 37.23 |
| 4  | 1  | 4          | 4        | 4                 | 4          | 32.06              | 36.20              | 34.13              | 34.13              | 30.66 |
| 5  | 2  | 1          | 2        | 3                 | 4          | 38.01              | 42.14              | 42.15              | 40.77              | 32.21 |
| 6  | 2  | 2          | 1        | 4                 | 3          | 86.48              | 90.06              | 87.68              | 88.08              | 38.90 |
| 7  | 2  | 3          | 4        | 1                 | 2          | 86.63              | 85.71              | 75.74              | 82.70              | 38.35 |
| 8  | 2  | 4          | 3        | 2                 | 1          | 94.20              | 92.02              | 92.73              | 93.00              | 39.36 |
| 9  | 3  | 1          | 3        | 4                 | 2          | 71.00              | 67.92              | 68.00              | 69.00              | 36.77 |
| 10 | 3  | 2          | 4        | 3                 | 1          | 40.09              | 44.50              | 39.98              | 42.84              | 32.64 |
| 11 | 3  | 3          | 1        | 2                 | 4          | 66.00              | 67.74              | 67.02              | 66.91              | 36.51 |
| 12 | 3  | 4          | 2        | 1                 | 3          | 95.90              | 98.33              | 93.78              | 96.00              | 39.65 |
| 13 | 4  | 1          | 4        | 2                 | 3          | 92.51              | 89.21              | 92.71              | 91.50              | 39.23 |
| 14 | 4  | 2          | 3        | 1                 | 4          | 90.00              | 89.90              | 93.76              | 91.05              | 39.19 |
| 15 | 4  | 3          | 2        | 4                 | 1          | 62.64              | 62.68              | 64.66              | 63.33              | 36.04 |
| 16 | 4  | 4          | 1        | 3                 | 2          | 56.00              | 48.71              | 54.87              | 53.11              | 34.50 |

We notice that the best interaction at experiment 12 was when pH was at level 3, concentration of BG at level 4, concentration of NaCl at level 2, particle size at level 1, and time at level 3.

### Parameter effect calculations

The effect of a parameter is defined as the absolute value of the difference between the average of the ratios (S/N) of two levels *i* and *j* of the parameter. This translates mathematically into the following relationship:

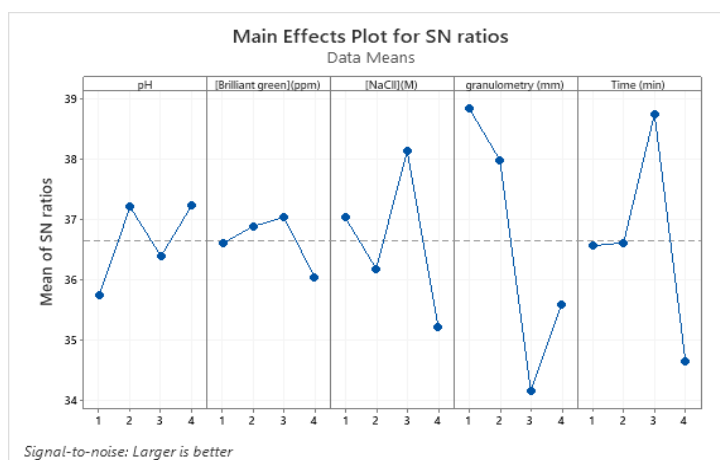
$$\Delta(S/N)_m = |[(S/N)_m]_j - [(S/N)_m]_i| \quad i < j \quad (12)$$

The parameter with the absolute value of the highest difference has the most significant effect on the response.

**Table 6.** Ratios (S/N) *m* and main effects of parameters for the adsorption of brilliant green on cypress leaves.

| Level | pH    | [Brilliant green](ppm) | [NaCl] (M) | Granulometry (mm) | Time (min) |
|-------|-------|------------------------|------------|-------------------|------------|
| 1     | 35.72 | 36.60                  | 37.02      | 38.86             | 36.54      |
| 2     | 37.22 | 36.90                  | 36.2       | 38.00             | 36.60      |
| 3     | 36.40 | 37.02                  | 38.15      | 34.16             | 38.76      |
| 4     | 37.25 | 36.03                  | 35.22      | 35.60             | 34.65      |
| Delta | 1.51  | 1.00                   | 2.5        | 4.71              | 4.12       |
| Rank  | 4     | 5                      | 3          | 1                 | 2          |

The highest plots of each parameter were chosen, as shown in Fig. 19. The ratio was chosen because the larger the ratio, the better [40]. The same optimum conditions can be seen in Table 6 by the delta values. Therefore, particle size (mm) is the most influential parameter on the adsorption yield. The ranking of the parameters in descending order of their percentage contribution to the adsorption process is as follows: granulometry, time, concentration of NaCl, pH, and concentration of BG.



**Fig. 19.** Graphs of the main effects of signal/noise ratios for the adsorption of BG by cypress leaves.

The segments of the S/N ratios and the average extraction yields of the BG defined by the various factors studied present an aspect when moving from level 1 to level 4. Particle size and time are the most significant factors.

### Analysis of variance (ANOVA)

Analysis of variance (ANOVA) is a statistical tool used to interpret the meaning and significance of experimental data and results.

The analysis of variance provides access to the optimal performance of the process parameters based on the determination of the significant differences between them. In the  $L_{16}$  Taguchi model, we used ANOVA to identify the main factors that could impact the adsorption of brilliant green. ANOVA can reveal the statistically significant change in process performance caused by a change in the level of a factor. The significant change was estimated by determining the F value (ratio of variance), and the contribution rate of each factor was calculated by the design parameters and error [48]. ANOVA was used to determine the sum of the squares of the factor ( $SS_F$ ), the total sum of the squares ( $SS_T$ ), the variance of error (VER), the mean of the MS squares, the associated F test of significance (5% of the risk), and the percentage of contribution of each factor (F). These quantities were calculated using equations 15 and 17 to 20. The results of the calculations are grouped in the table.

$$SS_F = \frac{mn}{L} \sum_{K=1}^L (\bar{E}_K^F - \bar{E}_T)^2 \quad (13)$$

$\bar{E}_T$ : is the cumulative average of extraction obtained by the  $L_{16}$  Taguchi design, given by Eq. (16).

$$\bar{E}_T = \sum_{j=1}^m \left( \sum_{i=1}^n E_i \right) / mn \quad (14)$$

where L is the number of levels of each factor and m is the experiment number carried from  $L_{16}$  Taguchi design.

$$SS_T = \sum_{j=1}^m \left( \sum_{i=1}^n E_i^2 \right) - mn(\bar{E}_T)^2 \quad (15)$$

$$V_{Er} = SS_T - \sum_{F=A}^D \frac{SS_F}{m(n-1)} \quad (16)$$

$$MS = \frac{SS_F}{DF} \quad (17)$$

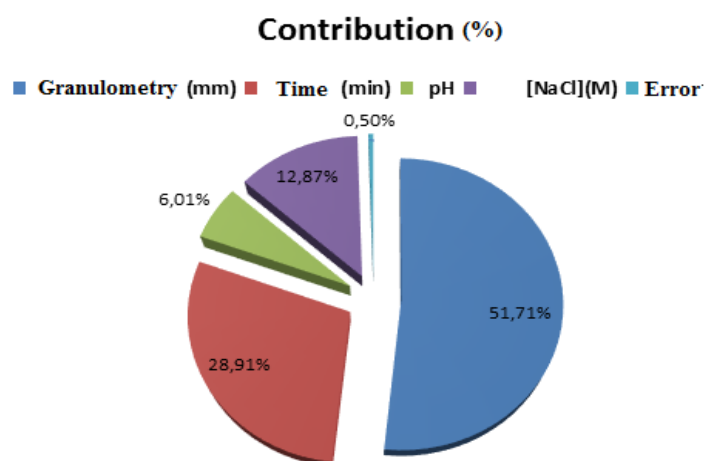
$$F - value = \frac{MS}{V_{Er}} \quad (18)$$

Table 7 shows that all parameters affect the color during the dyeing process. When the F-ratio is greater than the F-table, the hypothesis null is rejected and otherwise [49]. By comparing F-table F (0.05, 3, 3) = 9.28 to F ratios with the level of significance  $\alpha = 5\%$ . We found that all F-ratios above are greater than 9.28. Therefore, all factors affect the responses. Particle size has the biggest contribution to dye extraction, followed by factor time, NaCl concentration, and pH. Also, the main effect for the granulometry and the time of the extraction are statistically significant at the significance level of  $\alpha = 0.05$  (the p-value is less than the

significance level  $\alpha$ ). We can conclude that a change in these variables is associated with a change in the response variable.

**Table 7.** ANOVA Approach.

| Source            | DF | SS <sub>F</sub> | MS      | F-Value | P-Value | Contribution (%) |
|-------------------|----|-----------------|---------|---------|---------|------------------|
| pH                | 3  | 356.56          | 118.85  | 11.97   | 0.036   | 6.01             |
| [NaCl](M)         | 3  | 764.34          | 254.78  | 25.65   | 0.012   | 12.87            |
| Granulometry (mm) | 3  | 3070.28         | 1023.43 | 103.04  | 0.002   | 51.71            |
| Time (min)        | 3  | 1716.29         | 572.10  | 57.60   | 0.004   | 28.91            |
| Error             | 3  | 29.80           | 9.93    | -       | -       | 0.50             |
| Total             | 15 | 5937.28         | -       | -       | -       | 100.00           |

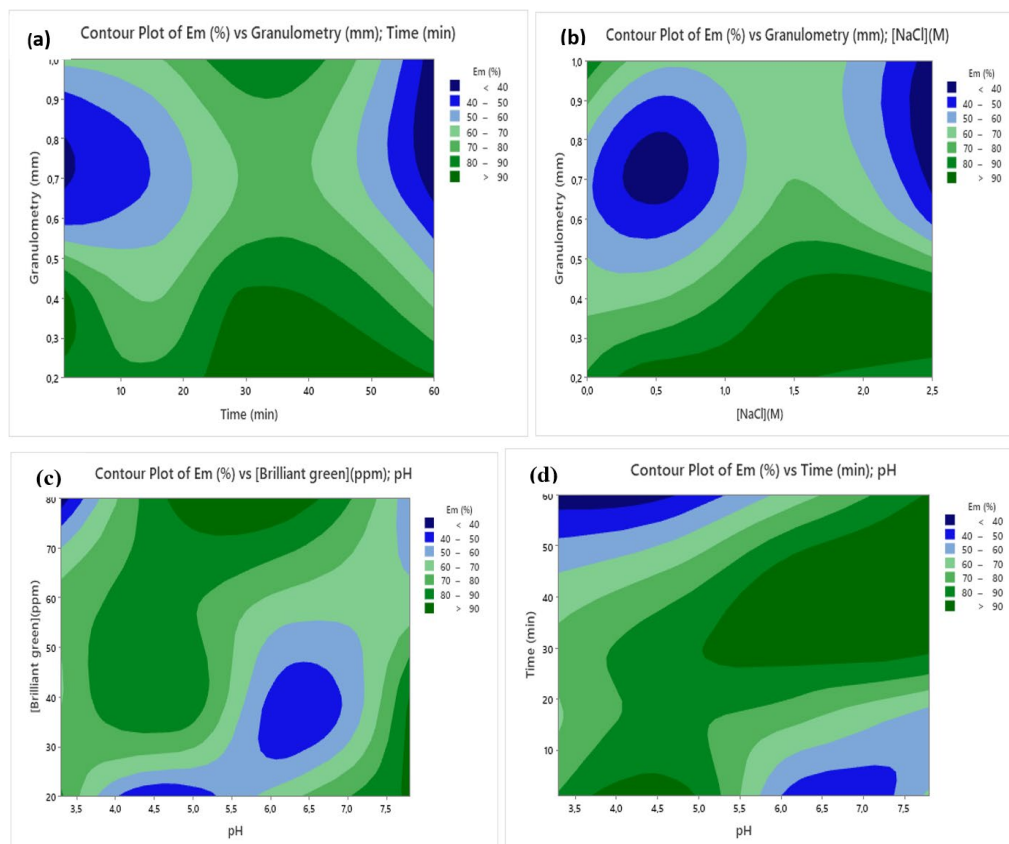


**Fig. 20.** Contribution of different parameters to the adsorption of brilliant Green on cypress leaves.

According to the results obtained, the particle size represent the largest contribution percentage. These results clearly indicate that the adsorption on the cypress leaves studied is considerably influenced by the particle size, contact time, ionic strength, and pH.

### Contour plot of extraction yield

This contour plot shows the relationship between the variables for  $E_m$  (%) used for the extraction of BG from cypress leaves.



**Fig. 21.** Contour plots between variables for  $E_m$  (%). **(a)** Interactive effect of granulometry and time on  $E_m$  (%). **(b)** Interactive effect of granulometry and NaCl concentration on  $E_m$  (%). **(c)** Interactive effect of pH and BG concentration on  $E_m$  (%). **(d)** Interactive effect of pH and time.

The contour plot lines signify the relationship and interaction effect of the two variables with varying  $E_m$  % on dye extraction. The third variable was appreciated at the middle level. These plots were created to learn about the changes in surface response. Plots are used to predict the extraction of the tested variables at different rates [50]. A contour plot indicates the type of interaction between the tested variables and the response.

Fig. 20 shows extraction up to 90 % in the broad pH range (5.2-8.0) with time (25–60 min), pH (4.7-6.5) with brilliant green concentration (73-80 ppm), NaCl concentration (0.25-2.5 M) with granulometry (0.2-0.45 mm), and time (23-50 min) with granulometry (0.2-0.4 mm).

## Conclusions

The main conclusions drawn from these study areas follow:

- The pseudo-second order model is the most appropriate to describe the kinetics of the extraction of the brilliant green dye by the adsorbent cypress.
- An adequate model to describe the kinetics of lanasyn black extraction is the pseudo second order.
- As the dye concentration increases, the yield decreases.
- The extraction depends on the pH change of the aqueous phase.

- The salts that promote adsorption are NaCl for brilliant green and Na<sub>2</sub>SO<sub>4</sub> for lanasyn black.
- The extraction yield increases with increasing temperature.
- The maximum retention rate was achieved at a stirring speed of 250 rpm.
- The increase in the particle size of the biosorbent decreases the yield.
- Brilliant green is more adsorbed in the range of concentration considered than lanasyn black.
- The application of adsorption isotherms shows that the adsorption of the two dyes follows the Freundlich model.
  - The process is multi-docking, reflecting the biosorption of BG and LN on the cypress leaves, which were examined by determining the active sites of our biosorbent.
  - The statistical study revealed that Taguchi's method with an L<sub>16</sub> (4<sup>5</sup>) orthogonal array design was successfully applied to the experimental optimization of brilliant green extraction.

## Acknowledgements

This article is fondly and respectfully dedicated to Dear Professor Mohamed Amine DIDI, who has just left us on January 17, 2023. We will never forget you, Dear Professor.

## References

1. Li, X.; Li, J.; Shi, W.; Bao, J.; Yang, X. *Mater.* **2020**, **13**, 332. DOI: <https://doi/10.3390/ma13020332>.
2. Aksu, Z.; Tezer, S. *Process. Bio. chem.* **2005**, **40**, 1347–1361. DOI: <https://doi/10.1016/j.procbio.2004.06.007>.
3. Forgacs, E.; Cserhatia, T.; Oros, G. *Environ. Int.* **2004**, **30**, 953–971. DOI: <https://doi/10.1016/j.envint.2004.02.001>.
4. Bhattacharya, K. G.; Sharma, A. *Dyes. Pigm.* **2005**, **65**, 51–59. DOI: <https://doi/10.1016/j.dyepig.2004.06.016>.
5. Fernandez, M. E.; Nunell, G. V.; Bonelli, P.R.; Cukierman, A. L. *Bioresour. Technol.* **2010**, **101**, 9500–9507. DOI: <https://doi/10.1016/j.biortech.2010.07.102>.
6. Kismir, Y.; Aroguz, A. Z. *J. Chem. Eng.* **2011**, **172**, 199–206. DOI: <https://doi/10.1016/j.ccej.2011.05.090>.
7. Belov, S.; Naumchik, G. *E3S. Web. Conf.* **2020**, **212**, 1–10. DOI: <https://doi/10.1051/e3sconf/202021201001>.
8. Papic, S.; Koprivanac, N.; Bozic, A. L. C. *Color. Technol.* **2000**, **116**, 352–358. DOI: <https://doi/10.1111/j.1478-4408.2000.tb00013>.
9. Adosinda, M.; Martins, M.; Nelson, L.; Silvestre, A. J. D.; Queiroz, M. J. *Chemosphere.* **2003**, **52**, 967–973. DOI: [https://doi/10.1016/S0045-6535\(03\)00286-8](https://doi/10.1016/S0045-6535(03)00286-8).
10. López, C.; Valade, A. G.; Combourieu, B.; Mielgo, I.; Bouchon, B.; Lema, J. M. *Anal. Biochem.* **2004**, **335**, 135–149. DOI: <https://doi/10.1016/j.ab.2004.08.037>.
11. Calabro, V.; Pantano, G.; Kang, R.; Molinari, R.; Drioli, E. *Desalination.* **1990**, **78**, 257–277. DOI: [https://doi/10.1016/0011-9164\(90\)80046-E](https://doi/10.1016/0011-9164(90)80046-E).
12. Van Der Bruggen, B.; Lejon, L.; Vandecasteele, C. *Environ. Sci. Technol.* **2003**, **37**, 3733–3738. DOI: <https://doi/10.1021/es0201754>.
13. Anselme, C.; Jacobs, E. P. *Water treatment membrane processes, New York. McGraw Hill Mallevalle.* **1996**, 401–1087.
14. Androzzzi, R.; Caprio, V.; Insola, A.; Marotta, R. *Catal. Today.* **1999**, **53**, 51–59. DOI: [https://doi/10.1016/S0920-5861\(99\)00102-9](https://doi/10.1016/S0920-5861(99)00102-9).
15. Koch, M.; Yediler, A.; Lienert, D.; Insel, G.; Kettrup, A. *Chemosphere.* **2002**, **46**, 109–113. DOI: [https://doi/10.1016/S0045-6535\(01\)00102-3](https://doi/10.1016/S0045-6535(01)00102-3).

16. Leszczyńska, M.; Hubicki, Z. *Desalin. Water. Treat.* **2009**, **2**, 160–165. DOI: <https://doi/10.5004/dwt.2009.254>.
17. Brillas, E.; Mur, E.; Sauleda, R.; Sanchez, L.; Peral, J.; Domenech, X.; Casado, J. *Appl. Catal. B: Environ.* **1998**, **16**, 31–42. DOI: [https://doi/10.1016/S0926-3373\(97\)00059-3](https://doi/10.1016/S0926-3373(97)00059-3).
18. Oturan, M. A. *J Appl Electrochem.* **2000**, **30**, 477–478. DOI: <https://doi/10.1023/A:1003994428571>.
19. Boye, B.; Dieng, M. M.; Brillas, E. *Environ. Sci. Technol.* **2002**, **36**, 3030–3035. DOI: <https://doi/10.1021/es0103391>.
20. Bellakhal, N.; Dachraoui, M.; Oturan, N.; Oturan, M. A. *J. Soc. Chim. Tun.* **2006**, **8**, 223–228.
21. Lambert, S. D.; Graham, N. J. D.; Sollars, C. J.; Fowler, G. D. *Water. Sci. Technol.* **1997**, **36**, 173–180. DOI: [https://doi/10.1016/S0273-1223\(97\)00385-5](https://doi/10.1016/S0273-1223(97)00385-5).
22. Lin, S. H. *J. Chem. Technol. Biotechnol.* **1993**, **57**, 387–391. DOI: <https://doi/10.1002/jctb.280570415>.
23. Ramakrishna, K. R.; Viraraghavan, T. *Water. Sci. Technol.* **1997**, **36**, 189–196. DOI: [https://doi/10.1016/S0273-1223\(97\)00387-9](https://doi/10.1016/S0273-1223(97)00387-9).
24. Benamraoui, F. Master's thesis, Ferhat Abbas-Setif University, **2014**, Algeria.
25. Khalifah, A.; Hayfaa, A. M.; Amoako, J.; Laith, A. A.; Al Khaddar, R.; Mawada, A.; Al-Janabi, A.; Hashim, K. S. *Conf. Ser: Mater. Sci. Eng.* **2020**, **888**, 012036. DOI: <https://doi/10.1088/1757-899X/888/1/012036>.
26. Gul, S.; Azra, G.; Hajera, G.; Rozina, K.; Muhammad, I.; Khan, S.U.; Khan, M. S.; Aouissi, H. A.; Andrejs, Krauklis. *Mater.* **2023**, **2**, 1–15. DOI: <https://doi.org/10.3390/ma16020521>.
27. Baidya, K. S.; Upendra, K. S. *Afr. J. Chem. Eng.* **2021**, **35**, 33–43. DOI: <https://doi.org/10.1016/j.sajce.2020.11.001>.
28. Samiyammal, P.; Kokila, A.L.A.; Rajakrishnan, R.; Rengasamy, S.; Ragupathy, S.M. K.; Vasudeva, R.M.R. *Environ. Res.* **2022**, **212**, 113497. DOI: <https://doi.org/10.1016/j.envres.2022.113497>.
29. Venkat, S.; Mane, P.V.; Vijay, B. *Desalination.* **2011**, **273**, 321–329. DOI: <https://doi.org/10.1016/j.desal.2011.01.049>.
30. Rehman, M. S.U.; Muhammad, M.; Muhammad, A.; Naim, R.; Muhammad, F.N.; Danish, M.; Han. *J. Chem. Eng.* **2013**, **228**, 54–62. DOI: <https://doi.org/10.1016/j.cej.2013.04.094>.
31. Nandi, B. K.; Amit, G.; Mihir, K, P. *J. Hazard. Mater.* **2009**, **161**, 387–395. DOI: <https://doi.org/10.1016/j.jhazmat.2008.03.110>.
32. Copaciu, F.; Virginia, C.; Mihaela, V.; Ocsana, O. *JPC-J. PLANAR. CHROMAT.* **2012**, **6**, 509–515. DOI: <https://doi.org/10.1556/jpc.25.2012.6.4>.
33. Amara-Rekkab, A. *Int. J. Health. Sci.* **2023**, **7**, 165–175. DOI: <https://doi.org/10.53730/ijhs.v7n3.14657>.
34. Belov, S.; Grigoriy, N. *E3S. Web. Conf.* **2020**, **212**, 01001. DOI: <https://doi.org/10.1051/e3sconf/202021201001>.
35. Samira, S.; DOMA, N. *H. Sci. Total. Environ.* **1989**, **79**, 71–279. DOI: [https://doi/10.1016/0048-9697\(89\)90342-2](https://doi/10.1016/0048-9697(89)90342-2).
36. Amara-Rekkab, A.; Didi, M.A. *Desalin. Water. Treat.* **2023**, **28**, 186–195. DOI: <https://doi/10.5004/dwt.2023.29147>.
37. Amara-Rekkab, A.; Didi, M.A. *J. Mater. Environ. Sci.* **2021**, **12**, 603–615.
38. Omri, A.; Benzima, M. *Desalin. Water. Treat.* **2012**, **51**, 2317–2326. DOI: <https://doi/10.1080/19443994.2012.734585>.
39. Chandarana, H.; Ponnusamy, S. K.; Muthulingam, S.; Madhava, A. K. *Chemosphere.* **2021**, **285**, 131–480. DOI: <https://doi/10.1016/j.chemosphere.2021.131480>.
40. Langmuir, I. *J. Am. Chem. Soc.* **1918**, **40**, 1361–1403. DOI: <https://doi/10.1021/ja02242a004>.
41. Freundlich, H. M. F. *Colloid and Capillary Chemistry, Methuen, London, UK*, **1926**.
42. Hossain, I.; Hossain, A.; Choudhury, I. A. *J. Text. Inst.* **2015**, **107**, 154–164. DOI: <https://doi/10.1080/00405000.2015.1018669>.
43. Savari, M.; Esfahani, S. H. Z.; Edalati, M.; Biria, D. *Protein. Expr. Purif.* **2015**, **114**, 128–135. DOI: <https://doi/10.1016/j.pep.2015.06.006>.
44. Necib, Y.; Bahi, A.; Merouane, F.; Bouadi, H.; Boulahrouf, K. *World. J. Pharm. Res.* **2015**, **4**, 1720–1733.

45. Morris, G.; Huey, R.; Lindstrom, W.; Sanner, M.; Belew, R.; Goodsell, D.; Olson, A. *J. Comput. Chem.* **2009**, *30*, 2785–2791. DOI: <https://doi.org/10.1002/jcc.21256>.
46. Kausar, N.; Murtaza, S.; Nadeem Arshad, M.; Munir, R.; Saleem, R. S. Z.; Rafique, H. T. *J. Mol. Struct.* 2021, 1244, 130983. DOI: <https://doi.org/10.1016/j.molstruc.2021.130983>.
47. Bensegueni, R.; Guergouri, M.; Bensouici, C.; Bencharif, M. *J. Rep. Pharm. Sci.* 2019, 8, 195-203. DOI: [https://doi.org/10.4103/jrptps.JRPTPS\\_46\\_18](https://doi.org/10.4103/jrptps.JRPTPS_46_18).
48. Asghar, A.; Abdul Raman, A. A.; Wan Daud, W. M. A. A. *Sci. World. J.* **2014**, 1-14. DOI: <https://doi/10.1155/2014/869120>.
49. Montgomery, D. C.; Runger, G. C. *Applied. Ed., John Wiley & Sons, Singapore*, **2014**.
50. Mohana, S.; Shrivastava, S.; Divecha, J.; Madamwar, D. *Bioresour. Technol.* **2008**, 99, 562–569. DOI: <https://doi/10.1016/j.biortech.2006.12.033>.



## Comparative Vibrational analysis, Electronic Properties, and molecular docking of Lantadene A and B (Potential anticancer agents) - A Computational DFT Study

Anoop Kumar Pandey<sup>1</sup>, Shashwat Shukla<sup>1</sup>, O.P. Yadav<sup>1</sup>, Vijay Singh<sup>2</sup>, Apoorva Dwivedi<sup>3\*</sup>

<sup>1</sup>Department of Physics, K. S. Saket P.G. College, Ayodhya, India.

<sup>2</sup>University of Dodoma, Dodoma, Tanzania.

<sup>3</sup>Department of Applied Science and Humanities, Seth Vishambhar Nath Institute of Engineering and Technology, Barabanki, India.

\*Corresponding author: Apoorva Dwivedi, email: [apoorvahri@gmail.com](mailto:apoorvahri@gmail.com); Phone: +919415289670.

Received May 2<sup>nd</sup>, 2023; Accepted January 22<sup>nd</sup>, 2024.

DOI: <http://dx.doi.org/10.29356/jmcs.v68i3.2060>

**Abstract.** We conducted a comprehensive analysis of Lantadene A and B using FTIR spectroscopy, beginning with geometry optimization. Subsequently, we calculated their fundamental vibrational frequencies and intensities using the B3LYP/6-311G (d, p) method. To provide a thorough vibrational assignment, we utilized potential energy distribution (PED). The results from our calculated spectra closely matched the experimental data, demonstrating the accuracy of our calculations. Furthermore, we assessed the electronic properties of Lantadene A and B. We computed the HOMO-LUMO gap and visualized the frontier orbital HOMO-LUMO surfaces, as well as Molecular Electrostatic Potential (MEP) surfaces. These analyses shed light on the reactive nature of these compounds, highlighting their potential applications. Moreover, our investigation explored the hyperpolarizability values, suggesting that Lantadene A and B hold promise for electro-optical applications due to their unique properties. Additionally, we conducted docking studies of Lantadene A and Lantadene B with BCL2L1 (BCL2 like 1) and IKBKB (inhibitor of nuclear factor kappa B kinase subunit beta) proteins, as provided by HGNC. These analyses revealed promising interactions, supporting the potential use of Lantadene A and B as agents with anti-cancer and anti-inflammatory properties. In summary, our research indicates that Lantadene A and B possess properties that make them strong candidates for use in the development of anticancer and anti-inflammatory agents, while also showing promise for electro-optical applications.

**Keywords:** Lantadene A and B; vibrational analysis; DFT; HOMO-LUMO and MESP; molecular docking.

**Resumen.** Utilizando la espectroscopía de FTIR realizamos un análisis integral de lantadeno A y B, empezando con la optimización de sus geometrías. Después, calculamos las frecuencias e intensidades de vibración utilizando el método B3LYP/6-311G (d, p). Para realizar una asignación vibracional exhaustiva, utilizamos la distribución de energía potencial (PED). Los espectros calculados están en buen acuerdo con los experimentales, lo cual demuestra la precisión de nuestros cálculos. Además, evaluamos las propiedades electrónicas de lantadeno A y B. Calculamos la brecha (gap) HOMO-LUMO, visualizamos las isosuperficies de los orbitales frontera, y también las isosuperficies del potencial electrostático molecular (MEP). Estos análisis ayudan a esclarecer la reactividad de estas moléculas, destacando sus aplicaciones potenciales. Se exploraron los valores de las hiperpolarizabilidades las cuales sugieren que el lantadeno A y B son compuestos prometedores para aplicaciones electroópticas. Adicionalmente, se realizaron estudios de acoplamiento molecular de lantadeno A y B con las proteínas BCL2L1 (BCL2 como 1) y IKBKB (inhibidor del factor kappa B de la subunidad beta quinasa), que se obtuvieron del HGNC. Estos análisis mostraron interacciones prometedoras, que apoyan el uso potencial de lantadeno A y B

como agentes anticancerígenos y con propiedades antiinflamatorias. En síntesis, nuestra investigación indica que las propiedades del lantadeno A y lantadeno B las hacen buenos candidatos para su uso en el desarrollo de agentes anticancerígenos y antiinflamatorios, además de también mostrar potencial en aplicaciones electroópticas.

**Palabras clave:** Lantadeno A y B; análisis vibracional; DFT; HOMO-LUMO y MESP; acoplamiento molecular.

---

## Introduction

Natural products have long captivated researchers for various reasons, including their potential as antibiotics and pharmacologically active agents. They offer immense promise for exploring the cellular processes they can inhibit. Fundamental and conformational studies help formulate hypotheses about their interactions with target ligands, while synthesis allows us to test these hypotheses by eventually creating derivatives [1,2]. Among these natural products, *Lantana camara*, a flowering decorative plant, has been used in traditional medicinal preparations to treat a range of ailments. It serves as a rich source of diverse classes of bioactive natural metabolites. Throughout history, its flowers, leaves, and fruits have been applied externally to treat wounds, cuts, and skin diseases. Additionally, the stems, leaves, and roots of *Lantana camara* were employed for gargles and to alleviate toothaches in ancient times [3-5]. Interestingly, toxin research from *Lantana* leaves has revealed two molecular forms, of which only one has been found to be hepatotoxic to guinea pigs [6]. Various pharmaceutical properties of the *Lantana* plant have been documented in the literature [7,8]. Extracts isolated from *Lantana* leaves have demonstrated antitumor activity [9], antithrombin activity [10], as well as anti-inflammatory, anti-nociceptive, and antipyretic effects [11]. In a study at the Central Drug Research Institute, the stem of *Lantana camara* exhibited anti-filarial activity [12]. Literature reports also indicate the presence of significant bioactive compounds in *L. camara*, such as lantadene A, lantadene B, lantadene C, and lantadene D, which have been isolated from its aerial parts [13-15]. Lantadenes, derived from this plant, have shown a wide range of pharmacological activities, including antitumor properties [16-17]. These compounds differ in the structure of the side chain attached at the C-22 position, suggesting that these structural variations play a crucial role in their pharmacological activities [18-21]. Notably, Lantadene A and Lantadene B are the primary triterpene components of the red variety of *Lantana Camara*.

In the realm of computational chemistry, Density Functional Theory (DFT) has emerged as the preferred electronic structure theory for both molecular and extended systems. Concurrently, docking methodology has become a standard computational tool in drug design, aiding in predicting the binding modes and affinities of small molecules within specific receptor targets. This approach is instrumental in lead compound optimization and virtual screening studies to discover novel biologically active molecules.

Given the significance of these theories [22-26], we have undertaken a comprehensive investigation involving Comparative Molecular Docking, Experimental FT-IR Spectra, UV-Vis Spectra, Vibrational Analysis, Electronic Properties, and Fukui Function Analysis of Lantadene A and B compounds with medicinal potential.

## Experimental details and computational methods

The FTIR spectrum of the investigated compound has been recorded in Perkin-Elmer spectrometer in the range of 4000–500 $\text{cm}^{-1}$ . The frequencies of all sharp bands are accurate to  $\pm 1 \text{ cm}^{-1}$ . The molecular structures of the title compounds A and B are made by molecular modeling. The model molecular structures of the compounds are given in Figures 1 and 2. Initial geometry was generated from the standard geometrical parameters and was minimized without any constraint in the potential energy surface. The gradient corrected Density Functional Theory (DFT) with the three-parameter hybrid functional (B3) [27] for the exchange part and the Lee-Yang-Parr (LYP) correlation function [28] has been employed for the computation of molecular structure, vibrational frequencies, HOMO-LUMO, and energies of the optimized structures, using GAUSSIAN 09 [29]. The calculated vibrational frequencies have also been scaled by a factor of 0.963 [30]. By combining the results of the GAUSSVIEW'S program [31] with symmetry considerations, vibrational frequency

assignments were made with a high degree of accuracy. The prediction of IR frequencies of title compound has been found to be very straightforward using this approach. To determine the form of the modes we used the potential energy distribution (PED) calculations and applied the VEDA program performing both the PED analysis and its optimization [32]. Density functional theory calculations are reported to provide excellent vibrational frequencies of organic compound if the calculated frequencies are scaled to compensate for the approximate treatment of electron correlation, for basis set deficiencies and for anharmonicity. A number of studies have been carried out regarding calculations of vibrational spectra by using B3LYP methods with 6-311 G (d, p) basis set. The scaling factor (0.963) was applied successfully for B3LYP method and was found to be easily transferable in a number of molecules. Thus, vibrational frequencies calculated by using the B3LYP functional with 6-311G (d, p) as basis set, can be utilized to eliminate the uncertainties in the fundamental assignment in the IR spectra. The docking action of Lant A and Lant B with selected protein has been performed by Auto Dock 4.2 software. The molecular docking indicates binding action of drug with appropriate protein.

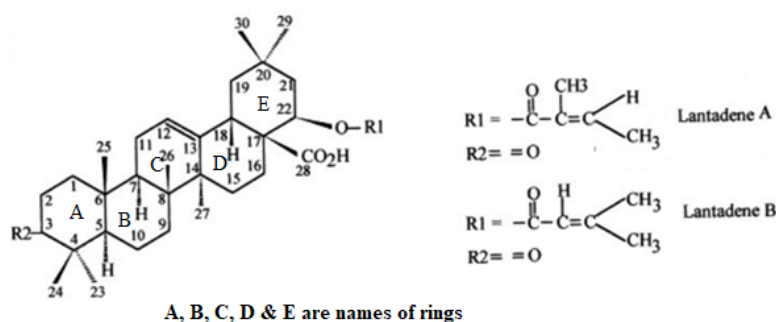


Fig. 1. Structures of Different Lantadene compounds.

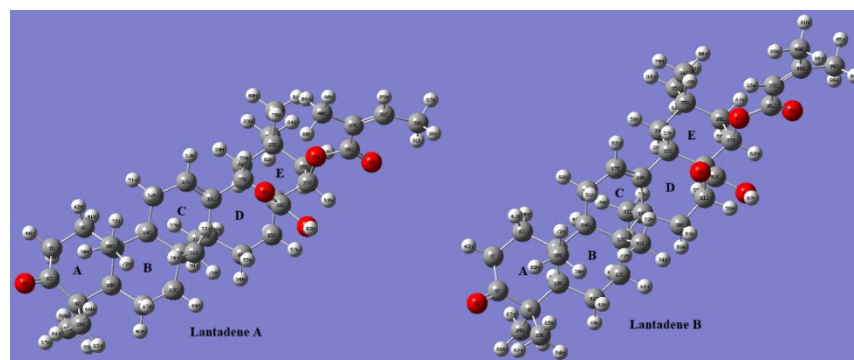


Fig. 2. Model Molecular Structure of Lantadene A and B.

## Results and discussion

The accuracy of Density Functional Theory (DFT) results, particularly when using the B3LYP functional and the 6-311 G (d, p) basis set, depends on several factors, including the specific system or molecule under investigation, the level of theory used, and the properties of interest. B3LYP is a widely used hybrid functional that combines the Becke88 exchange functional with the Lee-Yang-Parr (LYP) correlation functional. The 6-311G (d, p) basis set is a commonly used basis set that includes polarization functions (d functions) on non-hydrogen atoms and diffuse functions (p functions) on hydrogen atoms. It is a good general-purpose basis set. Accurate geometry optimization is crucial for obtaining reliable results. Ensure that the

optimization converges to a true minimum on the potential energy surface. Use tight convergence criteria and consider potential energy surface scans to explore different conformations.

### Geometry optimization

The geometry optimization of Lant A and B is obtained by B3LYP/6-311 G (d, p) method. The energy of optimized Lant A and B at ground state is -1740.6908 a.u. and -1741.474 a.u. respectively. The optimized geometries of Lant A and B in plane drawing and 2 D dimensions are presented in Figures 1 and 2 respectively. The A/B and B/C rings are in trans conformation while the D/E rings are cis fused. The packing of the molecule is stabilized by O--H...O hydrogen bonds. Bond lengths and angles (supplementary Table 1) agree with the values observed in similar compounds as maytenfolic acid.

**Table 1.** Calculated electronic transitions: E (eV), oscillatory strength (f),  $\lambda_{\max}$ (nm) using TD-DFT/B3LYP/6-311G(d,p) method.

| S. No.             | Electronic Transition                    | E (eV) | Osci.Str. (f) | Cal. ( $\lambda_{\max}$ ) | % Contribution | Assignment              |
|--------------------|------------------------------------------|--------|---------------|---------------------------|----------------|-------------------------|
| <b>Lantadene A</b> |                                          |        |               |                           |                |                         |
| 1                  | HOMO-1→ LUMO+1<br>HOMO→LUMO+1            | 4.26   | 0.0003        | 291                       | 95<br>2        | $n_p \rightarrow R_y^*$ |
| 2                  | HOMO→LUMO<br>HOMO -4→LUMO                | 4.71   | 0.0002        | 263                       | 93<br>5        | $n_p \rightarrow R_y^*$ |
| 3                  | HOMO -4→LUMO<br>HOMO 3→LUMO<br>HOMO→LUMO | 4.81   | 0.0005        | 258                       | 80<br>12<br>5  | $n_p \rightarrow R_y^*$ |
| <b>Lantadene B</b> |                                          |        |               |                           |                |                         |
| 1                  | HOMO-1→LUMO+1                            | 4.26   | 0.0003        | 291                       | 95             | $n_p \rightarrow R_y^*$ |
| 2                  | HOMO→LUMO                                | 4.59   | 0.0002        | 270                       | 98             | $n_p \rightarrow R_y^*$ |
| 3                  | HOMO-4→LUMO<br>HOMO-3→LUMO               | 4.79   | 0.0003        | 259                       | 92<br>4        | $n_p \rightarrow R_y^*$ |

### PES scan of lant A and lant B

We conducted a Potential Energy Surface (PES) scan to explore the dihedral angles C22-C33-O3-H92 and C22-C33-O3-H87, with values of 177.710 and 177.770, respectively, in both Lantadene A and Lantadene B. This scan involved a total of 36 steps, with 10 steps for each angle in both compounds. We employed the HF/6-31G level of theory for these initial scans. The resulting data was used to generate Relative Energy vs. Scan Coordinate plots for Lantadene A and Lantadene B, as shown in Supplementary Fig. S1 and S2. The minimum energy configurations were identified at dihedral angles C22-C33-O3-H92=177.71 and C22-C33-O3-H87=177.77 for both Lantadene A and Lantadene B, after performing the PES scan.

To refine our understanding of these minima, we subjected the initial geometries corresponding to these energy minima in Lantadene A and Lantadene B to further optimization. For this optimization, we utilized a combination of the DFT/B3LYP method and the 6-311G (d,p) basis set, which is known for its accuracy in describing molecular structures and properties.

In summary, our study involved a thorough investigation of the potential energy surfaces of Lantadene A and Lantadene B, focusing on specific dihedral angles of interest. The resulting data and optimized geometries will contribute to a better understanding of the structural properties and behaviors of these compounds.

### Vibrational analysis

Assignments of the FTIR (supplementary Fig. 3) frequencies are achieved by comparing the band positions and intensities observed in the FTIR spectra with wave numbers and intensities from molecular modeling calculations. The molecules Lantadene A and B both have 92 atoms with 270 normal modes of vibration. The calculated vibrational frequencies and the experimental values are listed in supplementary tables 2 and 3. Here we have discussed only FTIR active modes. The experimental frequencies of Lantadene A and B and frequencies calculated by B3LYP/6-311 G (d, p) method are nearly the same. Some Important modes of vibration are discussed below.

**Table 2.** Calculated  $\epsilon_{\text{HOMO}}$ ,  $\epsilon_{\text{LUMO}}$ , energy band gap ( $\epsilon_{\text{LUMO}} - \epsilon_{\text{HOMO}}$ ), chemical potential ( $\mu$ ), electronegativity ( $\chi$ ), global hardness ( $\eta$ ), global softness ( $S$ ), and global electrophilicity index ( $\omega$ ) for compound A, B at B3LYP/6-311 G (d, p) level.

| Folder | $\epsilon_{\text{H}}$ | $\epsilon_{\text{L}}$ | $\epsilon_{\text{H}} - \epsilon_{\text{L}}$ | $\chi$ | $\mu$  | $\eta$ | $S$    | $\omega$ | $\Delta N \text{ max}$ |
|--------|-----------------------|-----------------------|---------------------------------------------|--------|--------|--------|--------|----------|------------------------|
| A      | -0.2253               | -0.0148               | -0.2105                                     | 3.266  | -3.266 | 2.863  | 0.1754 | 1.871    | 1.141                  |
| B      | -0.2312               | -0.0470               | -0.1842                                     | 3.785  | -3.785 | 2.506  | 0.1999 | 2.863    | 1.142                  |

**Table 3.** Topological parameters for bonds of interacting atoms: LANTADENE-A and B electron density ( $\rho_{\text{BCP}}$ ), Laplacian of electron density ( $\nabla^2\rho_{\text{BCP}}$ ), total electron energy density ( $H_{\text{BCP}}$ ), estimated interaction energy ( $E_{\text{int}}$ ) at bond critical point (BCP).

| LANT A  |                     |                             |                                            |                  |                  |                                  |                  |                                |        |
|---------|---------------------|-----------------------------|--------------------------------------------|------------------|------------------|----------------------------------|------------------|--------------------------------|--------|
| Bond    | $\rho_{\text{BCP}}$ | $\nabla^2\rho_{\text{BCP}}$ | $\left \frac{\lambda_1}{\lambda_3}\right $ | $V_{\text{BCP}}$ | $G_{\text{BCP}}$ | $\left \frac{V(r)}{G(r)}\right $ | $H_{\text{BCP}}$ | $E_{\text{int}}$<br>(kcal/mol) | Nature |
| H88-O4  | 0.00347             | 0.01170                     | 0.11970                                    | -0.00195         | 0.00243          | 0.80247                          | 0.00048          | 0.61210                        | VW     |
| H73-O4  | 0.00456             | 0.01481                     | 0.14080                                    | -0.00264         | 0.00317          | 0.83281                          | 0.00053          | 0.82800                        | VW     |
| H55-H75 | 0.01450             | 0.05280                     | 0.32110                                    | -0.00859         | 0.01088          | 0.78952                          | 0.00229          | 2.69500                        | W      |
| O1-H79  | 0.01138             | 0.03972                     | 0.13120                                    | -0.00746         | 0.00869          | 0.85846                          | 0.00123          | 2.34100                        | W      |
| H71-H74 | 0.01288             | 0.04076                     | 0.11940                                    | -0.00677         | 0.00481          | 1.40748                          | -0.00196         | 2.12400                        | W      |
| H77-H50 | 0.01374             | 0.04730                     | 0.13020                                    | -0.00784         | 0.00984          | 0.79675                          | -0.0020          | 2.46000                        | W      |
| LANT B  |                     |                             |                                            |                  |                  |                                  |                  |                                |        |
| Bond    | $\rho_{\text{BCP}}$ | $\nabla^2\rho_{\text{BCP}}$ | $\left \frac{\lambda_1}{\lambda_3}\right $ | $V_{\text{BCP}}$ | $G_{\text{BCP}}$ | $\left \frac{V(r)}{G(r)}\right $ | $H_{\text{BCP}}$ | $E_{\text{int}}$<br>(kcal/mol) | Nature |
| H72-O4  | 0.00450             | 0.01470                     | 0.13030                                    | -0.00259         | 0.00310          | 0.83548                          | 0.00051          | 0.8130                         | VW     |
| H86-O5  | 0.01730             | 0.06050                     | 0.12950                                    | -0.01140         | 0.01314          | 0.86758                          | 0.00174          | 3.5770                         | W      |
| H78-O1  | 0.01190             | 0.04160                     | 0.11820                                    | -0.00782         | 0.00910          | 0.85934                          | 0.00128          | 2.4530                         | W      |
| H51-H71 | 0.01290             | 0.04410                     | 0.12070                                    | -0.00718         | 0.00911          | 0.78815                          | 0.00193          | 2.2530                         | W      |
| H54-H74 | 0.01420             | 0.05280                     | 0.14080                                    | -0.00859         | 0.00109          | 7.8807                           | -0.00750         | 2.6950                         | W      |
| H75-H59 | 0.01270             | 0.03840                     | 0.13210                                    | -0.00659         | 0.00809          | 0.81459                          | 0.00150          | 2.0680                         | W      |

### O-H and -CH modes of vibration

The Lantadene A and B both have hydroxyl group (-OH). In general, -OH stretching modes of vibration are observed in the range 3400–3600  $\text{cm}^{-1}$  [33]. The -OH modes of vibration appears at higher frequency region due to lower reduced mass. A significant polarized IR peak with polarization vector appears along plane appears at 3466  $\text{cm}^{-1}$  in Lantadene A with PED 100% and corresponding sharp peak superimpose in Lantadene B at 3610  $\text{cm}^{-1}$  with 100 % PED. At lower frequencies region a very intense polarized peak appears at 1018  $\text{cm}^{-1}$  in Lant A and corresponding peaks appears at 1110  $\text{cm}^{-1}$  with several mixing mode of vibrations due to in plane bending of -OH vibration. At lower frequencies region two back to back intense peaks are calculated at 591  $\text{cm}^{-1}$  and 614  $\text{cm}^{-1}$  for Lant A and 589  $\text{cm}^{-1}$ , 605  $\text{cm}^{-1}$  for Lant B due to wagging modes of -OH with mixing of several modes of vibrations too. All these calculated peaks are in good agreement with experimental FTIR.

In general, hetero aromatic geometry C-H stretching modes of vibration appears in between 2800–3100  $\text{cm}^{-1}$  [34]. In the present study, two sharp polarized peak appears at 2993 and 3002  $\text{cm}^{-1}$  with PED 95% appears due C-H stretching mode of vibration in Lantadene A and corresponding peak appears at 2993 and 3008  $\text{cm}^{-1}$  in Lantadene B with PED 99% which are also supported with literature. At lower end of frequencies in-plane and out of plane -CH bending appears. In present calculation polarized peaks appears due in plane -CH bending appears at 1298  $\text{cm}^{-1}$  in Lantadene A, however corresponding peaks appears at 1123  $\text{cm}^{-1}$  for Lantadene B with significant PED. Below 1100  $\text{cm}^{-1}$ , out of plane -CH bending mode mixing with wagging of -CH<sub>2</sub>/CH<sub>3</sub> appears at the appropriate range in the calculated spectrum for Lantadene A and B which are well matched with experimental FTIR.

### -C=O absorption vibration and C–C vibrations

The absorption bands (sharp stretching modes of vibration) of the carbonyl group (C=O) are observed in between 1600–1800  $\text{cm}^{-1}$  [35]. The intense-C=O absorption intense peaks due to stretching of both carbon and oxygen with equal amplitude. In present communication most, intense polarized peaks with polarization vector directed along plane of adjacent rings are appeared at 1640 and 1668  $\text{cm}^{-1}$  with PED 99 %, and 65 % in Lantadene A while 1695, 1711 and 1745  $\text{cm}^{-1}$  with PED of 95 %, respectively in Lantadene B.

The vibrations relating to C-C stretching in the ring absorb in the region from 1400- 1600  $\text{cm}^{-1}$  [36] in aromatic hydrocarbons. In the present calculation, intense polarized peak appears at 1102  $\text{cm}^{-1}$  due to -CC in plane bending mode of vibration in Lantadene A and stretching mode of vibration with mixed modes at 1104  $\text{cm}^{-1}$  in Lantadene B. The bending of -CCC modes appears at middle frequencies in calculated IR spectra of Lantadene A and B. At lower region of IR spectra, some intense polarized peaks are found due to out of plane bending -CH along with mixing of other bending mode for Lantadene A as well as Lantadene B. All these calculated peaks are matched well with experimental FTIR.

### Methylene(-CH<sub>2</sub>) and Methyl (-CH<sub>3</sub>) group vibrations

The CH<sub>2</sub>/CH<sub>3</sub> groups due to internal coordinate arrangement [37], having six different mode of vibration namely asymmetric, symmetric stretch, rocking, scissoring, twisting as well as wagging. In general, symmetric stretching -CH<sub>2</sub>/CH<sub>3</sub> appears middle/lower frequencies region due to weaker bond strength and characteristic region for symmetric -CH<sub>2</sub>/CH<sub>3</sub> observed in between 2800  $\text{cm}^{-1}$  to 3000  $\text{cm}^{-1}$  however antisymmetric stretching vibration for -CH<sub>2</sub>/CH<sub>3</sub> observed some higher frequencies region 3100  $\text{cm}^{-1}$ –3400  $\text{cm}^{-1}$  due to strong bond strength [38]. In the present study, the scissoring mode of deformation CH<sub>2</sub> groups shows some sharp peaks appears at 1455  $\text{cm}^{-1}$ , 1481  $\text{cm}^{-1}$  in Lantadene A however an intense polarized peak appears at 1430  $\text{cm}^{-1}$  due scissoring mode of deformation CH<sub>3</sub> groups appears in calculated spectra of Lantadene B. Some other polarized peaks appear due mixing of in plane deformation rocking due to -CH<sub>3</sub> appears at 1084  $\text{cm}^{-1}$  and 1196  $\text{cm}^{-1}$  in Lantadene B. At lower region of calculated IR spectra of Lantadene A, sharp polarized peak of -CH<sub>2</sub>/CH<sub>3</sub> appears at 1043  $\text{cm}^{-1}$ /1211  $\text{cm}^{-1}$  while in Lantadene B, 733  $\text{cm}^{-1}$ /964  $\text{cm}^{-1}$  due to mixing of wagging with twisting modes frequencies. All these calculated peaks are in good agreement with experimental FTIR spectra.

### TDDFT analysis

The TDDFT method is utilized by using optimized geometry of Lantadene A and Lantadene B molecule to calculate UV spectrum. The calculated transition state and transition orbital and their %

contribution, Transition energy, oscillatory strength  $\lambda_{\max}$ , are calculated and listed in table 1. The UV spectra of Lantadene A and Lantadene B are shown in Fig. 3. In Fig. 3, the green vertical lines are showing the peaks of calculated wave length in graph having greater oscillatory strength. From this figure a prominent peak appears at 258 nm with  $f=0.0005$  in Lantadene A while 259 and 291 nm with  $f=0.0003$  for both wave length in Lantadene B respectively. The transition energy of electron is 4.81 eV and 4.79/4.26 eV in Lantadene A and Lantadene B respectively. The peak emerges due to transition of electron in between HOMO -4 $\rightarrow$ LUMO with contribution of 80 % in Lantadene A while HOMO-4 $\rightarrow$ LUMO/ HOMO-1 $\rightarrow$ LUMO+1 with contribution of 92 %/95 % in Lantadene B. Two other less sharp peak appears at 291nm ( $f=0.0003$ ) and 263nm (0.0002) in Lantadene A while one at 270 nm ( $f=0.0002$ ) in Lantadene B. The calculated transition energy corresponds to these transitions at 4.26/4.71 eV for Lantadene A while 4.59 eV for Lantadene B.

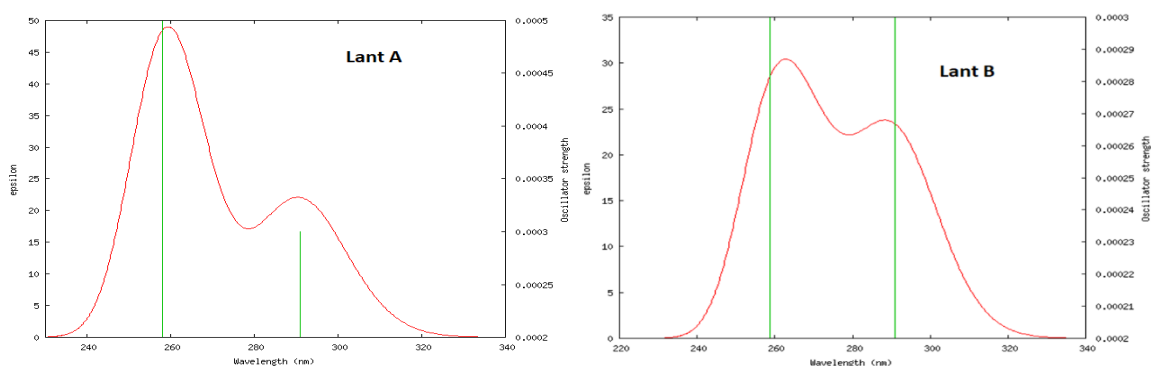


Fig. 3. UV spectrum of Lantadene A and B.

### Electronic properties (HOMO-LUMO, MESP Plots of Lantadene A and Lantadene B)

The chemical reactivity or chemical stability is determined by frontier molecular orbitals (FMO). In FMO, the highest occupied molecular orbital is termed as HOMO and lowest unoccupied molecular orbital is termed as LUMO. The supplied energy to transition of electron from HOMO to LUMO is known forbidden energy band gap. The energy gap is directly related with chemical stability [39-40]. The calculated energy gap shows that chemical reactivity of Lantadene A (5.7256 eV) is little bit less than Lantadene B (5.0102 eV). The HOMO and LUMO plots of Lantadene A and Lantadene B are shown in Fig. 4(a) and 4(b). The HOMO of Lant A is distributed over Ring C and associated group and LUMO is nearly over ring E. The HOMO of Lant B is distributed over Ring C and associated group and LUMO is nearly over ring E. The transition from HOMO $\rightarrow$ LUMO shows that electron transfer from Ring C and associated group to ring E to gain stability in both molecules.

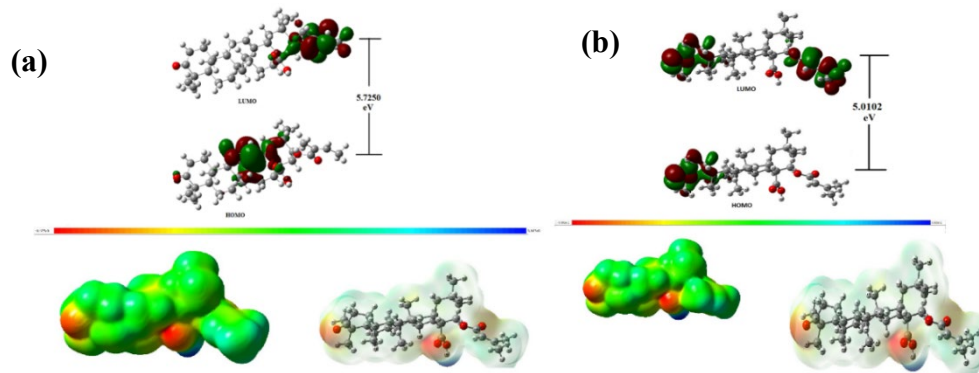


Fig. 4. (a) Pictures of HOMO-LUMO and Molecular Electrostatic Potential of Lantadene A, (b) Pictures of HOMO-LUMO and Molecular Electrostatic Potential of Lantadene B.

The ionization potential and electron affinity are any chemical system is determined by HOMO and LUMO energy. The energy needed to remove one electron from HOMO orbital is known as electronic potential and energy needed to add additional electron in LUMO is known as electron affinity. The Parr et.al [41], suggest that negative eigen value of HOMO is called ionization potential (IP) however negative eigen value of LUMO is called electron affinity (EA).

$$IP = -\text{HOMO} \quad (1)$$

$$EA = -\text{LUMO} \quad (2)$$

By using EA and IP chemical hardness and absolute electronegativity are determined by using following equations [42, 43],

$$\mu = - (IP+EA)/2 \quad (3)$$

$$\eta = (IP-EA)/2 \quad (4)$$

The calculated value of energy gap implies that Lantadene B is more chemically reactive than Lantadene A. The electron affinity of Lantadene B is more than Lantadene A, this implies that Lantadene B have better tendency to gain additional electron to gain stability which is also reflect calculated value of chemical potential of both species. The calculated chemical hardness of Lantadene A is higher than Lantadene B. This means that any reagent easily interacts with Lantadene B rather than Lantadene A. The chemical softness implies that how easily any reagent interacts with given species and shows reverse effect with chemical hardness. The reciprocal of chemical hardness is termed as the global softness,

$$S = 1/2\eta \quad (5)$$

[44-45]

The calculated value  $N_{\max}$  is ratio of chemical potential and chemical hardness and show direction of charge transport to gain stability. All these parameters are listed in table 2.

$$(\Delta N_{\max})_I = - \frac{\mu_I}{\eta_I} \quad (6)$$

The direction charge transport is determined by magnitude of chemical potential due to electrophilic species is accomplished to receive charge from donor atom consequently system get stabilized and attend lower energy.

The electrophilicity index is a global reactivity descriptor of a molecule that provides a quantitative classification of the global electrophilic nature of the molecule. The chemical potential of a species in a mixture can be defined as the slope of the free energy of the system with respect to a change in the number of moles of that species. It is a form of potential energy that can be absorbed or released during a chemical reaction. Although electronegativity is defined in many different ways, the most logical and rational definition of it is the electron holding power of the atoms or molecules.

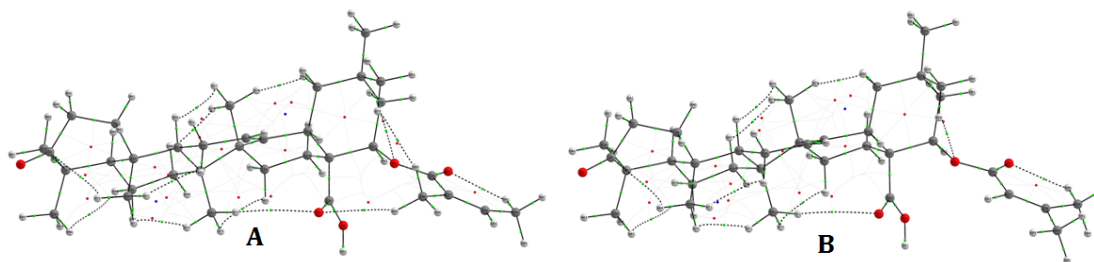
The molecular electrostatic energy potential plot is very important picture to determine nature of potential of atomic sites within the molecule. The nature of electron potential surface is determined in term of color coding. The consequence of MESP lies in the detail that it concurrently displays molecular size, shape, and positive, negative, and neutral electrostatic potential regions in terms of color grading example yellow color means neutral potential surface blue color shows electropositive surface and red color as electronegative surface [46-49]. The MESP plots of Lantadene A and B are also shown on Fig. 4(a) and 4(b). From this figure, red color encircled over  $-\text{COO}-\text{C}_2\text{H}_5\text{CH}_3$  group and over  $-\text{COOH}-$  and  $-\text{CO}$  of ring A in Lant A and Lant B respectively so behaves as most electronegative surface in Lant A and Lant B. In both Lant A and Lant B, blue



color encircled over -OH in -CH<sub>2</sub>OH group attached at ring D and E. The white color encircled over whole molecule in Lant A and Lant B.

### QATIM analysis

The quantum atomic theory in molecule QAIM [50] is significant tool to determine nature and strength of nonbonding or bonding interactions by using topological parameters. The bond critical point is known as four critical point (3,-1) is introduced by Bader which provides information to define interactions like covalent and non-covalent interaction in any chemical system. The nature and strength of non-covalent interaction are calculated by some topological parameters e.g. electron density  $\rho(r)$ , local potential energy density  $V(r)$ , Laplacian  $\Delta^2 \rho(r)$ , Total energy density  $H(r)=V(r)+G(r)$ , etc. The topological parameters at bond critical point (BCP) for Lant A and Lant B are calculated and listed in table-3 respectively. The graphical AIM pictures of interactions for Lant A Lant B are shown in Fig. 5. The electron density ( $\rho_{H...A}$ ) falls in between 0.002–0.040 a.u. and Laplacian ( $\nabla^2 \rho_{BCP}$ ) falls in between 0.024–0.139 a.u. for nonbonding interactions [51]. Based on these criteria of nonbonding six nonbonding interactions appear in both Lant A and Lant B for nonbonding. In Lant A molecule six nonbonding interactions are H<sub>88</sub>-O<sub>4</sub>, H<sub>73</sub>-O<sub>4</sub>, H<sub>55</sub>-H<sub>75</sub>, O<sub>1</sub>-H<sub>79</sub>, H<sub>71</sub>-H<sub>74</sub>, H<sub>77</sub>-H<sub>50</sub> however in Lant B corresponding interactions are H<sub>72</sub>-O<sub>4</sub>, H<sub>86</sub>-O<sub>5</sub>, H<sub>78</sub>-O<sub>1</sub>, H<sub>51</sub>-H<sub>71</sub>, H<sub>54</sub>-H<sub>74</sub>, H<sub>75</sub>-H<sub>59</sub>. The charge density  $\rho_{BCP}$  at BCP in Lant A varies from 0.00347a.u.-0.01450a.u. and got its maximum for H<sub>55</sub>-H<sub>75</sub> and minimum value for H<sub>88</sub>-O<sub>4</sub> however charge density at BCP for Lant B varies in between 0.00450 a.u.-0.01420a.u. The maximum value of  $\rho_{BCP}$  for H<sub>54</sub>-H<sub>74</sub> and minimum value of  $\rho_{BCP}$  for H<sub>72</sub>-O<sub>4</sub>. The charge density at BCP for O-H interaction varies in between 0.00450- 0.01190 a.u. in Lant B and 0.00347-0.01138 a.u. in Lant A. From this data,  $\rho_{BCP}$  for O-H interaction for LantB > LantA. The calculated  $\rho_{BCP}$  for H-H interaction 0.01288-0.01450 a.u. in Lant A and corresponding charge density for H-H interaction in Lant B varies in between 0.01270 to 0.01420. One important thing noticed  $\rho_{BCP}$  for H-H interaction >O-H interaction. For both Lant A and Lant B order of magnitude of charge density  $\rho(r)$  are smaller as compared with typical covalent bond but lesser value of  $\rho(r)$  between these interactions for O-H in both Lant A Lant are comparable with to 0.007 au in HCl---HF [52]. The second derivative of laplacian charge density ( $\nabla^2 \rho_{BCP}$ ) for Lant A varies from 0.01170 to 0.05280 a.u. and attained maximum value  $\nabla^2 \rho_{BCP} = 0.05280$ a.u. for H<sub>55</sub>-H<sub>75</sub> however Laplacian second derivatives of electron charge density varies from 0.01470 -0.05280 for Lant B and attained maximum value for  $\nabla^2 \rho_{BCP} = 0.05280$  a.u. for H<sub>54</sub>-H<sub>74</sub>. The existence of small delocalization between both interacting atoms shown by using calculated  $\nabla^2 \rho_{BCP}$  in both natural products. In both natural product Lant A and Lant B for all six interactions  $\nabla^2 \rho_{BCP} > 0$  and  $\rho_{BCP} > 0$  means all interaction are electrovalent nature. The sign of Laplacian electron density  $\nabla^2 \rho_{BCP}$  shows that concentration of charge in a exhausted or “closed shell. In Lant A for all six interaction  $\nabla^2 \rho_{BC} > 0$  and  $\rho_{BCP}$  lies within range  $10^{-3}$  for H<sub>73</sub>-O<sub>4</sub>, H<sub>88</sub>-O<sub>4</sub> for Lant A and H<sub>72</sub>-O<sub>4</sub> for Lant B falls within van der Waals ‘interaction [53]. The rest all interaction in both Lant A and Lant B  $\rho_{BCP}$  lies within range  $10^{-2}$  and falls within hydrogen bonding interactions [54]. The calculated potential energy density at BCP are determine nature and strength of interactions. The nonbonding at BCP is weak when  $\nabla^2 \rho_{BCP} > 0$ , HBCP > 0 and interaction is called electrovalent for  $\nabla^2 \rho_{BCP} > 0$ , HBCP < 0. The all interactions in both Lant A and Lant B are weak except H<sub>77</sub>-H<sub>50</sub> H<sub>71</sub>-H<sub>74</sub> for Lant A H<sub>54</sub>-H<sub>74</sub> for Lant B falls in electrovalent category. The interactions in between atoms are calculated by following equation  $\Delta E = -1/2V$  [55]. All interactions are falls within weak interaction lies within range 1kcal/mol < IE < 5 kcal/mol except H<sub>88</sub>-O<sub>4</sub>, H<sub>73</sub>-O<sub>4</sub> for Lant A H<sub>72</sub>-O<sub>4</sub> in Lant B lies IE < 1 kcal/mol falls very weak type interaction [56]. The strongest interaction appears for H<sub>55</sub>-H<sub>75</sub> in Lant A and H<sub>86</sub>-O<sub>5</sub> Lant B. The chemical natures of any chemical systems are calculated by using curvature point of second derivative of electron density  $\nabla^2 \rho_{BCP}$  at BCP  $\lambda_1, \lambda_2, \lambda_3$ . One of another parameter's ratio  $\left| \frac{\lambda_1}{\lambda_3} \right|$  is useful to calculate nature and types of chemical bond. [57]. All six interactions indicative of weak CSIs in Lant A and Lant B because for all six interactions  $\left| \frac{\lambda_1}{\lambda_3} \right| \ll 1$ . The ratio  $\left| \frac{V(r)}{G(r)} \right|$  is important indicator to know about nature of interaction. For all interaction  $|V(r)|/G(r) < 1$  in both Lant A and Lant B except H<sub>71</sub>-H<sub>74</sub> for Lant A H<sub>54</sub>-H<sub>74</sub> for Lant B where  $|V(r)|/G(r) > 1$  so all five interactions in both Lant A, Lant B are characteristic of hydrogen bonding, ionic, and van der Waals interaction however H<sub>71</sub>-H<sub>74</sub> for Lant A H<sub>54</sub>-H<sub>74</sub> for Lant B interaction are covalent.



**Fig. 5.** AIM picture of Lantadene A and B representing hydrogen interaction (dotted line) with Green points and red points represent as BCPs and RCP.

### NBO analysis

The NBO analysis is important method to calculate charge transfer from donor to acceptor to determine interaction in any molecular systems [58]. The strength of interaction in term of charge transfer from donor to acceptor is determine by second order perturbation energy  $E^{(2)}$ . The strength of interaction among electron donors and electron acceptors are directly related by second order perturbation energy of  $E^{(2)}$  means the strength of interaction increases with second order perturbation energy of  $E^{(2)}$ . The strength of interaction is calculated by (or stabilization energy) [59-60]

$$E^{(2)} = -q_i \frac{(F_{ij})^2}{\epsilon_j - \epsilon_i} \quad (7)$$

In this equation population of donor orbital is  $q_i$  however orbital energies (diagonal elements) of donor are  $\epsilon_i$ ,  $\epsilon_j$ . The fock matrix donor acceptor orbitals and their occupancies as well as second-order perturbation energy of Lant A and Lant B is calculated and listed in table 4 by using same level theory. They stabilizes the system due to charge transfer in between donor and acceptor orbital overlap  $Lp \rightarrow \pi^*/\sigma^*$ . In first type of interaction  $Lp \rightarrow \sigma^*$  appears due to charge transfer in between  $Lp(2)O_5 \rightarrow \sigma^*(C_{36}-C_{37})$  orbitals stabilized system by 16.54kcal/mol and 16.40 kcal/mol for Lant A and Lant B respectively which further enhance charge transfer from  $Lp(2)O_5 \rightarrow \sigma^*(C_{36}-O_1)$  is stabilized by 32.11kcal/mol and 32.57kcal/mol in Lant A and Lant B respectively. Another significant interaction appears due to charge transfer  $Lp(2)O_4 \rightarrow \sigma^*(C_{22}-C_{33})$  which stabilized by 18.84kcal/mol and 19.10kcal/mol for Lant A and Lant B respectively. This strength of interaction  $Lp(2)O_4 \rightarrow \sigma^*(O_3-C_{33})$  further enhance by 31.07kcal/mol and 33.49kcal/mol in Lant A and Lant B respectively. The significant interaction appears in between  $Lp(2)O_2 \rightarrow \sigma^*(C_8-C_9)$  stabilize by 9.81kcal/mol and 20.43kcal/mol for Lant A and Lant B respectively which further enhance in interactions  $Lp(2)O_2 \rightarrow \sigma^*(C_7-C_8)$  by 19.82kcal/mol and 20.21kcal/mol for Lant A and Lant B respectively. In second type interaction one important interactions happens in among  $Lp(2)O_3 \rightarrow \pi^*(O_4-C_{33})$  which stabilize by 43.40kcal/mol and 43.57kcal/mol for Lant A and Lant B respectively. Another important interaction appears in between  $Lp(2)O_1 \rightarrow \pi^*(O_5-C_{36})$  which stabilize Lant A and Lant B by 42.81kcal/mol and 42.61kcal/mol respectively.

**Table-4.** NBO analysis of donor acceptor orbitals and their occupancies second order perturbation interaction energy for Lant A and Lant B

| LANT-A              |              |                           |              |                      |                   |              |
|---------------------|--------------|---------------------------|--------------|----------------------|-------------------|--------------|
| Donor NBO(i)        | occupancy(i) | Acceptor NBO(j)           | occupancy(j) | $E^{(2)}$ (kcal/mol) | $(E_j - E_i)$ a.u | $F(i,j)$ a.u |
| Lp(2)O <sub>5</sub> | 1.84332      | $\sigma^*(C_{36}-C_{37})$ | 0.0669       | 16.54                | 0.69              | 0.097        |
| Lp(2)O <sub>5</sub> | 1.84332      | $\sigma^*(C_{36}-O_1)$    | 0.1121       | 32.11                | 0.62              | 0.127        |

| Lp(2)O <sub>4</sub> | 1.85624      | σ*(C <sub>22</sub> -C <sub>33</sub> ) | 0.0724       | 18.84                       | 0.63                                  | 0.099      |
|---------------------|--------------|---------------------------------------|--------------|-----------------------------|---------------------------------------|------------|
| Lp(2)O <sub>4</sub> | 1.85624      | σ*(O <sub>3</sub> -C <sub>33</sub> )  | 0.0941       | 31.07                       | 0.61                                  | 0.125      |
| Lp(2)O <sub>3</sub> | 1.82363      | π*(O <sub>4</sub> -C <sub>33</sub> )  | 0.0210       | 43.40                       | 0.34                                  | 0.109      |
| Lp(2)O <sub>2</sub> | 1.89039      | σ*(C <sub>8</sub> -C <sub>9</sub> )   | 0.0778       | 19.81                       | 0.65                                  | 0.102      |
| Lp(2)O <sub>2</sub> | 1.89039      | σ*(C <sub>7</sub> -C <sub>8</sub> )   | 0.0618       | 19.82                       | 0.66                                  | 0.103      |
| Lp(2)O <sub>1</sub> | 1.79238      | π*(O <sub>5</sub> -C <sub>36</sub> )  | 0.2002       | 42.81                       | 0.34                                  | 0.108      |
| <b>LANT-B</b>       |              |                                       |              |                             |                                       |            |
| Donor NBO(i)        | occupancy(i) | Acceptor NBO(j)                       | occupancy(j) | E <sup>(2)</sup> (kcal/mol) | (E <sub>j</sub> -E <sub>i</sub> ) a.u | F(i,j) a.u |
| Lp(2)O <sub>5</sub> | 1.84493      | σ*(C <sub>36</sub> -C <sub>37</sub> ) | 0.1025       | 16.40                       | 0.70                                  | 0.098      |
| Lp(2)O <sub>5</sub> | 1.84493      | σ*(C <sub>36</sub> -O <sub>1</sub> )  | 0.1025       | 32.57                       | 0.62                                  | 0.129      |
| Lp(2)O <sub>4</sub> | 1.84347      | σ*(C <sub>22</sub> -C <sub>33</sub> ) | 0.0769       | 19.10                       | 0.63                                  | 0.100      |
| Lp(2)O <sub>4</sub> | 1.84347      | σ*(O <sub>3</sub> -C <sub>33</sub> )  | 0.1017       | 33.49                       | 0.61                                  | 0.129      |
| Lp(2)O <sub>3</sub> | 1.82589      | π*(O <sub>4</sub> -C <sub>33</sub> )  | 0.0224       | 43.57                       | 0.35                                  | 0.111      |
| Lp(2)O <sub>2</sub> | 1.88771      | σ*(C <sub>8</sub> -C <sub>9</sub> )   | 0.0788       | 20.43                       | 0.65                                  | 0.104      |
| Lp(2)O <sub>2</sub> | 1.88771      | σ*(C <sub>7</sub> -C <sub>8</sub> )   | 0.0613       | 20.21                       | 0.67                                  | 0.105      |
| Lp(2)O <sub>1</sub> | 1.79787      | π*(O <sub>5</sub> -C <sub>36</sub> )  | 0.0223       | 42.61                       | 0.34                                  | 0.109      |

### NLO properties

The nonlinear optical properties NLO of Lant A and Lant B are calculated by using several parameters like dipole moment, mean polarizability, anisotropic polarizability, molar refractivity (MR) hyperpolarizability etc. In three dimensional Cartesian coordinate system dipole moment, mean polarizability, hyperpolarizability are calculated by using following equation [61]

$$\mu = (\mu_x^2 + \mu_y^2 + \mu_z^2)^{1/2} \quad (8)$$

$$\langle \alpha \rangle = 1/3 [\alpha_{xx} + \alpha_{yy} + \alpha_{zz}] \quad (9)$$

$$\beta_{\text{Total}} = (\beta^2_x + \beta^2_y + \beta^2_z)^{1/2} = [(\beta_{xxx} + \beta_{xyy} + \beta_{xzz})^2 + (\beta_{yyy} + \beta_{yxx} + \beta_{yzz})^2 + (\beta_{zzz} + \beta_{zxx} + \beta_{zyy})^2]^{1/2} \quad (10)$$

The hyperpolarizability ( $\beta$ ), a nonlinear-optical property of a molecule, is the second-order electric susceptibility per unit volume. The electric susceptibility is a dimensionless proportionality constant that indicates the degree of polarization of a dielectric material in response to an applied electric field. The greater the electric susceptibility, the greater the ability of a material to polarize in response to the field, and thereby reduce the total electric field inside the material (and store energy). It is in this way that the electric susceptibility influences the electric permittivity of the material.

$$\Delta\alpha = \left[ \frac{(\alpha_{xx} - \alpha_{yy})^2 + (\alpha_{yy} - \alpha_{zz})^2 + (\alpha_{zz} - \alpha_{xx})^2}{2} \right]^{1/2} \quad (11)$$

The Lorenz-Lorentz are used by using molar refractive index [62-64]

$$MR = \left[ \frac{n^2 - 1}{n^2 + 2} \right] \left( \frac{MR}{\rho} \right) = 1.33 \alpha \pi N \quad (12)$$

In this equation,  $\alpha$  is the mean polarizability and  $N$  is the Avogadro number. The polarizability ( $\alpha_e$ ) along x axis and polarizability along y axis is ( $\alpha_o$ ). By using these polarizability ordered parameter is computed by following equation [65-66]

$$S = \frac{\alpha_e - \alpha_o}{\alpha_e + \alpha_o} \quad (13)$$

(For  $\alpha$ : 1 a.u. =  $0.1482 \times 10^{-24}$  esu; for  $\beta_0$ : 1 a.u. =  $8.639 \times 10^{-33}$  esu)

The dipole moment of any system is signature of magnitude charge distribution on any that system without application electric field. The calculated dipole moment of Lant A and Lant B are nearly 1.5 times of dipole moment of water (1.85D). This large dipole moment reported due to unsymmetrical distribution of title molecules with unequal electronegative atoms like oxygen hydrogen and carbon however calculated dipole moment of Lant B > Lant A molecule. The polarizability as well as well hyperpolarizability of any system are described by applied electric field. The mean polarizability, hyperpolarizability, molar refractivity (MR), order parameters. Anisotropic polarizability, of Lant A and Lant B are calculated and listed in table 5. The greater calculated mean polarizability anisotropic polarizability based on direction molar refractivity (MR) for Lant B established superiority over NLO properties for Lant A molecule. The calculated order parameters for both Lant A and Lant B are still lower as compared with established NLO materials but order parameter for Lant A is greater than Lant B. The calculated hyperpolarizability of Lant B Lant A are nearly six times greater than corresponding value of reference molecule urea ( $0.1947 \times 10^{-30}$  e.s.u.) however calculated hyperpolarizability of Lant B is greater than Lant A. The NLO activity appears on Lant A and Lant B due moment of  $\pi$  electron from donor to acceptor in both Lant A and Lant B.

**Table 5.** Polarizability and Hyper Polarizability of Lant A and Lant B.

| Species | $\langle \alpha \rangle$ (a.u.) | $\Delta \alpha$ (a.u.) | MR (e.s.u.) | S        | Cos $\phi$ | $\beta_{total}$ (a.u.) | $\mu$ (D) |
|---------|---------------------------------|------------------------|-------------|----------|------------|------------------------|-----------|
| Lant A  | 394.4213                        | 162.8472               | 147.1586    | 0.19350  | 0.46233    | 120.7553               | 3.123     |
| Lant B  | 397.3975                        | 163.678                | 148.269     | 0.193138 | 0.46209    | 124.4178               | 3.427     |

## Molecular docking

The molecular docking indicates binding action of drug with appropriate protein. The docking action of Lant A and Lant B with selected protein has been performed by Auto Dock 4.2 software [67]. In docking process grid of  $60 \text{ \AA} \times 60 \text{ \AA} \times 60 \text{ \AA}$  size was selected for docking. In preparation process of protein, we removed co-crystallized ligands and water molecules from selected PDB file. By using UCSF Chimera program [68] Gasteiger charges as well as hydrogen atoms were allocated to protein residues. The Lant A and Lant B were docked with prepared protein by using Auto Dock 4.2 program package which consider Lamarckian Genetic Algorithm (LGA) [69]. The Discovery Studio software [70] utilized for visualization of interactions between Lant A and Lant B with suitable protein.

The appropriate targets are calculated by using Swiss dock is online server [71]. The swiss dock online server predicts three proteins for docking with Lant A and Lant B molecule. The Swiss dock is online server which based on newton mechanics utilized to predict target protein for docking. In target prediction by swiss dock online server we have uploaded optimized geometry of LantA and Lant B uploaded smile code of optimized geometry on swissdock server. The docking of the proteins of all structures of BCL2L1 and IKBKB with participating atoms of Lant A and Lant B and corresponding bond lengths are listed in tables 6 and 7 and all possible interaction during docking were presented by LIGPLOT. The binding affinity is closely related with number of atoms in ligand so ligand efficiency index of title molecule with respect to particular targets. The

ligand efficiency is designed separating the score found in the docking simulation by the total number of non-hydrogen atoms of the ligand.

**Table 6.** Different parameters for molecular docking of Lant A and B with different protein structures.

| Target Proteins                                                                           | Selected PDB structures with their resolutions | Hydrogen Bonding residues      |                                  | Ligand efficiency |        | Inhibition constant ( $\mu$ M) |          | Binding energy (kcal/mol) |        |
|-------------------------------------------------------------------------------------------|------------------------------------------------|--------------------------------|----------------------------------|-------------------|--------|--------------------------------|----------|---------------------------|--------|
|                                                                                           |                                                | Lant A                         | Lant B                           | Lant A            | Lant B | Lant A                         | Lant B   | Lant A                    | Lant B |
| <b>BCL2L1</b><br><b>BCL2</b><br>like<br>1provided<br>by HGNC                              | 6WGZ<br>2.20 Å                                 | TRPA:140<br>GLUA:326           | ASNA:140                         | 0.1475            | 0.1675 | 74.3354                        | 75.09123 | -5.9                      | -6.7   |
|                                                                                           | 6WH0<br>1.99 Å                                 | TYRA:29                        | LYSA:355                         | 0.1525            | 0.1625 | 23.5650                        | 27.2025  | -6.1                      | -6.5   |
|                                                                                           | 202M<br>2.25 Å                                 | ASNA:140<br>GLYA142            | ASNA:140                         | 0.1275            | 0.1450 | 124.9156                       | 124.8355 | -5.1                      | -5.8   |
| <b>IKBKB</b><br>inhibitor<br>of nuclear<br>factor<br>kappa B<br>kinase<br>subunit<br>beta | 4kik<br>2.83 Å                                 | LIUB:21<br>LYSB:147<br>TRYB:98 | CYSB:99                          | 0.1475            | 0.1350 | 107.8772                       | 109.2227 | -5.9                      | -5.4   |
|                                                                                           | 3rzf<br>4.0 Å                                  | ASNA:140<br>GLYA:142           | ASPA:103<br>GLYA:102<br>LYSA:106 | 0.1575            | 0.1800 | 80.8633                        | 81.0748  | -6.3                      | -7.2   |

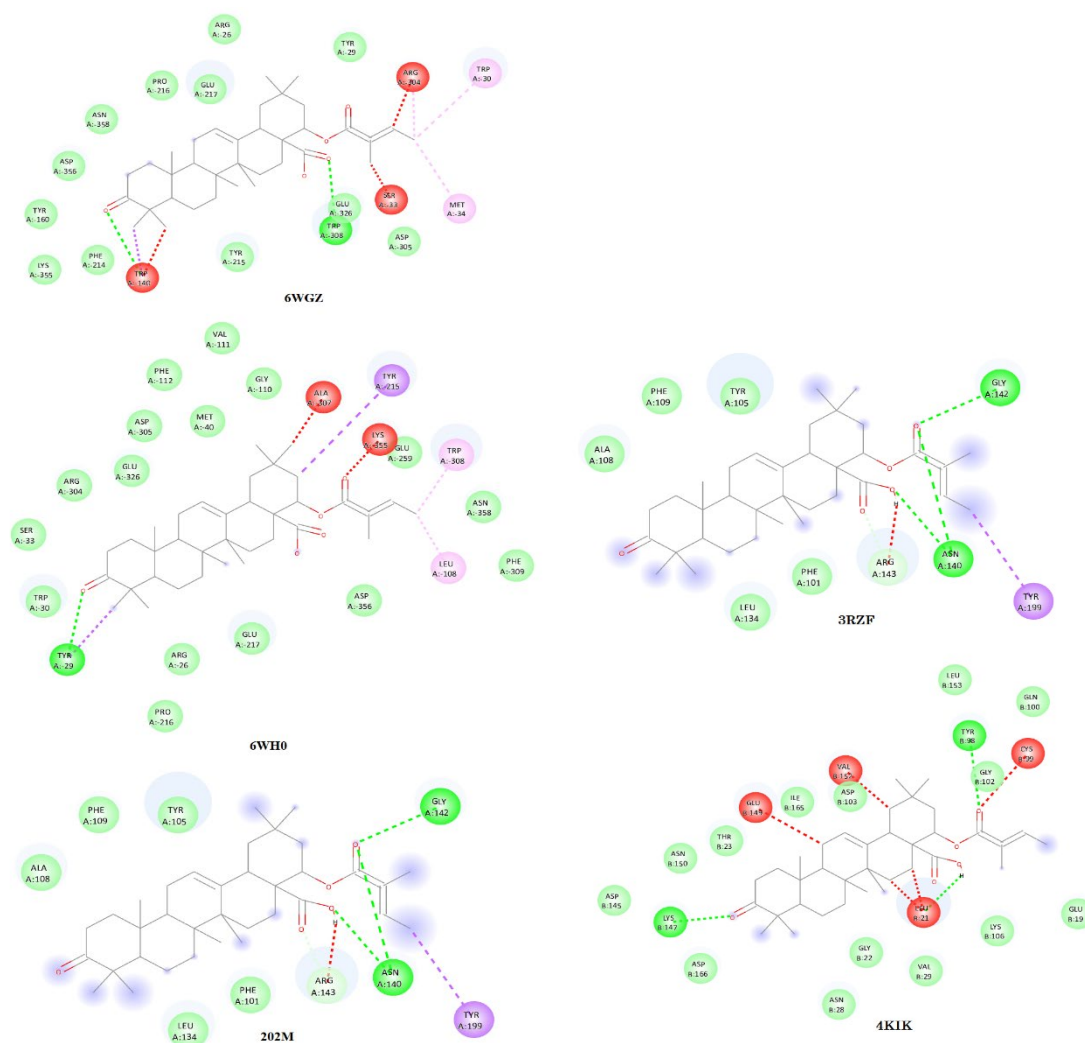
**Table 7.** Hydrogen bonding residues, Binding atoms and Bond length for molecular docking of Lant A and B with different protein structures.

| Target Proteins                                                                           | Selected PDB structures with their resolutions | Hydrogen Bonding residues      |                                  | Binding atoms  |                | Bond length             |                         |
|-------------------------------------------------------------------------------------------|------------------------------------------------|--------------------------------|----------------------------------|----------------|----------------|-------------------------|-------------------------|
|                                                                                           |                                                | Lant A                         | Lant B                           | Lant A         | Lant B         | Lant A                  | Lant B                  |
| <b>BCL2L1</b><br><b>BCL2</b> like<br>1provided<br>by HGNC                                 | 6WGZ<br>2.20 Å <sup>0</sup>                    | TRPA:140<br>GLUA:326           | ASNA:140                         | O3<br>O2       | O5             | 2.319<br>2.132          | 2.103                   |
|                                                                                           | 6WH0<br>1.99 Å <sup>0</sup>                    | TYRA:29                        | LYSA:355                         | O2             | O5             | 1.419                   | 1.813                   |
|                                                                                           | 202M<br>2.25 Å <sup>0</sup>                    | ASNA:140<br>GLYA142            | ASNA:140                         | O3<br>O5       | O2             | 2.464<br>2.032          | 2.723                   |
| <b>IKBKB</b><br>inhibitor<br>of nuclear<br>factor<br>kappa B<br>kinase<br>subunit<br>beta | 4kik<br>2.83 Å <sup>0</sup>                    | LIUB:21<br>LYSB:147<br>TRYB:98 | CYSB:99                          | O3<br>O2<br>O5 | O3             | 1.976<br>1.945<br>1.932 | 2.221                   |
|                                                                                           | 3rzf<br>4.0Å <sup>0</sup>                      | ASNA:140<br>GLYA:142           | ASPA:103<br>GLYA:102<br>LYSA:106 | O5<br>O3       | O3<br>O1<br>O5 | 2.255<br>2.469          | 2.421<br>2.221<br>2.404 |

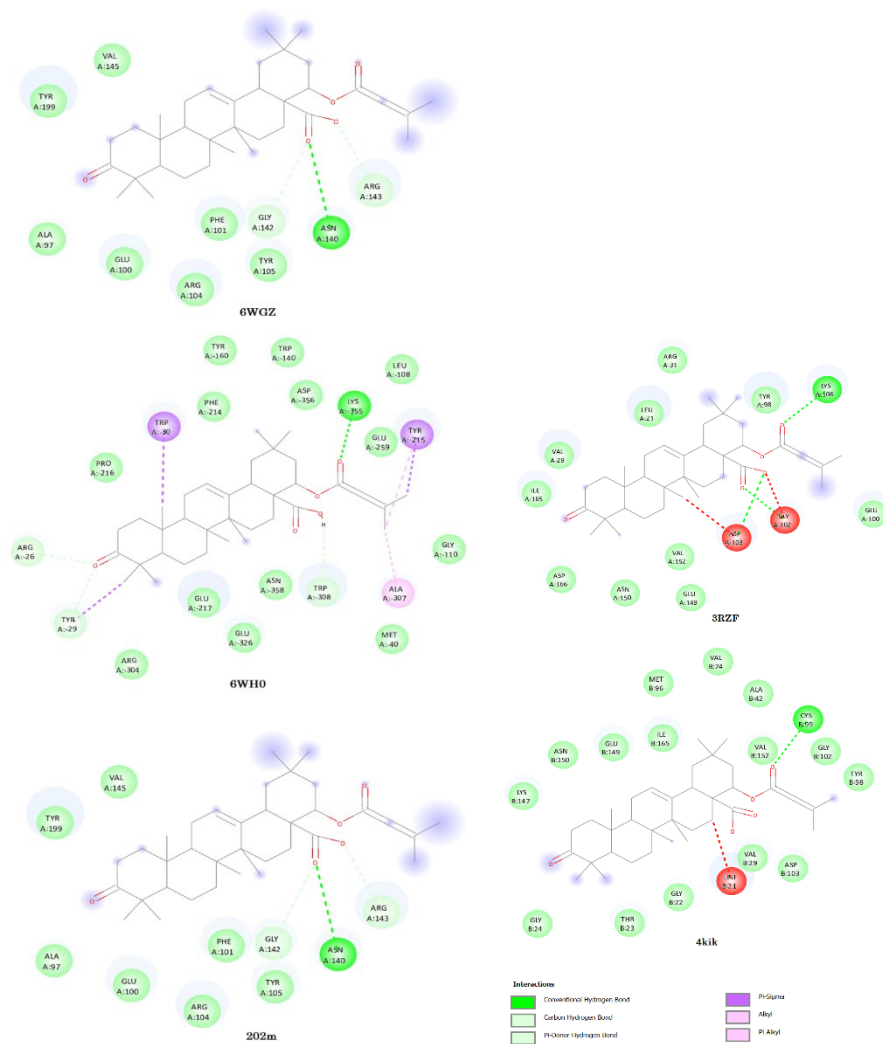
### Docking of lant A and lant B with BCL2L1 protein

In western world colorectal cancer (CRC) is the second important reason of cancer. The BCL2L1 protein determined by this gene fits to the BCL-2 protein family. BCL-2 family member's systems hetero- or homodimers and item as anti- or pro-apoptotic regulators that is complicated in an extensive variability of cellular activities. The BCL2L1 protein interacts with the tumor suppressor P53 after experience to cell strain. The BCL2L1 has a practical character in colorectal cancer [72]. To discover the inhibition action of Lant A and Lant B against BCL2L1, we have selected three pdb geometry of protein 2O2M [73], 6wh0 [74], 6wgz [75] with resolution 2.25Å<sup>0</sup>, 1.99Å and 2.20Å<sup>0</sup> respectively.

In these geometries of BCL2L1 dock with Lant A and Lant B highest binding energy 6WH0 (-6.1kcal/mol) and (-6.5kcal/mol) respectively. The docking of these selected geometries with Lant A and Lant B are shown in Figures 6(a) and 6(b) and 7(a) and 7(b). The inhibition constant for 6WH0 pdb structures having lowest compared with other two pdb structures. The highest ligand efficiency for Lant A (0.1525) and Lant B (0.1625) and lower inhibition constant proposed that Lant A and Lant B probably good candidate for anticancer drugs.



**Fig. 6. (a)** Docking Of various PDB structure of BCL2L1 protein with Lant A, **(b)** Docking Of various PDB structure of IKBKB protein with Lant A.



**Fig. 7. (a)** Docking Of various PDB structure of BCL2L1 protein with Lant B, **(b)** Docking Of various PDB structure of IKBKB protein with Lant B.

### Docking of IKBKB with lant A and lant B

The IKK- $\beta$  having an important character in brain cells resulting as a stroke [76]. The Inhibition of IKK and IKK-related kinases has been examined as a healing choice for the dealing of inflammatory diseases and cancer [77] In this communication to explore the binding affinity and inhibition capability of Lant A and Lant B with IKBKB we have selected two pdb file of protein IKBKB are 4kik [78], 3rzf [79] having resolution 2.83 Å and 4.0 Å respectively and were preferred and originate to have potential inhibition activity in contradiction of IKBLB protein. The binding energy of LantA and Lant B highest for 4kik (6.5kcal/mol) and 3rzf (-7.2kcal/mol) respectively. The docking figure shows that binding energy is highest in Lant A. The hydrogen bonding appears in between O5, O3 atoms in Lant A bind with residue ASNA: 140, GLYA:142 of 3rzf protein structure of IKBKB with bond length 2.225 Å and 2.469 Å respectively. In Lant B, in binding three hydrogen bond appears in between O3,O1,O5 in Lant B with ASPA:103, GLYA:102, LYSA:106 residue with bond length 2.421 Å, 2.221 Å, 2.404 Å respectively. The highest ligand efficiency is high for 3rzf structure of IKBKB protein for LantA (0.1575) and Lant B (0.1800) respectively. The calculated inhibition constant is

80.8633  $\mu\text{M}$  and 81.0784  $\mu\text{M}$  respectively for Lant A and Lant B which lies corresponding lower value for 4kik structure. The other pdb geometry 4kik of IKBKB loosely binds with residues. The docking of these selected geometries with Lant A and Lant B are shown in Figures 6(a) and 6(b) and 7(a) and 7(b).

## Conclusions

Our study delves into the characterization of Lantadene A and B through FTIR spectroscopy, employing the B3LYP/6-311G (d, p) method to calculate their fundamental vibrational frequencies. A comprehensive assignment of vibrational wavenumbers has been achieved through potential energy distribution (PED) analysis, demonstrating an impressive concordance between our calculated spectra and experimental observations. Additionally, to substantiate our findings, we conducted TDDFT calculations. In our quest to illustrate the reactivity of Lantadene A and B, we computed several chemical parameters, including the HOMO-LUMO gap. We further visualized their frontier orbitals, HOMO-LUMO surfaces, and Molecular Electrostatic Potential (MEP) surfaces, shedding light on their inherent reactivity. Furthermore, our investigation into hyperpolarizability values suggests the potential utility of these compounds in electro-optical applications. We also explored the molecular docking interactions of Lantadene A and B with suitable protein targets, offering a detailed analysis of the results. Our findings suggest that these compounds hold promise as candidates for anticancer and anti-inflammatory applications. In summary, our study underscores the potential of Lantadene A and B in the realms of both molecular reactivity and therapeutic applications, particularly in the context of anticancer and anti-inflammatory agents, while also highlighting their suitability for electro-optical endeavors.

## Acknowledgements

One of the authors Anoop Kumar Pandey is grateful and thanks the Uttar Pradesh government (India) [No: 46/2021/603/sattar-4-2021-4(56)/2020] for providing him financial support. V.S. thanks the CHPC Lengau, South Africa, for the computational facility.

## References

1. Nadkarni, A.K., Nadkarni, K.M., *Indian Materia Medica*, Bombay Popular Prakashan, Bombay, 1976.
2. Guthikonda, R.N., Cama, L.D., Quesada, M., Woods, M.F., Salzmann, T.N., Christensen, B.G., *Pure & Appl. Chem.* **1987**, 3, 455-458. DOI: <http://dx.doi.org/10.1351/pac198759030455>.
3. Ross, I. A., *Medicinal plants of the world*, Human Press, New Jersey, 1999. DOI: <https://doi.org/10.1007/978-1-59259-365-1>.
4. Kurian, A., K, Shankar M., *Medicinal Plants-Horticulture Sciences*, New India Publication Agency, India, 2007.
5. The Wealth of India. The Council of Scientific and Industrial Research, *Ind Med Gaz.* **1949**, 84(10), 476-477. PMID: PMC5189551.
6. Vasantha, P., Sukumar, N., Sharma, O. P., *Acta Cryst.* **1991**, C47, 810-812.
7. Ghisalberti, E.L., *Fitoterapia*, **2000**, 71, 467-485. DOI: [http://doi.org/10.1016/S0367-326X\(00\)00202-1](http://doi.org/10.1016/S0367-326X(00)00202-1)
8. Duke, J. A., Boca Raton, *CRC Press*, 1992.
9. Shashi, B.M., Niranjana, P.S., Subodh, K.R., Sharma, O.P., *Tetrahedron*, **1994**, 50, 9439-9446. DOI: [http://doi.org/10.1016/S0040-4020\(01\)85518-6](http://doi.org/10.1016/S0040-4020(01)85518-6).



10. O' Neill, M.J., Lewis, J.A., Noble, H.M., Holland, S., Mansat, C., Farthing, J.E., Foster, G., Noble, D., Lane, S.J., Sidebottom, P.J., Lynn, S.M., Hayes, M.V., Dix, C.J., *J. Nat. Prod.*, **1998**, 61, 1328- 1331. DOI: <http://doi.org/10.1021/np970464j>.
11. Uzcategui, B., Avila, D., Heberto, S.R., Quintero, L., Ortega, J., Gonzalez, Y.B., *Investigacion Clinica*, **2004**, 45, 4.
12. Misra, N., Sharma, M., Raj K., Dangi, A., Srivastava, S., Misra, S., *Parasitol. Res.*, **2007**, 100, 439-448. DOI: <http://doi.org/10.1007/s00436-006-0312-y>.
13. Begum, S., Wahab, A., Siddiqui, B., Qamar, F., *Chem. Pharm. Bull.* **2003**, 51, 134–137. DOI: <http://doi.org/10.1248/cpb.51.134>.
14. Zandi-Sohani, N., Hojjati, M., Carbonell, B., Angel, A., *Chil. J. Agric. Res.*, **2012**, 72, 502-506. DOI: <http://dx.doi.org/10.4067/S0718-58392012000400007>
15. Shamsi, Z. R., Al-Saffar, A.Z., Al-Shanon, A.F., Al-Obaidi, J.R., *Mol. Biol. Rep.*, **2019**, 46, 381-390. DOI: <http://doi.org/10.1007/s11033-018-4482-3>.
16. Inada, Nakanishi, T., Tokuda, H., Nishino, H., Iwashina, A., and Sharma, O. P., *Planta. Med.*, **1995**, 61, 558.
17. Inada, Nakanishi, T., Tokuda, H., Nishino, H., Iwashina, A., and Sharma, O. P., *Planta. Med.*, **1997**, 63, 272.
18. Nethaji, M., Rufes, C., Sadasivao, C., Pattashi, V. Sharma, O., *J. Crystallogr. Spectrosc. Res.*, **1993**, 6, 469-472.
19. Goswami, G. A., Sawant, N., *Biosci. Biotechnol. Res. Asia*, **2011**, 2, 821-824. <https://www.biotech-asia.org/?p=9684>.
20. Sharma, M., Sharma, P., Bansal, M., *Indian J. Pharmacol.*, **2007**, 39,140-144.
21. Sharma, M., Dalal, R. Sharma, N, *Design Nat. Prod. Res.*, **2011**, 4, 387-396. DOI: <http://doi.org/10.1080/14786411003792173>.
22. Dwivedi, A., Srivastava, A. K., Bajpai, A., *Spectrochim. Acta, Part A.*, **2015**, 149, 343-351. DOI: <https://doi.org/10.1016/j.saa.2015.04.042>.
23. Dwivedi, A., Pandey, A. K., Raj, K., Misra, N., *Spectrosc. Int. J.*, **2012**, 3, 155-166. DOI: <http://doi.org/10.1155/2012/486304>.
24. Pandey, A. K., Siddiqui, S. A., Dwivedi, A., Raj, K., Misra, N., *Spectrosc. Int. J.*, **2011**, 25, 287-302. DOI: <http://doi.org/10.3233/SPE-2011-0517>.
25. A. K. Pandey, A. Dwivedi, N. Misra, *Spectrosc. Int. J.*, **2013**. Article ID 937915, 11 pages. DOI: <https://doi.org/10.1155/2013/937915>.
26. Dwivedi, A., Kumar, A. *Polycyclic Aromat. Compd.*, **2021**, 41, 387-399. DOI: <https://doi.org/10.1080/10406638.2019.1591466>.
27. Becke, A.D., *J. Chem. Phys.*, **1993**, 98, 5648-5652. DOI: <https://doi.org/10.1063/1.464913>.
28. Lee, C., Yang, W., Parr, R.G. *Phys. Rev. B.*, **1988**, 37, 785. DOI: <https://doi.org/10.1103/PhysRevB.37.785>.
29. Frisch, M. J., et al *Gaussian 09*; Gaussian, Inc., Pittsburgh, PA, 2009.
30. Fast, P.L., Corchado, J., Sanches, M.L., Truhlar D.G., *J. Phys.Chem. A.* **1999**, 103, 3139-3143. DOI: <https://doi.org/10.1021/jp9900382>.
31. Frisch, A., Nelson, A.B., Holder, A.J., *Gauss view*, Inc.Pittsburgh PA, 2000.
32. Jamroz M. H., *Vibrational Energy Distribution Analysis: VEDA 4 program*, Warsaw (2004).
33. Andersson, M.P., Uvdal, P. *J. Phys. Chem. A*, **2005**, 12, 2937–2941. DOI: <https://doi.org/10.1021/jp045733a>.
34. Colthup, N.B., Daly, L.H., Wiberley, S.E., *Introduction to Infrared and Raman Spectroscopy*, Academic Press, New York, 1990.

35. Abraham, C.S., Muthu, S., Prasana, J.C., Armaković, S., Armaković, S.J., Geoffrey B., *Spectrochim. Acta, Part A*, **2019**, 222, 117188. DOI: <https://doi.org/10.1016/j.saa.2019.117188>.
36. Thamarai, A., Vadamar, R., Raja, M., Muthu, S., Narayana, B., Ramesh, P., R. Muhamed, R., Sevvanthi, S., Aayisha, S., *Spectrochim. Acta, Part A*, **2020**, 226, 117609. DOI: <https://doi.org/10.1016/j.saa.2019.117609>.
37. Silverstein, R.M., Bassler, G.C., Morrill, T.C., *Spectrometric Identification of Organic Compounds*, 4th ed. John Wiley and Sons, New York, 1981.
38. Pulay, P., Fogarasi, G., Pang, F., Boggs, J.E., *J. Am. Chem. Soc.*, **1979**, 101, 2550–2560. DOI: <https://doi.org/10.1021/ja00504a009>.
39. Gutowski, M., Chalasinski, G., *J. Chem. Phys.* **1993**, 98, 4540–4554.
40. Bose, S. C., Saleem, H., Erdogdu, Y., Rajarajan, G., Thanikachalam, V., *Spectrochim. Acta, Part A*, **2011**, 82, 260–269. DOI: <https://doi.org/10.1016/j.saa.2011.07.046>.
41. Parr, R. G., Pearson, R.G., *J. Am. Chem. Soc.* **1983**, 105, 7512–7516. DOI: <https://doi.org/10.1021/ja00364a005>.
42. Geerlings, P., Proft, F. D., Langenaeker, W., *Chem. Rev.* **2003**, 103, 1793–1874. DOI: <https://doi.org/10.1021/cr990029p>
43. Parr, R.G., Donnelly, R.A., Levy, M., Palke, W.E., *J. Chem. Phys.*, **1978**, 68, 3801. DOI: <https://doi.org/10.1063/1.436185>.
44. Komorowski, L., *Chem. Phys.*, **1987**, 114, 55.
45. Parr, R.G., Szentpály, L., Liu, S., *J. Am. Chem. Soc.*, **1999**, 121, 1922–1924.
46. Gadre, S.R., Pathak, R.K., *J. Chem. Phys.*, **1990**, 93, 1770–1774. DOI: <https://doi.org/10.1063/1.459703>.
47. Gadre, S.R., Shrivastava, I.H., *J. Chem. Phys.*, **1991**, 94, 4384–4390. DOI: <https://doi.org/10.1063/1.460625>.
48. Murray J.S., Sen, K., *Molecular Electrostatic Potentials, Concepts and Applications*, Elsevier, Amsterdam, 1996.
49. Alkorta I., Perez, J.J., *Int. J. Quant. Chem.* **1996**, 57, 123–135. DOI: [https://doi.org/10.1002/\(SICI\)1097-461X\(1996\)57:1<123::AID-QUA14>3.0.CO;2-9](https://doi.org/10.1002/(SICI)1097-461X(1996)57:1<123::AID-QUA14>3.0.CO;2-9)
50. Matta, I.F., Boyd, R.J., *The Quantum Theory of Atoms in Molecules*, WILEY-VCH Verlag GmbH & Co. KGaA, Weinheim, 2007.
51. Koch, U., Popelier, P., *J. Phys. Chem. A*, **1995**, 99, 9747–9754. DOI: <https://doi.org/10.1021/j100024a016>.
52. Carroll, M. T., Bader, R. F. W., *Mol. Phys.*, **1988**, 65, 695. DOI: <http://doi.org/10.1080/00268978800101351>.
53. Cremer, D., Kraka, E., *Croat. Chem. Acta.*, **1984**, 57, 1259–1281. DOI: <https://hrcak.srce.hr/194019>
54. Rozas, I., Alkorta, I., Elguero, J., *J. Am. Chem. Soc.*, **2000**, 122, 11154–11161. DOI: <https://doi.org/10.1021/ja0017864>.
55. Bader, R. F. W., *Atoms in Molecules: A Quantum Theory* (2<sup>nd</sup> ed.) Oxford: New York, NY. 1990
56. Erdogdu, Y., Unsalan, O., Gulluoglu, M.T., *J. Raman Spectrosc.*, **2010**, 41, 820–828. DOI: <https://doi.org/10.1002/jrs.2520>
57. Erdogdu, Y., Unsalan, O., Amalanathan, M., Hubert, J. I., *J. Mol. Struct.*, **2010**, 980, 24–30. DOI: <https://doi.org/10.1016/j.molstruc.2010.06.032>
58. Gonohe, N., Abe, H., Mikami, N., Ito, M., *J. Phys. Chem.*, **1985**, 89, 3642–3648. DOI: [https://doi.org/10.1016/0009-2614\(83\)85053-2](https://doi.org/10.1016/0009-2614(83)85053-2)
59. Alyar, H., Kantarci, Z., Bahat, M., Kasap, E., *J. Mol. Struct.*, **2007**, 834, 516–520. DOI: <https://doi.org/10.1016/j.molstruc.2006.11.066>.

60. Padrón, J.A., Carasco, R., Pellón, R.F., *J. Pharm. Pharmaceut. Sci.*, **2002**, 5, 258–266.
61. Verma, R.P., Hansch, C., *Bioorg. Med. Chem.*, **2005**, 13, 2355–2372. Doi: <https://doi.org/10.1016/j.bmc.2007.01.011>.
62. Verma, R.P., Kurup, A., Hansch, C., *Bioorg. Med. Chem.*, **2005**, 13, 237–255. DOI: <https://doi.org/10.1016/j.bmc.2004.09.039>
63. Vuks, M.F., *Opt. Spectrosc.*, **1966**, 20, 361–368.
64. Kumar, A., Srivastava, A.K., Tiwari, S.N., Misra, N., Sharma, D., *Mol. Cryst. Liq. Cryst.*, **2019**, 1, 23–31.
65. Morris, G.M., Huey, R., Lindstrom, W., Sanner, M.F., Belew, R.K., Goodsell, D.S., Olson, A.J., *J. Comput. Chem.*, **2009**, 16, 2785–2791. DOI: <https://doi.org/10.1002/jcc.21256>
66. Pettersen, E.F., Goddard, T.D., Huang, C.C., Couch, G.S., Greenblatt, D.M., Meng, E.C., Ferrin, T.E., *J. Comput. Chem.* **2004**, 25, 1605–1612. DOI: <http://doi.org/10.1002/jcc.20084>
67. Morris, G.M., Goodsell, D.S., Halliday, R.S., Huey, R., Hart, W.E., Belew, R.K., Olson, A.J., *J. Comput. Chem.*, **1998**, 19, 1639–1662. DOI: [https://doi.org/10.1002/\(SICI\)1096987X\(19981115\)19:14%3C1639::AID-JCC10%3E3.0.CO;2-B](https://doi.org/10.1002/(SICI)1096987X(19981115)19:14%3C1639::AID-JCC10%3E3.0.CO;2-B).
68. *Discovery Studio 4.5 Guide*, Accelrys Inc., San Diego, 2009. <http://www.accelrys.com>
69. Oost, M., Belli, T.K., Ding, B.A., Joseph, H., Kunzer, M.K., Martineau, A., McClellan, D., Mitten, W.J., et.al, *J. Med. Chem.*, **2007**, 50, 641–662. <https://files.rcsb.org/view/2O2M.cif>.
70. Swain, S.S., Singh, S.R., Sahoo, A., Hussain, T., Pati, S., *J. Biomol. Struct. Dyn.*, **2021**, 40, 6463–6476.
71. [www.swissdock.ch](http://www.swissdock.ch)
72. Sillars-Hardebol, A. H., Carvalho, B., Beliën, J., Wit, M., Delis-van P. M. et. al., *The Journal of pathology*, **2012**, 226, 3, 442–450. DOI: <http://doi.org/10.1002/path.2983>
73. Kvensakul, M., Hinds, M.G., Banjara, S., *Biochem. J.*, **2020**, 477, 3287–3297.
74. <https://files.rcsb.org/view/6WH0.cif>.
75. <https://files.rcsb.org/view/6WGZ>.
76. Herrmann, O., Baumann, B., de Lorenzi, R., Muhammad, S., Zhang, W., Kleesiek, J., et al. *Nat. Med.*, **2005**, 12, 1322–9. DOI: <http://doi.org/10.1038/nm1323>.
77. Llona-Minguez, S., Baiget, J., Mackay, S.P., *Pharm. Pat. Anal.* **2013**, 4, 481–498. DOI: <https://doi.org/10.4155/ppa.13.31>.
78. Liu, S., Misquitta, Y.R., Olland, A., Johnson, M.A., Kelleher, K.S., Kriz, R., Lin, L.L., Stahl, M., Mosyak, L. *J Biol. Chem.*, **2013**, 288, 22758–22767. <https://www.rcsb.org/structure/4KIK>
79. Xu, G., Lo, Y.C., Li, Q., Napolitano, G., Wu, X., Jiang, X., Dreano, M., Karin, M., Wu, H., *Nature*, **2011**, 472, 325–330. <https://www.rcsb.org/structure/3rzf>

## Quantum Computational Chemistry and Optoelectronic Properties of a New Synthesis Organic Compound

---

Dyari Mustafa Mamand<sup>1</sup>, Dara Muhammed Aziz<sup>2</sup>, Hiwa Mohammad Qadr<sup>1,\*</sup>, Awat Hamad Awla<sup>2</sup>

<sup>1</sup>University of Raparin, College of Science, Department of Physics, Sulaymaniyah, Iraq.

<sup>2</sup>University of Raparin, College of Science, Department of Chemistry, Sulaymaniyah, Iraq.

\*Corresponding author: Hiwa Mohammad Qadr, email: [hiwa.physics@uor.edu.krd](mailto:hiwa.physics@uor.edu.krd)

Received January 20<sup>th</sup>, 2023; Accepted August 25<sup>th</sup>, 2023.

DOI: <http://dx.doi.org/10.29356/jmcs.v68i3.1946>

**Abstract.** For useful photovoltaic technology applications, organic materials with interesting electrical and optoelectronic properties are in great demand. Research on synthetic small organic molecules has gained great attraction for their potential applications in low-cost, ultra-thin and flexible commodities. They are also expected to play a transformative role in life today. 4-((2-hydroxy benzyldene) amino)-N-(thiazol-2-yl) benzenesulfonamide produced by using many important identification tools such as <sup>13</sup>C NMR, <sup>1</sup>H NMR, FTIR and UV-visible spectrum. In this study, there are some parameters such as band gap energy, refractive index, reflectivity, dielectric constant, electrical and optical conductivity to find suitable applications such as solar cells and photovoltaics. Based on quantum computational chemistry, HOMO, LUMO, band gap energy, ionization energy, softness, hardness, electronegativity, electrophilicity, nucleophilicity, electron transfer and back donation energy were calculated by using DFT at the (B3LYP/6-311++G(d, p)) level.

**Keywords:** <sup>13</sup>C NMR; <sup>1</sup>H NMR; FTIR; UV-visible spectrum; C<sub>16</sub>H<sub>13</sub>N<sub>3</sub>O<sub>3</sub>S<sub>2</sub>.

**Resumen.** Para la aplicación útil en tecnologías fotovoltaicas se requiere de materiales orgánicos con propiedades eléctricas y optoelectrónicas específicas. La investigación de moléculas orgánicas pequeñas ha ganado interés por sus aplicaciones potenciales como materias primas ultradelgadas y flexibles. También se espera que jueguen un papel transformador en la vida cotidiana. Se estudió el 4-((2-hidroxibencilidén) amino)-N-(thiazol-2-il) bencénésulfonamida con varias espectroscopías tales como <sup>13</sup>C NMR, <sup>1</sup>H NMR, FTIR y UV-visible. Para la aplicación de estos compuestos en celdas solares y dispositivos fotovoltaicos es necesario conocer parámetros como la brecha o gap de energía, el índice de refracción, la constante dieléctrica, y las conductividades eléctricas y ópticas. Utilizando la DFT con la metodología B3LYP/6-311++G(d, p), se calcularon las siguientes propiedades: energías del HOMO y LUMO, brecha (gap) HOMO-LUMO, primer potencial de ionización, blandura, dureza, electronegatividad, electrofilicidad, nucleofilicidad, transferencia electrónica y retrodonación.

**Palabras clave:** <sup>13</sup>C NMR; <sup>1</sup>H NMR; FTIR; espectro UV-visible; C<sub>16</sub>H<sub>13</sub>N<sub>3</sub>O<sub>3</sub>S<sub>2</sub>.

---

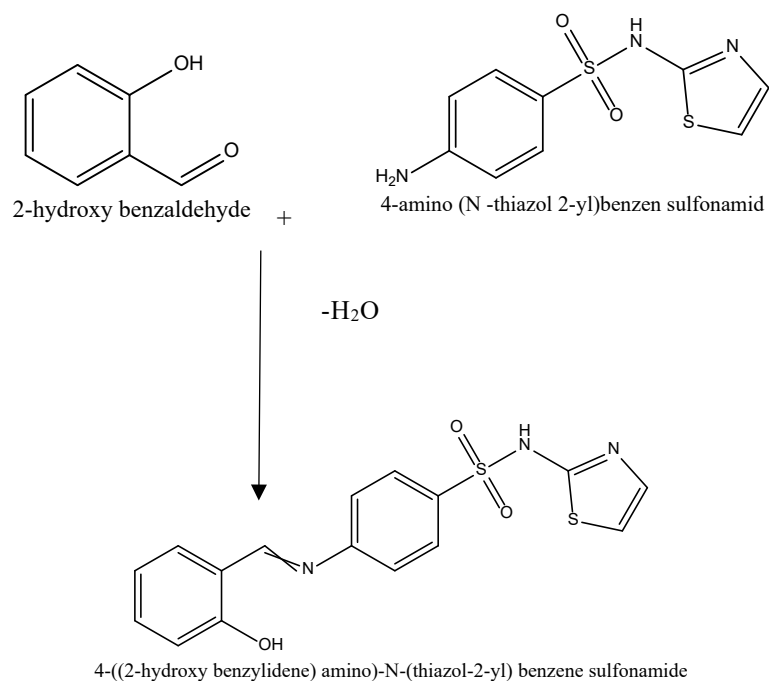
## Introduction

Organic semiconductors (OS) bear different properties from conventional inorganic semiconductors due to their low cost and simplicity of fabrication [1]. Operating system applications include thin-film transistors (TF), light-emitting diodes (LEDs), solar cells (SCs) and photo-refractive devices [2-4]. Small-molecular-weight in solution-processed materials of particular technological relevance can be incorporated into a high-performance conductor where TF [5,6]. Organic photovoltaic (OPV) materials are appealing alternatives to their inorganic counterparts due to their cheap costs, ease of manufacturing, and compatibility with large-area and flexible substrates [5]. An organic solar cell (also known as a plastic solar cell) is a form of solar cell that produces electricity from sunlight by using conductive organic polymers or tiny molecules for light absorption and charge transfer [7,8]. Optical and electrical characteristics of the molecules employed in OPVs at an interface remain unknown in comparison to the bulk [9,10]. The charge carriers in an organic device must flow through the organic/ electrode interfaces. As a result, the electronic structures of molecules are crucial elements influencing the overall efficiency of OPVs. Wide-band gap semiconductors enable devices to function at significantly higher voltages, frequencies and temperatures than typical semiconductor materials such as silicon and gallium arsenide [11-13]. They are an essential component in the production of short-wavelength (green-UV) or lasers and they are also utilized in some radio frequency applications, most notably military radars [14]. Their inherent properties make them suitable for a wide range of different applications, and they are among the best candidates for next-generation semiconductor usage. The bigger band gap is especially essential since it allows devices to function at considerably higher temperatures of 300 °C [15]. This makes them very appealing for military purposes where they have seen some use [16]. Because of the great temperature tolerance, these devices can function at substantially higher power levels under typical settings. Furthermore, most wide-band gap semiconductors have a critical electrical field density that is 10 times higher than that of typical semiconductors [17]. These qualities, when integrated, allow them to function at significantly greater voltages and currents, making them extremely important in military, radio, and power conversion applications. Wide band gap semiconductor materials has lagged behind that of conventional semiconductors which have received considerable development since the 1970s [18,19]. However, their obvious key advantages in many implementations, in conjunction with some special characteristics not found in conventional semiconductors, have renewed interest in their use in everyday electronic devices rather than silicon. Analytical chemistry and thermosetting polymers both make extensive use of sulfathiazole derivatives. Sulfonamide-based compounds exhibit antibacterial, carbonic anhydrase inhibitor, antitubercular, proper semiconductor material, antiviral, insulin release inducer and anti-inflammatory properties [20-22]. In this study, a new material with specified properties has been produced. By using UV spectrum, many optical properties have been found. The properties of this new material have been studied by using Gaussian09 program. Then, experimental of ethanol was compared with experimental of acetone.

## Materials and methods

### Synthesis

Fig. 1 shows synthetic reaction of 4-((2-hydroxy benzylidene) amino)-N-(thiazol-2-yl) benzenesulfonamide. In a 250 mL flask, boiling ethanol was used to dissolve 2-hydroxy benzaldehyde (10 mmol) which was then followed by the addition of 4-amino-N-(thiazol-2-yl) benzenesulfonamide (10 mmol) and catalytic amounts of glacial acetic acid (0.3 mL). The reaction mixture was refluxed until completion. Furthermore, the reaction progress was monitored by using TLC (Ethyl acetate: diethyl ether (1:1) ratio), and the solvent was removed from the resultant mixture using rotary evaporation and then purified using flash chromatography with an eluent ratio of DCM/MeOH 30:2 [1]



**Fig. 1.** Synthetic reaction of 4-((2-hydroxy benzylidene) amino)-N-(thiazol-2-yl) benzenesulfonamide

**Table 1.** <sup>13</sup>C NMR, <sup>1</sup>H NMR and FTIR peaks of 4-((2-hydroxy benzylidene) amino)-N-(thiazol-2-yl) benzenesulfonamide.

|                                                                                                                                                   |                                                                                                                                                                                                                                                                                                                                                                                                                                           |
|---------------------------------------------------------------------------------------------------------------------------------------------------|-------------------------------------------------------------------------------------------------------------------------------------------------------------------------------------------------------------------------------------------------------------------------------------------------------------------------------------------------------------------------------------------------------------------------------------------|
| <b>Yield:</b> 83.67 %<br><b>Melting point:</b> 201 °C                                                                                             | <b>Molecular formula:</b> C <sub>16</sub> H <sub>13</sub> N <sub>3</sub> O <sub>3</sub> S <sub>2</sub><br><b>Molecular weight:</b> 359.039g/mol                                                                                                                                                                                                                                                                                           |
| <b>Element analysis:</b><br>%C    %H    %N    %S<br><b>Calculated:</b> 53.47   3.65   11.69   17.84<br><b>Found:</b> 53.41   3.71   11.72   17.81 |                                                                                                                                                                                                                                                                                                                                                                                                                                           |
| <b>IR:</b><br>3163.22 (NH),<br>3060.22 (aromatic CH),<br>1628.86 (C=N).                                                                           | <b><sup>1</sup>H NMR (DMSO-d<sub>6</sub>, δ ppm):</b><br>6.582-6.604 (1H, d, thiazole, J= 8.8 Hz),<br>7.172-7.192 (1H, d, thiazole, J= 8.0 Hz),<br>7.277-7.308 (2H, d, arH, J= 14.4Hz),<br>7.678-7.686 (1H, d, arH, J= 3.2 Hz),<br>8.065-8.085 (1H,d, arH, J= 8.0 Hz),<br>8.170-8.192 (2H, d, arH, J= 8.8 Hz),<br>8.248-8.270 (1H,d, arH, J= 9.6 Hz),<br>8.793-8.826 (1H, d, arH, J= 13.2 Hz),<br>8.947 (1H,s, HC=N), 12.746 (1H, s, NH). |

**<sup>13</sup>C NMR (DMSO-d<sub>6</sub>, δ ppm):**  
 112.23 (CH, 2-thiazole), 119.44 (2CH, arC),  
 123.56 (CH, arC), 124.92(CH, arC),  
 127.53 (2CH, arC), 128.43 (CH, arC),  
 135.11 (CH, arC), 137.10 (CH, thiazole),  
 137.46 (CH, arC), 138.22 (C, arC-S),  
 142.10 (C,arC-NO<sub>2</sub>), 155.25 (CH, arC-N),  
 165.66 (CH, HC=N), 169.22 (CH, 2-thiazole, N=C-N)

### Optical and electronic studies of the solutions of the zinc phthalocyanine

UV–visible spectroscopy is a very significant and most beneficial optical method for studying optical and electronic characteristics of nanomaterials such as polymers, organic semiconductors and organic light-emitting material [23]. The UV-visible spectra indicates the basic electronic features of the sample. The UV-visible spectrum of the C<sub>16</sub>H<sub>13</sub>N<sub>3</sub>O<sub>3</sub>S<sub>2</sub> compound was achieved in ethanol and acetone as shown in Fig. 2. By considering the UV-visible application, two absorption bands associated with ethanol solvent at 297 and 362.1 nm. The maximum absorption for acetone solvent is 306 nm. The wavelength of UV-visible result located at the visible region which can determine optical band gap energy from the following equation.

$$E = h\nu \quad (1)$$

Equation 1 refers to energy between HOMO and LUMO which is the energy required to evolve a valence electron to become a conduction electron. The band gap energy in any structure is the main factor in determining electrical conductivity. Materials with a small band gap indicate conductivity due to HOMO and LUMO overlap, but a large band gap leads to insulation [24].

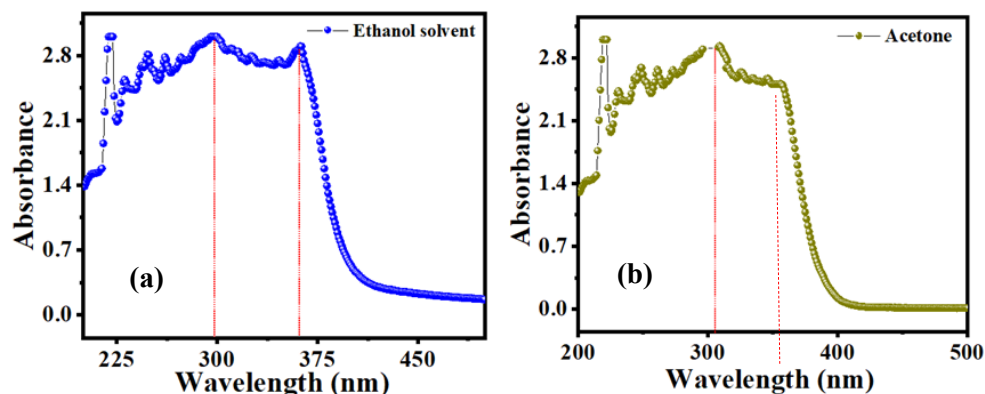


Fig. 2. UV-visible spectrum of C<sub>16</sub>H<sub>13</sub>N<sub>3</sub>O<sub>3</sub>S<sub>2</sub> molecule.

Semiconductors are materials with a nonzero band gap that are intermediate in size and behave as an insulator at 0 K, but permit thermal excitation of electrons into their conduction band below their melting point. The properties of this new material were calculated at low temperatures 295 °K where the band gap is relatively large, but all semiconductors become good conductors with increasing temperature. Furthermore, at room temperature, most semiconductors behave as non-conductors. Band gap was found for each of the highest absorptions which are 4.17 and 3.42 eV in the solvent of ethanol at 297 and 362 nm. On the other hand, acetone solvent is equal to 4.05 and 3.44 eV at 303 and 360 nm.

The transmittance is a useful parameter and has a relation with the refractive index of the materials, the significance of transmittance estimation techniques gives comprehensive information on the refractive index of the sample [25]. Several molecule characteristics have a strong relationship with the transmittance of light through the compounds such as concentration, refractive index of the host medium, color of particle, shape, impurities, the thickness of the sample and wavelength of light while striking on the molecule [26].

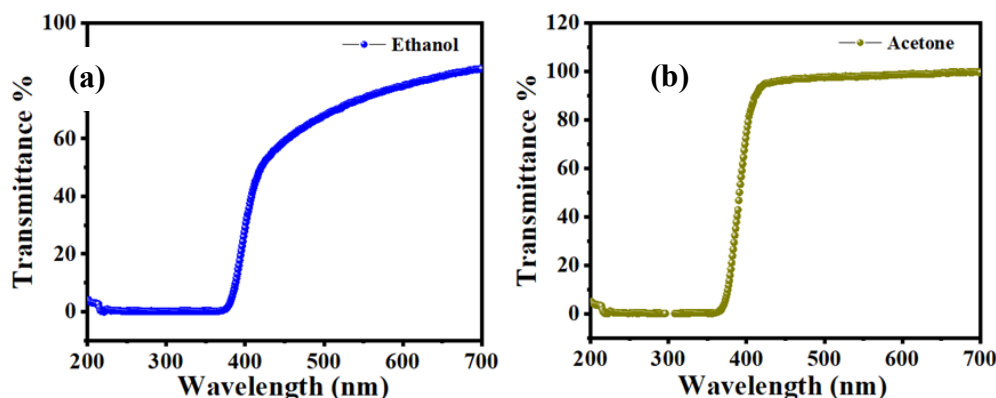


Fig. 3. Transmittance parentage and wavelength of C<sub>16</sub>H<sub>13</sub>N<sub>3</sub>O<sub>3</sub>S<sub>2</sub>.

The shift comparative with 200 nm indicates the presence of impurity. For C<sub>16</sub>H<sub>13</sub>N<sub>3</sub>O<sub>3</sub>S<sub>2</sub> compound, the vertical shift depends on the concentration in the highest wavelength constant near 800 nm. The transmittance and the concentration have a strong opposite relation, the value of the light transmittance through the compound decreases with an increase in the concentration of the compound, because of the scattering of light of the C<sub>16</sub>H<sub>13</sub>N<sub>3</sub>O<sub>3</sub>S<sub>2</sub>. The highest value of transmittance was achieved at 700 nm which is associated with the refractive index of 0.1162 as shown in Fig. 3(a) and (b).

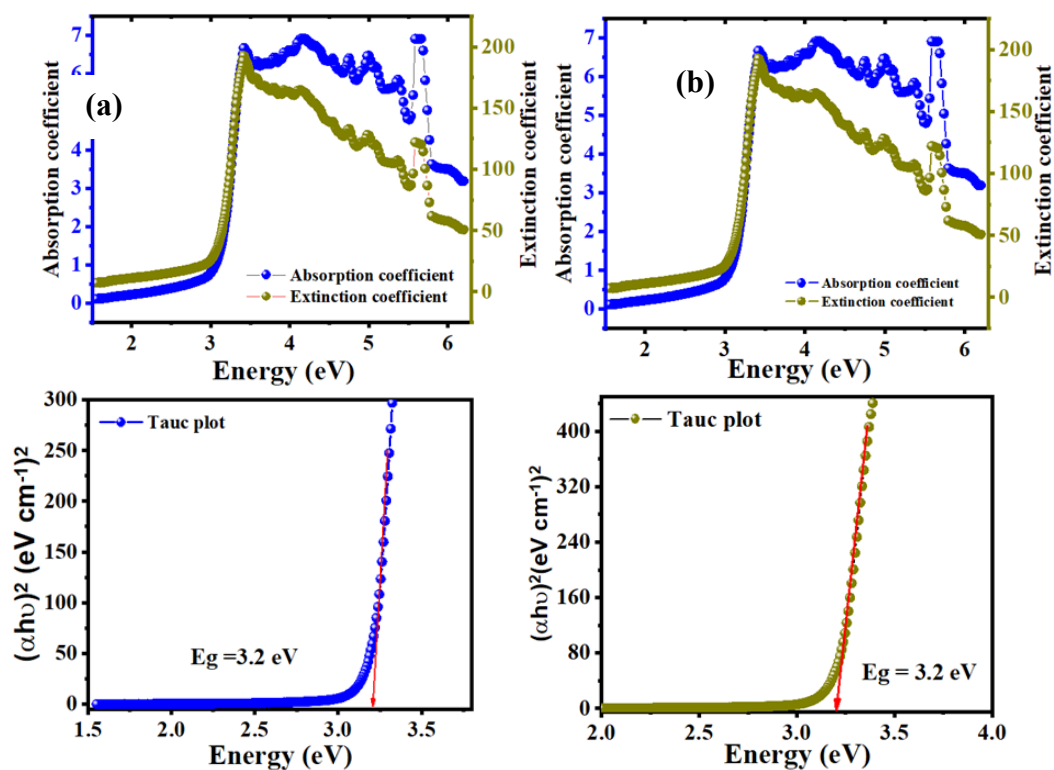
Another significant parameter for optoelectronic applications is extinction coefficient. The extinction coefficient and band gap energy of C<sub>16</sub>H<sub>13</sub>N<sub>3</sub>O<sub>3</sub>S<sub>2</sub> dissolved in ethanol and acetone are shown in Fig. 4(a) and (b). The extinction coefficient of the new compound varies with photon energy. Semiconductor materials have crucial properties for the absorption of light and light absorption can be shown in the duration of the absorption coefficient ( $\alpha$ ) on photon energy ( $h\nu$ ). The forbidden bandwidth of optical transitions or optical band gap for semiconductors was determined using the following relationship [27].

$$(\alpha h\nu)^m = A^*(h\nu - E_g)^m \quad (2)$$

The value of  $m$  is not constant and it varies parameters related to the measuring variety of band gaps, the value of  $m$  is equal to 2 for allowing indirect transitions,  $m$  is equal to 3 for forbidden indirect transitions, the value of  $m$  is equal to 1/2 for allowing direct translations, and  $m$  is 3/2 for forbidden direct transitions [28]. For zinc phthalocyanine semiconductor, the proper value of  $m$  determined to be 2, that is, for electrical dipole-allowed indirect band gap transitions [29].

$$(\alpha h\nu)^{1/2} = A^*(h\nu - E_g)^{1/2} \quad (3)$$





**Fig. 4.** Extinction coefficient, absorption coefficient and Tauc plot variation of  $C_{16}H_{13}N_3O_3S_2$  in (a, c) ethanol and (b, d) acetone solvents

The allowed indirect band gap of  $C_{16}H_{13}N_3O_3S_2$  molecule in ethanol and acetone solvents achieved associated with the Tau-plot method as shown in Fig. 4(c) and d,  $E_g$  value is equal to 3.2 eV. Achieved outcomes in our production imply that the optical band gap of the  $C_{16}H_{13}N_3O_3S_2$  is to be a good semiconductor due to suitable  $E_g$  which can be used in optoelectronic devices.

An important parameter for optoelectronic applications and technologies is refractive index. The relation between the refractive index and the band gap energy is opposite. The refractive index of the materials increases with band gap energy. The following relationship can achieve the  $n$  value of zinc phthalocyanine [30,31].

$$n = \left\{ \left[ \frac{4R}{(R-1)^2} - k^2 \right]^{\frac{1}{2}} - \frac{R+1}{R-1} \right\} \quad (4)$$

The optical and electronic characteristic of semiconductor material principles is based on two important parameters which are band gap energy and refractive index, decided by these two fundamental properties. Semiconductors' transparency to incident photons can be measured using refractive index, whereas a semiconductor's threshold of photon absorption determines its band gap energy. Fig. 5 shows refractive variations with band gap energy at 22 K.

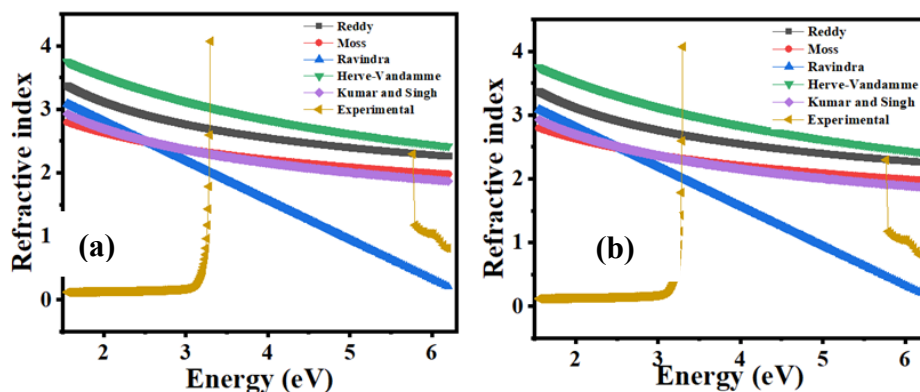


Fig. 5. Refractive variations with band gap energy of  $C_{16}H_{13}N_3O_3S_2$  in 22 K.

There are many relationships between  $E_g$  value of semiconductor material and refractive index, including Moss, Ravindra, Herve-Vandamme, Reddy and Kumar and Singh [32]. The refractive index values of the  $C_{16}H_{13}N_3O_3S_2$  semiconductor in the proper optical band gap for ethanol and acetone solution were determined from equation 4 and the received  $n$  values are presented in Table 2.

Herve-Vandamme relation gives the highest refractive index values for  $C_{16}H_{13}N_3O_3S_2$ , while Ravindra relation gives the lowest refractive index values as shown in Table 2. A higher correlation is achieved through the Herve-Vandamme relation than any other.

Table 2. The refractive indices of the  $C_{16}H_{13}N_3O_3S_2$  for various relations

| Energy-gap | Moss  | Ravindra | Herve-Vandamme | Reddy | Kumar and Singh | Average |
|------------|-------|----------|----------------|-------|-----------------|---------|
| 1.85       | 2.458 | 2.277    | 3.242          | 2.892 | 2.478           | 3.820   |
| 1.94       | 2.458 | 2.277    | 3.242          | 2.892 | 2.478           | 3.741   |

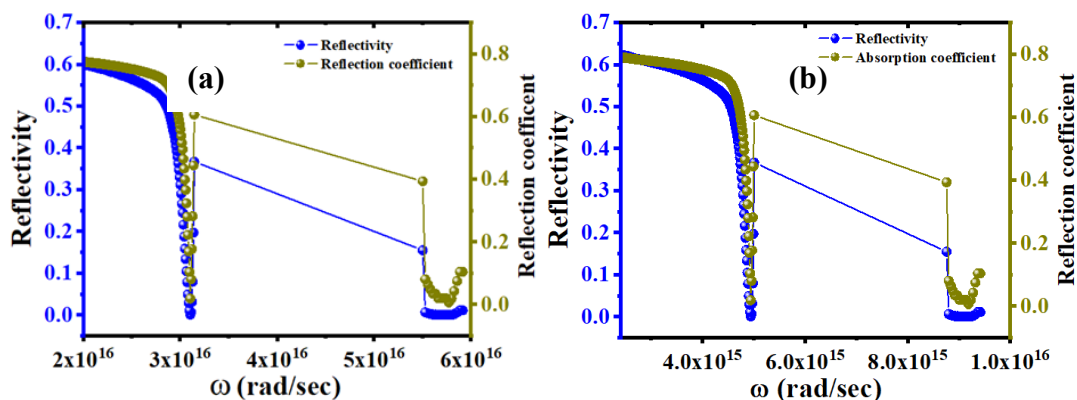
### Reflectivity

The following relationships can be used to calculate the fractional amplitude of the reflected electromagnetic field by examining the relationship between reflectance ( $R$ ) and reflection coefficient ( $r$ ) [33,34].

$$R = \frac{(n - 1)^2}{(n + 1)^2} \quad (5)$$

$$r = \sqrt{R} \quad (6)$$

Reflectance is an important parameter for materials because a material with high reflectivity is a sign of a good conductor, but a low refractive index and reflectivity suggest that the material has low conductivity. We can achieve the same purpose by relying on other laws, for example Hagen–Rubens law [35].



**Fig. 6.** Reflectivity and reflection coefficient variation with an angular frequency of  $C_{16}H_{13}N_3O_3S_2$ . (a) ethanol solvent, (b) acetone solvent

Optical characteristics of these novel compounds display metal-like behavior at lower frequencies, but at higher frequencies, there is insulation-like activity. Plasma frequency is the frequency at which the real portion of the dielectric function disappears, as well as at which the material transitions from metallic to dielectric behavior. Plasma frequency changed due to the effect of solvents as shown in Fig. 6(a) and (b) which is higher in ethanol than acetone.

### Electrical and optical conductivity

Optical conductivity and electrical conductivity are important properties of materials which are calculated by the following equations [36,37].

$$\sigma_{opt} = \frac{\alpha nc}{4\pi} \quad (7)$$

$$\sigma_{ele} = \frac{2\lambda\sigma_{opt}}{\alpha} \quad (8)$$

In general, optical conduction as electronic conduction is a matter of placing electrons in the conduction band. Another way to achieve this purpose is to provide an electron bound to the atoms with enough energy to break the bond and freed it to move. This can be achieved simply by illuminating the material with light, as the photons have energy that allows bonds to be broken. According to the solid-state field, photons can boost electrons from the valence to the conduction band, leaving a gap in the valence band. The free hole and the electron can then contribute to the electrical conductivity of the material. An important purpose of manufacturing electronic gadgets on the molecular level is the ability to measure and control the electric current through a single molecule. Additional applications concentrate on the insight given by these practices in the field of charge transport which is a recurrent phenomenon in various biological and chemical processes [38].

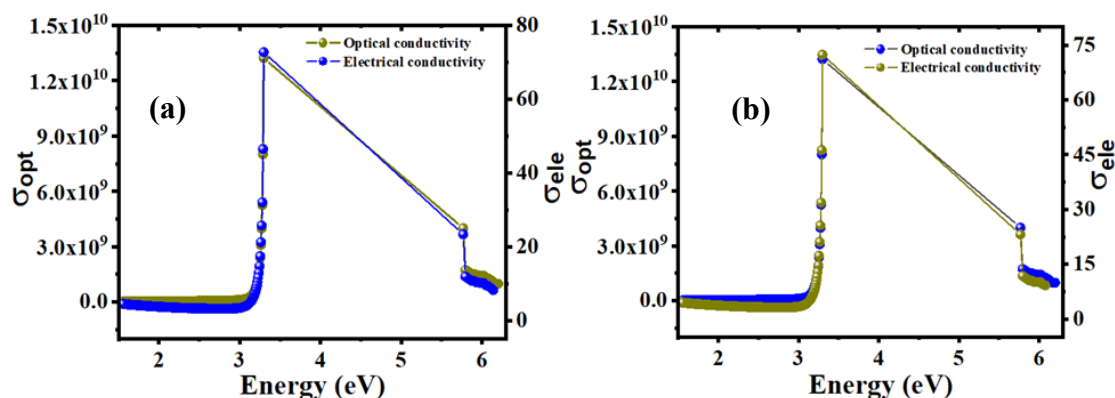


Fig. 7. Optical and electrical variation with energy of  $C_{16}H_{13}N_3O_3S_2$  at 22 K in (a) ethanol and (b) acetone solvents.

Fig. 7(a) and (b) show electrical and optical conductivity for each solvent but they do not affect optical properties. When the band gap is zero, the electrical and optical conductivity are both zero, but after 3.2 eV they both increase to their highest levels. This material has good conductivity compared to other materials. Electrical conductivity may be readily described using the Drude model [39]. Using solid band theory, the valence and conduction bands overlap, resulting in more free electrons in the conduction band. Conduction electrons are responsible for conduction, although the material has resistance due to scattering process. Optical conductivity measures the electrical conductivity in an oscillating field. As a result, the dielectric constant comes into play which governs the propagation of light into matter. The terms plasma frequency and relaxation time are used in this context. These two main physical parameters govern optical propagation. If radiation strikes matter, it pushes the electron, and if there is no scattering, light is totally reflected, which is why metals are bright. Above plasma frequency, reflection decreases, and transmission takes over which can easily distinguish between electrical and optical conductivity. This component also influences the color of the metals.

### Dielectric properties

The dielectric properties of the material are related to the electro-optical properties which are significant for optical materials. Dielectric constants are the key to explaining the polarization and permittivity of the material which is related to the forbidden energy gap and state density of materials. The real part of the dielectric constant provides information about the speed of light that can be slow into the material. Another part of the dielectric constant is the imaginary part which shows the absorption of energy by an electric field due to dipole motion [40].

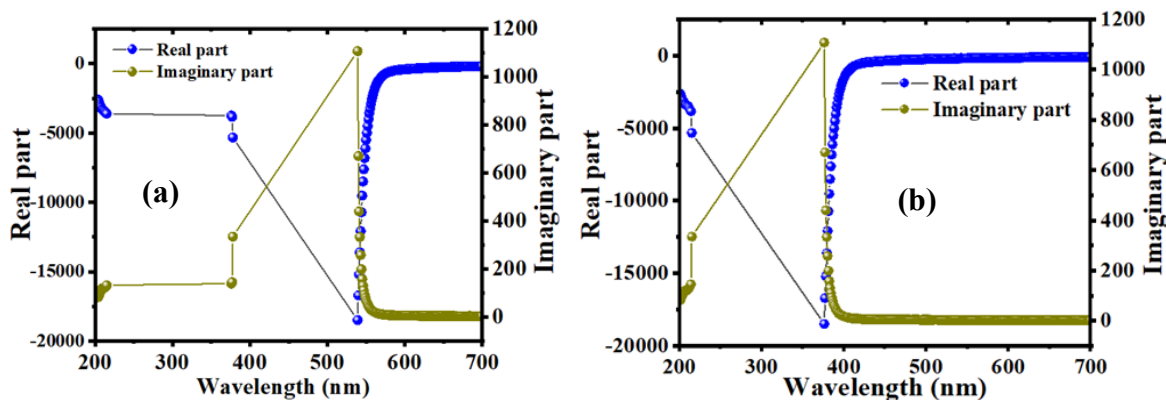


Fig. 8. Dielectric constants of  $C_{16}H_{13}N_3O_3S_2$ , (a) ethanol, (b) acetone solvents.

The difference in the imaginary and real part of the dielectric constant have an opposite trend. The minimum value of the real part is 300 nm which shows the lowest absorption. The maximum value of the real part of  $C_{16}H_{13}N_3O_3S_2$  in ethanol solvent is 540 nm and in acetone solvent is 380 nm which shows the highest absorption as shown in Fig. 8(a) and (b).

According to Koop's theory which is based on the Maxwell–Wagner model during the lower frequency range can be explained as the highest value of the dielectric constant [41]. The highest dielectric constant can be determined at low frequency, the main contribution to the dielectric constant comes from the grain boundaries, but the smallest dielectric constant depends on the high frequency and the grains with a small dielectric constant dominate. The relaxation processes are related to the dielectric property because the real dielectric constant of the compound decreases with increasing frequency which may be associated with electrostatic relaxation processes. In the low-frequency region, the imaginary dielectric part and frequency have a relationship. The dielectric loss also decreases with frequency. The permittivity of the imaginary part becomes less sensitive at high frequency, the high resistivity indicates the low frequency due to the dominant effect of the grain boundaries, to jumping between the energy levels more energy required. In the high region of the frequency, the energy required to transfer electrons between the levels is low, hence the energy loss is small.

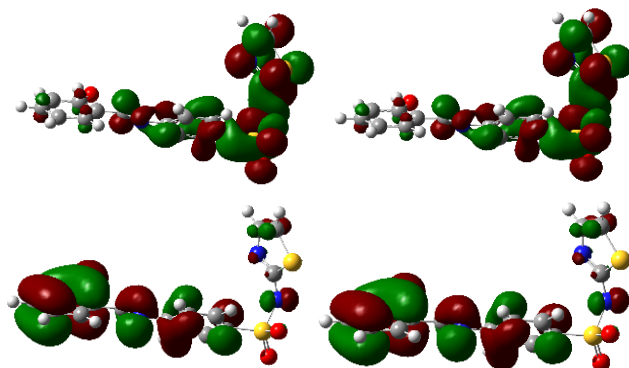
### Electronic structure of $C_{16}H_{13}N_3O_3S_2$

The molecular structures of the  $C_{16}H_{13}N_3O_3S_2$  compound were optimized utilizing the quantum mechanical approach in the ethanol and acetone solvents at the B3LYP/6-311++G(d, p). The global chemical reactivity characteristics (Table 3) such as ionization potential (I), electron affinity (A), the lowest unoccupied molecular orbital ( $E_{LUMO}$ ), the highest occupied molecular orbital ( $E_{HOMO}$ ) and energy gap are all included ( $E_g$ ). electronegativity ( $\chi$ ), chemical potential ( $\mu$ ), molecular hardness ( $\eta$ ), molecular softness ( $s$ ), nucleophilicity and electrophilicity index ( $\omega$ ) are all terms used to describe the properties of molecules.

**Table 3.** Quantum chemical parameters based on DFT calculations at 6-311++G(d, p) basis set in different solvents.

| Quantum chemical parameters        | Acetone solvent | Ethanol solvent |
|------------------------------------|-----------------|-----------------|
| HOMO                               | -6.342          | -6.341          |
| LUMO                               | -2.904          | -2.886          |
| HOMO-1                             | -6.689          | -6.691          |
| LUMO+1                             | -2.084          | -2.085          |
| Total energy                       | -1803.285       | -1803.286       |
| Dipole moment (Debye)              | 14.675          | 14.5429         |
| Ionization energy (eV)             | 6.342           | 6.341           |
| Electron affinity (eV)             | 2.904           | 2.886           |
| Band-gap energy (eV)               | 3.438           | 3.454           |
| Hardness (eV)                      | 1.719           | 1.727           |
| Softness (eV)                      | 0.581           | 0.578           |
| Electronegativity (eV)             | 4.623           | 4.613           |
| Chemical potential (eV)            | -4.623          | -4.613          |
| Electrophilicity (eV)              | 6.218           | 6.162           |
| Nucleophilicity (eV) <sup>-1</sup> | 0.160           | 0.162           |
| $\Delta E$ Back-donation (eV)      | -0.429          | -0.431          |
| Transfer electrons                 | 0.691           | 0.690           |

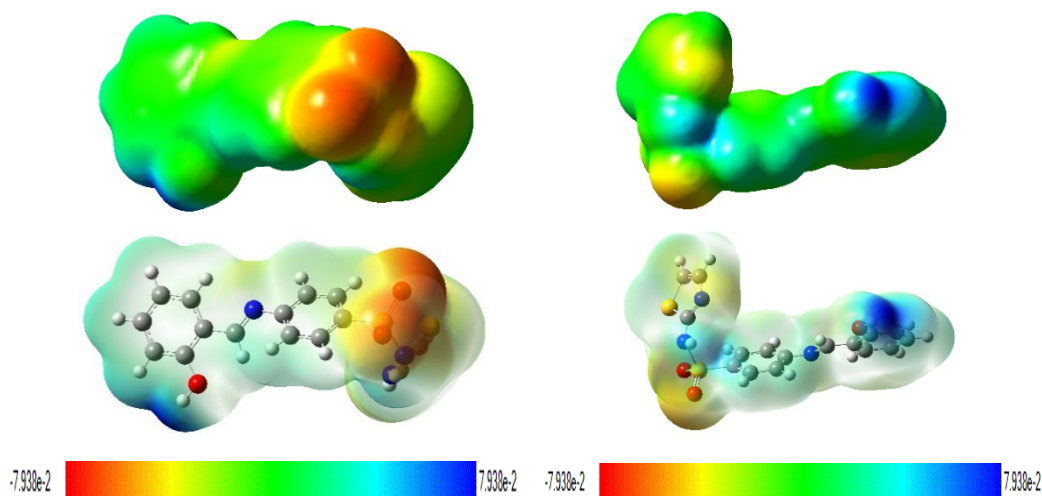
Density functional theory using the basis set (B3LYP/6-31++G(d, p)) is used to calculate the frontier energy gap,  $E_{\text{HOMO}}$  and  $E_{\text{LUMO}}$  energy of this molecule in the ethanol and acetone solvents. Optical and electrical characteristics of this new molecule are highly related to the HOMO-LUMO gap [42,43]. The ability to supply electrons is represented by the energy of the HOMO, while the ability to accept electrons is represented by the energy of the LUMO [44]. The energy difference between HOMO and LUMO orbitals defines molecule chemical stability, optical polarizability and chemical reactivity [45]. It is easier to move an electron from the HOMO orbital to an excited state (LUMO) when the energy gap between HOMO and LUMO is narrower (soft) [46]. Fig. 9 shows HOMO and LUMO based on DFT calculation.



**Fig. 9.** HOMO and LUMO of  $\text{C}_{16}\text{H}_{13}\text{N}_3\text{O}_3\text{S}_2$  based on DFT calculation.

In quantum chemical processes, electronegativity and electronic chemical potential are key properties. A high electronegativity indicates that the atoms or molecules have a greater ability to attract electrons, while a high chemical potential indicates a greater reactivity and less stability. Table 3 can be shown that this molecule has a higher electronegativity in acetone than other solvents.  $\text{C}_{16}\text{H}_{13}\text{N}_3\text{O}_3\text{S}_2$  has the highest chemical potential in the ethanol solvent.

The magnitude of the electrophilicity index is utilized as a chemical structural descriptor for examining the chemical reactivity of compounds. A more reactive nucleophile has a lower value of ( $\omega$ ) than a strong electrophile with a high value of ( $\omega$ ).  $\text{C}_{16}\text{H}_{13}\text{N}_3\text{O}_3\text{S}_2$  in ethanol solvent is a more reactive nucleophile. As shown in Table 3, this molecule is an excellent electrophile when compared to ethanol solvent.



**Fig. 10.** Electrostatic potential map of  $\text{C}_{16}\text{H}_{13}\text{N}_3\text{O}_3\text{S}_2$ .

The electrostatic potential map reveals information about the atomic charges which may indicate the advantages of the electrostatic potential map (EPM) [25]. The former is used to define polarity and non-polarity in the structures of the molecule. The second advantage is that it can be used to compare the charge of one molecule to another for determining the result of a chemical process. The third component examines the electron cloud form of the atom and determines an irregularity that may be used to determine which regions have the highest electron density and which locations have the lowest electron density or depletion. Red as negative extreme and blue as positive extreme. The red colour with negative indicates the minimum electrostatic potential (that means it is bound loosely or excess electrons) and act as electrophilic attack. The interaction of molecules is similar to why molecules aggregate and how polymer complexes are formed. These reactions are similar to chemical reactions. The electric potential map holds a three-dimensional molecular outline and is useful for describing the charge distribution on the molecule surface and examining the molecular properties. They allow the researcher to visualize the shape and size of the molecule. The electric potential is very effective in predicting the behavior of complex molecules. The default color scale progresses from red to deeper blue electron density is higher in the region, indicating that electrostatic potential has dropped to its lowest point in the region. The oxygen atoms have a higher electron density in both solvents as shown in Fig. 10.

## Conclusions

The main objective of this study was to synthesize an organic material. The structure of the material is established using a variety of identification technologies such as  $^{13}\text{C}$  NMR,  $^1\text{H}$  NMR, and FTIR. Several basic properties were studied to establish optoelectronic properties. Band gap energy is the most important attribute important for researchers. This material has a large vacuum which is around 4 eV in ethanol and acetone solvents. The optical band gap was determined by Tauc plot method which is 3.2 eV. Although these traits were found at 22 K which can be controlled by increasing the temperature. This new semiconductor material has a good ability to conduct electricity based on its ability to reflect a lot of light. While, electrical and optical conductivity of this material were calculated, the highest dielectric constant was found in the 540- 380 nm range, indicating its polarization ability.

## References

1. Forrest, S.R. *IEEE J. Sel. Top. Quantum Electron.* **2000**, 6, 1072-1083. DOI: <https://doi.org/10.1109/2944.902156>.
2. Yakuphanoglu, F.; Şenkal, B. *J. Phys. Chem. C.* **2007**, 111, 1840-1846. DOI: <https://doi.org/10.1021/jp0653050>.
3. Yao, L.; Rahmanudin, A.; Guijarro, N.; Sivula, K. *Adv. Energy Mater.* **2018**, 8, 1802585. DOI: <https://doi.org/10.1002/aenm.201802585>.
4. Qadr, H.M. *At. Indones.* **2020**, 46, 47-51. DOI: <https://doi.org/10.17146/ajj.2020.923>.
5. Liu, C.; Cheng, Y.-B.; Ge, Z. *Chem. Soc. Rev.* **2020**, 49, 1653-1687. DOI: <https://doi.org/10.1039/C9CS00711C>.
6. Qadr, H.M. *Russ. J. Non-Ferr.* **2021**, 62, 561-567. DOI: <https://doi.org/10.3103/S1067821221050096>.
7. Brabec, C.J.; Sariciftci, N.S.; Hummelen, J.C. *Adv. Funct. Mater.* **2001**, 11, 15-26. DOI: [https://doi.org/10.1002/1616-3028\(200102\)11:1%3C15::AID-ADFM15%3E3.0.CO;2-A](https://doi.org/10.1002/1616-3028(200102)11:1%3C15::AID-ADFM15%3E3.0.CO;2-A).
8. Dennler, G.; Sariciftci, N.S. *Proc. IEEE.* **2005**, 93, 1429-1439. DOI: <https://doi.org/10.1109/JPROC.2005.851491>.
9. Nakano, K.; Tajima, K. *Adv. Mater.* **2017**, 29, 1603269. DOI: <https://doi.org/10.1002/adma.201603269>.
10. Mamand, D.M.; Qadr, H.M. *Corros. Rev.* **2023**, 41, 427-441. DOI: <https://doi.org/10.1515/corrrev-2022-0085>.



11. Ozpineci, B.; Tolbert, L.M. in: *Comparison of wide-bandgap semiconductors for power electronics applications*, United States. Department of Energy, **2004**.
12. Elasser, A.; Chow, T.P. *Proc. IEEE.* **2002**, *90*, 969-986. DOI: <https://doi.org/10.1109/JPROC.2002.1021562>.
13. Mamand, D.M.; Anwer, T.M.K.; Qadr, H.M. *J. Indian Chem. Soc.* **2023**, *100*, 101018. DOI: <https://doi.org/10.1016/j.jics.2023.101018>.
14. Iacopi, F.; Van Hove, M.; Charles, M.; Endo, K. *Mrs Bull.* **2015**, *40*, 390-395. DOI: <https://doi.org/10.1557/mrs.2015.71>.
15. Neudeck, P.G.; Okojie, R.S.; Chen, L.-Y. *Proc. IEEE.* **2002**, *90*, 1065-1076. DOI: <https://doi.org/10.1109/JPROC.2002.1021571>.
16. Reich, B.; Hakim, E.B. *Microelectron. Reliab.* **1976**, *15*, 29-33. DOI: [https://doi.org/10.1016/0026-2714\(76\)90138-4](https://doi.org/10.1016/0026-2714(76)90138-4).
17. Torres, R.A.; Dai, H.; Lee, W.; Jahns, T.M.; Sarlioglu, B. in: *2018 IEEE Transportation Electrification Conference and Expo (ITEC)*, IEEE, **2018**, 1002-1008.
18. Shi, J.; Zhang, J.; Yang, L.; Qu, M.; Qi, D.-C.; Zhang, K.H. *Adv. Mater.* **2021**, *33*, 2006230. DOI: <https://doi.org/10.1002/adma.202006230>.
19. Nunn, W.; Truttman, T.K.; Jalan, B. *J. Mater. Res.* **2021**, 1-19. DOI: <https://doi.org/10.1557/s43578-021-00377-1>.
20. Wang, P.; Xiao, H.; Duan, C.; Wen, B.; Li, Z. *Polym. Degrad. Stab.* **2020**, *173*, 109078. DOI: <https://doi.org/10.1016/j.polymdegradstab.2020.109078>.
21. Gündüz, M.G.; Tahir, M.N.; Armaković, S.; Koçak, C.Ö.; Armaković, S.J. *J. Mol. Struct.* **2019**, *1186*, 39-49. DOI: <https://doi.org/10.1016/j.molstruc.2019.03.010>.
22. Aziz, D.M.; Azeez, H.J. *J. Mol. Struct.* **2020**, *1222*, 128904. DOI: <https://doi.org/10.1016/j.molstruc.2020.128904>.
23. Hussein, M.; Nasir, E.; Al-Aarajiy, A. *Int. J. Thin Film Sci. Tec.* **2012**, *1*, 71-76.
24. Ajayaghosh, A. *Chem. Soc. Rev.* **2003**, *32*, 181-191. DOI: <https://doi.org/10.1039/B204251G>.
25. Mamand, D.M.; Anwer, T.M.K.; Qadr, H.M. *Oxid. Commun.* **2022**, *45*, 600-627.
26. Mamand, D.M.; Qadr, H.M. *Prot. Met. Phys. Chem.* **2021**, *57*, 943-953. DOI: <https://doi.org/10.1134/S207020512105018X>.
27. Orek, C.; Gündüz, B.; Kaygili, O.; Bulut, N. *Chem. Phys. Lett.* **2017**, *678*, 130-138. DOI: <https://doi.org/10.1016/j.cplett.2017.04.050>.
28. Sassi, M.; Oueslati, A.; Moutia, N.; Khirouni, K.; Gargouri, M. *Ionics.* **2017**, *23*, 847-855. DOI: <https://doi.org/10.1007/s11581-016-1903-y>.
29. Mamand, D.M.; Qadr, H.M. *Russ. J. Phys. Chem. A.* **2022**, *96*, 2155-2165. DOI: <https://doi.org/10.1134/S0036024422100193>.
30. Epstein, R.; Sheik-Bahae, M.; Hehlen, M. in: *Science and Applications of Laser Cooling of Solids.*, Wiley, **2009**. DOI: <https://doi.org/10.1002/9783527628049>.
31. Turan, N.; Kaya, E.; Gündüz, B.; Çolak, N.; Körkoca, H. *Fibers Polym.* **2012**, *13*, 415-424. DOI: <https://doi.org/10.1007/s12221-012-0415-2>.
32. Tripathy, S. *Opt. Mater.* **2015**, *46*, 240-246. DOI: <https://doi.org/10.1016/j.optmat.2015.04.026>.
33. Brust, D.; Phillips, J.; Bassani, F. *Phys. Rev. Lett.* **1962**, *9*, 94. DOI: <https://doi.org/10.1103/PhysRevLett.9.94>.
34. Mamand, D.M.; Anwer, T.M.K.; Qadr, H.M.; Mussa, C.H. *Russ. J. Gen. Chem.* **2022**, *92*, 1827-1838. DOI: <https://doi.org/10.1134/S1070363222090249>.
35. Silveira, F.; Kurcbart, S. *EPL.* **2010**, *90*, 44004. DOI: <https://doi.org/10.1209/0295-5075/90/44004>.
36. Akinlami, J.; Olateju, I. in: *Semicond. phys. quantum electron. optoelectron.* **2012**, 281-284.
37. Qadr, H.M.; Mamand, D.M. *Azerbaijan Chem. J.* **2023**, 19-29. DOI: <https://doi.org/10.32737/0005-2531-2023-2-19-29>.



38. Gebhard, F. in: *The Mott Metal-Insulator Transition*. **1997**, 1-48. DOI: [https://doi.org/10.1007/3-540-14858-2\\_1](https://doi.org/10.1007/3-540-14858-2_1).
39. Bade, W.L. *J. Chem. Phys.* **1957**, 27, 1280-1284. DOI: <https://doi.org/10.1063/1.1743991>.
40. Rajkumar, M.; Saravanabhavan, M.; Chandramohan, A. *Opt. Mater.* **2017**, 72, 247-256. DOI: <https://doi.org/10.1016/j.optmat.2017.06.011>.
41. Koops, C. *Phys. Rev.* **1951**, 83, 121. DOI: <https://doi.org/10.1103/PhysRev.83.121>.
42. Qadr, H.M.; Mamand, D.M. *J. Bio- Tribo-Corros.* **2021**, 7, 140. DOI: <https://doi.org/10.1007/s40735-021-00566-9>.
43. Mamand, D.M.; Qadr, H.M. *Him. Fiz. Tehnol. Poverhni.* **2023**, 14, 159-172. DOI: <http://jnas.nbu.gov.ua/article/UJRN-0001412158>.
44. Erdoğan, Ş.; Safi, Z.S.; Kaya, S.; Işın, D.Ö.; Guo, L.; Kaya, C. *J. Mol. Struct.* **2017**, 1134, 751-761. DOI: <https://doi.org/10.1016/j.molstruc.2017.01.037>.
45. Pearson, R.G. *PNAS.* **1986**, 83, 8440-8441. DOI: <https://doi.org/10.1073/pnas.83.22.8440>.
46. Mamand, D.M.; Awla, A.H.; Anwer, T.M.K.; Qadr, H.M. *Chim. Techno Acta.* **2022**, 9, 20229203. DOI: <https://doi.org/10.15826/chimtech.2022.9.2.03>.

## DFT Calculation, ADME/T and Molecular Docking Approach of Methyl 2-oxo-1,2-dihydrofuro[3,4-d] pyrimidine-3(4H)carboxylate

---

Gühergül Uluçam\*

Chemistry Department, Faculty of Science, Trakya University, 22030 Edirne, Turkey.

\*Corresponding author: Gühergül Uluçam, email: [gulergul@trakya.edu.tr](mailto:gulergul@trakya.edu.tr); Phone: +90 284 2351105; Fax: +90 284 2351198

Received March 7<sup>th</sup>, 2023; Accepted August 3<sup>rd</sup>, 2023.

DOI: <http://dx.doi.org/10.29356/jmcs.v68i3.1995>

**Abstract.** The optimized geometry of methyl 2-oxo-1,2-dihydrofuro[3,4-d] pyrimidine-3(4H) carboxylate (FP) was determined by density functional theory calculations. Geometric properties of FP such as bond length, bond angle, dihedral bond angle, and HOMO-LUMO energies in the gas phase were calculated by using the Gaussian program. Delocalization of the molecule's charge was analyzed using Mulliken Population Analysis (MPA) and Natural Population Analysis (NPA) approaches. Electrophilic and nucleophilic regions of FP were identified by drawing a molecular electrostatic potential map. NMR and FTIR spectra were calculated with the B3LYP and 6-311++G (2d, p) basis set and a detailed FTIR analysis was performed by using the VEDA program. To determine the consistency of the calculated NMR and FTIR spectra, they were compared with their corresponding experimental NMR and FTIR spectra. Molecular insertion studies of FP with six different cancer proteins were analyzed and their interactions were evaluated. Data on the pharmacokinetics and drug affinity of FP were obtained through the Swiss ADME and ADMET programs.

**Keywords:** Dihydrofuro [3,4-d] pyrimidine; DFT/B3LYP; molecular docking; swiss ADME; ADMET.

**Resumen.** Se optimizó la geometría del metil 2-oxo-1,2-dihidrofuro[3,4-d] pirimidina-3(4H) carboxilato (FP) por medio de la teoría de funcionales de la densidad. Utilizando el programa Gaussian, se calcularon en fase gas las propiedades geométricas del FP como longitudes de enlace, ángulos de enlace, ángulos diedros, y la diferencia de energías entre HOMO y LUMO. Se analizó la deslocalización de la carga en la molécula utilizando los análisis de población de Mulliken (MPA) y de población natural (NPA). Se identificaron las regiones electrofílicas y nucleofílicas mediante mapas del potencial electrostático molecular. Utilizando el funcional B3LYP y la base 6-311++G (2d, p) se calcularon los espectros de NMR y FTIR; se realizó un análisis detallado de los espectros de FTIR utilizando el programa VEDA. Para determinar la confiabilidad de los espectros calculados de NMR y FTIR, se compararon con los resultados experimentales. Se analizaron estudios de inserción molecular del FP a seis diferentes proteínas involucradas en cáncer para determinar sus interacciones. Utilizando los programas Swiss ADME y ADMET se determinaron la farmacocinética y la afinidad del FP.

**Palabras clave:** Dihidrofuro [3,4-d] pirimidina; DFT/B3LYP; acoplamiento molecular; Swiss ADME; ADMET.

---

## Introduction

Pyrimidine, an aromatic heterocyclic compound containing nitrogen, is found in the structure of DNA and RNA, which are important for life. Synthesized pyrimidine-derived compounds can be used in many areas due to their features such as antifungal, anti-tumor, anti-inflammatory, anti-viral, anti-bacterial, anti-proliferative, anti-Alzheimer's, anti-tuberculosis, anti- $\beta$ -glucuronidase, anti-HIV and diuretic [1-10]. Also, some cancer drugs like Xeloda [11], cytarabine [12] and gemcitabine [13], 5-fluorouracil [14] contain pyrimidine as the main component. Furopyrimidine compounds are synthesized by forming a pyrimidine ring next to the furan ring by various reactions. These compounds have biological properties similar to pyrimidines, which have been the subject of many studies in recent years [15-17]. It can be said that there is not much literature on quantum chemical calculations, molecular docking, ADME, and ADMET for furopyrimidine derivative compounds. For this purpose, methyl 2-oxo-1,2-dihydrofuro[3,4-d] pyrimidine-3(4H) carboxylate (FP) was first optimized using density functional theory (DFT). Bond angles, dihedral angles, bond lengths, dipole moments, molecular electrostatic potential map (MEP), highest occupied molecular orbital (HOMO), and lowest unoccupied molecular orbital (LUMO) of FP were obtained with the Gaussian G09w package program [18]. Then, the calculated spectrum values of FTIR and NMR were compared with the experimental spectrum values reported by Yilmaz et al. [19]. Finally, the biopotential of FP was evaluated by molecular docking with six different cancer proteins. Data on the pharmacokinetics and drug affinity of FP were obtained through the Swiss ADME [20] and ADMET programs [21].

## Theoretical method

Geometric calculations and molecular configuration of the FP were performed in the Gaussian G09w package program with the 6-311++G (2d, p) basis set using B3LYP [22-24]. MAP and FMO were also calculated by the same method. The gauge invariant atomic orbitals (GIAO) method was used for  $^1\text{H}$  and  $^{13}\text{C}$  NMR. Since the experimental data were obtained in dimethylsulphoxide (DMSO), theoretical calculations were made in DMSO for comparison, and the solvent effect on the chemical shift value was also investigated by calculating NMR in the gas phase. The calculated IR vibration frequencies are multiplied by the correction factor 0.9613 which provides the best agreement between the theoretical data and the experimental FTIR frequencies for B3LYP/6-31G(d) method [24]. A detailed potential energy distribution (PED) analysis was also performed using the VEDA program. The visualization of all data was carried out in GaussView 5.0 [25-27].

## Molecular docking

Since many in vivo and in vitro experiments are required, it is very difficult to determine whether the synthesized compounds have biological effects. Molecular docking calculation of ligand-receptor interactions provides easier information about the bioactivity of the compound [28-31]. The best ligand-receptor interaction can be examined by choosing the lowest energy interaction among the molecular docking results. Molecular docking studies were performed with Auto Dock Tools 1. 5. 6. [32,33]. Molecular docking FP with various cancer proteins, namely brain cancer, breast cancer, gastric cancer, liver cancer, lung cancer, and skin cancer [34-39]. The 3D crystal structure of cancer proteins was taken from Protein Data Bank (Brain Cancer Protein PDB ID: 1QHT, [40] Breast Cancer Protein PDB ID: 1JNX [41], Gastric Cancer Protein PDB ID: 1BJ7 [42], Liver Cancer Protein PDB ID: 3WZE [43], Lung Cancer Protein PDB ID: 2ITO [44], Skin Cancer Protein PDB ID: 2VCJ [45]. Water molecules were removed, and polar hydrogens and Kollman United charges were added as the biomolecules were prepared for docking. The FP molecule was prepared for docking by minimizing its energy at the Gaussian 09w program [18]. Partial Charges of FP was calculated by Geistenger Method. The spacing between grid points was 0.375 Å. Autodock docking studies were examined by using the Lamarckian Genetic Algorithm (LGA). As a result of the calculations, the lowest energy interaction was selected, and the results were interpreted. All FP-biomolecule interactions were

illustrated using Pymol and Chimera software [46-48]. LigPlot+ v.1.4.5 software was used to show the H bonds in detail [49].

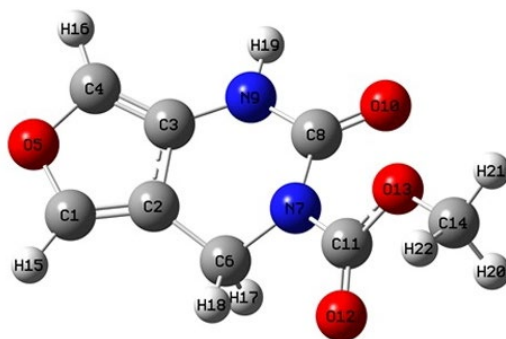
### Swiss ADME and ADMET Lab

It is important to evaluate the bioavailability of compounds using computer-based programs for the discovery of new drugs. Compounds can be classified as drug-like and non-drug-like according to the Lipinski rule [50]. Physicochemical and pharmacokinetic properties of FP were obtained using the Swiss ADME free website <http://www.swissadme.ch/index.php> (Swiss Institute of Bioinformatics, Switzerland) [20]. ADMET (absorption, distribution, metabolism, elimination, toxicity) is an important part of drug discovery and provides information about the drug's behaviour in metabolism. ADMET properties of FP were obtained using the online ADMET database, <https://admetmesh.scbdd.com/service/screening/molecule> [51].

## Results and discussion

### Molecular geometry

Molecular geometry is defined as a three-dimensional arrangement of atoms in a molecule. According to the differences in the positions and orientations of the atoms, a lot of conformations can be determined for a compound. Each different conformation affects the energy of the molecule, its physical and chemical properties, its reactivity, and its interaction with other molecules [52]. The most stable optimized geometry of the FP at its minimum energy level obtained by DFT calculations is shown in Fig. 1.



**Fig. 1.** Molecular configuration of FP.

The selected parameters for structural analysis, namely bond lengths, bond angles, and dihedral bond angles for the gas phase and in the DMSO solution of FP are given in Table 1. The Cartesian coordinates of the atoms in the minimized structure in the gas phase are given in supplementary S1. There are slight differences between the calculation in the gas phase and DMSO, except for dihedral angle H19-N9-C8-O10 as it turns to a positive value for the “in DMSO” case from its negative value for the gas phase. The dihedral angles (C6-C2-C3-N9) is  $1(1)^\circ$  on average of the values obtained from both cases, while (C2-C6-N7-C8) is  $\sim 44.58(35)^\circ$  exhibiting a bent pyrimidine ring. The flat dihedral angle (C1-C2-C3-N9) is  $\sim 180^\circ$  showing that the (C6-C2-C3-N9) side of pyrimidine and furan rings are almost in the same plane while the angle  $\sim 162.89(1,18)^\circ$  of (N9-C8-N7-C11) indicates the separation of the FP tail from (C2-C6-N7-C8) plane of the pyrimidine ring.

**Table 1.** Theoretical bond lengths (Å), bond angles (°), and dihedral bond angles (°) of FP. Atom labels refer to Fig. 1.

| Bond Length (Å) |       |       | Bond Angles (°) |        |        | Dihedral Bond Angles (°) |         |         |
|-----------------|-------|-------|-----------------|--------|--------|--------------------------|---------|---------|
|                 | Gas   | DMSO  |                 | Gas    | DMSO   |                          | Gas     | DMSO    |
| C1-C2           | 1.354 | 1.354 | C1-C2-C3        | 105.97 | 106.06 | H16-C4-O5-C1             | -179.31 | -179.55 |
| C2-C3           | 1.423 | 1.423 | C3-C4-O5        | 108.75 | 108.53 | C1-C2-C3-C4              | -0.16   | -0.18   |
| C1-H15          | 1.076 | 1.076 | C3-C4-H16       | 134.58 | 134.48 | C2-C3-C4-O5              | -0.31   | -0.27   |
| C6-H18          | 1.086 | 1.085 | H16-C4-O5       | 116.65 | 116.99 | C4-C3-C2-C6              | 178.21  | 178.03  |
| C14-H20         | 1.089 | 1.088 | C4-O5-C1        | 107.53 | 107.68 | C6-C2-C3-N9              | -1.98   | -2.19   |
| C4-O5           | 1.371 | 1.373 | O5-C1-C2        | 116.17 | 109.99 | H19-N9-C8-O10            | -1.34   | 0.23    |
| C1-O5           | 1.364 | 1.364 | N7-C11-O12      | 122.17 | 122.19 | N9-C8-N7-C11             | -164.08 | -161.71 |
| C8-O10          | 1.209 | 1.218 | C11-O13-C14     | 115.19 | 115.61 | N9-C8-N7-C6              | 28.54   | 29.15   |
| C11-O12         | 1.210 | 1.215 | C2-C6-N7        | 108.62 | 108.49 | O10-C8-N7-C11            | 16.69   | 19.05   |
| C14-O13         | 1.438 | 1.444 | C6-N7-C8        | 120.75 | 120.65 | C8-N7-C11-O12            | -158.54 | -158.83 |
| C6-N7           | 1.484 | 1.488 | N7-C8-N9        | 114.16 | 114.78 | N7-C11-O13-C14           | -178.25 | -179.53 |
| C8-N7           | 1.420 | 1.419 | H19-N9-C3       | 121.91 | 121.24 | C11-O13-C14-H21          | 177.59  | 178.19  |
| C8-N9           | 1.382 | 1.370 | N9-C8-O10       | 121.14 | 121.29 | O12-C11-O13-C14          | 5.13    | 3.76    |
| C3-N9           | 1.389 | 1.391 | O10-C8-N7       | 124.69 | 123.92 | C1-C2-C3-N9              | 179.63  | 179.60  |
| C11-N7          | 1.399 | 1.395 | C8-N7-C11       | 122.81 | 122.89 | C2-C6-N7-C8              | -44.95  | -44.22  |
| N9-H19          | 1.009 | 1.009 | O12-C11-O13     | 124.75 | 124.35 | C6-C2-C3-N9              | -1.99   | -2.19   |

The charge distribution in the atoms in the molecule is important for determining the electrostatic interaction and molecular force fields [53,54]. The atomic charge distributions of the FP are obtained by Mulliken Population Analysis (MPA), and Natural Population Analysis (NPA) methods within the framework Gaussian 09, which are listed in Table 2. There are differences when comparing the calculated atomic charges in the two methods. The charges such as C1, C2, and C3 are given discrepant by the two methods. MPA(C1) is -0.116 and NPA(C1) is 0.154 with a change in the sign. C2 has the same issue. Other atoms, even though they show the same sign, they differ in magnitude; for example, MPA(C3) is 0.312, and NPA(C3) is 0.078. However, the two methods provide good agreement on the charges of some atoms, such as O5, C4, C11, and H16. Overall, the oxygen and nitrogen atoms in the molecule are negatively charged, while the hydrogen atoms are positively charged, as usual. Amongst the carbon atoms, the highest negative charge is located on C14, while the highest positive charge is located on C11. The carbon atoms have negative or positive charges with respect to the electronegative atoms around them.

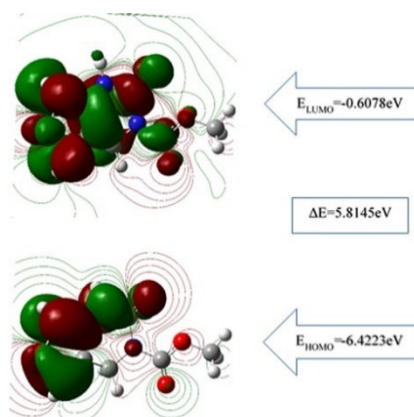
**Table 2.** Atomic charges of FP compound by Mulliken Population Analysis (MPA), and Natural Population Analysis (NPA) methods. Labels refer to Fig. 1.

| Atom | MPA    | NPA    | Atom | MPA    | NPA    |
|------|--------|--------|------|--------|--------|
| C1   | -0.116 | 0.154  | O13  | -0.318 | -0.533 |
| C2   | 0.549  | -0.147 | N7   | -0.343 | -0.564 |
| C3   | 0.312  | 0.078  | N9   | -0.509 | -0.616 |
| C4   | 0.055  | 0.082  | H15  | 0.181  | 0.200  |
| C6   | -0.963 | -0.176 | H16  | 0.180  | 0.200  |
| C8   | 0.559  | 0.843  | H17  | 0.161  | 0.205  |
| C11  | 0.713  | 0.968  | H18  | 0.212  | 0.244  |
| C14  | -0.121 | -0.200 | H19  | 0.275  | 0.412  |
| O5   | -0.366 | -0.455 | H20  | 0.164  | 0.186  |
| O10  | -0.458 | -0.608 | H21  | 0.145  | 0.187  |
| O12  | -0.468 | -0.644 | H22  | 0.157  | 0.184  |

The MPA and NPA methods obtain the results sensitively depending on their basis sets which induce change in the calculated net charges [54]. However, the results given by NPA are supposed to be more reliable as their calculations are based on the natural charges [55].

### Molecular orbital energy analysis and electronic properties

Quantum chemical parameters were calculated with FMO analysis, and the highest occupied molecular orbital energy ( $E_{\text{HOMO}}$ ), the lowest unoccupied molecular orbital energy ( $E_{\text{LUMO}}$ ) together with the energy gap ( $\Delta E = E_{\text{LUMO}} - E_{\text{HOMO}}$ ) given in Fig.2.  $\Delta E$  determines the molecular properties, namely softness and chemical reactivity [54,56-58]. In this respect, the  $\Delta E$  energy difference of the FP calculated using the B3LYP and the 6-311++G (2d, p) basis set was 5.81 eV as a single molecule ( 5.64 eV in DMSO) related to the dipole moments of FP molecule which were found  $\mu_{\text{gas}} = 1,92$  Debye and  $\mu_{\text{DMSO}} = 2,99$  Debye in the gas phase and iMSO, respectively. The dipole moments were obtained by the conformal minimization of the molecule. These values make FP a high enough polarized pyrimidine molecule as compared to that of 4.86 eV for 5-Fluorouracil, a commercial anticancer reagent [59].



**Fig. 2.**  $E_{\text{HOMO}}$  and  $E_{\text{LUMO}}$  energy levels for FP.

The calculations of  $E_{\text{HOMO}}$  and  $E_{\text{LUMO}}$  energy levels lead to automatic determination of ionization energy ( $I$ ) and electron affinity ( $A$ ) which are expressed as

$$I = -E_{\text{HOMO}} \quad (1)$$

and

$$A = -E_{\text{LUMO}} \quad (2)$$

As  $E_{\text{HOMO}}$  indicates the electron-donating ability while  $E_{\text{LUMO}}$  refers to the electron-accepting ability. Once reaching the concerning parameters above, some characterizing parameters such as electronegativity ( $\chi$ ), chemical hardness ( $\eta$ ), and softness ( $\sigma$ ) from the following relations:

$$\chi = \frac{I + A}{2} \quad (3)$$

$$\eta = \frac{I - A}{2} \quad (4)$$

and

$$\sigma = \frac{1}{\eta} \quad (5)$$

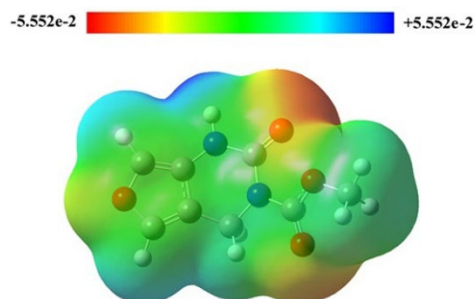
The molecular electronic properties of FP obtained are given in Table 3. The high electronegativity values  $\chi_{\text{gas}} = 3.51$  eV and  $\chi_{\text{DMSO}} = 3.53$  eV indicates the strong attraction to covalent bonds [34]. Also, the large chemical hardness  $\eta_{\text{gas}} = 2.91$  eV and  $\eta_{\text{DMSO}} = 2.82$  eV indicates chemical stability, and the molecule can be considered as nontoxic because of the low softness values  $\sigma_{\text{gas}} = 0.34$  eV<sup>-1</sup> and  $\sigma_{\text{DMSO}} = 0.35$  eV<sup>-1</sup>.

**Table 3.** Electronic structure values of FP.

| Phase | $E_{\text{HOMO}}$ (eV) | $E_{\text{LUMO}}$ (eV) | $\Delta E$ (eV) | $I$ (eV) | $A$ (eV) | $\chi$ (eV) | $\eta$ (eV) | $\sigma$ (eV <sup>-1</sup> ) |
|-------|------------------------|------------------------|-----------------|----------|----------|-------------|-------------|------------------------------|
| gas   | -6.42                  | -0.61                  | 5.81            | 6.42     | 0.61     | 3.51        | 2.91        | 0.34                         |
| DMSO  | -6.36                  | -0.71                  | 5.64            | 6.36     | 0.71     | 3.53        | 2.82        | 0.35                         |

### Molecular electrostatic potential

The molecular electrostatic potential of FP was calculated and shown in Fig. 3. It shows the positively charged parts of the molecule in blue colour and the negatively charged parts in red colour [60-62].



**Fig. 3.** Molecular electrostatic potential for FP.

As MEP allows us to have insight into the chemical reactivity of a molecule, the highest negative charge  $-0.059$  region by red shade in Fig.3 is the electrophilic region. The negative electrostatic potential indicates the concentrated electron density in the molecule interacting with the receptors and forming hydrogen bonds with the positive sites of amino acids. They correspond to the tops of two carbonyls. The highest positive charge  $+0.059$  region by blue shade is the nucleophilic region which corresponds to the hydrogen in the N-H bond. The green area can be considered almost a neutral region.

#### Experimental and theoretical $^{13}\text{C}$ NMR and $^1\text{H}$ NMR chemical shift values

Experimental and theoretical  $^1\text{H}$  NMR and  $^{13}\text{C}$  NMR chemical shift values of FP are listed in Table 4 according to TMS  $\delta/\text{ppm}$ . The experimental NMR values were taken in DMSO [19], and theoretical NMR data were calculated in the gas phase and DMSO phase. In the FP structure, there are five different hydrogens attached to aliphatic and aromatic carbons and amine-bound, and all H peaks were observed as a singlet. In addition, eight different carbon peaks were found in the aliphatic, aromatic, and carbonyl structures.

When discussing the  $^1\text{H}$  NMR spectra of the FP, the experimental chemical shift values of the protons-bound aliphatic carbons were observed as a singlet in a value, while the theoretical chemical shift values were seen as two different peaks. The experimental value of the ring protons,  $\text{CH}_2$  was at 4.71 ppm as a singlet, while the theoretical values of H17 and H18 were 4.50 and 5.19 ppm, respectively. Ester protons,  $\text{CH}_3$  experimental value was in the 3.78 ppm as a singlet, while the theoretical values of H21 and H20, H22 were in 3.72 and 3.87 ppm, respectively. The experimental value of amine proton was 9.96 ppm as a broad singlet, whereas the theoretical value of H19 was 6.42 ppm. The experimental values of aromatic ring protons were at 7.27 and 7.46 ppm, whereas the theoretical values of H15 and H16 were at 7.31 and 7.37 ppm, respectively.

**Table 4.** The experimental and theoretical  $^1\text{H}$  NMR and  $^{13}\text{C}$  NMR chemical shift values of FP according to TMS  $\delta/\text{ppm}$ . (s.: singlet, br.: broad Assign.: assignments) The hydrogen and carbon labels can be followed in Fig. 1.

| $^1\text{H}$ NMR |                      |             |           |      |
|------------------|----------------------|-------------|-----------|------|
| Experimental     |                      | Theoretical |           |      |
| Assign.          | $\delta(\text{ppm})$ | Assign.     | Gas phase | DMSO |
| $\text{CH}_3$    | 3,73 (s)             | H21         | 3.56      | 3.72 |
|                  |                      | H20, H22    | 3.83      | 3.87 |
| $\text{CH}_2$    | 4.71 (s)             | H17         | 4.34      | 4.50 |
|                  |                      | H18         | 5.14      | 5.19 |
| NH               | 9.96 (br. s)         | H19         | 5.75      | 6.42 |
| CH (arom.)       | 7.27 (s)             | H15         | 7.05      | 7.31 |
| CH (arom.)       | 7.46 (s)             | H16         | 7.12      | 7.37 |



| <sup>13</sup> C NMR |        |             |           |        |
|---------------------|--------|-------------|-----------|--------|
| Experimental        |        | Theoretical |           |        |
| Assign.             | δ(ppm) | Assign.     | Gas phase | DMSO   |
| CH <sub>2</sub>     | 29.74  | C6          | 43.24     | 44.06  |
| CH <sub>3</sub>     | 54.28  | C14         | 54.87     | 55.95  |
| C(arom.)            | 111.13 | C2          | 117.37    | 117.28 |
| CH(arom.)           | 124.88 | C4          | 126.54    | 129.19 |
| C(arom.)            | 126.17 | C3          | 132.70    | 131.85 |
| CH(arom.)           | 136.96 | C1          | 140.50    | 141.87 |
| C=O                 | 150.05 | C8          | 153.01    | 156.06 |
| C=O                 | 155.32 | C11         | 162.07    | 163.40 |

Considering the <sup>13</sup>C NMR spectra of the FP, the experimental values of the aliphatic ring (CH<sub>2</sub>) and ester methyl carbon peaks (CH<sub>3</sub>) were at 29.74 and 54.28 ppm, whereas the theoretical values of C6 and C14 were at 44.06 and 55.95 ppm, respectively. The aromatic carbons' experimental values were 111.13, 124.88, 126.17, and 136.96 ppm, whereas theoretical values of C2, C4, C3, and C1 were 117.28, 129.18, 131.85, and 141.87, respectively. The experimental values of ring carbonyl carbon and aliphatic carbonyl carbon were at 150.05 and 155.32 ppm, while theoretical values of C8 and C11 were at 156.06 and 163.40 ppm, respectively. According to the NMR results, the experimental and theoretical chemical shift values are compatible. The theoretical and experimental NMR spectra were given in the supplementary (S2-S5).

#### Experimental and theoretical vibration frequencies

The molecular structure of FP contains twenty-two atoms, which gives forty-four normal modes of vibrations. While experimental vibration values were taken from the literature [19], theoretical vibration values were calculated using the DFT/B3LYP method and 6-311++G (2d, p) basis set. The FTIR spectrum was analyzed based on characteristic peaks such as amine, aromatic, carbonyl, and CH<sub>2</sub> vibrations. The experimental and theoretical values of the vibrational wavenumber of FP are shown in Fig. 4. For analysis, all the calculated FTIR, compared to experimental values, and details of the percentage of potential energy distribution (PED) assignment are listed in Table 5. When performing PED assignments, it was found that there were thirty-four stretching vibrations, thirty-six in-plane bending vibrations, four out of plane bending vibrations, and eighteen torsional vibrations. When the experimental and theoretical values were compared, they were found to be well-matched.

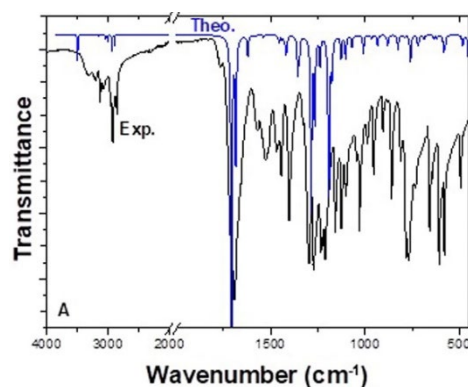


Fig. 4. Experimental and theoretical FTIR spectrum of FP (cm<sup>-1</sup>).

**Table 5.** Experimental and theoretical FTIR values of FP (cm<sup>-1</sup>).

| No | Experimental | Theoretical |        | Vibration assignment (PED)                                                                                |
|----|--------------|-------------|--------|-----------------------------------------------------------------------------------------------------------|
|    |              | Unscaled    | Scaled |                                                                                                           |
| 1  | 3321         | 3633        | 3492   | νN9-H19 (100)                                                                                             |
| 2  | 3071         | 3282        | 3155   | νC4-H16 (95)                                                                                              |
| 3  | 3048         | 3271        | 3144   | νC1-H15 (95)                                                                                              |
| 4  |              | 3158        | 3036   | νC14-H21 (80), νC14-H20 (19), νC14-H22 (19)                                                               |
| 5  |              | 3137        | 3016   | νC6-H18 (98)                                                                                              |
| 6  | 2980         | 3127        | 3006   | νC14-H20, νC14-H22 (100)                                                                                  |
| 7  |              | 3054        | 2936   | νC14-H20, νC14-H21 (80)                                                                                   |
| 8  | 2925         | 3010        | 2894   | νC6-H17 (98)                                                                                              |
| 9  | 1694         | 1777        | 1708   | νC8-O10 (77)                                                                                              |
| 10 | 1686         | 1752        | 1684   | νC11-O12 (81)                                                                                             |
| 11 | 1571         | 1686        | 1621   | νC1-C2, νC3-C4 (76)                                                                                       |
| 12 | 1528         | 1599        | 1537   | νC1-C2 (52), νC3-N9 (52) δH15-C1-O5 (12), δH16-C4-O5 (12), δC1-O5-C4 (11), δC3-C4-O5 (11)                 |
| 13 | 1465         | 1513        | 1454   | δH18-C6-H17 (74), τH18-C6-C2-C1 (12)                                                                      |
| 14 | 1458         | 1497        | 1439   | δH20-C14-H22 (70), τH20-C14-O13-C11 (21), τH22-C14-O13-C11(21)                                            |
| 15 | 1440         | 1485        | 1428   | δH21-C14-H20 (38), δH22-C14-H21 (35), τH21-C14-O13-C11 (15), τH20-C14-O13-C11 (10), τH22-C14-O13-C11 (10) |
| 16 | 1406         | 1469        | 1412   | δH19-N9-C3, δC2-C1-O5 (44)                                                                                |
| 17 | 1326         | 1411        | 1356   | δC6-N7-C8 (14)                                                                                            |
| 18 | 1301         | 1402        | 1348   | νC3-C4, νC3-N9 (24)                                                                                       |
| 19 | 1293         | 1337        | 1285   | νC11-N7 (44), νC11-O13 (44), δH17-C6-C2 (10)                                                              |
| 20 | 1270         | 1289        | 1239   | νC8-N9 (10)                                                                                               |
| 21 | 1234         | 1244        | 1196   | δH16-C4-O5, δH15-C1-O5 (67)                                                                               |
| 22 | 1205         | 1224        | 1177   | δC8-N7-C11, δN9-C8-O10, δC3-N9-C8, δO12-C11-O13, δC3-C4-O5 (15)                                           |
| 23 | 1159         | 1172        | 1127   | νC1-O5, νC6-N7 (54)                                                                                       |

|    |      |      |      |                                                                                        |
|----|------|------|------|----------------------------------------------------------------------------------------|
| 24 | 1128 | 1147 | 1103 | $\nu$ C1-O5, $\nu$ C4-O5, $\nu$ C6-N7 (61)                                             |
| 25 | 1100 | 1112 | 1069 | $\nu$ C11-N7 (22), $\nu$ C11-O13 (22), $\nu$ C14-O13 (11)                              |
| 26 | 1040 | 1049 | 1008 | $\nu$ C1-O5, $\nu$ C4-O5 (64)                                                          |
| 27 | 985  | 1005 | 966  | $\tau$ H17-C6-C2-C1 (26)                                                               |
| 28 | 951  | 916  | 881  | $\delta$ C1-O5-C4, $\delta$ N7-C8-N9 (44)                                              |
| 29 | 902  | 858  | 825  | $\delta$ C3-C4-O5, $\delta$ N9-C8-O10, $\delta$ N7-C8-N9 (76)                          |
| 30 | 859  | 822  | 790  | $\delta$ O12-C11-O13, $\delta$ C11-O13-C14, $\delta$ C3-N9-C8 (41)                     |
| 31 | 781  | 790  | 759  | $\tau$ H15-C1-O5-C4 (57), $\tau$ C1-O5-C4-C3 (11), $\gamma$ O12-N7-O13-C11 (66)        |
| 32 | 766  | 749  | 720  | $\gamma$ O10-N9-N7-C8 (85)                                                             |
| 33 | 724  | 743  | 714  | $\nu$ C8-N7 (12), $\tau$ C6-N7-C8-N9 (10)                                              |
| 34 | 660  | 715  | 687  | $\tau$ H16-C4-O5-C1 (45), $\tau$ C2-C1-O5-C4 (18), $\tau$ C1-O5-C4-C3 (18)             |
| 35 | 608  | 606  | 583  | $\delta$ C3-N9-C8, $\delta$ O12-C11-O13, $\delta$ N9-C8-O10 (35)                       |
| 36 | 580  | 502  | 483  | $\tau$ H19-N9-C3-C2 (30)                                                               |
| 37 | 489  | 435  | 418  | $\delta$ N7-C11-O13, $\delta$ N9-C8-O10, $\delta$ O12-C11-O13, $\delta$ C8-N7-C11 (49) |
| 38 |      | 334  | 321  | $\gamma$ N9-C2-C4-C3 (23)                                                              |
| 39 |      | 324  | 311  | $\delta$ C11-O13-C14, $\delta$ C8-N7-C11 (60)                                          |
| 40 |      | 296  | 285  | $\tau$ N7-C8-N9-C3 (10)                                                                |
| 41 |      | 257  | 247  | $\delta$ C8-N7-C11, $\delta$ C11-O13-C14, $\delta$ N7-C11-O13, $\delta$ N7-C8-N9 (10)  |
| 42 |      | 222  | 213  | $\tau$ C8-N9-C3-C2 (34), $\tau$ C14-O13-C11-N7 (11)                                    |
| 43 |      | 169  | 162  | $\gamma$ C11-C6-C8-N7 (17)                                                             |
| 44 |      | 62   | 60   | $\tau$ O13-C11-N7-C6 (71)                                                              |

### NH vibrations

The stretching vibrations of the amide NH bond were observed around 3300-3600  $\text{cm}^{-1}$  [62,63]. In FP, N9-H19 stretching vibration was theoretically observed at 3492  $\text{cm}^{-1}$  with PED contribution is 100 % and experimentally at 3321  $\text{cm}^{-1}$  as a strong peak. Furthermore, H19-N9-C3 in-plane bending vibration was observed theoretically at 1412  $\text{cm}^{-1}$  and experimentally at 1406  $\text{cm}^{-1}$ . The H19-N9-C3-C2 torsional vibration was observed theoretically at 483  $\text{cm}^{-1}$  and experimentally at 580  $\text{cm}^{-1}$ .

### Aromatic CH vibrations

Aromatic CH bond stretching vibrations are usually just over 3000  $\text{cm}^{-1}$  [63,64]. There are two different aromatic CH in the FP structure, and their vibrational values were very close. C4-H16 and C1-H15

stretching vibrations were theoretically observed at 3144  $\text{cm}^{-1}$  and 3157  $\text{cm}^{-1}$ , and experimentally at 3193  $\text{cm}^{-1}$  and 3139  $\text{cm}^{-1}$ , respectively. H16-C4-O5 and H15-C1-O5 in-plane bending vibrations had the same value and two vibrations; theoretically observed at 1537  $\text{cm}^{-1}$  and 1196  $\text{cm}^{-1}$ , experimentally at 1528  $\text{cm}^{-1}$  and 1234  $\text{cm}^{-1}$ . Moreover, H15-C1-O5-C4 and H16-C4-O5-C1 torsional vibrations were observed theoretically at 759  $\text{cm}^{-1}$  and 687  $\text{cm}^{-1}$  experimentally at 781  $\text{cm}^{-1}$  and 660  $\text{cm}^{-1}$ , respectively.

### Carbonyl vibrations

Depending on the electronegative atoms attached to the carbonyl group, the carbonyl group gives a stretching vibration in the range of 1650-1800  $\text{cm}^{-1}$  [62,63]. There are two different carbonyl groups located between nitrogen-nitrogen and oxygen-nitrogen in the FP structure. The carbonyl group (C8-O10) located between nitrogen and nitrogen in the ring structure gave a higher frequency peak than the other (C11-O12). While C8-O10 and C11-O12 stretching frequency were observed theoretically at 1708 and 1684  $\text{cm}^{-1}$ , experimentally at 1694 and 1686  $\text{cm}^{-1}$ , respectively. In addition, N9-C8-O10 in-plane bending vibrations were theoretically observed at 1177, 825, 583, 418  $\text{cm}^{-1}$ , and experimentally at 1205, 902, 608, 489  $\text{cm}^{-1}$ .

### CH<sub>2</sub> vibrations

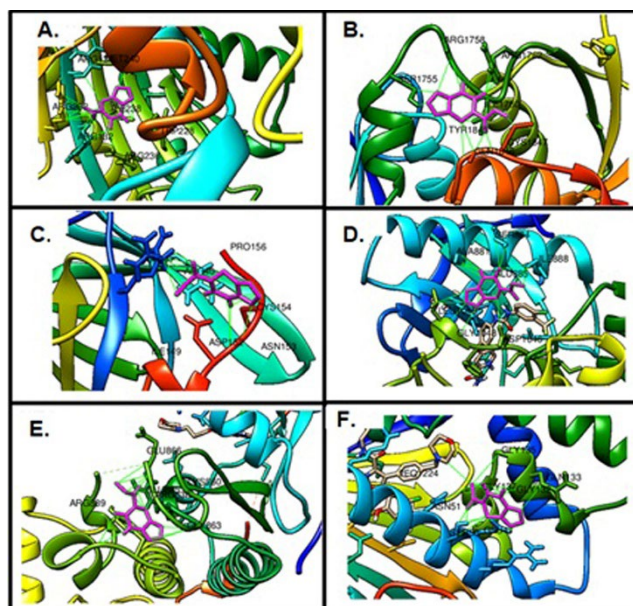
The characteristic vibration of the CH<sub>2</sub> is the stretching vibration in the range of 2900-3000  $\text{cm}^{-1}$  and the in-plane bending vibration around 1450  $\text{cm}^{-1}$  [65]. The C6-H18 and C6-H17 stretching vibrations were observed theoretically at 3016 and 2894  $\text{cm}^{-1}$ , respectively, and experimentally at 2925  $\text{cm}^{-1}$ . H18-C6-H17 in-plane bending vibration was observed theoretically at 1454  $\text{cm}^{-1}$  and experimentally at 1465  $\text{cm}^{-1}$ .

### Molecular docking

Molecular docking calculations are used to gain information about ligand-receptor interactions and play an important role in drug discovery. As a result of these calculations, it can be found out which region of the protein the ligand binds to, what kind of interactions it makes, and their binding energies [54,60,66,67]. In this study, molecular docking calculations with the brain (PDB ID: 1QHT), breast (PDB ID: 1JNX), gastric (PDB ID: 1BJ7), liver (PDB ID: 3WZE), lung (PDB ID: 2ITO), and skin (PDB ID: 2VCJ) cancer proteins to see the biological potential of FP were examined. Many docking studies were carried out and the lowest energies interaction was selected. The calculated lowest binding energies of the target biomolecules and FP are given in Table 6. In addition, FP makes more stable interactions with brain and liver cancer cells than others. The binding sites of FP with target biomolecules are shown in Figure 5. Looking at the structure of the FP compound, it is seen that it is an active compound-containing pyrimidine ring, furan ring, and ester. When calculated results are examined, FP makes hydrophobic interactions with ARG130, ARG132, TRP228, ARG236, ILE238, MET240, ARG292 amino acids in brain cancer protein, SER1755, ARG1758, LYS1759, ILE1760, ARG1762, TYR1845, GLN1846, CYS1847 amino acids in breast cancer protein, ARG40, ILE149, ASP152, ASN153, CYS154, PRO156 amino acids in gastric cancer protein, HIS816, LYS868, ALA881, SER884, GLU885, ILE888, ARG1027, ASP1046, GLY1048, LEU1049, BAX1201 amino acids in liver cancer protein, SER 719, ALA722, PHE723, VAL726, LYS745, ARG841, LEU844, ASP855, IRE2020 amino acids in lung cancer protein, ARG46, GLU47, SER50, ASN51, GLY132, GLN133, GLY135, GLY137 amino acids in skin cancer protein.

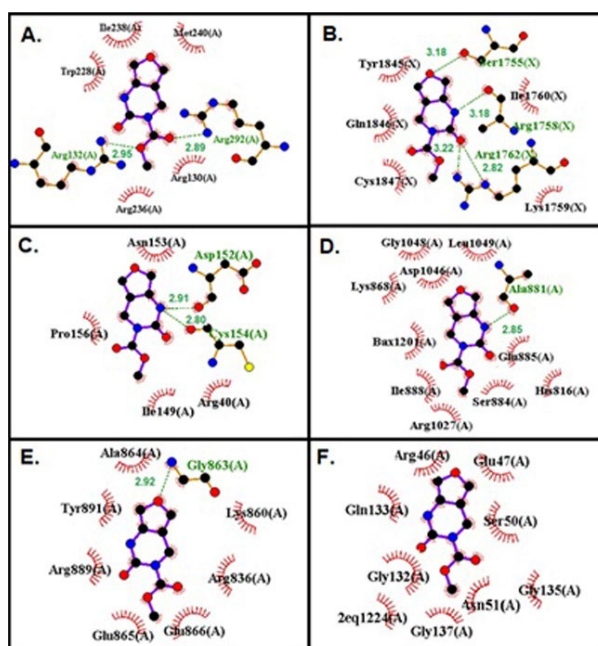
**Table 6.** The binding energies of FP and target biomolecules.

| Protein (PDB ID) | Types of cancer | Binding energy (kcal/mol) |
|------------------|-----------------|---------------------------|
| 1QH4             | Brain cancer    | -6.1                      |
| 1JNX             | Breast cancer   | -4.9                      |
| 1BJ7             | Gastric cancer  | -4.4                      |
| 3WZE             | Liver cancer    | -6.1                      |
| 2ITO             | Lung cancer     | -5.9                      |
| 2VCJ             | Skin cancer     | -4.8                      |



**Fig. 5.** The binding site of FP on target proteins, (A) Brain cancer protein, (B) Breast cancer protein, (C) Gastric cancer protein, (D) Liver cancer protein, (E) Lung cancer protein, (F) Skin cancer protein.

H bonds are strong interactions that hold molecules together and the number of the H bonds gives information about the strength of the interaction. The H bond interactions between FP and targeted biomolecules are given in Fig. 6. Also, the number of H bonds made by FP with each biomolecule and the atoms forming the H bond are listed in Table 7.



**Fig. 6.** The H bond interactions between FP and target proteins, (A) Brain cancer protein, (B) Breast cancer protein, (C) Gastric cancer protein, (D) Liver cancer protein, (E) Lung cancer protein, (F) Skin cancer protein.

**Table 7.** Summary of hydrogen bonding of fuopyrimidine molecule with different types of biomolecule targets.

| Protein (PDB ID) | Number of H bond | Bonded residues    |               | Bond distance (Å) |
|------------------|------------------|--------------------|---------------|-------------------|
| 1QH4             | 2                | Protein ARG292:HN  | Ligand: O12   | 2.89              |
|                  |                  | Protein ARG132:HN  | Ligand:O13    | 2.95              |
| 1JNX             | 4                | Protein SER1755:OH | Ligand: O5    | 3.18              |
|                  |                  | Protein ARG1758:O  | Ligand: N9H19 | 3.18              |
|                  |                  | Protein ARG1762:HN | Ligand: O12   | 2.82              |
|                  |                  | Protein ARG1762:HN | Ligand: O12   | 3.22              |
| 1BJ7             | 2                | Protein ASP152:O   | Ligand: N9H19 | 2.91              |
|                  |                  | Protein CYS154:O   | Ligand: N9H19 | 2.80              |
| 3WZE             | 1                | Protein ALA881:O   | Ligand: N9H19 | 2.85              |
| 2ITO             | 1                | Protein LYS745:NH  | Ligand: O12   | 3.21              |
| 2VCJ             | -                | -                  | -             | -                 |

When it is examined in this study, FP makes two H bonds with ARG 132, ARG 292 amino acids in brain cancer protein, it makes four H bonds with SER1755, ARG1758, ARG1752 amino acids in breast cancer protein, it makes two H bonds with ASP152, CYS 154 amino acids in gastric cancer protein, it makes one H bond with ALA881 amino acid liver cancer protein, it makes one H bond with GLY863 amino acid in liver cancer protein, it doesn't make H bond with an amino acid in skin cancer protein, and it makes two H bond with DA5.

When the H bonds were examined, it was seen that N9 in the FP structure is the H bond donor, and O5, O12, and O13 are H bond acceptors. It can be said that N9 and O12 atoms in the FP structure are the most active ones in forming H bonds.

### Evaluation of pharmacokinetics and drug-likeness properties of FP

By evaluating the pharmacokinetic properties, toxicity, and bioavailability of the compounds, their usage or development as a drug can be achieved [68-70]. As shown in Table 8, FP follows the Lipinski Rule, Pfizer Rule, and GlaxoSmithKline Rule as a drug candidate. According to the ADME result, FP has a high GI (gastrointestinal) absorption value, which means that the drug is rapidly absorbed.

The molecular weight of FP being 196.16 g/mol and having 2 rotatable bonds indicate the conformity of the molecule. The number of hydrogen bond acceptors and donors is within the expected range, which indicates that they can interact strongly enough. Log P is a measure of the hydrophilicity and hydrophobicity of a molecule. The log P value of FP is compatible with the Lipinski rule. The topological polar surface area (TPSA) value of FP 71.78Å<sup>2</sup> indicates that they have good permeability during the cellular plasma membrane and blood-brain barrier.

**Table 8.** Data of Lipinski rule, Pharmacokinetics, and Drug likeness.

| Mw     | NBR | HBA | HBD | TPSA/A2 (≤140) | Consensus Log Po/w | Bioavailability Score | GI abs. |
|--------|-----|-----|-----|----------------|--------------------|-----------------------|---------|
| 196,16 | 2   | 4   | 1   | 71.78          | 0.21               | 0.55                  | high    |

Mw: Molecular weight, NBR: Number of rotatable bonds, HBA: Number of Hydrogen bond acceptors, HBD: Number of Hydrogen bond donors, TPSA: Topological polar surface area, Consensus Log Po/w: Log Poctane/water, GI: Gastrointestinal.

The ADMET data of the FP which is computationally forecasted from its given molecular structure are shown in Table 9. It is exhibited that the FP has oral bioavailability, and is rapidly absorbed in the human intestine. Also, FP does not show skin sensitivities, AMES toxicity, and respiratory toxicity. The FP is not a P-glycoprotein inhibitor or substrate. Since P-glycoprotein pumps drugs back into the lumen, reducing drug absorption, it can be said that the bioavailability and bioactivity of the FP are high. A summary of the ADMET properties of FP is shown in Fig. 7.

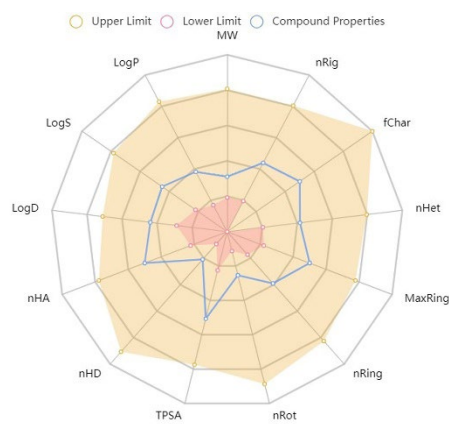


Fig. 7. Radar chart involved in ADMET properties of FP.

Table 9. Pharmacokinetics and ADMET Data.

|                                    |      |                                                              |     |
|------------------------------------|------|--------------------------------------------------------------|-----|
| <b>Lipinski Rule</b>               | yes  | <b>Respiratory toxicity</b>                                  | no  |
| <b>Pfizer Rule</b>                 | yes  | <b>P-glycoprotein inhibitor</b>                              | no  |
| <b>GlaxoSmithKline Rule</b>        | yes  | <b>P-glycoprotein substrate</b>                              | no  |
| <b>Human Intestinal Absorption</b> | high | <b>Solubility</b>                                            | yes |
| <b>AMES toxicity</b>               | no   | <b>hERG (the human Ether-à-go-go-Related Gene) inhibitor</b> | no  |
| <b>Skin sensitization</b>          | no   |                                                              |     |

## Conclusions

In this study, the FP geometry was optimized using the B3LYP/6-311G++ (2d, p) method within density functional theory. The bond lengths, bond angles, dihedral angles, MEP, dipole moments, HOMO, and LUMO of FP were obtained with the Gaussian G09w program. Theoretical FTIR and NMR spectrum values were found to be compatible with the experimental spectrum values. Due to the wide biological activities of pyrimidine compounds, molecular docking studies of FP were carried out with various biomolecules. As a result of molecular docking studies, it was determined that N9 and O12 atoms of FP were the most active ones, and they make hydrogen bonds and hydrophobic interactions with biomolecules. Data on the pharmacokinetic and drug-likeness of FP was observed. For future studies, the synthesis of new dihydrofuro [3,4-d] pyrimidine derivatives may be desirable and could be a source of similar studies to determine their mechanisms as potential anticancer agents.

## References

1. Abdel-Aziz, S. A.; Taher, E. S.; Lan, P.; Asaad, G. F.; Gomaa, H. A.; El-Koussi, N. A.; Youssif, B. G. *Bioorg. Chem.* **2021**, *111*, 104890. DOI: <https://doi.org/10.1016/j.bioorg.2021.104890>.
2. Aksinenko, A. Y.; Goreva, T. V.; Epishina, T. A.; Trepalin, S. V.; Sokolov, V. B. *J. Fluor. Chem.* **2016**, *188*, 191-195. DOI: <https://doi.org/10.1016/j.jfluchem.2016.06.019>.
3. Ballesteros-Casallas, A.; Paulino, M.; Vidossich, P.; Melo, C.; Jiménez, E.; Castillo, J.-C.; Portilla, J.; Miscione, G. P. *Eur. J. Med. Chem.* **2022**, *4*, 100028. DOI: <https://doi.org/10.1016/j.ejmcr.2021.100028>.
4. Basyouni, W. M.; Abbas, S. Y.; El-Bayouki, K. A.; Dawood, R. M.; El Awady, M. K.; Abdelhafez, T. H. *J. Heterocycl. Chem.* **2021**, *58*, 1766-1774. DOI: <https://doi.org/10.1002/jhet.4307>.
5. Elkanzi, N. A. A. *Orient. J. Chem.* **2020**, *36*, 1001-1015. DOI: <http://dx.doi.org/10.13005/ojc/360602>.
6. Ali, F.; Khan, K. M.; Salar, U.; Iqbal, S.; Taha, M.; Ismail, N. H.; Perveen, S.; Wadood, A.; Ghufuran, M.; Ali, B. *Bioorg. Med. Chem.* **2016**, *24*, 3624-3635. DOI: <https://doi.org/10.1016/j.bmc.2016.06.002>.
7. Katariya, K. D.; Reddy, D. V. *J. Mol. Struct.* **2022**, *1253*, 132240. DOI: <https://doi.org/10.1016/j.molstruc.2021.132240>.
8. Lamie, P. F.; Philoppes, J. N. *Bioorg. Chem.* **2021**, *116*, 105335. DOI: <https://doi.org/10.1016/j.bioorg.2021.105335>.
9. Manzoor, S.; Prajapati, S. K.; Majumdar, S.; Raza, M. K.; Gabr, M. T.; Kumar, S.; Pal, K.; Rashid, H.; Kumar, S.; Krishnamurthy, S. *Eur. J. Med. Chem.* **2021**, *215*, 113224. DOI: <https://doi.org/10.1016/j.ejmech.2021.113224>.
10. Raju, K. S.; AnkiReddy, S.; Sabitha, G.; Krishna, V. S.; Sriram, D.; Reddy, K. B.; Sagurthi, S. R. *Bioorg. Med. Chem. Lett.* **2019**, *29*, 284-290. DOI: <https://doi.org/10.1016/j.bmcl.2018.11.036>.
11. Fei, X.; Wang, J.-Q.; Miller, K. D.; Sledge, G. W.; Hutchins, G. D.; Zheng, Q.-H. *Nucl. Med. Biol.* **2004**, *31*, 1033-1041. DOI: <https://doi.org/10.1016/j.nucmedbio.2004.02.006>.
12. Scappini, B.; Gianfaldoni, G.; Caracciolo, F.; Mannelli, F.; Biagiotti, C.; Romani, C.; Pogliani, E. M.; Simonetti, F.; Borin, L.; Fanci, R. *Am. J. Hematol.* **2012**, *87*, 1047-1051. DOI: <https://doi.org/10.1002/ajh.23308>.
13. Halbrook, C. J.; Pontious, C.; Kovalenko, I.; Lapienyte, L.; Dreyer, S.; Lee, H.-J.; Thurston, G.; Zhang, Y.; Lazarus, J.; Sajjakulnukit, P. *Cell Metab.* **2019**, *29*, 1390-1399. DOI: <https://doi.org/10.1016/j.cmet.2019.02.001>.
14. Verissimo, L. M.; Cabral, I.; Cabral, A. M.; Utzeri, G.; Veiga, F. J.; Valente, A. J.; Ribeiro, A. C. *J. Chem. Thermodyn.* **2021**, *161*, 106533. DOI: <https://doi.org/10.1016/j.jct.2021.106533>.
15. Abd El-Mageed, M. M.; Eissa, A. A.; Farag, A. E.-S.; Osman, E. E. A. *Bioorg. Chem.* **2021**, *116*, 105336. DOI: <https://doi.org/10.1016/j.bioorg.2021.105336>.
16. Gregorić, T.; Sedić, M.; Grbčić, P.; Paravić, A. T.; Pavelić, S. K.; Cetina, M.; Vianello, R.; Raić-Malić, S. *Eur. J. Med. Chem.* **2017**, *125*, 1247-1267. DOI: <https://doi.org/10.1016/j.ejmech.2016.11.028>.
17. Hossam, M.; Lasheen, D. S.; Ismail, N. S.; Esmat, A.; Mansour, A. M.; Singab, A. N. B.; Abouzid, K. A. *Eur. J. Med. Chem.* **2018**, *144*, 330-348. DOI: <https://doi.org/10.1016/j.ejmech.2017.12.022>.
18. Frisch, M. J.; Trucks, G. W.; Schlegel, H. B.; Scuseria, G. E.; Robb, M. A.; Cheeseman, J. R.; Scalmani, G.; Barone, V.; Mennucci, B.; Petersson, G. A.; Nakatsuji, H.; Caricato, M.; Li, X.; Hratchian, H. P.; Izmaylov, A. F.; Bloino, J.; Zheng, G.; Sonnenberg, J. L.; Hada, M.; Ehara, M.; Toyota, K.; Fukuda, R.; Hasegawa, J.; Ishida, M.; Nakajima, T.; Honda, Y.; Kitao, O.; Nakai, H.; Vreven, T.; Montgomery, J. A.; Peralta, J. E.; Ogliaro, F.; Bearpark, M.; Heyd, J. J.; Brothers, E.; Kudin, K. N.; Staroverov, V. N.; Kobayashi, R.; Normand, J.; Raghavachari, K.; Rendell, A.; Burant, J. C.; Iyengar, S. S.; Tomasi, J.; Cossi, M.; Rega, N.; Millam, J. M.; Klene, M.; Knox, J. E.; Cross, J. B.; Bakken, V.; Adamo, C.; Jaramillo, J.; Gomperts, R.; Stratmann, R. E.; Yazyev, O.; Austin, A. J.; Cammi, R.; Pomelli, C.; Ochterski, J. W.; Martin, R. L.; Morokuma, K.; Zakrzewski, V. G.; Voth, G.



- A.; Salvador, P.; Dannenberg, J. J.; Dapprich, S.; Daniels, A. D.; Farkas, Foresman, J. B.; Ortiz, J. V.; Cioslowski, J.; Fox, D. J., Gaussian 09, Revision B.01, Gaussian Inc., Wallingford CT, 2009.
19. Yılmaz, A. Ş.; Kaçan, M. *Tetrahedron*. 2017, 73, 4509-4512. DOI: <https://doi.org/10.1016/j.tet.2017.05.072>.
20. Daina, A.; Michielin, O.; Zoete, V. *Sci Rep*. 2017, 7, 42717. DOI: <https://doi.org/10.1038/srep42717>.
21. Yang, H.; Lou, C.; Sun, L.; Li, J.; Cai, Y.; Wang, Z.; Li, W.; Liu, G.; Tang, Y. *Bioinformatics*. 2018, 35, 1067-1069. DOI: <https://doi.org/10.1093/bioinformatics/bty707>.
22. Qu, R.; Zhang, X.; Zhang, Q.; Yang, X.; Wang, Z.; Wang, L. *Spectrochim. Acta A Mol. Biomol. Spectrosc.* 2011, 81, 261-269. DOI: <https://doi.org/10.1016/j.saa.2011.06.008>.
23. Manikandan, D.; Swaminathan, J.; Tagore, S. S.; Gomathi, S.; Sabarinathan, N.; Ramalingam, M.; Balasubramani, K.; Sethuraman, V. *Spectrochim. Acta A Mol. Biomol. Spectrosc.* 2020, 239, 118484. DOI: <https://doi.org/10.1016/j.saa.2020.118484>.
24. Foresman, J.; Frish, E. in: *Exploring Chemistry with Electronic Structure Methods*, Gaussian Inc., Pittsburg, USA, 1996.
25. Sayin, K.; Karakaş, D. *Spectrochim. Acta A Mol. Biomol. Spectrosc.* 2015, 144, 176-182. DOI: <https://doi.org/10.1016/j.saa.2015.02.086>.
26. Uluçam, G.; Okan, Ş. E.; Aktaş, Ş.; Yentürk, B. *J. Mol. Struct.* 2021, 1230, 129941. DOI: <https://doi.org/10.1016/j.molstruc.2021.129941>.
27. Dennington, R.; Keith, T.; Millam, J. Gauss View, Version 5. Semichem Inc., Shawnee Mission, 2009.
28. Zhen, Y.; Shan, X.; Li, Y.; Lin, Z.; Zhang, L.; Lai, C.; Qin, F. *Phytomed. Plus*. 2022, 100244. DOI: <https://doi.org/10.1016/j.phyplu.2022.100244>.
29. Yadav, V.; Krishnan, A.; Baig, M. S.; Majeed, M.; Nayak, M.; Vohora, D. *Biophys. Chem.* 2022, 285. DOI: <https://doi.org/10.1016/j.bpc.2022.106808>.
30. Anju, K.; Shoba, G.; Sumita, A.; Balakumaran, M. D.; Vasanthi, R.; Kumaran, R. *Spectrochim. Acta, Part A*. 2021, 258, 119814. DOI: <https://doi.org/10.1016/j.saa.2021.119814>.
31. Crampon, K.; Giorkallos, A.; Deldossi, M.; Baud, S.; Steffanel, L. A. *Drug Discovery Today*. 2021, 151-164. DOI: <https://doi.org/10.1016/j.drudis.2021.09.007>.
32. Trott, O.; Olson, A. J. *J. Comput. Chem.* 2010, 31, 455-461. DOI: <https://doi.org/10.1002/jcc.21334>.
33. Morris, G. M.; Huey, R.; Lindstrom, W.; Sanner, M. F.; Belew, R. K.; Goodsell, D. S.; Olson, A. J. *J. Comput. Chem.* 2009, 30, 2785-2791. DOI: <https://doi.org/10.1002/jcc.21256>.
34. Fatima, A.; Khanum, G.; Sharma, A.; Verma, I.; Arora, H.; Siddiqui, N.; Javed, S. *Polycycl. Aromat. Compd.* 2023, 43, 1263-1287. DOI: <https://doi.org/10.1080/10406638.2022.2026989>.
35. Yavuz, S. Ç.; Akkoç, S.; Tüzün, B.; Şahin, O.; Saripinar, E. *Synth. Commun.* 2021, 51, 2135-2159. DOI: <https://doi.org/10.1080/00397911.2021.1922920>.
36. Xavier, T.; Kenny, P. T.; Manimaran, D.; Joe, I. H. *Spectrochim. Acta A Mol. Biomol. Spectrosc.* 2015, 145, 523-530. DOI: <https://doi.org/10.1016/j.saa.2015.02.087>.
37. Suresh, D.; Amalanathan, M.; Joe, I. H.; Jothy, V. B.; Diao, Y.-P. *Spectrochim. Acta A Mol. Biomol. Spectrosc.* 2014, 130, 591-603. DOI: <https://doi.org/10.1016/j.saa.2014.03.043>.
38. Devi, K.S.; Subramani, P.; Parthiban, S.; Sundaraganesan, N. *J. Mol. Struct.* 2020, 1203, 127403. DOI: <https://doi.org/10.1016/j.molstruc.2019.127403>.
39. Adwin Jose, P.; Sankarganesh, M.; Dhavethu Raja, J.; Senthilkumar, G. S.; Nandini Asha, R.; Raja, S. J.; Sheela, C. D. *J. Biomol. Struct. Dyn.* 2021, 21, 10715-10729. DOI: <https://doi.org/10.1080/07391102.2021.1947382>.
40. Rodriguez, A. C.; Park, H.-W.; Mao, C.; Beese, L. S. *J. Mol. Biol.* 2000, 299, 447-462. DOI: <https://doi.org/10.1006/jmbi.2000.3728>.
41. Williams, R. S.; Green, R.; Glover, J. *Nat. Struct. Biol.* 2001, 8, 838-842. DOI: <https://doi.org/10.1038/nsb1001-838>.
42. Rouvinen, J.; Rautiainen, J.; Virtanen, T.; Zeiler, T.; Kauppinen, J.; Taivainen, A.; Mäntyjärvi, R. *J. Biol. Chem.* 1999, 274, 2337-2343. DOI: <https://doi.org/10.1074/jbc.274.4.2337>.

43. Okamoto, K.; Ikemori-Kawada, M.; Jestel, A.; von König, K.; Funahashi, Y.; Matsushima, T.; Tsuruoka, A.; Inoue, A.; Matsui, J. *ACS Med. Chem. Lett.* **2015**, *6*, 89-94. DOI: <https://doi.org/10.1021/ml500394m>.
44. Yun, C.-H.; Boggon, T. J.; Li, Y.; Woo, M. S.; Greulich, H.; Meyerson, M.; Eck, M. J. *Cancer cell.* **2007**, *11*, 217-227. DOI: <https://doi.org/10.1016/j.ccr.2006.12.017>.
45. Brough, P. A.; Aherne, W.; Barril, X.; Borgognoni, J.; Boxall, K.; Cansfield, J. E.; Cheung, K.-M. J.; Collins, I.; Davies, N. G.; Drysdale, M. J. *J. Med. Chem.* **2008**, *51*, 196-218. DOI: <https://doi.org/10.1021/jm701018h>.
46. Masand, V. H.; Rastija, V. *Chemom. Intell. Lab. Syst.* **2017**, *169*, 12-18. DOI: <https://doi.org/10.1016/j.chemolab.2017.08.003>.
47. DeLano, W. L. <http://www.pymol.org>, **2002**.
48. Pettersen, E. F.; Goddard, T. D.; Huang, C. C.; Couch, G. S.; Greenblatt, D. M.; Meng, E. C.; Ferrin, T. E. *J. Comput. Chem.* **2004**, *25*, 1605-1612. DOI: <https://doi.org/10.1002/jcc.20084>.
49. Laskowski, R. A.; Swindells, M. B. *J. Chem. Inf. Model.* **2011**, *51*, 2778-2786 DOI: <https://doi.org/10.1021/ci200227u>.
50. Lipinski, C. A. *Drug. Discov. Today. Technol.* **2004**, *1*, 337-41. DOI: <https://doi.org/10.1016/j.ddtec.2004.11.007>.
51. Cheng, F.; Li, W.; Zhou, Y.; Shen, J.; Wu, Z.; Liu, G.; Lee, P. W.; Tang, Y. *J. Chem. Inf. Model.* **2012**, *52*, 3099-3105. DOI: <https://doi.org/10.1021/ci300367a>.
52. Saravanan, R.; Seshadri, S.; Gunasekaran, S.; Mendoza-Meroño, R.; García-Granda, S. *Spectrochim. Acta A Mol. Biomol. Spectrosc.* **2015**, *139*, 321-328. DOI: <https://doi.org/10.1016/j.saa.2014.12.026>.
53. Demircioğlu, Z.; Kaştaş, Ç. A.; Büyükgüngör, O. **2015**, *1091*, 183-195. DOI: <https://doi.org/10.1016/j.molstruc.2015.02.076>.
54. Obu, Q. S.; Louis, H.; Odey, J. O.; Eko, I. J.; Abdullahi, S.; Ntui, T. N.; Offiong, O. E. *J. Mol. Struct.* **2021**, *1244*, 130880. DOI: <https://doi.org/10.1016/j.molstruc.2021.130880>.
55. Mumit, M. A.; Pal, T. K.; Alam, M. A.; Islam, M. A.-A.-A.-A.; Paul, S.; Sheikh, M. C. *J. Mol. Struct.* **2020**, *1220*, 128715. DOI: <https://doi.org/10.1016/j.molstruc.2020.128715>.
56. Ouaket, A.; Chraka, A.; Raissouni, I.; El Amrani, M. A.; Berrada, M.; Knouzi, N. *J. Mol. Struct.* **2022**, *1259*, 132729. DOI: <https://doi.org/10.1016/j.molstruc.2022.132729>.
57. Abdou, A.; Omran, O. A.; Nafady, A.; Antipin, I. S. *Arabian J. Chem.* **2022**, *15*, 103656. DOI: <https://doi.org/10.1016/j.arabjc.2021.103656>.
58. Ulucam, G.; Yenturk, B.; Okan, S. E.; Aktas, S. *Chem. Pap.* **2020**, *74*, 1881-1889. DOI: <https://doi.org/10.1007/s11696-019-01037-9>.
59. Almeida, M. O.; Barros, D. A. S.; Araujo, S. C.; Faria, S.; Maltarollo, V. G.; Honorio, K. M. *Spectrochim. Acta A Mol. Biomol. Spectrosc.* **2017**, *184*, 169-176. DOI: <https://doi.org/10.1016/j.saa.2017.04.070>.
60. Boshala, A.; Said, M. A.; Assirey, E. A.; Alboriki, Z. S.; AlObaid, A. A.; Zarrouk, A.; Warad, I. *J. Mol. Struct.* **2021**, *1238*, 130461. DOI: <https://doi.org/10.1016/j.molstruc.2021.130461>.
61. Kargar, H.; Fallah-Mehrjardi, M.; Behjatmanesh-Ardakani, R.; Munawar, K. S.; Ashfaq, M.; Tahir, M. N. *J. Mol. Struct.* **2022**, *1250*, 131691. DOI: <https://doi.org/10.1016/j.molstruc.2021.131691>.
62. Anwer, K. E.; Sayed, G. H.; Ramadan, R. M. *J. Mol. Struct.* **2022**, *1256*, 132513. DOI: <https://doi.org/10.1016/j.molstruc.2022.132513>.
63. Śmiszek-Lindert, W. E.; Chelmecka, E.; Lindert, O.; Dudzińska, A.; Kaczmarczyk-Sedlak, I. *Spectrochim. Acta A Mol. Biomol. Spectrosc.* **2018**, *201*, 328-338. DOI: <https://doi.org/10.1016/j.saa.2018.05.021>.
64. Umar, Y. *J. Mol. Struct.* **2022**, 133230. DOI: <https://doi.org/10.1016/j.molstruc.2022.133230>.
65. Unsalan, O.; Szolnoki, B.; Toldy, A.; Marosi, G. *Spectrochim. Acta A Mol. Biomol. Spectrosc.* **2012**, *98*, 110-115. DOI: <https://doi.org/10.1016/j.saa.2012.08.050>.

66. Uluçam, G.; Bağcı, U.; Şuekinçi Yılmaz, A.; Yentürk, B. *Spectrochim. Acta. A Mol. Biomol. Spectrosc.* **2022**, 279, 121429. DOI: <https://doi.org/10.1016/j.saa.2022.121429>.
67. Mary, Y. S.; Mary, Y. S.; Resmi, K.; Kumar, V. S.; Thomas, R.; Sureshkumar, B. *Heliyon*. **2019**, 5, e02825. DOI: <https://doi.org/10.1016/j.heliyon.2019.e02825>.
68. Daina, A.; Michielin, O.; Zoete, V. *J. Chem. Inf. Model.* **2014**, 54, 3284-3301. DOI: <https://doi.org/10.1021/ci500467k>.
69. Daina, A.; Zoete, V. *Chem. Med. Chem.* **2016**, 11, 1117-21. DOI: <https://doi.org/10.1002/cmdc.201600182>.
70. Walters, W. P.; Murcko, M. A. *Adv. Drug Delivery Rev.* **2002**, 54, 255-71. DOI: [https://doi.org/10.1016/S0169-409X\(02\)00003-0](https://doi.org/10.1016/S0169-409X(02)00003-0).





